MAGNETIC MEDICAL CAPSULE ROBOTS

By

Christian Di Natali

Dissertation
Submitted to the Faculty of the
Graduate School of Vanderbilt University
in partial fulfillment of the requirements
for the degree of

DOCTOR OF PHILOSOPHY
in

Mechanical Engineering

August, 2015

Nashville, Tennessee

Approved:	Date:
Dr. Pietro Valdastri	5/21/2015
Dr Nabil Simaan	5/21/2015
Dr Robert J. Webster III	5/21/2015
Dr. Karl Zelik	5/21/2015
Dr. Keith L. Obstein	5/21/2015

MECHANICAL ENGINEERING

MAGNETIC MEDICAL CAPSULE ROBOTS

CHRISTIAN DI NATALI

Thesis under the direction of Professor Pietro Valdastri

Over the last decade, researchers have started exploring the design space of Medical Capsule Robots (MCRs): devices that can operate within the human body performing functionalities such as diagnosing, monitoring, and treating diseases. Clinical applications for MCRs span from abdominal surgery to endoscopy. MCRs are severely resource constrained devices in size and in available mechanical/electrical power.

Magnetic manipulation is becoming one of the main strategies for MCRs navigation and remote actuation, as it allows the transmission of forces across a physical barrier without requiring an internal source of power.

The current state of the art lacks proprioceptive systems able to control magnetic actuation to enable MCRs to perform medical procedures. This dissertation presents controllable strategies for remote and local magnetic manipulation of MCRs combined with real-time proprioceptive sensing.

The study focuses on two main applications: magnetic pose detection for navigation of Wireless Capsule Endoscope (WCE) along the gastrointestinal (GI) tract, and Local Magnetic Actuation (LMA) for powering Degrees of Freedoms (DOFs) of abdominal surgical robots.

The proposed magnetic pose detection algorithms were successfully applied to remote navigation on several WCE prototypes during *in-vivo* trials. Two different approaches for magnetic pose detection compatible with magnetic actuation based on sensor fusion are presented and evaluated. The first approach takes advantage of the magnetic field mathematical derivation based on cylindrical symmetry, performing absolute pose detection for 50 Hz real-time systems. The second algorithm achieves a refresh rate of 1 kHz applying a least square interpolation to the finite element solution of the magnetic field, to obtain Jacobians closed-form expression function of capsule poses changes. A third algorithm estimates the force generated by magnetic coupling along the magnetization direction to study the force required to drag WCEs along the GI tract.

The second topic covers the design and control for the LMA. This concept allows the transmission of rotary motion by applying the magnetic spur gear concept to actuate robotic DOFs of MCRs. The proposed dynamic model is used to design closed-loop control strategies. Two surgical tools based on the LMA are presented: a single-DOF retractor and a 4-DOF manipulator.

Approved Dr. Pietro Valdastri Date 5/21/2015

Contents

Page

LIST OF TABLES viii

LIST OF FIGURES x

ACRONYMS 1

I. MAGNETIC MEDICAL CAPSULE ROBOT: INTRODUCTION 3

- I.1. Overview and Objectives 4
- I.2. Background and Significance: Magnetic Medical Capsule Robots . 6
  - I.2.1. Magnetic MCR applied to Minimally Invasive Surgery (MIS) 7
  - I.2.2. Magnetic MCR applied to Endoscopy 8
  - I.2.3. Magnetic Localization to Guide Robotic Endoscopes . . . 9
  - I.2.4. Magnetic Gears 12
- I.3. Abdominal Surgery and Endoscopy: Requirements and Specifications 14
- I.4. Remote and Local Magnetic Manipulation: Dissertation Overview 14

II. REMOTE MAGNETIC MANIPULATION: NAVIGATION OF WCE AND FLEXIBLE SCOPE 16

- II.1. Technical specification 16
- II.2. Technical Contribution 17
  - II.2.1. Magnetic Analysis for Position Estimation 17
    - II.2.1.1. Inertial Sensing for Orientation Estimation 22
    - II.2.1.2. Iterative Solution for Position Estimation 23
    - II.2.1.3. Magnetic Attraction Force Feedback 28
- II.3. Design contribution 32
  - II.3.1. Wireless Surgical Palpator Design 32
    - II.3.1.1. Wireless *In-Vivo* Platform for Resistance Forces Measurement of WCE Inside the GI Tract 35
    - II.3.1.2. High refresh rate Jacobian-based Iterative Method For Magnetic Localization in WCE 38

III. LOCAL MAGNETIC MANIPULATION FOR ROBOTIC ABDOMINAL SURGERY 41

- III.1. Magnetic Spur Gear for Remote Rotary Motion Transmission: Technical Specification and Objectives 41
- III.2. Technical Contribution: Speed control of a magnetic spur gear . . 46

III.2.1. Controlling a rotational Local Magnetic Actuation Unit . 46
III.2.2. Static Analysis of the Magnetic Spur Gear Coupling . . . 47
III.2.3. Dynamic Analysis of the Magnetic Coupling 50
III.2.4. Sensor Feedback 55
III.2.5. Close-Loop Control on Motor Side 57
III.2.6. Close-loop Control on Load Side 58
III.2.7. Control Strategies Comparison and Performances 59
III.3. Design contribution 70
III.3.1. 1 DOF Laparoscopic Tissue Retractor Based on LMA . . 70
III.3.2. 4 DOFs LMA-based surgical robotic manipulator design . 73

IV. CONCLUSIONS AND FUTURE WORKS 77

IV.1. Conclusion: Magnetic Navigation and Pose Detection 77
IV.2. Conclusion: Local Magnetic Actuation 82
IV.3. Research Outcomes 88

APPENDICES 92

A. REAL-TIME POSE DETECTION FOR MAGNETIC MEDICAL DEVICES 93

A.1. Abstract 93
A.2. Introduction 93
A.3. Materials 94
A.3.1. Principle of Operation 94
A.3.2. Platform Overview 97
A.4. Experimental Validation and Results 98
A.5. Conclusion 100

B. WIRELESS TISSUE PALPATION FOR INTRAOPERATIVE DETECTION OF LUMPS IN SOFT TISSUE 101

B.1. Abstract 101
B.2. Introduction 101
B.3. Materials 103
B.3.1. Principle of Operation 103
B.3.2. Wireless Palpation Probe Development 105
B.3.3. Communication Protocol and User Interface 108
B.3.4. Wireless Palpation Probe Characterization 109
B.3.4.1. Localization 109
B.3.4.2. Pressure Sensing Head 109
B.3.4.3. Electronics 110
B.4. Wireless Palpation Probe Assessment 111
B.4.1. Assessment of Local Stiffness Identification 111
B.4.2. In Vivo Validation 111

B.5. Conclusions and Future Work 116

C. JACOBIAN-BASED ITERATIVE METHOD FOR MAGNETIC LOCALIZATION IN ROBOTIC CAPSULE ENDOSCOPY 118

C.1. Abstract 118
C.2. Introduction 118
C.3. Motivation and Clinical Context 120
C.4. Method 121
  C.4.1. Iterative Method for Magnetic Localization 121
  C.4.2. Direct and Inverse Magnetic Relationship 123
  C.4.3. Three Dimensional Reconstruction 128
C.5. Capsule Orientation Algorithm 128
C.6. Simulation-Based Validation 130
  C.6.1. Magnetic Direct Relationship 130
  C.6.2. Magnetic Inverse Relationship 131
C.7. Experimental Assessment 132
  C.7.1. Experimental Platform 132
    C.7.1.1. Hardware 132
    C.7.1.2. Wireless Capsule 133
    C.7.1.3. Software Architecture 134
  C.7.2. Experiments and Results 135
    C.7.2.1. Capsule orientation algorithm assessment 135
    C.7.2.2. Steady state positional drift evaluation 136
    C.7.2.3. Robustness to initialization errors 137
    C.7.2.4. Robustness to positional lag 138
    C.7.2.5. General assessment 139
C.8. Conclusions 141

D. WIRELESS PLATFORM FOR MEASUREMENT OF RESISTANT PROPERTIES OF THE GI TRACT: A WIRELESS PLATFORM FOR *IN VIVO* MEASUREMENT OF RESISTANCE PROPERTIES OF THE GASTROINTESTINAL TRACT 144

D.1. Abstract 144
D.2. Introduction 144
D.3. Materials and Methods 146
  D.3.1. Method Overview 146
  D.3.2. Platform Overview 147
  D.3.3. Force and Motion Sensing Module 148
    D.3.3.1. Intermagnetic Force Estimation 150
    D.3.3.2. Capsule Motion Estimation 151
  D.3.4. Communication and Power Supply Modules 153
  D.3.5. User Interface 154
D.4. Platform Assessment 154

    D.4.1. Validation of Intermagnetic Force and Capsule Position Estimation . . . 154
    D.4.2. Validation of Resistant Force Estimation . . . 156
    D.4.3. In Vivo Validation . . . 158
  D.5. Conclusions and Future Work . . . 160

E. TRANS-ABDOMINAL ACTIVE MAGNETIC LINKAGE FOR ROBOTIC SURGERY: CONCEPT DEFINITION AND MODEL ASSESSMENT . . . 165

  E.1. Abstract . . . 165
  E.2. Introduction . . . 165
  E.3. Principle of Operation . . . 167
  E.4. Modeling . . . 171
  E.5. Experimental Assessment . . . 174
  E.6. Discussion and Conclusion . . . 177

F. CLOSED-LOOP CONTROL OF LOCAL MAGNETIC ACTUATION FOR ROBOTIC SURGICAL INSTRUMENTS . . . 180

  F.1. Abstract . . . 180
  F.2. Introduction . . . 180
    F.2.1. Clinical Motivation . . . 181
    F.2.2. Technical Contribution . . . 183
  F.3. Controlling a LMA Actuation Unit . . . 184
    F.3.1. Dynamic Model of the Magnetic Gear Coupling . . . 185
    F.3.2. Actuator Model and Sensor Feedback . . . 188
      F.3.2.1. Actuator Model . . . 188
      F.3.2.2. Sensor Feedback . . . 188
    F.3.3. Closing the Control Loop . . . 190
      F.3.3.1. Motor-side Closed-Loop Control . . . 190
      F.3.3.2. Load-side Closed-Loop Control . . . 190
  F.4. Model Validation and Experimental Assessment . . . 191
    F.4.1. Experimental Platform . . . 191
    F.4.2. Dynamic Model Validation . . . 193
    F.4.3. Closed-Loop Control Validation . . . 194
    F.4.4. Load Rejection and Torque Transmission . . . 198
    F.4.5. Performance Evaluation of LMA . . . 201
  F.5. Conclusions and Future Work . . . 206
  F.6. Appendix: Appendix of Multimedia Extensions . . . 208

G. LAPAROSCOPIC TISSUE RETRACTOR BASED ON LOCAL MAGNETIC ACTUATION . . . 209

  G.1. Abstract . . . 209
  G.2. Introduction . . . 210

G.3. Clinical Consideration 212
G.4. Principle of Operation 214
G.5. Design of the LapR-LMA Platform 215
  G.5.1. Magnetic Design 215
    G.5.1.1. Anchoring Unit 215
    G.5.1.2. Actuation Unit 215
  G.5.2. Mechanical train design 218
    G.5.2.1. Planetary Gearhead 218
    G.5.2.2. Power Screw 220
    G.5.2.3. Offset Crank Mechanism 221
    G.5.2.4. Additional components and system integration . . 223
  G.5.3. LapR-LMA modeling 224
    G.5.3.1. Tissue lifting model 224
    G.5.3.2. Tissue supporting model 225
  G.5.4. External Controller 226
G.6. Experimental Assessment 226
  G.6.1. Benchtop Experiments 227
  G.6.2. Ex vivo trials 228
  G.6.3. In vivo trials 229
G.7. Conclusions and Future Developments 231

H. SURGICAL ROBOTIC MANIPULATOR BASED ON LOCAL MAGNETIC ACTUATION 234

H.1. Background 234
H.2. Methods 235
H.3. Results 236
H.4. Interpretation 237

BIBLIOGRAPHY 238

List of Tables

Page

I.1. Technical specification required for the distal surgery robotic instrument during abdominal surgery. 15

I.2. Technical specification required for localization of capsule endoscope during passive locomotion and magnetic navigation along the GI tract. . . . 15

III.1. Mean relative errors in T_L estimation at different velocities and intermagnetic distances within the loaded regime. 56

III.2. Expected amount of torque transmitted, $\tilde{T}_G^{Dd}$, experimental amount of torque transmitted using the load-side closed-loop control, T_L^{max}, and efficiency defined as percentage of the theoretical amount of torque transmitted at different intermagnetic distances. 68

III.3. Off-the-shelf EM Motors comparable with the size of the driven magnet used in this work. 68

IV.1. Features and performances of the algorithms proposed in this dissertation. 78

IV.2. Scientific and medical contribution presented in this dissertation. 79

IV.3. LMA's actuation and anchoring unit features and performances. 83

IV.4. Design contribution presented in this dissertation. 84

A.1. Localization success rate for different $|\vec{d}|$ 100

C.1. Portions of $\mathcal{G}'$ showing different levels of relative error in the interpolated magnetic field from the proposed method and the single magnetic dipole model. 131

C.2. Results of the steady state positional drift experiment (T01). For the eight trials, the radial and axial coordinates of the EPM were fixed to 80 mm and 130 mm, respectively. The azimuth coordinate θ_{EPM} is reported in the first column. Average radial and axial error for each trial are reported in the second and third column, respectively. 137

F.1. Mean relative errors in T_L estimation at different velocities and intermagnetic distances within the loaded regime. 195

F.2. Expected amount of torque transmitted, $\tilde{T}_G^{Dd}$, experimental amount of torque transmitted using the load-side closed-loop control, T_L^{max}, and efficiency defined as percentage of the theoretical amount of torque transmitted at different intermagnetic distances. 204

F.3. Off-the-shelf EM Motors comparable with the size of the driven magnet used in this work. 205

List of Figures

Page

I.1. (a) Natural orifice surgery using a Medical Capsule Robot for in-vivo procedure [1]. (b) Approximate dimensions of the natural orifice translumenal endoscopic surgery (NOTES) robot [1]. (c) Magnetic guidance system for Olimpus's WCE [2]. (d) Possible maneuvers of the Olimpus's WCE inside the stomach [2] and (e) an extract from the video recorded by the Olimpus's WCE [2]. 5

I.2. Schemagtic rappresentation of a MCR 6

I.3. (a) Minimally Invasive Surgery scenario representation where magnetic coupled robots are operating [3]. (b) Magnetic coupled surgical tissue retractor [3]. (c) Magnetic coupled endoscope camera [4]. (d) Magnetic coupled endoscope camera during in-vivo procedure [3]. 8

I.4. (a) MAC, WCE equipped with sensors, magnets, camera, illumination tool channel and air insufflation channel [5]. (b) Experimental platform overview [5]. (c) Image stream from the MAC while insufflating the colon [5]. (d) Hybrid capsule principle of operation (WCE equipped with magnets and motor actuated legs for locomotion inside the colon) [6]. (e) Schematic view of the hybrid capsule internal mechanism and cross section view of the locomotion unit [6]. 10

I.5. (a) Scheme of the cube magnetic sensor array and (b) its set up [7]. (c) Schematic representation of the motion sensing system by [8], (d) The four pictures show the Given Imaging M2A capsule, the drawing of the two semicylindrical parts of the considered shell, the picture of the internal arrangement of the capsule and the schematic sectional drawing of the device components: 1: optical dome, 2: focal lens, 3: white LEDs, 4: CMOS imager, 5: batteries, 6: application-specified integrated circuit (ASIC) transmitter, 7: RF antenna, and 8: magnetic shell [9]. (e) Niobe magnetic navigation system developed by Stereotaxis. It includes the following. (a) and (b) Couple of permanent magnets. (c) Fluoroscopic scanner. (d) Visualization displays. (e) Patients table [9]. 11

I.6. (a) [10] states: "Magnetism? Yes, that is possible- the gear rotors motion couples through a modulated interaction between the flux generated by magnets on input and output rotors. If the torque on the input exceeds maximum design levels, the magnetic gears simply slip; there are no broken teeth, ground-up gears or worse, a fire." (b) Axial magnetic gear enragement such in [11]. Concentric magnetic gear [12], (c) front view of the structure and (d) assembly component view. 13

II.1. Schematic view of the magnetic navigation platform for endoscopic procedure. 16

II.2. Schematic view of the External Permanent Magnet (EPM) and the capsule with the different reference frames used in the algorithm. A slice of the magnetic field map is represented in the lower left quadrant of the workspace. 18

II.3. Schematic view of the magnetic field distribution for a cylindrical axially-magnetized permanent magnet. (A) View of the $\mathcal{H}$ planes, its subset $\mathcal{H}'$ and the domain $\mathcal{G}'$, (B) shows the radial distribution of the magnetic field on the plane $[\hat{r}, \hat{\theta}]$ 19

II.4. Schematic representation of the source of magnetic field (External Permanent Magnet (EPM) in figure) and two sequential positions (i.e., $\mathbf{p}_i$ and $\mathbf{p}_{i+1}$) of the capsule to be localized. 24

II.5. Schematic view of the wireless capsule for measuring resistant properties of the GI tract. 28

II.6. Magnetic field sensor (MFS) position with respect to the internal permanent magnet. 29

II.7. (A) Lateral view of the IPM. (B) Schematic view of the i-th quadrant of the IPM. 32

II.8. Principle of operation for wireless tissue palpation using a Wireless Palpation Probe (WPP). 33

II.9. The WPP during indentation and the external source of magnetic field with a slice of the magnetic field map. Vectors $\mathbf{r}_0$ and $\mathbf{r}_f$ represent the WPP position $\mathbf{r}$ at the beginning and at the end of the indentation. They are represented at the interface of WPP and tissue, rather than at O_w, for a better understanding of their physical meaning. 34

II.10. Schematic representation of the principle of operation. The attraction force $\mathbf{F}_a$ is generated by magnetic coupling between an EPM and a magnet embedded in the capsule. The intermagnetic force $\mathbf{F}_a$ and the capsule position $\mathbf{d}$ with respect to the EPM are recorded wirelessly in real time. $\mathbf{F}_r$ is the resistant force, $\mathbf{g}$ is the gravitational acceleration vector, R_c is the rotational matrix of the capsule reference frame with respect to the global Cartesian coordinate system, while R_m is the rotational matrix of the reference frame at the EPM with respect to the global Cartesian coordinate system. 37

II.11. Experimental platform: a) Robotic Manipulator (RM) and EPM. b) Visual rendering of the WCE and its internal components. 39

III.1. Concept of a magnetically actuated surgical platform. On the left are shown several DOFs that can be obtained by simple magnetic coupling. . 42

III.2. Functional representation of a LMA-based robotic instrument coupled across the abdominal wall. 42

III.3. Two examples of combining LMA units to obtain End Effector (EE)'s DOFs: (A) Combination of an anchoring unit and two translational Local Magnetic Actuation (tLMA) units. (B) Combination of an anchoring unit and two rotational Local Magnetic Actuation (rLMA) units. In both combinations showed in the examples, two actuation units can operate asymmetrically achieving yaw of the platform. Lift can be obtained by a symmetric operation, while push is possible only in the example (A), because rigid transmission allow push and pull. 45

III.4. Block diagram for the closed-loop control of a LMA actuation unit. . . . 46

III.5. Schematic representation of EPM and Internal Permanent Magnet (IPM) for a typical LMA unit. The EPM is a cube in the anchoring and in the tLMA units and a cylinder in the rLMA unit. 47

III.6. (a) Schematic cross-section of the EDM and IDM composing the actuation unit. (b) Torque transferred from the EDM to the IDM as a function of the angular displacement between EDM and IDM. The cross-section view of the actuation unit is reported below the plot. (c) Vertical attraction force generated by the actuation unit as the magnets rotate. This plot assumes $\Delta\theta = 0$. The cross section view of the actuation unit is reported below the plot. 50

III.7. (a)T_{max} and its exponential regression at different separation distances, the solid horizontal line represents the average nominal torque for commercially available EM motors that would fit a volume similar to the IDM. (b)$F_v and F_h$ and their exponential regressions at different separation distances, assuming $\Delta\theta = 0$. The selected Internal Driven Magnet (IDM) was 9.52mm in outside diameter (OD), 2.38 mm in internal diameter (ID), and 9.52 mm in length (L). It was made out of NdFeB, with a relative magnetic permeability of 1.05, and a magnetization grade of N42 (1.32 T magnetic remanence). The External Driving Magnet (EDM) was 25.4 mm in OD, 6.32 mm in ID, 25.4 mm in L, and presented the same magnetic features as the IDM. 51

III.8. Schematic overview (a) and lateral cross section (b) of the LMA actuation unit based on two diametrical magnetized cylindrical magnets. 52

III.9. Equivalent model of a magnetic spur gear pair with asymmetrical magnets. 53

III.10. Block diagram of the open-loop magnetic gear system. 54

III.11. Comparison between the estimated and the reference load torque for h=4 cm and ω_D=1000 rpm. The unloaded, loaded and pole-slipping regimes are highlighted by the dashed vertical lines. 56

III.12. Angular position (θ_D and θ_d), angular speed (ω_D and ω_d), angular displacement of the drive train ($\Delta\theta$), and its time derivative ($\Delta\omega$) are obtained through direct measurement of the magnetic field (B_D and B_d) generated by the driving and the driven magnets along the vertical direction. 57

III.13. Motor-side speed control system with PI controller. 58

III.14. Load-side speed control system with the custom controller fed by ω_d. . . 59

III.15. Bode amplitude diagrams for the motor-side (a) and load-side (b) open-loop transfer functions for six discrete values of h (i.e., $h = [2, 3, 4, 5, 6, 7]$ cm). 60

III.16. Simulated step response for the motor-side (a) and load-side (b) closed-loop control for six discrete values of h (i.e., $h = [2, 3, 4, 5, 6, 7]$ cm). 61

III.17. (a) Simulated and experimental step response at h=4 cm for motor-side closed-loop control. Both the measured ω_D and ω_d are reported in the figure. (b) Simulated and experimental step response at h=4 cm for load-side closed-loop control. Both the measured ω_D and ω_d are reported in the figure. 63

III.18. Experimental step responses for motor-side closed-loop control (a, b, c) and load-side closed-loop control (d, e, f) with T_L at 20% (a, d), 50% (b, e), and 80% (c, f) of $\tilde{T}_G^{Dd}$. Experiments were performed at h=4 cm imposing a ω_{ref}=1000 rpm. Each plot shows the measured values for both ω_D and ω_d. 64

III.19. Experimental load rejection responses for motor-side closed-loop control (a) and load-side closed-loop control (b). The profile of T_L, moving from 28% of $\tilde{T}_G^{Dd}$ to 85% of $\tilde{T}_G^{Dd}$ and back to its initial value, is represented below the speed plot. Experiments were performed at h=4 cm setting ω_{ref}=1500 rpm. Each plot shows the measured values for both ω_d and ω_D and the trend of the applied load torque. 65

III.20. Maximum torque at the load before entering the pole-slipping regime, measured using the motor-side (a) and the load-side (b) controller at different speeds and separation distances. Each data point is the result of ten independent trials. 67

III.21. Maximum torque at the load before entering the pole-slipping regime as a function of the intermagnetic distance. Theoretical value, $\tilde{T}_G^{Dd}$, and experimental data obtained by using the load-side closed-loop control, T_L^{max}. 69

III.22. Perspective rendering of the assembled LapR-LMA in the closed (γ=0) configuration (a) and in the open ($\gamma = \pi/2$) configuration (b). (c) The LapR-LMA prototype, where part of the outer shell was removed to shows the internal components. (d) Schematic representation of the LapR-LMA and the external controller components. (e) Maximum weight that can be lifted by operating the LapR-LMA (dashed line), and maximum weight that can be statically supported by the LapR-LMA (solid line). Both weight limitations are plotted as functions of the intermagnetic distance and the opening angle of the retracting lever. The measurements obtained during benchtop experiments are presented as single data points. 70

III.23. Schematic view of the MultiDOF-LMA design (A), the spherical wrist schematic design (B) and the prototype implementation picture (C). . . . 75

III.24. (A)Configuration of the MultiDOF-LMA prototype during introduction phase through the single port access, and (B) is the deployed configuration of the device during surgical operation phase. (C) Prototype of the manipulator's body with representation of each DOF and (D) represents the mobility of one of the DOFs. 76

III.25. (A) Actuation Unit, where the part of the outer shell was removed to show the internal components. (1) represents the embedded permanent magnet or the IDM. (2) Two stages planetary gear with transmission ratio of 1:16. (3) Worm gear system with gear ratio of 1:15. (4) Spur gear system (2:1) and pulley where the cables are connected. (B) Two stages planetary gear components and (B) spur gears components fabricated in wire-cut Electrical Discharge Machining. 76

A.1. Schematic view of the EPM and the capsule with the different reference frames used in the algorithm. A slice of the magnetic field map is represented in the lower left quadrant of the workspace. 95

A.2. Validation of the proposed pose detection method: (A) View of the platform; (B) Close view of the capsule and the gimbal; (C) Schematic view of the capsule. 98

A.3. Error bar plot for the proposed pose detection method in the six DOF, reported for three different values of $|\vec{d}|$. The bar height represents the average error, while the whiskers account for standard deviation. 99

B.1. Principle of operation for wireless tissue palpation using a wireless palpation probe (WPP). 103

B.2. The WPP during indentation and the external source of magnetic field with a slice of the magnetic field map. Vectors $\mathbf{r}_0$ and $\mathbf{r}_f$ represent the WPP position $\mathbf{r}$ at the beginning and at the end of the indentation. They are represented at the interface of WPP and tissue, rather than at O_w, for a better understanding of their physical meaning. 104

B.3. (A) Schematic view and (B) picture of the wireless palpation probe. The signal conditioning stage, the triaxial accelerometer, the power regulation unit, and the wireless microcontroller are mounted on separate printed circuit boards (PCB) with a diameter of 9.9 mm. In particular, the signal conditioning stage was separated into two boards due to PCB area constraints. 106

B.4. Step response of the WPP pushing against a reference load cell. 110

B.5. Experimental data acquired by standard and wireless indentation for two different silicone samples. For this trial, relative errors in local stiffness identification were equal to 4.72% for sample 1 and 3.17% for sample 2. . 112

B.6. Picture of the surgical setup during the *in vivo* trial. (A) Snapshot of the laparoscopic camera view and the user interface during the creation of the volumetric stiffness map. (B) Picture of the surgical field. 113

B.7. Laparoscopic view of the WPP operated by the surgeon through a laparoscopic grasper during *in vivo* trials. 114

B.8. Local stiffness map acquired *in vivo* for a 6 cc agar gel lump injected into the liver. Since the surface of the liver was almost flat in the palpated region, a bidimensional projection of the map is shown. The local stiffness values inside areas A, B, and C were compared with the *ex vivo* map represented in Fig. B.9. 115

B.9. Stiffness map obtained with a standard uniaxial MTS, overlayed on the right lateral segment of the explanted porcine liver. The local stiffness values inside areas A, B, and C were compared with the *in vivo* map represented in Fig. B.8. 116

C.1. Schematic representation of the source of magnetic field (External Permanent Magnet (EPM) in figure) and two sequential positions (i.e., $\mathbf{p}_i$ and $\mathbf{p}_{i+1}$) of the capsule to be localized. α and β are the capsule's orientational angles yaw and pitch. 121

C.2. Block diagram of the proposed iterative algorithm for WCE's pose detection. In the schematic are displayed system's input, output, Jacobian of the MDR, 3D reconstruction and the off-line least square fit calibration, which lead to the characteristic matrices $\mathbf{A}_r$ and $\mathbf{A}_z$. 123

C.3. Schematic view of the magnetic field distribution for a cylindrical axially-magnetized permanent magnet. (A) View of the $\mathcal{H}$ planes, its subset $\mathcal{H}'$ and the domain $\mathcal{G}'$, (B) shows the radial distribution of the magnetic field on the plane $[\hat{r}, \hat{\theta}]$. 124

C.4. Relative error for the radial (A) and axial (B) magnetic field estimated by the MDR within $\mathcal{G}'$. 132

C.5. The ratio of relative errors of the single dipole model to the interpolation model for the radial (A) and axial (B) magnetic field components. Black regions stem from visualization artifacts due to oscillations in the ratio from 3 to 8 times. 133

C.6. Simulated motion of a capsule along a spiral trajectory in the center of $\mathcal{G}'$. The black line represents the reference trajectory, while the crossed line shows the capsule position estimated by applying the Jacobian-based iterative method. The cyan ellipses represent the ellipsoid of localization uncertainty due to magnetic field sensor noise. Colors in the crossed line express the relative error in position detection for the radial component. . 134

C.7. Experimental platform: (A) Robotic Manipulator (RM) and External Permanent Magnet (EPM). (B) Visual rendering of the Wireless Capsule Endoscope (WCE) and its internal components, where FMSM is the Force and Motion Sensing Module, WMC is the Wireless MicroController and PS is the Power Supply. 135

C.8. Schematic representation of the global frame, EPM frame and capsule frame. The capsule orientation angles $[\alpha, \beta, \gamma]$ are shown with respect the global frame. 136

C.9. Results for the steady state positional drift experiment (T01) and for the initialization error evaluation (T02) with an initialization error of $10mm$. Both T01 and T02 results are evaluated for the radial (left column) and the axial (right column) component. (a) Reference position vs. estimation. (b) Absolute positional errors. (c) Relative positional errors. (d) Residual measurement noise. The azimuth error is presented in Fig. C.12. 138

C.10. Position estimation results during the positional lag trial with uniform acceleration of 1.984 $\frac{m}{s^2}$. 139

C.11. Three-dimensional representation of the EPM trajectory and its estimation by the localization algorithm. 140

C.12. Typical trends for the radial (a), the axial (c) and the azimuth (e) component during the final experiment, and related absolute and relative errors (b, d, and f, respectively). 141

D.1. Schematic representation of the principle of operation. The attraction force $\mathbf{F}_a$ is generated by magnetic coupling between an external permanent magnet (EPM) and a magnet embedded in the capsule. The intermagnetic force $\mathbf{F}_a$ and the capsule position $\mathbf{d}$ with respect to the EPM are recorded wirelessly in real time. $\mathbf{F}_r$ is the resistant force, $\mathbf{g}$ is the gravitational acceleration vector, R_c is the rotational matrix of the capsule reference frame with respect to the global Cartesian coordinate system, while R_m is the rotational matrix of the reference frame at the EPM with respect to the global Cartesian coordinate system. 147

D.2. Schematic view of the wireless capsule for measuring resistant properties of the GI tract. 148

D.3. Magnetic field sensor (MFS) position with respect to the internal permanent magnet. 149

D.4. (A) Lateral view of the IPM. (B) Schematic view of the i-th quadrant of the IPM. 152

D.5. Experimental setup used to assess the intermagnetic force and capsule position estimation. 155

D.6. Modules of the estimated force $\mathbf{F}_a$, the reference force along $\mathbf{z}_c$, the estimated position $\mathbf{d}$, and the reference position as measured by the robotic manipulator encoders for part of a trial where the EPM was moved mainly along the $\mathbf{z}_c$ axis (i.e., from {x_c=8 mm, y_c=-10 mm, z_c=62 mm} to {x_c=8 mm, y_c=-5 mm, z_c=148 mm}. 156

D.7. Experimental setup used to validate the reconstruction of a known resistant force. 157

D.8. (A) Time variation of the modules of the resistant force estimated with the proposed method (solid blue line) and reference (dashed green line). The dashed vertical line indicates the instant when the EPM was moved towards the capsule by 2 mm, but the the magnetic force was not enough to overcome the elastic force. The solid vertical line indicates a second 2-mm motion of the EPM towards the capsule. This event is almost coincident with the start of capsule motion as detected by Eq. D.10. (B) Modules of the resistant force estimated with the proposed method (solid blue line) and reference (dashed green line) plotted as a function of capsule position. 162

D.9. Photograph of the operative setup during the *in vivo* trial. (A) The wireless capsule being introduced in the porcine large intestine. (B) The surgical field during measurement. 163

D.10. Plot of the modules of $\mathbf{F}_r$ and $\mathbf{d}$ acquired during the *in vivo* trial. The dashed vertical line indicates the instant when the EPM was moved closer to the capsule, while the solid vertical line indicates the instant when capsule motion started. 164

E.1. Concept of a magnetically actuated surgical platform. On the left are shown the several DoF that can be obtained by simple magnetic coupling. 166

E.2. Two examples of combining TAML units to obtain 2 DoF: (A) Combination of an anchoring unit and two t-TAML units; (B) Combination of an anchoring unit and two r-TAML units. 168

E.3. Schematic representation of EPM and IPM for a typical TAML unit. The EPM is a cube in the anchoring and in the t-TAML units and a cylinder in the r-TAML unit. 170

E.4. Configuration of the bench test used to evaluate the anchoring force. . . . 173

E.5. Experimental data and model prediction for the force F$_{x'}$ available at the IPM for the t-TAML unit. 174

E.6. Experimental data and model prediction for the force F$_{x'}$ available at the IPM for the t-TAML unit. 176

E.7. Bench test developed to evaluate the actuating torque $\tau_{x'}$ for the r-TAML unit. 176

E.8. Experimental data and model prediction for the torque $\tau_{x'}$ scaled by the shaft radius r_{shaft}, as a function of $\Delta\theta_{EPM}$, defined as the angle displacement between magnets' magnetization direction. This is the force available at the IPM for the r-TAML unit. 177

E.9. A possible design implementation combining 2 anchoring units and one r-TAML to operate a single DoF. 179

F.1. Functional representation of a LMA-based robotic instrument coupled across the abdominal wall. 182

F.2. Block diagram for the closed-loop control of a LMA actuation unit. . . . 184

F.3. Schematic overview (a) and lateral cross section (b) of the LMA actuation unit based on two diametrical magnetized cylindrical magnets. 186

F.4. Equivalent model of a magnetic spur gear pair with asymmetrical magnets. 186

F.5. Block diagram of the open-loop magnetic gear system. 187

F.6. Dynamic model of the EM DC motor with current monitoring. 189

F.7. Angular position (θ_D and θ_d), angular speed (ω_D and ω_d), angular displacement of the drive train ($\Delta\theta$), and its time derivative ($\Delta\omega$) are obtained through direct measurement of the magnetic field (B_D and B_d) generated by the driving and the driven magnets along the vertical direction. 189

F.8. Motor-side speed control system with PI controller. 190

F.9. Load-side speed control system with the custom controller fed by ω_d. . . 191

F.10. Picture of the experimental platform. The upper left inset shows the placement of the MFS next to the driving magnet. 192

F.11. FEM estimations of the maximum transmissible torque functions and their exponential fittings for different intermagnetic distances. 193

F.12. Comparison between the estimated and the reference load torque for h=4 cm and ω_D=1000 rpm. The unloaded, loaded and pole-slipping regimes are highlighted by the dashed vertical lines. 195

F.13. Bode amplitude diagrams for the motor-side (a) and load-side (b) open-loop transfer functions for six discrete values of h (i.e., $h = [2, 3, 4, 5, 6, 7]$ cm). 196

F.14. Simulated step response for the motor-side (a) and load-side (b) closed-loop control for six discrete values of h (i.e., $h = [2, 3, 4, 5, 6, 7]$ cm). 197

F.15. (a) Simulated and experimental step response at h=4 cm for motor-side closed-loop control. Both the measured ω_D and ω_d are reported in the figure. (b) Simulated and experimental step response at h=4 cm for load-side closed-loop control. Both the measured ω_D and ω_d are reported in the figure. 199

F.16. Experimental step responses for motor-side closed-loop control (a, b, c) and load-side closed-loop control (d, e, f) with T_L at 20% (a, d), 50% (b, e), and 80% (c, f) of $\tilde{T}_G^{Dd}$. Experiments were performed at h=4 cm imposing a ω_{ref}=1000 rpm. Each plot shows the measured values for both ω_D and ω_d. 200

F.17. Experimental load rejection responses for motor-side closed-loop control (a) and load-side closed-loop control (b). The profile of T_L, moving from 28% of $\tilde{T}_G^{Dd}$ to 85% of $\tilde{T}_G^{Dd}$ and back to its initial value, is represented below the speed plot. Experiments were performed at h=4 cm setting ω_{ref}=1500 rpm. Each plot shows the measured values for both ω_d and ω_D and the trend of the applied load torque. 202

F.18. Maximum torque at the load before entering the pole-slipping regime, measured using the motor-side (a) and the load-side (b) controller at different speeds and separation distances. Each data point is the result of ten independent trials. 203

F.19. Maximum torque at the load before entering the pole-slipping regime as a function of the intermagnetic distance. Theoretical value, $\tilde{T}_G^{Dd}$, and experimental data obtained by using the load-side closed-loop control, T_L^{max}.205

G.1. An external controller is required to anchor and actuate an LMA-based surgical instrument. The anchoring unit supports the device because of the attraction force that the External Anchoring Magnet (EAM) generates on the Internal Anchoring Magnet (IAM). The magnetic coupling between the External Driving Magnet (EDM) and the Internal Driven Magnet (IDM) provides actuation. A mechanism connected to the IDM controls a DoF of the end effector. 212

G.2. Schematic representation of the LapR-LMA and the external controller components. 214

G.3. FEA simulation and two term exponential fit for the magnetic attraction force at increasing intermagnetic separation distance. 216

G.4. (a) Schematic cross-section of the EDM and IDM composing the actuation unit. (b) Torque transferred from the EDM to the IDM as a function of the angular displacement between EDM and IDM. The cross-section view of the actuation unit is reported below the plot. (c) Vertical attraction force generated by the actuation unit as the magnets rotate. This plot assumes $\Delta\theta = 0$. The cross section view of the actuation unit is reported below the plot. 217

G.5. (a)T_{max} and its exponential regression at different separation distances, the solid horizontal line represents the average nominal torque for commercially available EM motors that would fit a volume similar to the IDM [26-28]. (b)$F_v and F_h$ and their exponential regressions at different separation distances, assuming $\Delta\theta = 0$. 218

G.6. (a) Three-stage PG components fabricated by spark erosion. (b) One of the three stages assembled. 219

G.7. Experimental setup used to test the efficiency of the PG 220

G.8. Schematic representation of the OCM. The slider is placed with an offset ($\overline{BC}$) with respect to the hinge point of the crank (O). Thanks to the connecting rod ($\overline{AB}$), the nut linear motion is converted in a crank angular displacement γ. 222

G.9. Mechanical pseudo-advantage Γ [mNm/N] of the OCM and its polynomial regression as a function of the lever angle γ [rad]. A maximum value of 9.63 mNm/N is obtained for $\gamma = 2\pi/17$, while a 4.67 mNm/N minimum occurs for the fully-open configuration (i.e., $\gamma = \pi/2$). 222

G.10. Perspective rendering of the assembled LapR-LMA in the closed (γ=0) configuration (a) and in the open (γ= $\pi/2$) configuration (b). (c) The LapR-LMA prototype, where part of the outer shell was removed to shows the internal components. 223

G.11. Maximum weight that can be lifted by operating the LapR-LMA (dashed line), and maximum weight that can be statically supported by the LapR-LMA (solid line). Both weight limitations are plotted as functions of the intermagnetic distance and the opening angle of the retracting lever. The measurements obtained during benchtop experiments are presented as single data points. 224

G.12. Structural model used to predict the weight that the LapR-LMA can statically support. (a) Cross-section of the LapR-LMA with the points of application of the different forces. (b) Free body diagram of the LapR-LMA. A is the extremity of the device at the side of the IAM, B is the point of application of F $_{anc}$, C is the point where the hinge of the lever is located, D is the point of application of F$_{act}$, X is the LapR-LMA center of mass. 226

G.13. Perspective rendering of the external controller. 227

G.14. Experimental setup during the benchtop experiments. 228

G.15. Sequence showing a single trial with a weight of 500g at d=2 cm. Lifting up the weight required 21 s, as indicated by the stopwatch in the lower right corner. 228

G.16. Ex vivo liver retraction using the LapR-LMA. In the sequence presented in (a), the intermagnetic distance is 2 cm, while in the sequence in (b) is 4 cm. 229

G.17. LapR-LMA performing liver retraction during the *in vivo* trials. 230

H.1. Schematic view of the MultiDOF-LMA design (A), the spherical wrist schematic design (B) and the prototype implementation picture (C). . . . 236

ACRONYMS

USB	Universal Serial Bus
EM	Electromagnetic
MCR	Medical Capsule Robot
PC	Personal Computer
PID	Proportional-Integral-Derivative
API	Application Programming Interface
MIS	Minimally Invasive Surgery
ADC	Analogue-to-Digital Converter
LDO	Low Drop Output
PMM	Power Management Module
ESD	Electrostatic Discharge
DC	Direct Current
FDA	U.S. Food and Drug Administration
IDE	Integrated Development Environment
FCS	Frame Check Sequence
RSSI	Received Signal Strength Indication
FSM	Finite State Machine
OS	Operating System
HAL	Hardware Abstraction Layer
LED	Light Emission Diode
SMAC	STORM Lab Modular Architecture for Capsules
MAC	Medical Air Capsule
PHY	Physical Layer
IMU	Inertial Measurement Unit
DOF	Degrees of Freedom
WCE	Wireless Capsule Endoscope
GI	gastrointestinal
CPU	Central Processing Unit
IDE	Investigational Device Exemption
WTP	Wireless Tissue Palpation
BEMF	Back Electromotive Force
NOTES	Natural Orifices Transluminal Endoscopic Surgery
WPD	Wireless Palpation Device
WSN	Wireless Sensor Networks

WMC	Wireless Microcontroller
FPC	Flat Printed Circuit Cable
WPP	Wireless Palpation Probe
LESS	Laparo-Endoscopic Single Site
MRI	Magnetic Resonance Imaging
CuDMM	Current Density Magnetic Model
ChDMM	Charge Density Magnetic Model
EPM	External Permanent Magnet
IPM	Internal Permanent Magnet
MDR	Magnetic Direct Relationship
MIR	Magnetic Inverse Relationship
FEM	Finite Element Method
FMSM	Force and Motion Sensing Module
MFS	Magnetic Field Sensor
LMA	Local Magnetic Actuation
AcU	Actuation Unit
AnU	Anchoring Unit
EE	End Effector
TAML	Trans-abdominal Active Magnetic Linkage
tLMA	translational Local Magnetic Actuation
rLMA	rotational Local Magnetic Actuation
EDM	External Driving Magnet
IDM	Internal Driven Magnet
IMU	Inertial Measurement Unit
LapR-LMA	Laparoscopic Tissue Retractor LMA-based
MultiDOF-LMA	Multi Degree Of Freedom LMA-based

Chapter I

MAGNETIC MEDICAL CAPSULE ROBOT: INTRODUCTION

The research objective of this dissertation is to study and develop strategies for controlled remote and local magnetic manipulation of MCR with a particular focus on gastrointestinal endoscopy and abdominal surgery application. These devices have the potential to enhance the diagnostic and interventional abilities for gastroenterologists and surgeons. This can be achieved by building controlled robotic platforms based on proprioceptive strategies to understand the magnetic coupling behavior in real-time. In details, the contributions of this dissertation focus on two main applications: magnetic pose detection for WCEs navigation along the GI tract, and LMA for powering DOFs of abdominal surgical robots.

The first topic aims to enable closed-loop control for magnetic navigation for WCE or soft tethered devices with magnetic tip. The proposed magnetic pose detection algorithms were successfully applied for remote navigation, monitoring several WCEs during *in-vivo* trials. Two different approaches for magnetic pose detection compatible with magnetic actuation based on sensor fusion, are presented and evaluated. The first approach performs absolute pose detection for 50 Hz real-time systems. The second algorithm achieves a refresh rate of 1 kHz by applying iterative magnetic pose detection, which is based on Jacobians closed-form expression of the magnetic field. The overall absolute error, considering both strategies for pose detection, ranges from 10 to 4 mm and from 9^o to 3^o.

The second topic is about design specification and control strategies for the LMA. This approach allows the transmission of rotary motion up to a distance of several centimeters. The rotation of a diametrically magnetized cylindrical driving magnet induces the rotation of another coupled alike magnet if constrained along its main axes. Therefore this magnetic coupling could be used as magnetic spur gear to actuate robotic DOFs of a MCRs across the abdominal patient's wall without the need of physical connections. The dynamic model, built upon mechanical and magnetic static models, describes the magnetic coupling physical behavior of this magnetic spur gear. The models are presented and experimentally validated and then used to design and compare the performances of two alternative closed-loop control strategies. The first control strategy is load side sensor free, whereas the second approach uses the load side angular speed and position to counter the characteristic oscillations of the magnetic system. Finally two surgical tools for MIS based on the LMA are presented and realized.

I.1 Overview and Objectives

Robotic systems have been applied to a wide range of surgical procedures including abdominal surgery, neurosurgery, cardiac surgery, otolaryngology, and urology [13]. In the future, one can expect to see many more customized robotic systems, purposely designed for specific clinical needs. From a technical perspective, the future trend in robotics will leverage extreme miniaturization to access and operate in environments that are out of reach for larger robots. A way to achieve it, using endoscope-like tools, is to move toward natural orifice surgery. An alternative approach is to cut the cord, making the robot completely untethered and mobile within the body. This enables the robot to enter the body though either a natural orifice (Natural Orifices Transluminal Endoscopic Surgery (NOTES)) or a very small incision (MIS), and then maneuver itself to a surgical site that may not be in close proximity to the point of entry [13].

Such mobile medical robotic systems may be created on a variety of scales, including micro- and nanoscales. Unlike micro- and nanoscale robots, which are useful in areas such as the eye [14] or the capillaries [15], where larger robots are precluded by anatomical constraints, mesoscale robots are ideal for areas like the GI tract and abdomen, where their larger payload capacity is advantageous.

The mesoscale (broadly defined as 1-100 mm) includes robots that are small, but easily visible and operable. Some robots in this category are designed to be inserted through incisions [1, 6, 16–19], and other are designed to be introduced by natural orifices [5, 20–27] (Fig. I.1).

As an emerging technology, many of these robots are still in the research and development phase and have not yet been clinically implemented, although an increasing number have been applied in animal studies [1, 5, 6, 18, 20–22, 24, 25]. Combined with the commercial and clinical success enjoyed by camera pills, the future of mesoscale mobile robots - referred in this research field as MCR - as platforms for diagnosis, prevention, monitoring, and surgical interventions, is bright.

In general, MCR are small in size (i.e., typically 1 cm in diameter), and they are able to collect information and interact with the surrounding environment. Therefore, MCRs are severely resource constrained in space available for power storage, mechanical power generation and mechanical power transmission. Therefore, the design of an MCR is often challenging and needs to consider the specific application constraints. In particular for remote navigation, the MCR is required to generate forces and torques to interact with

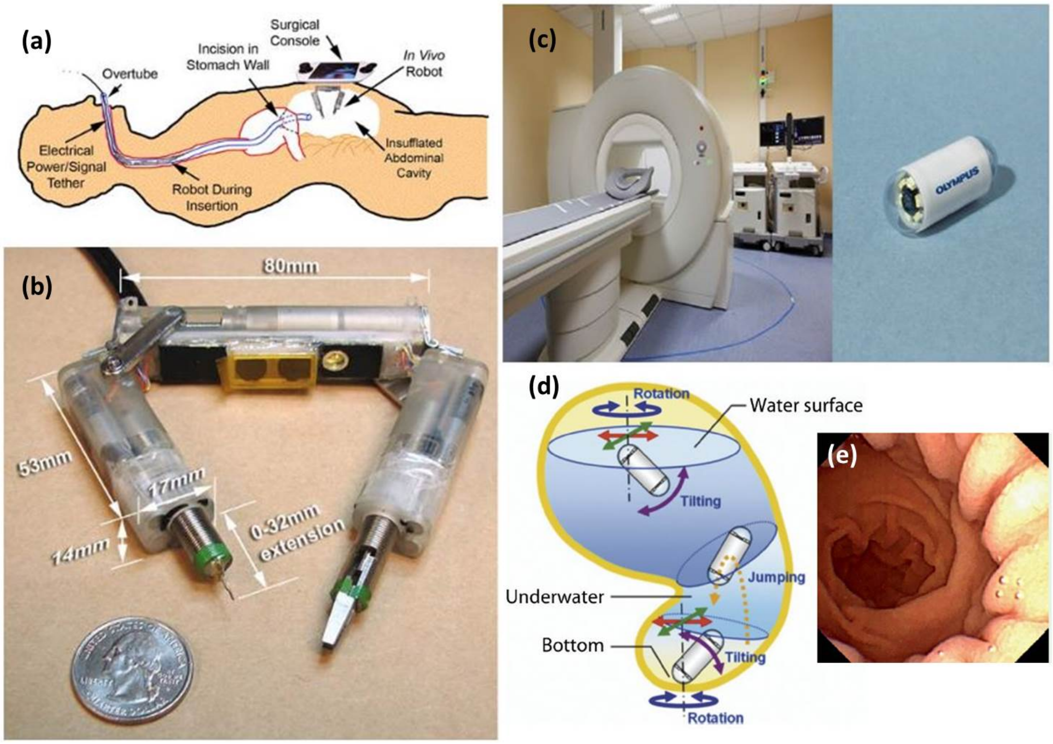

Figure I.1: (a) Natural orifice surgery using a Medical Capsule Robot for in-vivo procedure [1]. (b) Approximate dimensions of the natural orifice translumenal endoscopic surgery (NOTES) robot [1]. (c) Magnetic guidance system for Olimpus's WCE [2]. (d) Possible maneuvers of the Olimpus's WCE inside the stomach [2] and (e) an extract from the video recorded by the Olimpus's WCE [2].

the environment. One of the medical platforms based on remote magnetic manipulation is the Stereotaxis Niobe system [20] available since 2005 for catheter steering. The primary advantage of remote magnetic manipulation, in comparison with internal active locomotion, is an accurate omnidirectional steering by continuously generating forces with no power consumption and, consequently, reduction in components required on board the capsule.

Nowadays, remote magnetic navigation and magnetic manipulation seems to be the main strategy pursued for mesoscale robotic actuation with increased safety and efficacy [2,26–33]. Magnetic coupling is one of the few physical phenomena capable of transmitting actuation forces across a physical barrier. Magnetic techniques for actuation are very promising in medicine, in particular, using permanent magnets, where the mechanical power can be transmitted remotely. Small magnets can generate a very large amount of force, that reduces with increase of distance. Therefore, particular magnetic coupling could be customized for accomplishing specific medical tasks allowing, at the same time, for the device miniaturization.

The goal of this dissertation is to focus on remote and local magnetic manipulation of MCRs combined with real-time proprioceptive sensing. Onboard actuation is a crucial limiting factor for capsule robots. The current state of the art lacks control strategies for magnetic manipulation. By addressing this issue, more efficient and reliable techniques could be employed for magnetic control of robotics instruments in the medical field. The study focus on remote magnetic manipulation to enable closed-loop control for capsules deep inside the human body, and local magnetic actuation to transfer controlled rotary motion across the abdominal wall for powering multiple DOFs of surgical robots.

The outline of this dissertation is organized as follows: background and significance are presented in Section I.2; a description of the dissertation overview about local and remote magnetic manipulation is presented in Section I.4; Chapter II presents the scientific contribution for the remote magnetic manipulation of WCE; Chapter III presents the scientific contribution for what concerns the local magnetic actuation for application in MIS. Conclusions and future works are presented in Chapter IV. Finally the research outcomes are presented Section IV.3.

I.2 Background and Significance: Magnetic Medical Capsule Robots

As schematically represented in Fig. I.2, the architecture of a capsule robot can be described by the following modular modules: (1) a central processing unit where intelligence is implemented; (2) a communication submodule that links the device with the user intent; (3) a source of energy that powers electrically the system; (4) sensors; (5) actuators; (6) mechanical transmission and (7) end-effector, which interact with the surrounding environment to accomplish one or more specific tasks and interact with the target site, according to the specific functions the device is required to fulfill.

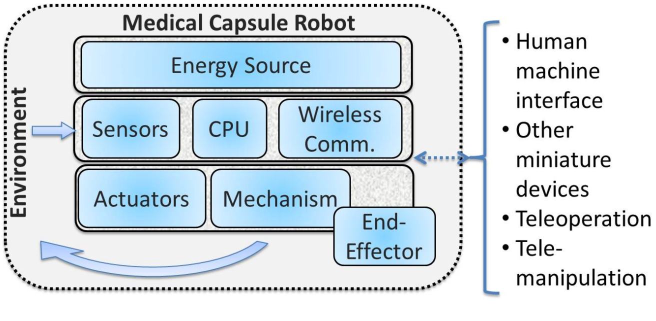

Figure I.2: Schemagtic rappresentation of a MCR

I.2.1 Magnetic MCR applied to MIS

In MIS, a promising approach in the direction of further reducing invasiveness is represented by continuum robotic platforms specifically developed for (or adapted to) Laparo-Endoscopic Single Site (LESS) surgery [34–39]. Actuation for the several DOF may be external, by means of cables or rigid connection [34, 35, 37]; internal, using on-board motors [36, 38]; or hybrid [39]. In any case, the mechanical continuity of the kinematic chain constrains the workspace proximally at the insertion point.

Magnetic coupling is a strategy to transmit actuation forces across a physical barrier. This approach can be applied in MIS to remotely control and manipulate robotic instruments as first proposed in [40]. Interrupting the mechanical continuity of such system by having surgical instruments and laparoscopic camera magnetically coupled across the abdominal wall greatly enhances both the workspace of operation [36, 38] and triangulation (i.e., the triangular positioning of the camera and surgical instruments in laparoscopy which mimics the positioning of the human head and arms [3]) without the need for multiple abdominal incisions (shown in Fig. I.3).

These instruments are able to enter the abdominal cavity through the same single incision, without taking up port space during the operation. Each single surgical instrument is coupled with an independent external handheld magnet. The main drawback of this approach is in the low dexterity and poor motion accuracy due to manual operation of the external magnets [41]. To overcome this limitation, magnetic coupling can be used mainly for gross positioning, while on-board Electromagnetic (EM) motors can be adopted for providing fine motion of the surgical end effector [6, 17, 19, 36, 38]. As previously mentioned, however, the on-board actuators that can fit through a single tiny incision are very limited in power and do not allow the performance of surgical tasks, such as lifting an organ or following in real-time the surgeons movements at the master interface. Larger, more powerful motors can be used at the expense of enlarging the access port [36], hence increasing the trauma for the patient.

Another approach for magnetic manipulation in MIS that recalls the principle of operation of EM motors – with an external source generating a rotating magnetic field and an internal rotor following it – is discussed in [42], where a magnetic resonance scanner (Magnetic Resonance Imaging (MRI)) generates the driving magnetic field, imposing the rotation of a small ferromagnetic body around an axis. The mechanical power transferred with this approach is used to drive one DOF of a needle injection robot.

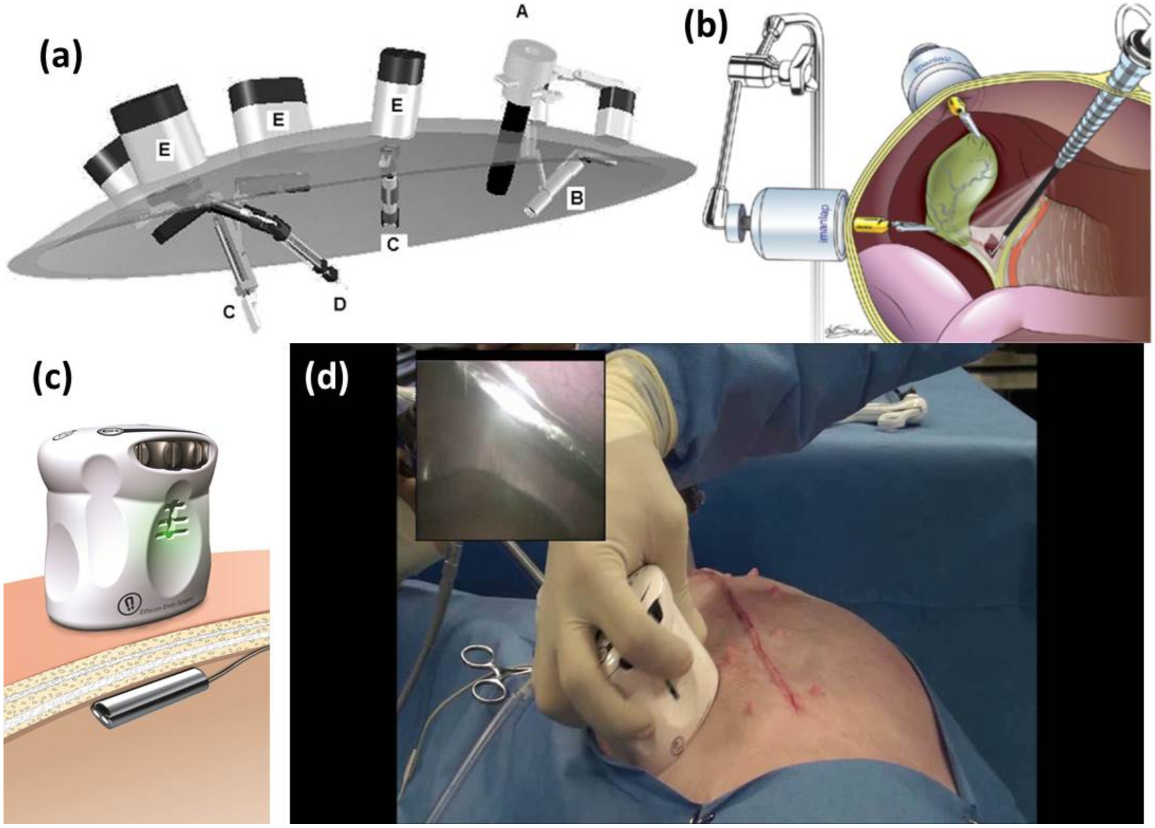

Figure I.3: (a) Minimally Invasive Surgery scenario representation where magnetic coupled robots are operating [3]. (b) Magnetic coupled surgical tissue retractor [3]. (c) Magnetic coupled endoscope camera [4]. (d) Magnetic coupled endoscope camera during in-vivo procedure [3].

I.2.2 Magnetic MCR applied to Endoscopy

The GI tract is home to many deadly human diseases. Colorectal cancer alone is the third most common cancer in men and the second in women worldwide [43]. However, most GI diseases can be prevented – or timely treated – if the diagnosis occurs at an early stage of development. For this reason, GI screening is playing an increasingly important role in healthcare systems worldwide [44, 45].

One method for GI screening that has quickly risen to become the preferred option is flexible endoscopy due to its ability to serve as both a diagnostic and therapeutic modality. Unfortunately, its application is sometimes limited due to its invasiveness, patient intolerance, and the need for sedation. These disadvantages are severe enough for some patients, that millions forgo or avoid recommended screening [44].

Over the past decade, WCE established itself as a patient-friendly procedure for diagnosis of diseases in the small intestine [46]. Specific wireless capsule endoscopes have been proposed for colon inspection, but have not reached the diagnostic accuracy of standard colonoscopy [47, 48]. One of the main limitations of commercially available capsule endoscopes is passive locomotion [49]. It is desirable for the endoscopist to be able to maneuver the camera arbitrarily rather than relying on peristalsis to drive the capsule for adequate visualization of GI mucosa. For this reason, a relevant number of technical solutions have been recently proposed to provide active locomotion to WCE, including walking [50] or crawling [51]. The most promising being remote magnetic manipulation [2, 26–33], where the MCR is equipped with a permanent magnet and an external magnetic field that can control MCR position and orientation.

The primary advantage of remote magnetic manipulation, in comparison with internal active locomotion, is an accurate omnidirectional steering by continuously generating forces with no power consumption and consequently reduction in components on board the capsule.

One of the requirements is a large and complex system outside the patient to generate the magnetic field, such as electromagnetic coils [14, 52], MRI system [15, 21, 25], or robotic platforms for catheter steering [20] (shown in Fig. I.5). The use of a permanent magnet to generate the external magnetic field was proposed by [22] and the device called Medical Air Capsule (MAC) is shown in Fig. I.4.a,b,c. Also other research groups implemented the same locomotion strategy [26, 27] and [6] which implements a hybrid locomotion, shown in Fig. I.4.d. In this case the external system consists of a cartesian robot manipulating the external permanent magnet. Methods to determine the necessary field characteristics for a desired capsule motion or force application are also open research areas [53, 54].

I.2.3 Magnetic Localization to Guide Robotic Endoscopes

In case of magnetic manipulation of a capsule endoscope in the gastrointestinal tract, the knowledge of capsule's position and orientation (i.e., the pose) is crucial to achieve a reliable control and an intuitive driving experience for the operator.

Most of the localization techniques developed to date –mainly designed to track the capsule endoscope as it passively travels in the GI tract- are not compatible with magnetic manipulation due to electromagnetic interference [55]. The same applies to magnetic tracking of a permanent magnet embedded in the capsule and detected by a skin-mounted magnetoresistive sensor array [7, 8, 56] (showed in Fig. I.5). A 3D magnetic system called 3d-MaGMa (Innovent Technology, Germany) uses 27 magnetic field sensors to determine the location of a magnetic pill and can achieve accuracies of 5mm in position and 2^o in orientation [57].

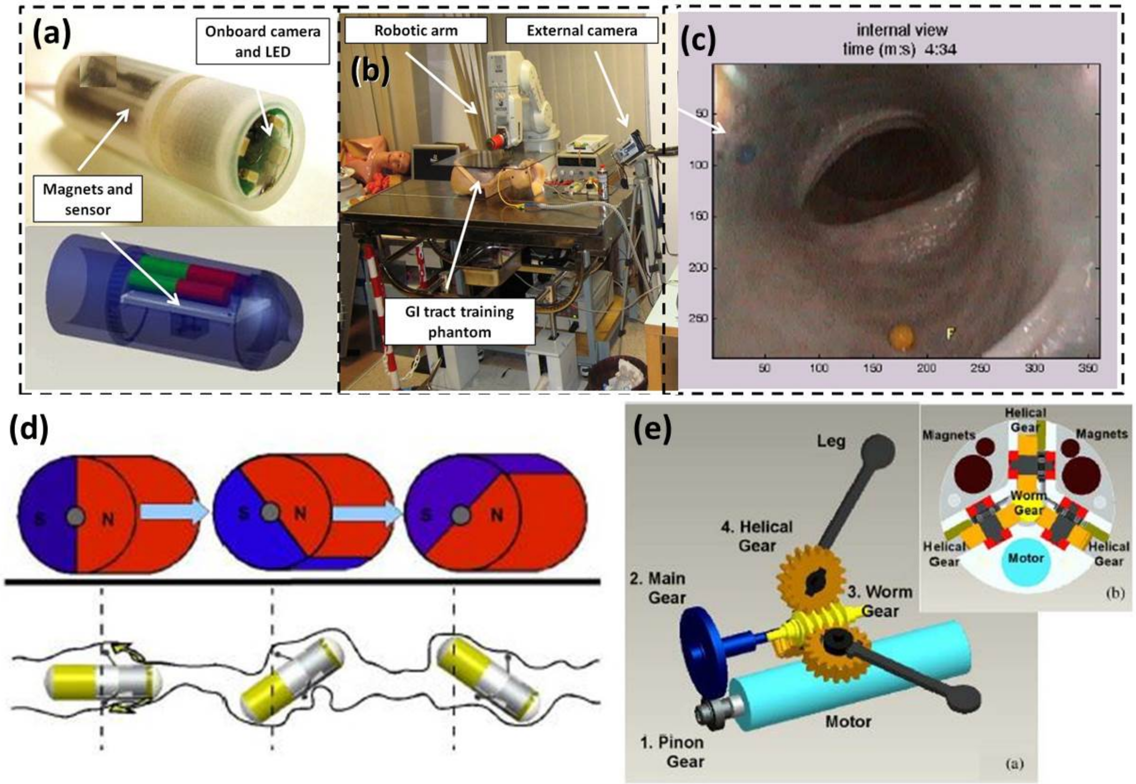

Figure I.4: (a) MAC, WCE equipped with sensors, magnets, camera, illumination tool channel and air insufflation channel [5]. (b) Experimental platform overview [5]. (c) Image stream from the MAC while insufflating the colon [5]. (d) Hybrid capsule principle of operation (WCE equipped with magnets and motor actuated legs for locomotion inside the colon) [6]. (e) Schematic view of the hybrid capsule internal mechanism and cross section view of the locomotion unit [6].

For the sake of completeness, we also need to cite a localization technique that is based on ionizing radiations (X-Ray) [58]. This approach shows encouraging results in terms of localization, but it is not applicable to humans due to the high dose required. A similar approach was taken by [20] (shown in Fig. I.5). This research group used fluoroscopic imaging in conjunction with a robotic navigation system (Niobe, Stereotaxis, inc.) for 3D localization and steering of a magnetic capsule [9]. They achieved 3D localization of the capsule with an error of 1 mm. A different research group used gamma scintigraphy to localize a drug delivery capsule. This method requires a radioactive agent to be placed inside the capsule, which can be tracked using gamma cameras [59].

A high-frequency alternating magnetic field, generated by pairs of Cartesian coils, can be used in conjunction with a resonating coil [60]. This approach can provide sub-millimeter

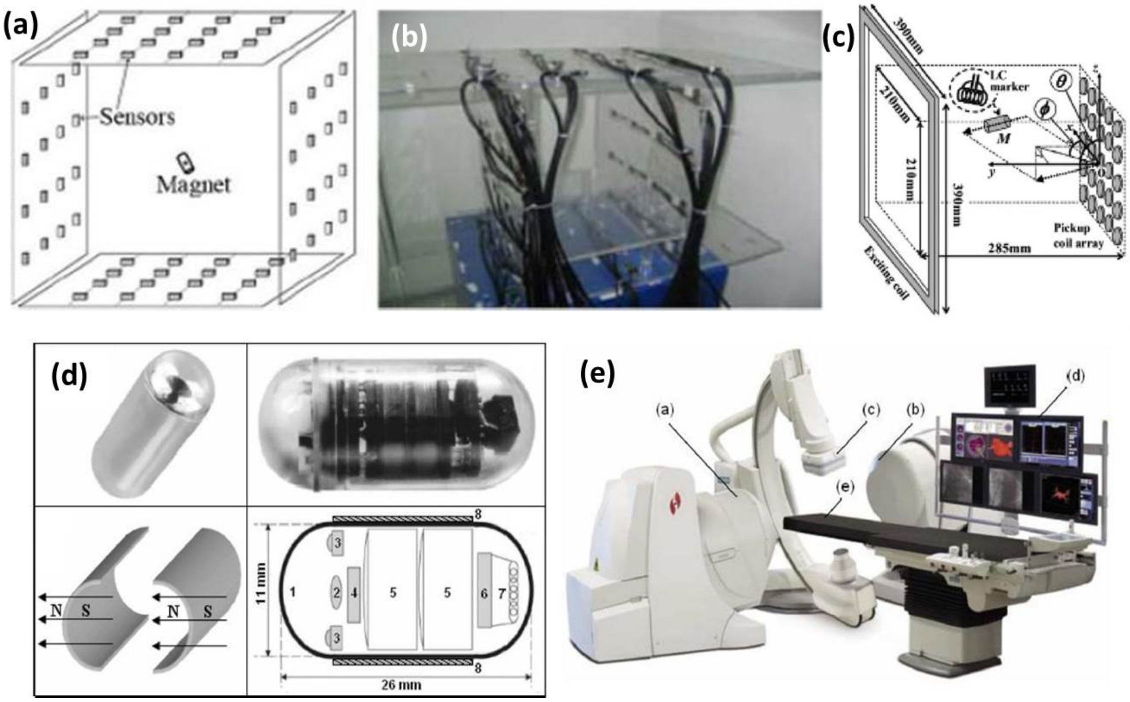

Figure I.5: (a) Scheme of the cube magnetic sensor array and (b) its set up [7]. (c) Schematic representation of the motion sensing system by [8], (d) The four pictures show the Given Imaging M2A capsule, the drawing of the two semicylindrical parts of the considered shell, the picture of the internal arrangement of the capsule and the schematic sectional drawing of the device components: 1: optical dome, 2: focal lens, 3: white LEDs, 4: CMOS imager, 5: batteries, 6: application-specified integrated circuit (ASIC) transmitter, 7: RF antenna, and 8: magnetic shell [9]. (e) Niobe magnetic navigation system developed by Stereotaxis. It includes the following. (a) and (b) Couple of permanent magnets. (c) Fluoroscopic scanner. (d) Visualization displays. (e) Patients table [9].

resolution, but is limited to three DOF. Inertial sensors or Hall Effect sensors are embedded in the capsule for localization during magnetic manipulation [61]. Electromagnetic localization using eight small magnetized coils was used to localize an inch-worm robot and was able to achieve positional errors below 10 mm and orientation errors below 2^o [62].

Since permanent magnets are exploited for remote manipulation of WCE as in [54, 63, 64], the localization approaches presented so far could present incompatibility due to electromagnetic interference. Therefore a different solution for the localization strategy should be pursued. Compared to coils, permanent magnets can generate higher fields in a smaller form factor.

A simpler localization approach achieved 6^o accuracy in estimating capsule orientation 2 DOF by using inertial sensing [65]. If the capsule is equipped with onboard sensors, the

WCE can be localized off-line by measuring the magnetic field generated by the external permanent magnet EPM [66]. This approach is adopted also in [63] to achieve capsule localization in 5 DOF with an accuracy of 15 mm. Inertial sensing is used in conjunction with Hall effect sensors to localize an endoscopic capsule driven by a robotic EPM in [67]. This method achieves a 10 mm accuracy on 3 DOF.

An example of open-loop control for a magnetically manipulated WCEis presented in [33], where optical tracking with external cameras is adopted to localize the capsule with a refresh rate of 25 Hz. To apply these results in a clinically relevant setting and move forward to the closed-loop manipulation of a magnetic WCE, online pose tracking of the capsule without line-of-sight is crucial [32, 68].

I.2.4 Magnetic Gears

Magnetic coupling can be used to transfer torque from one shaft to another without a physical connection. Magnetic shaft couplings (or magnetic gears) are most often used for liquid pumps and propeller systems, since a static, physical barrier can be placed between the two shafts to separate the fluid from the motor operating in air. Magnetic shaft couplings preclude the use of shaft seals, which eventually wear out and fail from the sliding of two surfaces against each other. Magnetic couplings are also used for ease of maintenance on systems that typically require precision alignment, when physical shaft couplings are used, since they allow a greater off axis error between the motor and the driven shaft.

In particular for what concern magnetic gears, these systems are designed as the mechanical gears with permanent magnets substituting the teeth. All cogs of each gear component of magnetic gears act as a constant magnet with periodic alternation of opposite magnetic poles on mating surfaces. Gear components are mounted with a backlash capability similar to other mechanical gearings. Although they cannot exert as much force as a traditional gear, such gears work without touching and so they are immune to wear, have very low noise and can slip without damage. Magnetic gears can be used in configurations that are not possible for traditional gears that must be physically touching and also they can operate with a non-metallic barrier completely separating the driving force from the load. The magnetic coupling can transmit force into a hermetically sealed enclosure without using a radial shaft seal, which may leak.

Torque densities comparable with mechanical gears can be achieved with an efficiency $> 99\%$ at full load and with much higher part load efficiencies than a mechanical gear.

In the last decades, magnetic gears were applied to fulfill several different functions, such as diver propulsion vehicles and remotely operated underwater vehicles, where the magnetic coupling is used to transfer torque from the electric motor to the propellers. Magnetic gearing is also being explored for use in utility scale wind turbines as a means of enhancing reliability. Some aquarium pumps are Magnetic Drive Pumps – they use magnetic coupling between the motor on the dry side of an aquarium wall and the propeller/impeller in the water on the other side of that aquarium wall. A magnetic stirrer is another example of magnetic gear coupling.

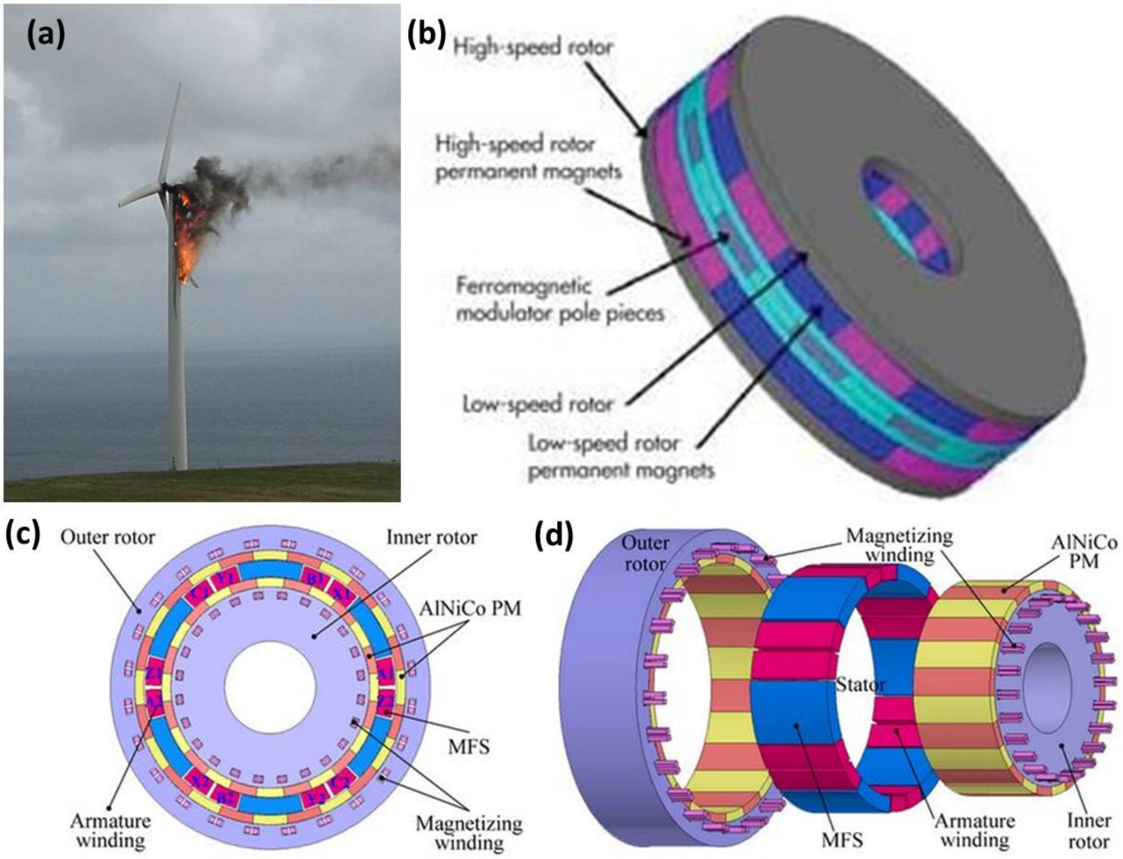

Figure I.6: (a) [10] states: "Magnetism? Yes, that is possible- the gear rotors motion couples through a modulated interaction between the flux generated by magnets on input and output rotors. If the torque on the input exceeds maximum design levels, the magnetic gears simply slip; there are no broken teeth, ground-up gears or worse, a fire." (b) Axial magnetic gear enragement such in [11]. Concentric magnetic gear [12], (c) front view of the structure and (d) assembly component view.

Since nineties, research groups studied and developed new magnetic gear designs and control strategies. The series of designs developed so far, are mainly focusing on the coaxial (or concentric) magnetic gear arrangement, as in [12, 69]. Also different kind of design for magnetic gears has been developed, such as the cycloid magnetic gear [70], axial magnetic gear enragement as in [11], the worm gear of [71], a planetary magnetic gear box developed by [72], a linear magnetic gear system by [73] and also the harmonic magnetic gear developed by [74].

Several years of development in this field for industrial applications, suggests that a coaxial concentric topology with radial coupling (i.e., driving and driven magnetic systems mounted one inside the other as in [75]) would enable a more efficient power transmission than other types of couplings. This is due to a more homogeneous distribution of the attractive force around the main axis of each gear, as all the pole pairs are simultaneously involved in the transmission of mechanical power [76]. For these reasons the spur magnetic gears approach has not been pursued from a research prospective [77].

I.3 Abdominal Surgery and Endoscopy: Requirements and Specifications

Robotic assistance in MIS extended the capabilities of surgeons via improved precision, dexterity and computer assistance [78, 79]. The performances achieved by the fifteen-year-old Da Vinci surgical system could be considered the benchmark for robotic surgical procedures. Recently, also LESS and NOTES have been investigated [80–82] for their potential benefits in reducing patient trauma and shortening their recovery time compared to MIS. However, LESS and NOTES also set strict requirements for instrument miniaturization, dexterity, and collision avoidance between surgical tools operating in confined spaces. The da Vinci has a single-site robotic platform commercially available for LESS [83], and a new system for LESS, FDA approved in 2014 [84]. Other examples of platforms for LESS, in the research stage, are [39, 85]. NOTES is still limited to a small number of research institutes and is in the surgical evaluation stage [1, 81, 82, 86]. From the technical specifications and results offered from the previous academic works and [87, 88], it is possible to provide the required forces, torques, speed and workspace for the distal part of the instrument during abdominal surgery. These specifications are displayed in table I.1. Table I.2 provides the requirements for capsule's localization during endoscopy along the GI tract [89]. These specifications are gathered from the literature cited in Section I.2.3, where techniques addressing the localization of capsule endoscope are presented. These techniques are grouped in two categories: localizations for passive capsule (moved along the GI tract by peristalsis) and localization for real-time capsule locomotion control. For the sake of completeness, Table I.2 presents both localization approaches but this dissertation focuses only on pose detection for controlled magnetic manipulation.

I.4 Remote and Local Magnetic Manipulation: Dissertation Overview

The work presented in this dissertation proposes mathematical instruments applied to magnetism for feedback elaboration and control, but also design strategies for magnetic

Requirements & Specifications for Distal Tools During MIS

Workspace (mm)	Working Speed	Working Load	Precision
50x50x60	$30mm/s$; $60^o/s$	Force: $2N$; Moment: 60mNm	$\pm 0.25mm$; $\pm 1^o$

Table I.1: Technical specification required for the distal surgery robotic instrument during abdominal surgery.

Requirements & Specifications for Capsule Endoscope's Localization

Capsule Dimension	Locomotion Typology	Addressed Needs	DOF	Refresh Rate	Precision
10x26mm	Passive	Diagnosis	Position (3)	1-5 Hz	$\pm 5mm$; $\pm 3^o$
18x26mm	Magnetic	Locomotion Control	Pose (6)	100-1000 Hz	$\pm 6mm$; $\pm 3^o$

Table I.2: Technical specification required for localization of capsule endoscope during passive locomotion and magnetic navigation along the GI tract.

actuation and monitoring, that are useful both in clinical applications and research. The contribution of this dissertation consists of two main elements.

The first contribution aims to enable a controllable strategy for magnetic remote guidance of WCE and/or flexible scope based on magnetic coupling. The capsule navigation must have a no line-of-sight localization feedback across the patient body. The localization technique has to be compatible with the locomotion strategy adopted and also, it has to be harmless for the patient. The main characteristics for the robotic magnetic guidance presented in this dissertation are the utilization of the same magnetic field source for both capsule navigation and capsule pose detection whereas the capsule is embedding sensors.

The second element of this dissertation aims to evaluate surgical robotic manipulators exploiting controllable local magnetic couplings for rotary motion transmission across the abdominal patient's wall for MIS. By moving the actuators outside the body, but still taking advantage of the reduced access trauma guaranteed by a trans-abdominal magnetic coupling, this approach provides dexterity, while preventing the need for powerful on-board motors. Replacing MCR's onboard motors with rotational magnetic coupled parts (magnetic spur gear) allows mechanical power transmission across the patient body tissue. The design of a magnetically coupled surgical manipulator has to consider constraints and specification typical for MIS.

Chapter II

REMOTE MAGNETIC MANIPULATION: NAVIGATION OF WCE AND FLEXIBLE SCOPE

II.1 Technical specification

From a technical prospective, in order to achieve a magnetic controlled platform for navigation of WCE and as well as soft tether robots, a magnetic pose detection based on compatible sensing strategies have to be addressed.

The proposed work of this dissertation presents a whole magnetic navigation platform based on the magnetic coupling of two cylindrical axial magnets (shown in Fig. II.1). The master magnet or EPM is used to guide the WCE or soft tether robot with magnetic tip, by generating on the slave magnet (or IPM placed inside the MCR) enough force to attract the WCE. The cylindrical magnet shape seems to be the more appropriate to be embedded in a capsule. The external magnet's shape, instead has no specific requirements, thus it has been chosen on the base of the localization algorithm presented in this dissertation. In particular the cylindrical symmetry intrinsic with the magnet shape allow the simplification and solution of the pose detection problem.

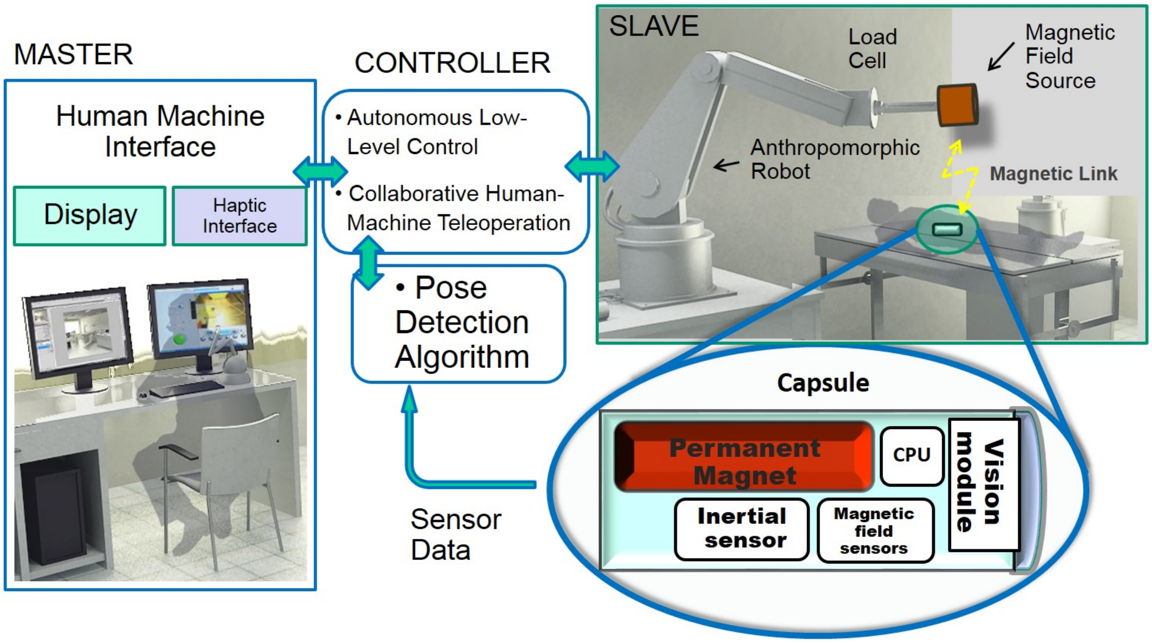

Figure II.1: Schematic view of the magnetic navigation platform for endoscopic procedure.

Usually the EPM is held and manipulated by an anthropomorphic robotic arm with at least 6 DOFs. The magnetic couple is designated to generate magnetic forces between the two magnets in order to reliably drag, tilt, pan and retroflex the WCE or the magnetic tip of a soft tether endoscope along the GI, with high precision and no power consumption. Therefore if the IPM is constrained in volume by the WCE standard dimensions, the EPM can be chosen as big as possible accordingly with the force generated and the robot payload. Workspace of magnetic field measurements by the sensors and magnetic force efficacy distance for manipulability are functions of magnet dimensions.

Quantitative measure of the propelling forces required to effectively move a capsule in the targeted GI segment have been published addressing this scientific need (as explained in the scientific paper attached in Section D). This allows to determine the parameters (i.e. magnets dimensions) to design an efficient magnetic propulsion mechanisms for WCEs.

Concerning the robotic control of WCE's magnetic navigation, position sensing is a requisite. The navigation feedback has to be available at the robot control level in order to give reliable feedbacks about how the hidden WCE is behaving during the procedure, thus adjusting the robotic manipulator trajectory compliantly with the WCE's pose localization. Also, the EPM has to be oriented freely allowing a proper navigation, thus, EPM pose feedback is required since magnetic manipulation is necessary. Computational time required for high level closed-loop control (i.e. path planning strategies) for commercial robotic manipulators (such as RV6SDL, Mitsubishi Corp., Japan) averages about 140 Hz [22].

The presented pose estimation system is based on having the WCE equipped with magnetic field, inertial sensors and an external magnetic field source (EPM). The sensor fusion strategy allows the simplification and solution of the pose detection in two parallel geometrical problems such as position and orientation. Therefore the position of the capsule could be achieved by solving the inverse problem of the magnetic field relationship (or Magnetic Direct Relationship (MDR)) for an axial magnetized EPM, whereas the capsule orientation could be obtained by inertial capsule measurements.

II.2 Technical Contribution

II.2.1 Magnetic Analysis for Position Estimation

In order to develop methods for magnetic localization, we need to consider the magnetic field generated by a known source as the following time-invariant non-linear mathematical expression:

$$\mathbf{B} = f(\mathbf{p}) \qquad f(\mathbf{p}_i) : \mathbb{R}^3 \rightarrow \mathbb{R}^3. \tag{II.1}$$

This equation will be denoted as MDR. Referring to Fig. II.2, the MDR associates the coordinates of the point $\mathbf{p}$ outside the magnetic field source $\mathbf{p} = [x, y, z]^T$ to a corresponding vector function of magnetic field values $\mathbf{B} = [B_x, B_y, B_z]^T$ applied on the capsule itself. $\overrightarrow{\mathbf{d}}$ is the intermagnetic distance between the EPM's center and the point $\mathbf{p}$ centered in WCE.

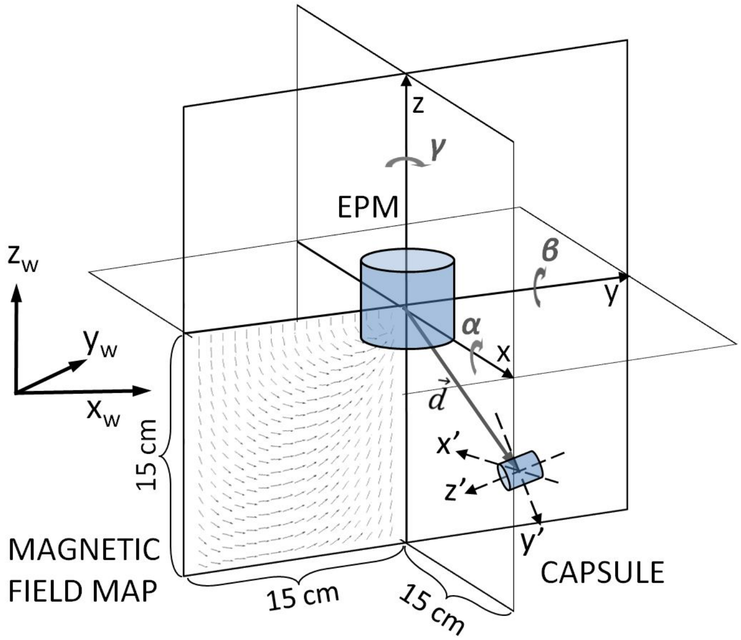

Figure II.2: Schematic view of the EPM and the capsule with the different reference frames used in the algorithm. A slice of the magnetic field map is represented in the lower left quadrant of the workspace.

The magnetic field of a cylindrical axially-magnetized permanent magnet exhibits cylindrical symmetry around its main axis ($\hat{\mathbf{z}}$) [90, 91]. If such a magnet is used as the external source of magnetic field for capsule manipulation, as suggested in our previous work [32, 68], the localization can take advantage of the symmetry to reduce the computational burden. In particular, the three-dimensional position tracking problem can be reduced to two dimensions (2D). Then, once the position in 2D is obtained, the third coordinate can be derived by sensor fusion.

As represented in Fig. II.3, the magnetic field is distributed around the main axis of symmetry of the EPM, $\hat{\mathbf{z}}$, while B_θ – angular component of the magnetic field along θ – is null. The vector $\tilde{\mathbf{p}}_c = [r, \theta, z]^t$ represents a generic point on the loci of points, whose location satisfies the condition of having the same magnetic field $\mathbf{B}_c$. This set of points of the locus generates a circumference Υ (represented in Fig. C.3) that can be analytically described as $\Upsilon = [r, \theta, z] | r, z = const \in \mathrm{I\!R},\ and\ \theta \in 0 \to 2\pi$. We refer to $\tilde{\mathbf{p}}_c = [r, \theta, z]^t$ as the generic point on the loci, which is expressed in the three cylindrical coordinates, instead $\mathbf{p}_c$ lies on the plane $\mathcal{H}$ and is obtained by applying a rotation about $\tilde{z}$ to $\tilde{\mathbf{p}}_c$. The plane $\mathcal{H}$ is defined as: $\mathcal{H} = \mathrm{I\!R}^2 : \{(r, z)|r, z \in \mathrm{I\!R}\ \mathit{and}\ \theta = 0\}$.

Considering the magnetic field applied on a generic point $\tilde{\mathbf{p}}_c$, its components are expressed as $\mathbf{B}_c = [B_r(r, z), B_\theta(r, z), B_z(r, z)]$, where $B_\theta(r, z) = 0$. Therefore, (II.1) could be furthermore simplified by defying the mathematical representation Ψ for the magnetic field $\mathbf{B}_c$. The magnetic field $\mathbf{B}_c$ is given by the two-dimensional transformation Ψ for any given point $\tilde{\mathbf{p}}_c$ around the magnetic field source, such as $\Psi : \tilde{\mathbf{p}}_c \rightarrow \mathbf{B}_c$. $B_r(r, z)$ and $B_z(r, z)$ are two scalar values representing the radial and the axial component of the magnetic field vector, which are function of axial and radial spatial coordinates with respect to the center of the EPM.

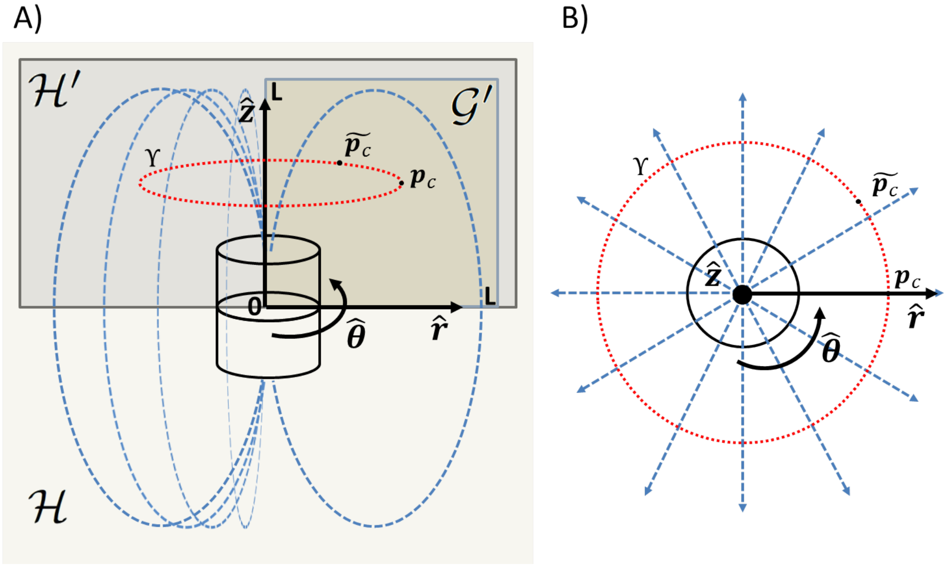

Figure II.3: Schematic view of the magnetic field distribution for a cylindrical axially-magnetized permanent magnet. (A) View of the $\mathcal{H}$ planes, its subset $\mathcal{H}'$ and the domain $\mathcal{G}'$, (B) shows the radial distribution of the magnetic field on the plane $[\hat{r}, \hat{\theta}]$

The solution to the system of equations expressed by the transformation Ψ – in terms of both radial $B_r(r, z)$ and axial $B_z(r, z)$ magnetic field – is unique in the semi-domain $\mathcal{H}^+$ defined as in Fig. II.3 (note that the semi-domain $\mathcal{H}^+$ can be either related to the south or the north pole of the cylindrical axially-magnetized EPM). Then, we define a finite domain $\mathcal{G}^+$, where the magnetic field radial component B_r is always positive. The region is a square plane having size L along $\hat{\mathbf{r}}$ and $\hat{\mathbf{z}}$, where the spatial transformation $f(\mathbf{p}_c)$ in (II.1) is simplified and solvable as

$$\begin{array}{c}\Psi(\mathbf{p}_c) : \mathbb{R}^2 \rightarrow \mathbb{R}^2 \\ where : \mathbf{p}_c \in \mathcal{G}' : \mathcal{G}' = \{(r, z) \in [0, L]\}\end{array} . \tag{II.2}$$

The transformation $\Psi(\mathbf{p}_c)$ can be expressed by two scalar mathematical functions, each with two inputs. The two functions provide the magnetic field radial component as

$$B_r = \psi_r(r, z) : \mathbb{R}^2 \rightarrow \mathbb{R}, \tag{II.3}$$

and the magnetic field axial component as

$$B_z = \psi_z(r, z) : \mathbb{R}^2 \rightarrow \mathbb{R}. \tag{II.4}$$

In order to track the WCE both the spatial orientation of the capsule and the external magnetic source pose must be known with respect to a common reference frame. The magnetic field vector $\mathbf{B}_c$ at the capsule position $\tilde{\mathbf{p}}_c$ – expressed in the capsule frame $[\hat{\mathbf{x}}_c, \hat{\mathbf{y}}_c, \hat{\mathbf{z}}_c]$ – is measured by the onboard sensors. This vector can be expressed in the EPM frame $[\hat{\mathbf{x}}, \hat{\mathbf{y}}, \hat{\mathbf{z}}]$ by applying the geometrical transformation $\mathbf{R}_c^{EPM}$, thus obtaining $\mathbf{B}$.

Then, considering Figs. III.14 and II.3, the magnetic field vector $\mathbf{B}$ is expressed in cylindrical coordinates from its cartesian coordinates, such as: $\mathbf{B} = [B_x, B_y, B_z]^T \rightarrow [\mathbf{B}_r, \mathbf{B}_z]^T$ *and* $\boldsymbol{\theta}$, where $\boldsymbol{\theta}$ also correspond to the azimuthal coordinate of the capsule position $\tilde{\mathbf{p}_c}$. The relationships that transform the magnetic field vector $\mathbf{B} = [B_x\hat{\mathbf{x}}, B_y\hat{\mathbf{y}}, B_z\hat{\mathbf{z}}]$ from cartesian to cylindrical coordinates are:

$$\begin{array}{l} B_r = \sqrt{(B_x\hat{\mathbf{x}})^2 + (B_y\hat{\mathbf{y}})^2}\hat{\mathbf{r}} \\ B_z = B_z\hat{\mathbf{z}} \\ \theta = atan2(B_y, B_x)\hat{\boldsymbol{\theta}} \end{array} \tag{II.5}$$

where B_x, B_y, B_z are the cartesian components of the magnetic field vector $\mathbf{B}$ with respect to the EPM frame $[\hat{\mathbf{x}}, \hat{\mathbf{y}}, \hat{\mathbf{z}}]$. The measured axial and radial magnetic field components can be fed into search function within the finite domain $\mathcal{G}^+$. The solution of the search as radial and axial coordinates of the capsule $\tilde{\mathbf{p}}_c = [p_r, p_z]$ satisfies the inverse relationship of (II.8) and (II.9).

The numerical solution of (II.8) and (II.9) can be obtained by either applying the Current Density Magnetic Model (CuDMM) or the Charge Density Magnetic Model (ChDMM), as demonstrated in [90, 91]. The CuDMM for an axially magnetized cylindrical magnet is expressed as follows

$$\overrightarrow{B(p)} = \frac{\mu_0}{4\pi} \oint_{S''} j_m(p'') \times \frac{(p - p'')}{|p - p''|^3} ds'' \tag{II.6}$$

where $\mathbf{p}$ indicates a generic point belonging to the workspace, $\mathbf{p}''$ is a point on the magnet surface, j_m is the equivalent surface current density, S'' is the EPM integration surface, and μ_0 is the vacuum permeability constant. Expressing Eq. A.3 in cylindrical coordinates, the magnetic field becomes

$$\overrightarrow{B^c(\mathbf{p})} = K \int_L^0 \int_0^{2\pi} \frac{(R - r)\hat{z} + (z - z')\hat{r}}{|R^2 + r^2 - 2rRc(\theta - \theta') + (z - z')^2)|^{\frac{3}{2}}} d\theta' dz' \tag{II.7}$$

where r, θ, and z are the cylindrical coordinates of the generic point $\mathbf{p}$, while R and L are the radius and the height of the EPM, respectively. The constant $K = \frac{\mu_0 M_s}{4\pi}$ accounts for the EPM magnetic remanence M_s.

As shown Fig. II.2 the magnetic field map collects all the solutions for the MDR of the whole space around the EPM. The values of the bi-dimensional map are calculated by applying (II.7) to the specific EPM used in our platform with a spatial resolution of 0.2 mm. The map's resolution is chosen as a trade-off between computational time and localization accuracy.

A sequential search is performed into the map –the magnetic field map is a topological space– to find $\tilde{\mathbf{p}}_c = [p_r, p_z]$ associated with the measured (B_r, B_z). The solution $\tilde{\mathbf{p}}_c$ satisfies the the inverse relationship of (II.8) and (II.9), such as:

$$p_r = \psi_r^{-1}(B_r, B_z) : \mathbb{R}^2 \rightarrow \mathbb{R}, \tag{II.8}$$

and for the position's axial component as

$$p_z = \psi_z^{-1}(B_r, B_z) : \mathbb{R}^2 \rightarrow \mathbb{R}. \tag{II.9}$$

The sequential search performs a double research within the magnetic domain $\mathcal{G}^+$. From the first search it is possible to obtain a set of points σ_r, where each of one has its radial magnetic field component $\tilde{B}_r = B_r \pm \delta$. Then a second search within σ_r constraining the result only to the points having $\tilde{B}_z = B_z \pm \delta$, results in a set of points $\sigma_{rz} = \tilde{\mathbf{p}}_c \pm \delta_{rz}$. σ_{rz} represents the loci of points, whose location satisfies the condition of having the same magnetic field $\mathbf{B}_c \pm \delta_{rz}$, where δ_{rz} is the confidence interval allowing the system solvability. The center of gravity of σ_{rz} is the most accurate solution for the estimation of the point $\tilde{\mathbf{p}}_c$ generated by this algorithm.

Then by using the result of the double sequential search $\tilde{\mathbf{p}}_c = [p_r, p_z]$ in combination with θ it possible deriving the three cartesian coordinates of the capsule as follows:

$$\begin{aligned} \mathbf{p}_x &= p_r cos(\theta)\hat{\mathbf{x}} \\ \mathbf{p}_y &= p_r sin(\theta)\hat{\mathbf{y}} \\ \mathbf{p}_z &= p_z\hat{\mathbf{z}} \end{aligned} \tag{II.10}$$

The capsule pose $p_c = [p_x\hat{\mathbf{x}}, p_y\hat{\mathbf{y}}, p_z\hat{\mathbf{z}}]$ is fully identified with respect to $[\hat{\mathbf{x}}, \hat{\mathbf{y}}, \hat{\mathbf{z}}]$.

II.2.1.1 Inertial Sensing for Orientation Estimation

This section presents the algorithm used to detect the change in capsule orientation and to generate the rotational matrix $\mathbf{R}_c$ with respect to the global frame.

The capsule orientation knowledge is required by the proposed algorithm of magnetic localization to express the magnetic field vector $\mathbf{B}_c$ in the EPM frame.

The algorithms for inclination detection based on inertial sensors are widely adopted in literature and an overview of the approach adopted in this work is provided here for the sake of completeness.

Referring to Fig. II.2, the accelerometer can be used as an inclinometer to obtain the absolute values of the two orientational angles α and β [92]. The rotations about $\mathbf{x}_c$ and $\mathbf{y}_c$ are derived directly from the gravitational vector $\mathbf{g}$ projection mapped on the three orthogonal axes of the onboard accelerometer as

$$\begin{aligned} \boldsymbol{\alpha} &= atan2(A_y, \sqrt{A_x^2 + A_z^2}) \\ \boldsymbol{\beta} &= atan2(A_x, \sqrt{A_y^2 + A_z^2}) \end{aligned} \tag{II.11}$$

where A_x, A_y, A_z are the three accelerometer outputs. By fusing the information of the two orientational angles α and β and the position estimation, previously presented in Section II.2.1, it is possible to achieve 5 DOF Localization as as shown in the paper included in Section B. Any rotation about an axes parallel to the gravitational axes is not measurable.

A second algorithm based on the fusion of inclinometer and gyroscope outputs has been developed in order to estimate the third orientation angle $\boldsymbol{\gamma}$ and it is presented in Section C. A number of techniques have been presented in the literature to estimate the rotational angle $\boldsymbol{\gamma}$ around the gravitational vector g. Most of them are based on fusing gyroscope and inclinometer measurement [93, 94] or by applying quaternion based methods [95] improving 3D angle measurement.

The approach presented in this dissertation consists in applying the axis-angle method for rotational matrices to the gyroscope outputs. Briefly, it is possible to extract the rotation

$\boldsymbol{\gamma}$ about the global axis $\mathbf{z}_w$ by building the rotational matrix $\Delta\mathbf{R}_c$ with respect to the moving frame attached to the capsule $[\mathbf{x}_c, \mathbf{y}_c, \mathbf{z}_c]$. The instantaneous variations in capsule orientation can be derived from the gyroscope outputs as

$$\Delta\alpha_c = G_x\Delta t \qquad \Delta\beta_c = G_y\Delta t \qquad \Delta\gamma_c = G_z\Delta t \tag{II.12}$$

where $\Delta[\alpha_c, \beta_c, \gamma_c]$ are the instantaneous angle variations at the capsule moving frame within a measurement loop that lasts Δt. The instantaneous capsule rotational matrix $\Delta\mathbf{R}_c$ is then defined as

$$\Delta\mathbf{R}_c = \mathbf{R}_x(\Delta\alpha_c)\mathbf{R}_y(\Delta\beta_c)\mathbf{R}_z(\Delta\gamma_c) \tag{II.13}$$

where $\mathbf{R}_x, \mathbf{R}_y, \mathbf{R}_z$ are the rotational matrixes with respect to the $\mathbf{x}_c$, $\mathbf{y}_c$, and $\mathbf{z}_c$ axis, respectively. Then, the axial-angle representation of the rotational matrix $\Delta\mathbf{R}_c$ is derived, thus achieving the angle of rotation θ and the axis of rotation ω:

$$\begin{aligned} \theta &= arccos(\tfrac{trace(\Delta\mathbf{R}_c)-1}{2}) \\ \omega &= \tfrac{1}{2sin(\theta)} \begin{bmatrix} \Delta\mathbf{R}_c(3,2) - \Delta\mathbf{R}_c(2,3) \\ \Delta\mathbf{R}_c(1,3) - \Delta\mathbf{R}_c(3,1) \\ \Delta\mathbf{R}_c(2,1) - \Delta\mathbf{R}_c(1,2) \end{bmatrix} \end{aligned} \tag{II.14}$$

Finally, the axial-angle representation θ, ω must be reoriented according to the capsule orientation with respect to the global frame at the previous time step, $\mathbf{R}_c^{t-1}$. The third coordinate of the axial-angle representation corresponds to the capsule angle variation $\Delta\gamma$ about $\mathbf{z}_w$. The capsule absolute orientation γ about the global axis $\mathbf{z}_w$ is achieved by summation of $\Delta\gamma$ at each loop.

II.2.1.2 Iterative Solution for Position Estimation

The iterative localization approach draws its inspiration from Jacobian-based methods (also known as resolved rates methods stemming from [96]). These methods are commonly used in robotics to solve systems of nonlinear equations subject to the limitations of first-order linearization. For this approach, we assume that the refresh rate for pose tracking is fast enough that only small movements of the WCE may occur between subsequent pose measurements.

In order to apply an iterative method to magnetic localization, we need to consider the magnetic field, generated by a known source, as the time-invariant non-linear mathematical expression II.1. Referring to Fig. F.9, the MDR associates the coordinates of a point outside

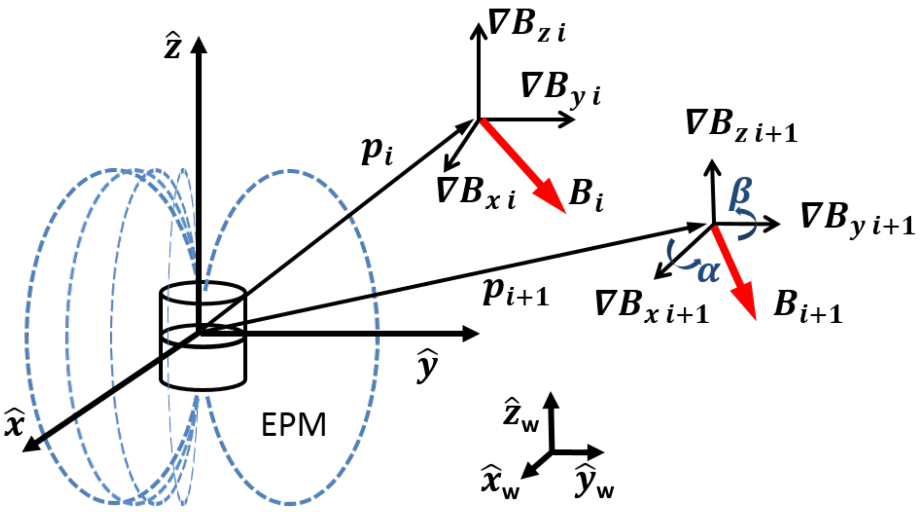

Figure II.4: Schematic representation of the source of magnetic field (External Permanent Magnet (EPM) in figure) and two sequential positions (i.e., $\mathbf{p}_i$ and $\mathbf{p}_{i+1}$) of the capsule to be localized.

the magnetic field source $\mathbf{p}_i = [x_i, y_i, z_i]^T$ to a corresponding vector function of magnetic field values $\mathbf{B}_i = [B_{ix}, B_{iy}, B_{iz}]^T$.

If the capsule position changes from $\mathbf{p}_i$ to $\mathbf{p}_{i+1}$ during time increment Δt, the displacement $\Delta\mathbf{p}$ produces a change in the magnetic field measurements from $\mathbf{B}_i$ to $\mathbf{B}_{i+1}$ according to (II.1). The partial derivative of the magnetic field vector, $\frac{\partial}{\partial p}\mathbf{B}_i$, is given by:

$$\frac{\partial \mathbf{B}_i}{\partial \mathbf{p}} = \bigtriangledown_p f(\mathbf{p}_i) = \begin{bmatrix} \frac{\partial \mathbf{B}_x}{\partial p_x} & \frac{\partial \mathbf{B}_x}{\partial p_y} & \frac{\partial \mathbf{B}_x}{\partial p_z} \\ \frac{\partial \mathbf{B}_y}{\partial p_x} & \frac{\partial \mathbf{B}_y}{\partial p_y} & \frac{\partial \mathbf{B}_y}{\partial p_z} \\ \frac{\partial \mathbf{B}_z}{\partial p_x} & \frac{\partial \mathbf{B}_z}{\partial p_y} & \frac{\partial \mathbf{B}_z}{\partial p_z} \end{bmatrix}. \tag{II.15}$$

where $\bigtriangledown_p f(\mathbf{p}_i)$ designates the gradient of each scalar function in f with respect to $\mathbf{p}$. Using (C.2) in a first-order Taylor series approximation, we obtain:

$$\mathbf{B}_{i+1} = \mathbf{B}_i + \frac{\partial \mathbf{B}_i}{\partial \mathbf{p}}\Delta\mathbf{p} = \mathbf{B}_i + \bigtriangledown_p f(\mathbf{p}_i)\Delta\mathbf{p}. \tag{II.16}$$

The Magnetic Inverse Relationship (MIR), providing the current capsule position $\mathbf{p}_{i+1}$, can be derived by inverting (C.3):

$$\mathbf{p}_{i+1} = \mathbf{p}_i + \bigtriangledown_p f^{-1}(\mathbf{p}_i)\Delta\mathbf{B}_i. \tag{II.17}$$

Moving from differential to the finite difference iterative method, $\frac{\partial \mathbf{B}}{\partial p}\Delta\mathbf{p}$ is replaced by

$\Delta\mathbf{B}_i$, where $\Delta\mathbf{B}_i$ is defined as $\Delta\mathbf{B}_i = (\mathbf{B}_{i+1} - \mathbf{B}_i)$. Also, according to [97], the gradient of a generic vectorial function, which is defined as $f(\mathbf{x}) : \mathrm{I\!R}^n \to \mathrm{I\!R}$, is the transpose of the Jacobian as: $\bigtriangledown_x f(\mathbf{x}) = (\mathbf{J}_x f(\mathbf{x}))^t$. Then, (C.4) becomes:

$$\mathbf{p}_{i+1} = \mathbf{p}_i + \mathbf{J}_p^{-1}\Delta\mathbf{B}_i, \tag{II.18}$$

where $\mathbf{J}_p^{-1}$ is the inverse of the Jacobian.

An explicit formulation of the MDR (II.1) can be obtained by finite element integration of magnetic field models, as suggested in [98], while a numerical estimate can be provided by a standard Finite Element Method (FEM) software package, such as Comsol Multiphysics or ANSYS Maxwell. In the next subsections, we introduce a non-linear interpolation method for a data-set of magnetic field values related to the position $\mathbf{p}_i$. Then, the interpolation is used to provide an analytical expression of the MDR through modal representation, numerical algebra theory, and the Kronecker product. Finally, a first order resolved rates method using the Jacobian expression for the MIR is derived.

The derived magnetic field numerical values can be casted in two data matrices $\mathbf{\Phi}_r \in \mathrm{I\!R}^{w\times s}$ and $\mathbf{\Phi}_z \in \mathrm{I\!R}^{w\times s}$. These matrices represent the $w\times s$ magnetic field numerical solutions for any given position $\mathbf{p}_c$ within $\mathcal{G}'$, where w is the number of magnetic field measurements taken along the $\hat{\mathbf{r}}$ direction and s is the number of magnetic field measurements taken along $\hat{\mathbf{z}}$. The collection of numerical solutions $[\mathbf{\Phi}_r, \mathbf{\Phi}_z]^T$ of (C.7) and (C.8), are expressed as in (C.9) and (C.10).

$$\mathbf{\Phi}_r = \\ \begin{bmatrix} \Phi_{r11}(r_1,z_1) & ... & \Phi_{r1j}(r_1,z_j) & ... & \Phi_{r1p}(r_1,z_p) \\ ... & & ... & & ... \\ \Phi_{ri1}(r_i,z_1) & ... & \Phi_{rij}(r_i,z_j) & ... & \Phi_{rip}(r_i,z_p) \\ ... & & ... & & ... \\ \Phi_{rn1}(r_m,z_1) & ... & \Phi_{rnj}(r_m,z_j) & ... & \Phi_{rnp}(r_m,z_p) \end{bmatrix} \tag{II.19}$$

$$\mathbf{\Phi}_z = \\ \begin{bmatrix} \Phi_{z11}(r_1,z_1) & ... & \Phi_{z1j}(r_1,z_j) & ... & \Phi_{z1p}(r_1,z_p) \\ ... & & ... & & ... \\ \Phi_{zi1}(r_i,z_1) & ... & \Phi_{zij}(r_i,z_j) & ... & \Phi_{zip}(r_i,z_p) \\ ... & & ... & & ... \\ \Phi_{zn1}(r_m,z_1) & ... & \Phi_{znj}(r_m,z_j) & ... & \Phi_{znp}(r_m,z_p) \end{bmatrix} \tag{II.20}$$

where $\mathbf{\Phi}_{rij}$ and $\mathbf{\Phi}_{zij}$ are the magnetic field values at position (i,j), which could be generally expressed as $\mathbf{\Phi}_{ij}$. The single matrix element $\mathbf{\Phi}_{ij}$ can be approximated by applying the modal representation defined in [99–101] as

$$\begin{gathered}\mathbf{\Phi}_{ij} = \mathbf{B}_i(r, z) = \boldsymbol{\omega}(r)^T \mathbf{a}(z), \\ where : (\mathbf{a}, \boldsymbol{\omega}) \in \mathbb{R}^n.\end{gathered} \tag{II.21}$$

The vector of the modal factors, $\mathbf{a}(z)$, can be expressed as

$$\begin{gathered}\mathbf{a}(z) = \mathbf{A}\boldsymbol{\gamma}(z), \\ where : (\mathbf{A}, \boldsymbol{\gamma}) \in \mathbb{R}^n.\end{gathered} \tag{II.22}$$

In this equation, $\mathbf{A}$ is the generic matrix of coefficients for the two orthogonal basis $\boldsymbol{\omega} = \{\omega_0, \omega_1, ..., \omega_n\}$ and $\boldsymbol{\gamma} = \{\gamma_0, \gamma_1, ..., \gamma_q\}$, which represent the interpolation functions that best approximate numerically the transformation $\mathbf{\Phi}_{ij}$ [102]. Once the interpolation functions $\boldsymbol{\omega}$ and $\boldsymbol{\gamma}$ are chosen, and the matrices of coefficients $\mathbf{A}_r$ and $\mathbf{A}_z$, for radial and axial magnetic field respectively, are derived, the interpolation problem can be easily solved. The best data-set interpolation is chosen by adopting the orthogonal function that minimizes the least square error between the reference measure $f(x)$ and the approximated value y^*, such as $||f(x) - y^*|| < \delta$. Examples of orthogonal functions investigated in this study include standard polynomial functions, Chebyshev polynomials [100, 101], Fourier harmonic basis [102, 103] and composition of these.

In the following paragraph, we describe how to derive the matrices of coefficients $\mathbf{A}_r$ and $\mathbf{A}_z$ for the algebraic equations system in (C.11) and (C.12) by using the following matrix representation, as suggested in [100, 101]:

$$\mathbf{\Phi} = \mathbf{\Omega}_{m\times n}\mathbf{A}_{n\times q}\mathbf{\Gamma}_{q\times p}, \tag{II.23}$$

where $\mathbf{\Phi}$ is either the MDR solutions of $\mathbf{\Phi}_r$ or $\mathbf{\Phi}_z$ within $r, z \in [0 \rightarrow L]$, while $\mathbf{\Omega}$ and $\mathbf{\Gamma}$ are the modal basis matrices and constitute the collection of n orthogonal basis for $\mathbf{\Omega}$ and q orthogonal basis for $\mathbf{\Gamma}$. Finally, m and p are the number of values estimated in the domain $r \in [0, L]$ and $z \in [0, L]$, respectively.

The solutions for $\mathbf{A}_r$ and $\mathbf{A}_z$ can be obtained by applying the Kronecker product theory as in [100, 101, 104], where the symbol $\otimes$ represents the Kronecker product of two matrices:

$$Vec(\mathbf{\Phi}) = [\mathbf{\Gamma}^T \otimes \mathbf{\Omega}]\, Vec(\mathbf{A}). \tag{II.24}$$

The result provided by the algebraic interpolation is the generic matrix of coefficients $\mathbf{A}$, which is given by

$$\begin{aligned} Vec(\mathbf{A}) &= [\mathbf{\Gamma}^T \otimes \mathbf{\Omega}]^{\dagger}\, Vec(\mathbf{\Phi}), \\ where: \; Vec(\mathbf{A}) &= [a_{11} ... a_{n1} ... a_{n2} ... a_{np}]^T. \end{aligned} \tag{II.25}$$

Once the matrices $\mathbf{A}_r$ and $\mathbf{A}_z$ are known, the MDR, such as $\psi(z, y) : (z, y) \to (\Phi_{ij})$, is solved for any point within the domain $\mathcal{G}' = \{(r, z) \in [0, L]\}$.

Given the calibration matrices $\mathbf{A}_r$ and $\mathbf{A}_z$, and the orthogonal basis $\boldsymbol{\omega}(r)$ and $\boldsymbol{\gamma}(z)$, the system of equation expressed in (C.11) and (C.12) is completely determined. By differentiating $\boldsymbol{\omega}(r)$ and $\boldsymbol{\gamma}(z)$ in ∂r and ∂z, respectively, we can obtain the complete formulation of the MIR in (C.2). The following system of equations – expressed for the single solution $[\mathbf{\Phi}_r, \mathbf{\Phi}_z]^T$ – provides the ground to derive the Jacobian:

$$\begin{cases} \mathbf{\Phi}_r = \boldsymbol{\omega}(r)\mathbf{A}_r\boldsymbol{\gamma}(z) \\ \mathbf{\Phi}_z = \boldsymbol{\omega}(r)\mathbf{A}_z\boldsymbol{\gamma}(z) \end{cases} \tag{II.26}$$

Applying (C.2) to this system of equations, and deriving the partial derivatives of $\mathbf{\Phi} = [\mathbf{\Phi}_r, \mathbf{\Phi}_z]^T$ such as $\frac{\partial \mathbf{\Phi}_r}{\partial r}, \frac{\partial \mathbf{\Phi}_r}{\partial z}, \frac{\partial \mathbf{\Phi}_z}{\partial r}, \frac{\partial \mathbf{\Phi}_z}{\partial z}$, the gradient of $\mathbf{\Phi}$ becomes

$$\nabla \mathbf{\Phi} = \begin{cases} \nabla \mathbf{\Phi}_r = \frac{\partial(\boldsymbol{\omega}(r)\mathbf{A}_r\boldsymbol{\gamma}(z))}{\partial r} + \frac{\partial(\boldsymbol{\omega}(r)\mathbf{A}_r\boldsymbol{\gamma}(z))}{\partial z} \\ \nabla \mathbf{\Phi}_z = \frac{\partial(\boldsymbol{\omega}(r)\mathbf{A}_z\boldsymbol{\gamma}(z))}{\partial r} + \frac{(\partial\boldsymbol{\omega}(r)\mathbf{A}_z\boldsymbol{\gamma}(z))}{\partial z} \end{cases} \tag{II.27}$$

Considering that the derivatives of $\mathbf{A}_r$ and $\mathbf{A}_z$ are null, as well as $\frac{\partial \boldsymbol{\omega}(r)}{\partial z}$ and $\frac{\partial \boldsymbol{\gamma}(z)}{\partial z}$, (C.17) simplifies to

$$\begin{aligned} \frac{\partial \mathbf{\Phi}_r}{\partial r} &= \frac{\partial \boldsymbol{\omega}(r)}{\partial r}\mathbf{A}_r\boldsymbol{\gamma}(z) \\ \frac{\partial \mathbf{\Phi}_r}{\partial z} &= \boldsymbol{\omega}(r)\mathbf{A}_r\frac{\partial \boldsymbol{\gamma}(z)}{\partial z} \\ \frac{\partial \mathbf{\Phi}_z}{\partial r} &= \frac{\partial \boldsymbol{\omega}(r)}{\partial r}\mathbf{A}_z\boldsymbol{\gamma}(z) \\ \frac{\partial \mathbf{\Phi}_z}{\partial z} &= \boldsymbol{\omega}(r)\mathbf{A}_z\frac{\partial \boldsymbol{\gamma}(z)}{\partial z} \end{aligned} \tag{II.28}$$

In order to obtain the expression of $\frac{\partial \boldsymbol{\omega}(r)}{\partial r}$ and $\frac{\partial \boldsymbol{\gamma}(z)}{\partial z}$, a derivation is applied to the vectors constituting the orthogonal basis $\omega(r), \gamma(z)$. This leads to the following expression for the Jacobian $\mathbf{J}_\Phi$:

$$\mathbf{J}_\Phi = \triangledown^T_{\tilde{p}_c} \Phi(r, z) = \begin{bmatrix} \frac{\partial \Phi_r}{\partial r} & \frac{\partial \Phi_r}{\partial z} \\ \frac{\partial \Phi_z}{\partial r} & \frac{\partial \Phi_z}{\partial z} \end{bmatrix} \tag{II.29}$$

Therefore, the magnetic field vector incremental difference $\Delta\mathbf{B}_i = [\Delta B_r, \Delta B_z]^T_i$ is given by

$$\Delta\mathbf{B}_i = \begin{bmatrix} \Delta B_r \\ \Delta B_z \end{bmatrix}_i = \mathbf{J}_\Phi \Delta\mathbf{p}_{ci} \tag{II.30}$$

This result can be used in (C.3) to estimate the magnetic field $\mathbf{B}_{i+1}$ by continuously updating $\Delta\mathbf{B}_i$ to the current magnetic field value:

$$\mathbf{B}_{i+1} = \mathbf{B}_i + \Delta\mathbf{B}_i = \mathbf{B}_i + \mathbf{J}_\Phi \Delta\mathbf{p}_{ci}. \tag{II.31}$$

In conclusion, (C.22) shows the iterative method to localize the WCE, estimating the current position $\mathbf{p}_{ci+1} = [r_{i+1}, z_{i+1}]^T$ of the capsule as

$$\mathbf{p}_{ci+1} = \mathbf{p}_{ci} + \Delta\mathbf{p}_{ci} = \mathbf{p}_{ci} + \mathbf{J}_\Phi^{-1} \Delta\mathbf{B}_i, \tag{II.32}$$

where $\mathbf{J}^{-1}$ is the inverse of the Jacobian, which applies the least squares method of optimization to the solution [105]. The term $\Delta\mathbf{B}_i$ is the difference in magnetic field recorded from the previous measurement.

This algorithm is been implemented in the scientific paper attached in Section C.

II.2.1.3 Magnetic Attraction Force Feedback

The wireless capsule, schematically represented in Fig. II.5, hosts a Force and Motion Sensing Module (FMSM), wireless communication, and power supply.

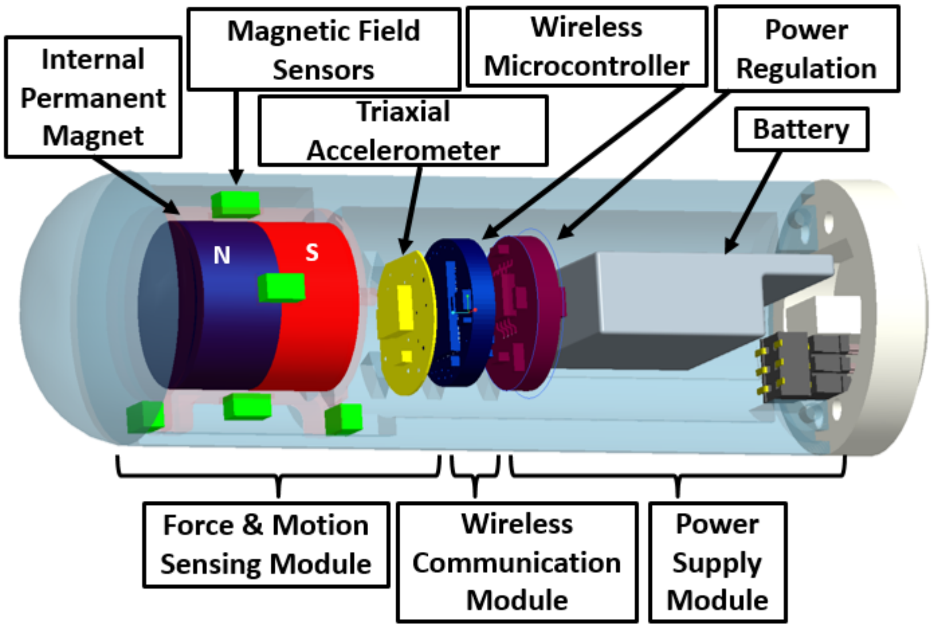

Figure II.5: Schematic view of the wireless capsule for measuring resistant properties of the GI tract.

The FMSM hosts the IPM that couples with the EPM to generate the force $\mathbf{F}_a$ applied to the WCE. The selected IPM is a cylindrical magnet axially magnetized. This EPM-IPM couple generates an intermagnetic force of 1 N when the two magnets are separated by 8 cm and the axes $\mathbf{z}_c$ and $\mathbf{z}_m$ are aligned.

The FMSM is responsible for acquiring the real time sensor readings required to estimate $\mathbf{F}_a$ and also the capsule position $\mathbf{p}$. The transducers embedded in the module are six linear Magnetic Field Sensor (MFS) based on the Hall effect and an inertial sensor for capsule orientation estimation. As represented in Fig. D.3, the MFS are mounted two by two orthogonally around the IPM. Each MFS measures the component of the magnetic field $\mathbf{B}$ that is perpendicular to the IPM surface at the MFS location (i.e., referring to Fig. D.3, MFS_i measures the component B_i for i ranging from 1 to 6). Similarly to [106], the position of each MFS has been selected to minimize the constant bias in the reading due to the field generated by the IPM.

The goal of this section is to describe a new method to estimate the intermagnetic force $\mathbf{F}_a$ acting on the main axis of the IPM (i.e., $\mathbf{z}_c$ in Fig. II.6) under the effect of an external magnetic field $\mathbf{B}_{ext}$. Current approaches either rely on the dipole-dipole magnetic

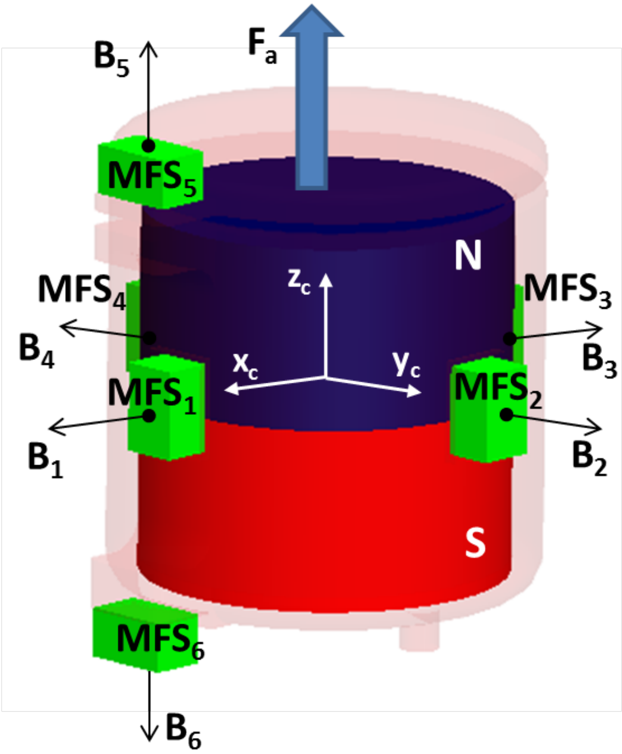

Figure II.6: Magnetic field sensor (MFS) position with respect to the internal permanent magnet.

field approximation [107] or finite element integration [108]. The first method provides an analytical expression of the magnetic field that is not accurate at the proximity of the magnetic field source. On the other hand, finite element integration allows the achievement of accurate results at the price of long computational times [108].

The method proposed in this study is based on the *finite element integration* of real-time sensor data and the FMSM design previously described. The analytical formulation derived in this subsection, can be used to estimate $\mathbf{F}_a$ in real time as a direct function of four MFS readings (i.e., MFS_1 to MFS_4) with low computational costs.

As described in [109], the magnetic force $\mathbf{F}$ acting on a permanent magnet under the effect of an external magnetic field $\mathbf{B}_{ext}$ can be expressed by applying the equivalent current magnetic model:

$$\mathbf{F} = \oint_S \mathbf{j}_m \times \mathbf{B}_{ext} \delta S, \tag{II.33}$$

where S is the IPM surface and $\mathbf{j}_m$ is the equivalent current surface density on the IPM. The current density $\mathbf{j}_m$ is derived from:

$$\mathbf{j}_m = \mathbf{M}_{IPM} \times \mathbf{n}, \tag{II.34}$$

where $\mathbf{M}_{IPM}$ is the IPM magnetization vector, having expression $B_r/\mu_0\hat{\mathbf{z}}$ – with $\hat{\mathbf{z}}$ denoting the unit vector along $\mathbf{z}_c$, while $\mathbf{n}$ is the normal vector coming out from the IPM surface, as represented in Fig. II.7.A.

From Eq. D.3, it is possible to conclude that, given an axially magnetized cylindrical IPM, $\mathbf{j}_m$ only flows on the lateral surface. Therefore, the component of $\mathbf{B}_{ext}$ along $\hat{\mathbf{z}}$ does not contribute to the estimation of $\mathbf{F}$ through the equivalent current magnetic model (Eq. D.2).

In order to provide an analytical expression for Eq. D.2, it is possible to take advantage of the axial symmetry of our problem, thus dividing the cross-section of the IPM into four identical quadrants, as represented in Fig. II.7.A. Focusing on the u-th quadrant and defining θ as the angular coordinate (see Fig. II.7.B), it is possible to express the current density $\mathbf{j}_m$ as:

$$\mathbf{j}_m(\theta) = M_{IPM}[-sin(\theta)\hat{\mathbf{x}} + cos(\theta)\hat{\mathbf{y}}], \tag{II.35}$$

where $\hat{\mathbf{x}}$ and $\hat{\mathbf{y}}$ are the unit vectors along $\mathbf{x}_c$ and $\mathbf{y}_c$, respectively.

In the proposed capsule design, the magnetic field $\mathbf{B}_u$ is measured by the MFS_u placed at $\theta = \pi/4$ in each quadrant and can be expressed as:

$$\mathbf{B}_u = B_u[cos(u\frac{\pi}{2} - \frac{\pi}{4})\hat{\mathbf{x}} + sin(u\frac{\pi}{2} - \frac{\pi}{4})\hat{\mathbf{y}}], \tag{II.36}$$

where B_u is the numerical value recorded by MFS_u and u ranges from 1 to 4.

Assuming that the magnetic field in each quadrant is coincident with the magnetic field $\mathbf{B}_u$, the surface integral in Eq. D.2 can be simplified in the following sum:

$$\mathbf{F} = \sum_{u=1}^{4}\sum_{\theta=0}^{\pi/2}(\mathbf{j}_m \times \mathbf{B}_u)\Delta S = \sum_{u=1}^{4} sgn[cos(u\frac{\pi}{2} - \frac{\pi}{4})]\sum_{\theta=0}^{\pi/2} f_u \Delta S \hat{\mathbf{z}}, \tag{II.37}$$

where *sgn* is the sign function, ΔS is the lateral surface of one quadrant of the IPM and is equal to $\pi/2rh$, in which r is the radius and h the height of IPM. f_u is the contribution to the module of the intermagnetic force acting on the u-th quadrant at a given θ and can be expressed as:

$$f_u = M_{IPM}\frac{B_u}{\sqrt{2}}(sin(\theta) + cos(\theta)). \tag{II.38}$$

Considering that

$$\sum_{\theta=0}^{\pi/2}[sin(\theta) + cos(\theta)] = \Theta = 1.27, \tag{II.39}$$

the analytical expression for the intermagnetic force becomes:

$$\mathbf{F} = \sum_{u=1}^{4} sgn[cos(u\frac{\pi}{2} - \frac{\pi}{4})]\frac{\Theta}{\sqrt{2}}M_{IPM}\frac{\pi}{2}rhB_u\hat{\mathbf{z}} \tag{II.40}$$

This simple equation can be used to get a fast estimate of the intermagnetic force $\mathbf{F}_a$ from the readings of MFS_1, MFS_2, MFS_3, MFS_4. The time required to estimate the magnetic force is 0.18 ± 0.05 ms.

The main contribution of this algorithm is presented in Section D as wireless platform for the measurement of the resistant force that an active capsule must overcome in order to move inside the GI tract. The proposed platform is validated with benchtop trials and through an *in vivo* experiment using a porcine colon model.

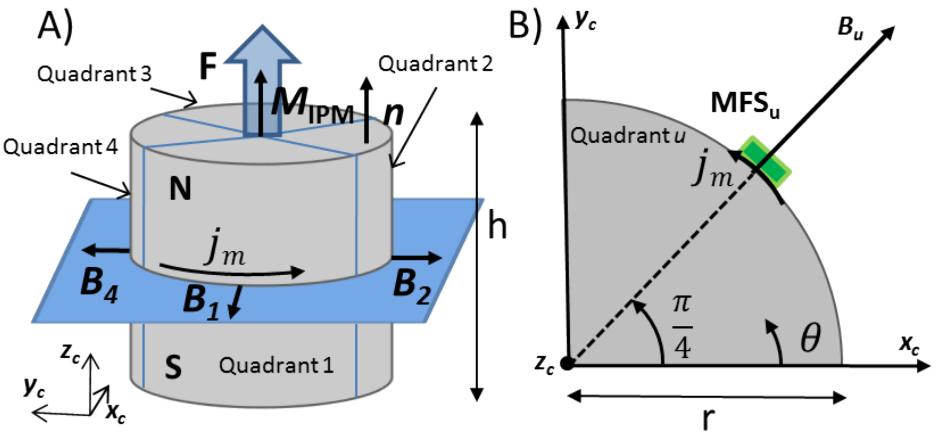

Figure II.7: (A) Lateral view of the IPM. (B) Schematic view of the i-th quadrant of the IPM.

II.3 Design contribution

II.3.1 Wireless Surgical Palpator Design

The main contribution of the paper attached in Section B, is to present a wireless platform for the measurements of the tissue property in order to restoring tactile and kinesthetic sensations in MIS and robotic MIS.

The WPP – schematically represented in Fig. II.8 and integrating pressor sensor, 3 MFS, an inclinometer and an external magnetic field source– can be deployed through a trocar incision and directly controlled by the surgeon to create a stiffness distribution map. The map can be used to localize tumor margins during soft tissue surgery, thus improving intraoperative diagnostic and interventional decisions. Wireless operation prevents the need for a dedicated port and reduces the chance of instrument clashing in the operating field.

Method Overview: A volumetric stiffness map can be created by estimating the local tissue stiffness $E(\mathbf{r})$ through the measurement of the indentation depth $\delta(\mathbf{r})$ and the tissue reaction pressure $P(\mathbf{r})$ at different positions $\mathbf{r}$ on the organ surface:

$$E(\mathbf{r}) \simeq \frac{P(\mathbf{r})}{\delta(\mathbf{r})}. \tag{II.41}$$

Referring to Fig. II.9, we can define (x, y, z) as the global Cartesian coordinate system, (x', y', z') as the reference frame at the external source of static magnetic field, and (x_w, y_w, z_w) as the coordinate system at the WPP. The origin O of (x, y, z) is coincident with the origin O' of (x', y', z'), while z_w is aligned with the main axis of the device. We

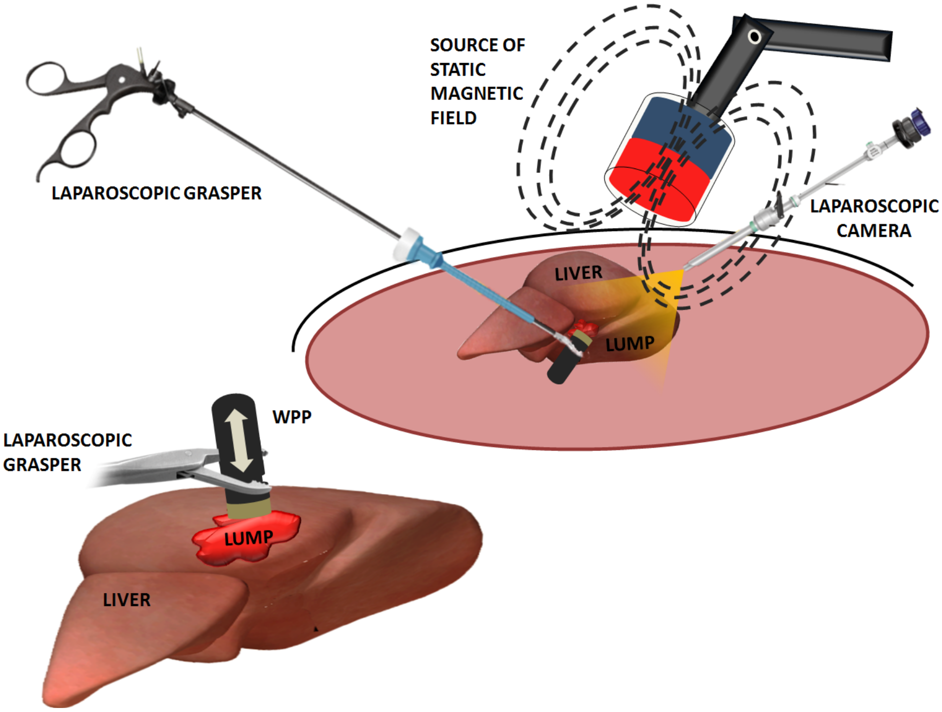

Figure II.8: Principle of operation for wireless tissue palpation using a WPP.

can assume the position vector $\mathbf{r}$ to identify the origin of (x_w, y_w, z_w) – noted as O_w – with respect to the global coordinate system (x, y, z). When the WPP is manipulated by the surgeon to palpate a tissue, its motion $\mathbf{d}$ is not constrained along z_w. Therefore, the following equation must be used to estimate the indentation depth $\delta(\mathbf{r})$:

$$\delta(\mathbf{r}) = \mathbf{d} \cdot \mathbf{z}_{w0} = (\mathbf{r}_f - \mathbf{r}_0) \cdot \mathbf{z}_{w0}, \tag{II.42}$$

where $\mathbf{r}_0$ and $\mathbf{r}_f$ are the WPP positions at the beginning and at the end of the indentation, respectively, while $\mathbf{z}_{w0}$ is the unit vector along z_w at the beginning of the indentation. In this approach, the beginning of the indentation is identified as the instant when the reading of the tissue reaction pressure $P(\mathbf{r})$ becomes significant. The end of each indentation is identified as the instant when $\delta(\mathbf{r})$ reaches the maximum value.

In our work, tissue reaction pressure is acquired by a barometric pressure sensor embedded in a silicone rubber at the probing surface of the WPP. This design is inspired by [110]. A threshold value P_{th}, independent from $\mathbf{r}$, is defined by calibration and takes into account both bias and noise of the pressure sensor. A single indentation starts as $P(\mathbf{r}) > P_{th}$.

The 5 DOF real-time localization of the WPP serves two purposes. First, the position where indentation is taking place must be recorded in 3 DOF in order to reconstruct the

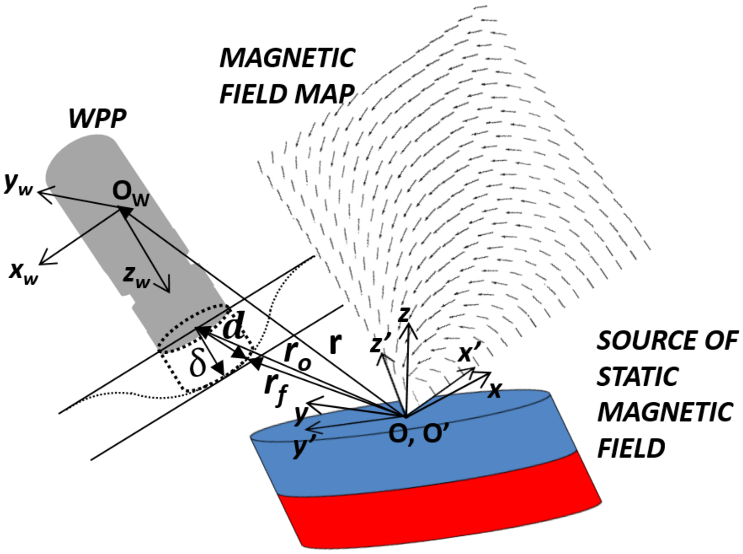

Figure II.9: The WPP during indentation and the external source of magnetic field with a slice of the magnetic field map. Vectors $\mathbf{r}_0$ and $\mathbf{r}_f$ represent the WPP position $\mathbf{r}$ at the beginning and at the end of the indentation. They are represented at the interface of WPP and tissue, rather than at O_w, for a better understanding of their physical meaning.

stiffness map. In this case, we assume the position $\mathbf{r}$ of each indentation to be coincident with WPP position as the indentation begins (*i.e.*, $\mathbf{r}_0$). A second goal for WPP tracking is to derive $\delta(\mathbf{r})$ as in Eq. II.42. In this case, real-time estimation of $\mathbf{r}$ and rotations of the WPP around x and y are required. Therefore, the WPP position and orientation in 5 DOF must be available in real-time. This is achieved by an on-board localization module, working in synergy with an external source of static magnetic field, as represented in Fig. II.8.

The on-board module consists of three orthogonally mounted magnetic field sensors and a triaxial accelerometer. The accelerometer – used here as an inclinometer – provides WPP rotations around x and y. The WPP position vector $\mathbf{r}$ is derived from the magnetic field sensor readings. The effective localization workspace is a cylinder with a diameter of 35 cm and a length of 35 cm, centered on the static magnetic field source. The 5-DOF WPP coordinates derived by the algorithm are referenced to a Cartesian frame at the center of the workspace. The hypothesis of functionality for the WPP is that the indentation phases have to be parallel to each other because the rotation about the gravitational axes is not detected.

Platform Overview & **User Interface:** The data from the barometric pressure sensor, the accelerometer, and the magnetic field sensors are acquired by a wireless microcontroller (CC2530, Texas Instrument, USA) through the SPI interface at a clock frequency of 1 Mbit/s. Each dataset is then bounded into a 28 byte payload together with a progressive package indicator, a time stamp, the battery level, and two synchronization start and stop bytes.

A multi-thread C++ application running on the PC unbounds the data and shares them with a parallel application developed in Matlab (Mathworks, USA) via TCP-IP communication. Refresh rate for displayed data runs at 30 Hz.

The user interface is conceived to work in two different modalities: (1) creation of the volumetric stiffness map, (2) display of WPP position on the volumetric stiffness map. In the first modality, the surgeon grasps the WPP and creates the map by palpating the region of interest. In this case, the user interface displays in real-time the x, y, z coordinates of the WPP, a plot of the indentation pressure, and the numeric value of the indentation depth in case the indentation pressure has exceeded P_{th}. Visual indicators are provided to warn the user if the WPP is outside the localization workspace. Once the region of interest has been palpated with the desired spatial resolution, a command is provided by the user through the keyboard to create the volumetric stiffness map. Once the map is available, the user interface switches to the second modality, overlaying the real-time position of the WPP in a 3D space centered on the map. Under the assumption that the region palpated does not undergo substantial movements, the surgeon can manipulate the WPP as a cursor to identify the margins of a stiffer region buried underneath the tissue.

II.3.1.1 Wireless *In-Vivo* Platform for Resistance Forces Measurement of WCE Inside the GI Tract

The main contribution of the paper attached in Section D, which is presenting the design of the WCE equipped with permanent magnet, 6 MFS and an inclinometer, is to present a wireless platform for the measurement of the resistant forces that an active capsule must overcome in order to move inside the GI tract. The platform described in this paper allows application of a force $\mathbf{F}_a$ to a capsule without the need for a tethered connection. This is achieved by leveraging magnetic coupling between an EPM and a magnet embedded inside the capsule (the IPM).

The proposed platform is validated with benchtop trials and through an *in vivo* experiment using a porcine colon model.

A secondary contribution of this paper is to present a real-time method to estimate the axial magnetic force acting on a wireless capsule manipulated by an external magnetic field.

Method Overview: A common method to measure the resistance properties of the intestine is to impose a motion to a capsule mock-up inside the lumen and to measure the associated force profile [111–113]. An equivalent approach, schematically represented in Fig. II.10, consists of imposing an increasing force $\mathbf{F}_a$ to the capsule and recording the motion profile to understand when the applied force $\mathbf{F}_a$ overcomes the resistant force $\mathbf{F}_r$. Referring to the instant when motion starts as t_0 and assuming a static equilibrium until that moment, the value $\mathbf{F}_a(\mathrm{t}_0)$=$\mathbf{F}_r(\mathrm{t}_0)$ quantifies the static resistant force that an active capsule must overcome to begin its motion. Then, as the motion builds up, driven by $\mathbf{F}_a$ increases, the system moves away from the equilibrium and the following equation can be used to describe its dynamics:

$$\mathbf{F}_{tot} = \mathbf{F}_a - \mathbf{F}_r = m\ddot{\mathbf{d}}, \tag{II.43}$$

where $\mathbf{d}$ is the position of the capsule center of mass O_c, and m is the capsule mass.

The applied force $\mathbf{F}_a$, the position $\mathbf{d}$, and the acceleration $\ddot{\mathbf{d}}$ are measured wirelessly in real time with respect to a reference frame $\{\mathbf{x}_m, \mathbf{y}_m, \mathbf{z}_m\}$ on the EPM. While just $\mathbf{F}_a$ and $\ddot{\mathbf{d}}$ would be sufficient for a complete characterization of $\mathbf{F}_r$, real-time knowledge of $\mathbf{d}$ allows adjustment of the setup during *in vivo* trials and to record the distance traveled by the capsule for each measurement. In addition, the capsule velocity $\dot{\mathbf{d}}$ can be calculated as the first derivative of $\mathbf{d}$ to provide additional information about the motion profile.

The applied force $\mathbf{F}_a$ can be adjusted by controlling the position of the EPM, which can be achieved by a robotic manipulator. Alternatively, the EPM position can be manually adjusted by an operator until the capsule starts its motion, as indicated by the real-time measurement of $\dot{\mathbf{d}}$ and $\ddot{\mathbf{d}}$.

Platform Overview: The platform is composed of a wireless capsule, the EPM, and a personal computer (PC) connected to a wireless transceiver via the universal serial bus (USB) port. The real-time algorithm runs on the PC and communicates with the capsule through the USB transceiver. The EPM is a NdFeB (magnetization N52, magnetic remanence 1.48 T) cylindrical permanent magnet with axial magnetization, as represented in Fig. II.10. The EPM diameter and length are both equal to 50 mm, while the mass is 772 g. A triaxial accelerometer (LIS331DL, STMicroelectronics, Switzerland) – used as inclinometer – is mounted on the EPM to provide pitch and yaw angles of $\{\mathbf{x}_m, \mathbf{y}_m, \mathbf{z}_m\}$ with respect to the global frame $\{\mathbf{x}, \mathbf{y}, \mathbf{z}\}$. These angles are used for the localization algorithm and fed directly to the PC through a 16-bit acquisition board (USB DAQ-6211, National Instrument, USA).

The wireless capsule, schematically represented in Fig. II.5, hosts the FMSM, wireless

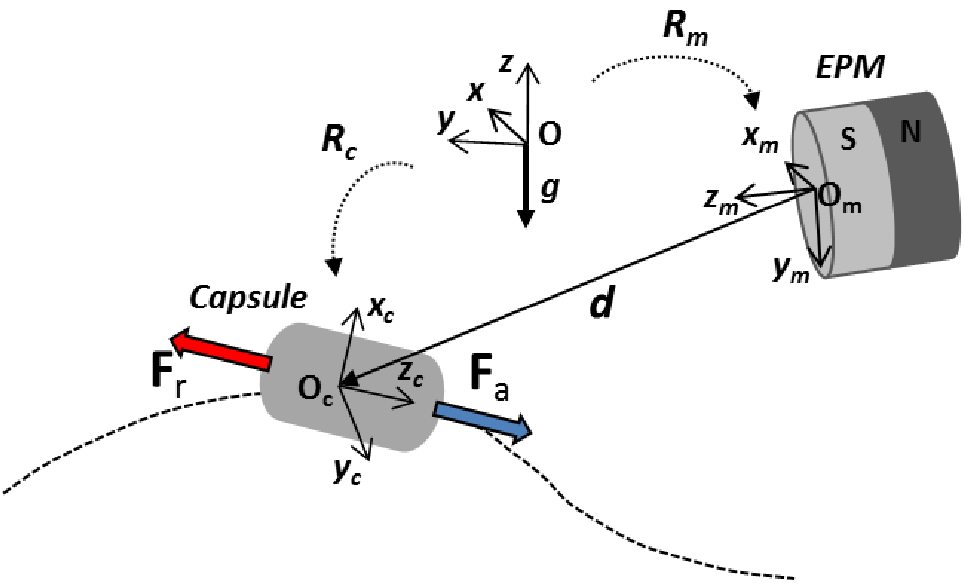

Figure II.10: Schematic representation of the principle of operation. The attraction force $\mathbf{F}_a$ is generated by magnetic coupling between an EPM and a magnet embedded in the capsule. The intermagnetic force $\mathbf{F}_a$ and the capsule position $\mathbf{d}$ with respect to the EPM are recorded wirelessly in real time. $\mathbf{F}_r$ is the resistant force, $\mathbf{g}$ is the gravitational acceleration vector, R_c is the rotational matrix of the capsule reference frame with respect to the global Cartesian coordinate system, while R_m is the rotational matrix of the reference frame at the EPM with respect to the global Cartesian coordinate system.

communication, and power supply. Each of these modules are described in detail in the following subsections. The outer shell was fabricated in biocompatible material – polyether-ether-ketone, PEEK – by traditional machining. The current prototype is 60 mm in length, 18 mm in diameter, 21 g in mass.

The readings of the sensors integrated in the FMSM are acquired by the onboard wireless microcontroller. The dataset is acquired every 4.4 ms by the microcontroller and used to build a 32-byte package together with the wireless signal strength indicator, the battery level, an incremental package number identifier, and the start/stop bytes. This package is then transmitted by the wireless microcontroller to the external transceiver over a 2.4 GHz carrier frequency, with a refresh time of 6 ms, resulting in sampling rate of 166 Hz. The power source used is a 50 mAh, 3.7 V rechargeable LiPo battery (Shenzhen Hondark Electronics Co., Ltd., China, 12 mm × 15 mm × 3 mm in size).

User Interface

A multi-thread C++ WIN32 application running on the PC unbundles the data and shares them via TCP-IP communication with a second application (developed in MATLAB, Mathworks, USA), which runs in parallel to implement the estimation algorithms and the user interface. The data transfer rate between the two applications is 30 Hz, while the refresh time for capsule position $\mathbf{d}$, acceleration $\ddot{\mathbf{d}}$, and intermagnetic force $\mathbf{F}_a$ is 50 ms (refresh rate 20 Hz). Two real-time plots are displayed on the main screen. The applied intermagnetic force $\mathbf{F}_a$ is shown on the left as a function of time, while the position and orientation of the capsule reference frame $\{\mathbf{x}_c, \mathbf{y}_c, \mathbf{z}_c\}$ with respect to the EPM reference frame $\{\mathbf{x}_m, \mathbf{y}_m, \mathbf{z}_m\}$ are displayed in real time on the right side. Numerical values for capsule position $\mathbf{d}$ and velocity $\dot{\mathbf{d}}$ are also shown, together with the most current values of the battery voltage and the wireless signal strength indicator. Capsule velocity $\dot{\mathbf{d}}$ is filtered by applying a 5-element moving average. A visual indicator alerts the user every time that motion starts. The user interface also allows the user to set the initial bias for the measurement and to record the data in a spreadsheet file.

II.3.1.2 High refresh rate Jacobian-based Iterative Method For Magnetic Localization in WCE

The main contribution of the paper included in Section C, which is presenting the design of the WCE equipped with permanent magnet, 6 MFS and an Inertial Measurement Unit (IMU), is to present a wireless platform featuring high refresh rate pose detection aimed to enable close-loop control of WCE's magnetic remote manipulation.

The computational time of proposed design and pose detection method is within 10 ms, considering both sensor acquisition and localization, allowing the implementation of a 100 Hz WCE manipulation closed-loop control. In the this work, we demonstrate our proposed algorithm on a WCE localization setup that includes an extracorporeal magnetic field source that manipulates an intracorporeal WCE. The localization strategy proposed herein provides the change in position of a WCE with respect to an external magnetic field source by knowing initial position and orientation.

Method Overview: The contribution of this activity stems from putting forward a new approach for WCE localization by using an iterative Jacobian-based method as shown in Fig. III.14 (also, the method is further described in Section C.4.2, and C). We leverage finite element solutions to the magnetic field problem and least-squares interpolation to obtain closed-form and fast estimates of the magnetic field. By defining a closed-form expression for the Jacobian of the magnetic field relative to changes in the WCE position we obtain an iterative WCE localization method without suffering from the inaccuracies stemming from dipole assumptions and without the downside of slow refresh rate.

Platform Overview: The experimental platform, represented in Fig. II.11.A, is composed of the WCE, the EPM, a robotic manipulator (RM), and a personal computer (PC) connected to a wireless transceiver via the universal serial bus (USB) port. The real-time algorithm runs on the PC and communicates with the capsule through a USB transceiver. The EPM is a NdFeB (magnetization N52, magnetic remanence 1.48 T) cylindrical permanent magnet with axial magnetization. The EPM diameter and length are both equal to 50 mm, while the mass is 772 g. A six-DOF robot (RV6SDL, Mitsubishi Corp., Japan) mounts at its end-effector the EPM. The robot is controlled in real time through a multi-thread C++ software application. The manipulator is used to control and track the EPM position and orientation with respect the reference global frame. The experimental platform global frame $[\hat{\mathbf{x}}_w, \hat{\mathbf{y}}_w, \hat{\mathbf{z}}_w]$ is assumed to be superimposed on the manipulator ground frame $[\hat{\mathbf{x}}_0, \hat{\mathbf{y}}_0, \hat{\mathbf{z}}_0]$. The current EPM pose for the localization algorithm is derived from the robot end-effector pose, which is available at the application interface level. The EPM orientation frame $[\hat{\mathbf{x}}, \hat{\mathbf{y}}, \hat{\mathbf{z}}]$ is an input for the localization algorithm, while the EPM pose as acquired by the robot encoders is used as reference position for the experimental assessment.

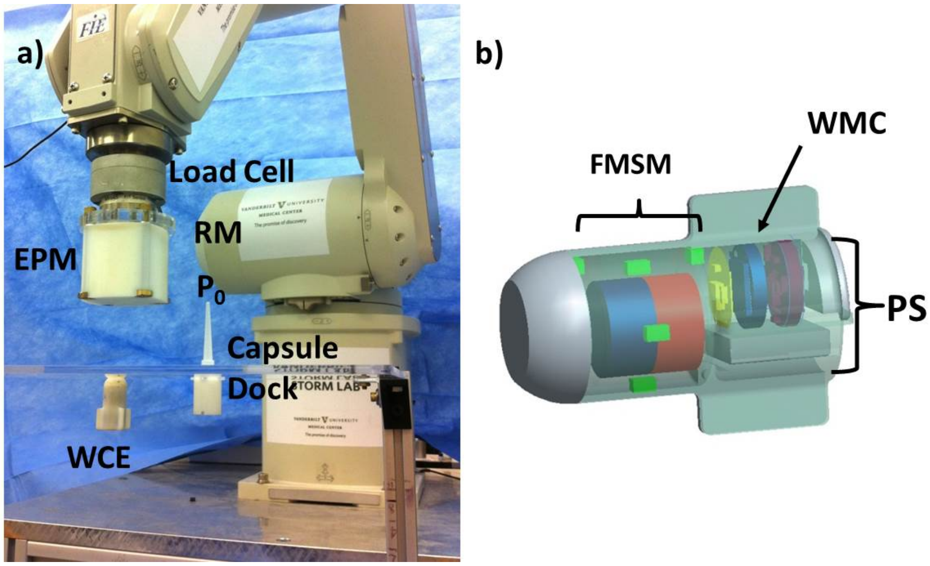

Figure II.11: Experimental platform: a) Robotic Manipulator (RM) and EPM. b) Visual rendering of the WCE and its internal components.

The WCE, schematically represented in Fig. II.11.B, hosts the FMSM, Wireless Microcontroller (WMC) (CC2530, Texas Instruments, USA), and power supply (PS). The outer shell is fabricated in VeroWhite 3D printer material. The current prototype is 36 mm in length, 17.5 mm in diameter, and 15 g in mass. The capsule shell has four lateral wings that are used to achieve a precise alinement with the capsule cartesian frame $[\hat{\mathbf{x}}_c, \hat{\mathbf{y}}_c, \hat{\mathbf{z}}_c]$ during the experiments.

The FMSM is composed of six MFS, an IMU sensor with accelerometer and gyroscope embedded, and an off-the-shelf NdFeB (N52) cylindrical magnet axially magnetized with 1.48 T of magnetic remanence, 11 mm in diameter and 11 mm in height.

The readings of the magnetic sensors integrated in the FMSM, and also, the six digitized values of acceleration and angular speed of the IMU are received by the WMC. This dataset is acquired every 4.4 ms and used to build a 36-byte package together with the capsule status indicators (i.e., battery level, start/stop bytes). This package is then transmitted by the WMC to the external transceiver over a 2.4 GHz carrier frequency, with a refresh time of 6 ms, resulting in sampling rate of 166 Hz. The external transceiver is based on an identical WMC which communicates with the PC through a USB-serial converter (UM232R, FTDI, UK).

The device's current consumption varies between 40 mA, when the microcontroller is in low power mode, and 20 mA when it is in IDLE mode with the radio active. Average current consumption rises to 48 mA during a single cycle of sensor data acquisition and wireless transmission. The power source used is a 50 mAh, 3.7 V rechargeable LiPo battery (Shenzhen Hondark Electronics Co., Ltd., China).

User Interface

A multi-thread C++ WIN32 application running on the PC unbundles the data and shares them to three other parallel threads. The first thread controls the robotic manipulator through a UDP/IP communication with refresh rate of 140 Hz. The thread first, sends the desired pose to the robot controller and then it receives the current robot pose feedback. The second thread implements a digital Kalman filter for each of the six MFS and the six IMU outputs before running the iterative localization algorithm. The algorithm outputs are 6-DOF capsule pose estimation $\mathbf{p} = [x, y, z, \alpha, \beta, \gamma]$ with respect to the EPM frame $[\hat{\mathbf{x}}, \hat{\mathbf{y}}, \hat{\mathbf{z}}]$. The third thread manages a TCP/IP communication with a MATLAB application (Mathworks, USA), which displays the localization algorithm estimation. The data transfer rate for the robot controller applications is 83 Hz. The refresh time for capsule pose estimation $\mathbf{p}$ and the capsule wireless data transfer is 6.8 ms (refresh rate 150 Hz). The MATLAB application displays the capsule position and orientation $\mathbf{p} = [x, y, z, \alpha, \beta, \gamma]$ with respect to the EPM reference frame $[\hat{\mathbf{x}}, \hat{\mathbf{y}}, \hat{\mathbf{z}}]$ in real time (refresh every 30 ms) on a 3D plot. Current pose numerical values are also displayed.

Chapter III

LOCAL MAGNETIC MANIPULATION FOR ROBOTIC ABDOMINAL SURGERY

In [114] is introduced the concept of LMA (also defined Trans-abdominal Active Magnetic Linkage (TAML)), where mechanical power is transferred across the abdominal wall by magnetic coupling, in order to drive a degree of freedom DOF of a laparoscopic robot, as represented in Fig. III.1 and described also in [115]. This approach prevents the need for embedded actuators, wired connections and eventually batteries.

As represented in Fig. III.2, each LMA-based device is composed of at least one Anchoring Unit (AnU), and an Actuation Unit (AcU) per independent DOF. The anchoring unit is composed of an external and an internal permanent magnet. Its function is to support the instrument during surgery. The actuation unit is composed of an external driving permanent magnet and an internal driven permanent magnet. The driving magnet is connected to a motor that can be actuated independently, causing the actuation of the respective driven magnet, coupled across the abdominal wall. The driven magnet is used to actuate, through a mechanism, one DOF of the laparoscopic robot.

An important requirement for a MCR in MIS is the deployment through the single surgical port. Also functionality, device encumbrance, workspace of robotic manipulability, forces and speed generated at the surgical EE, are to be addressed as specified in these scientific papers [39, 85, 116].

Another important parameter that has to be considered for design of LMA-based devices is the average abdominal tissue thickness upon insufflation, where for a population that includes obese patients (body mass index > 30 kg/m^2) is 4 cm [117].

III.1 Magnetic Spur Gear for Remote Rotary Motion Transmission: Technical Specification and Objectives

As represented in Fig. III.1, two manipulators and one camera can be introduced into the abdomen by a single incision, as demonstrated in [115], and each one can be coupled with an external magnet held by a robotic arm. If the EE and the internal modules are properly designed, up to 5 DOF can be transmitted by moving the EPM. Referring to the left arm in Fig. III.1, roll and X Y translation will work against the friction of the internal module on the abdominal wall, while pitch and yaw must counteract the elasticity of the

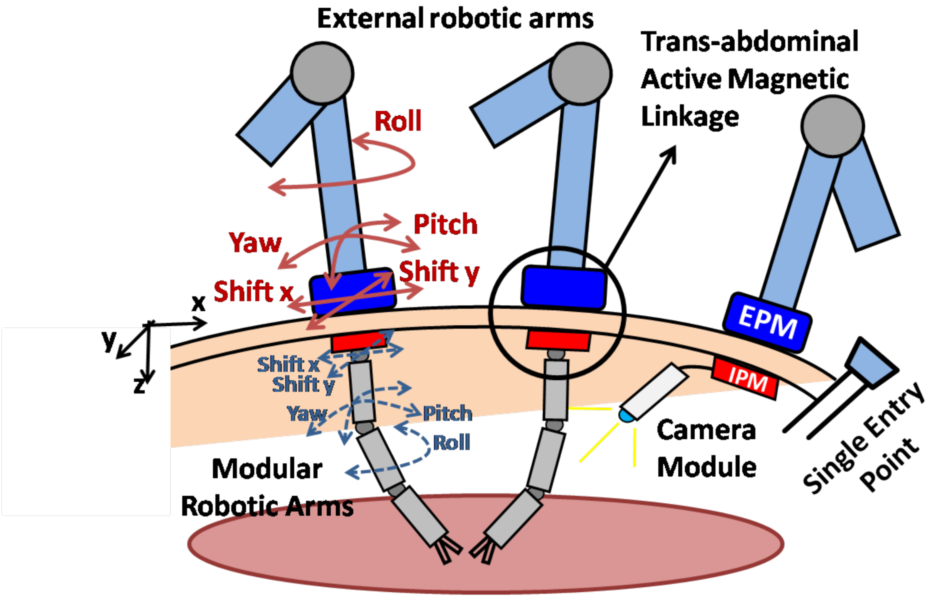

Figure III.1: Concept of a magnetically actuated surgical platform. On the left are shown several DOFs that can be obtained by simple magnetic coupling.

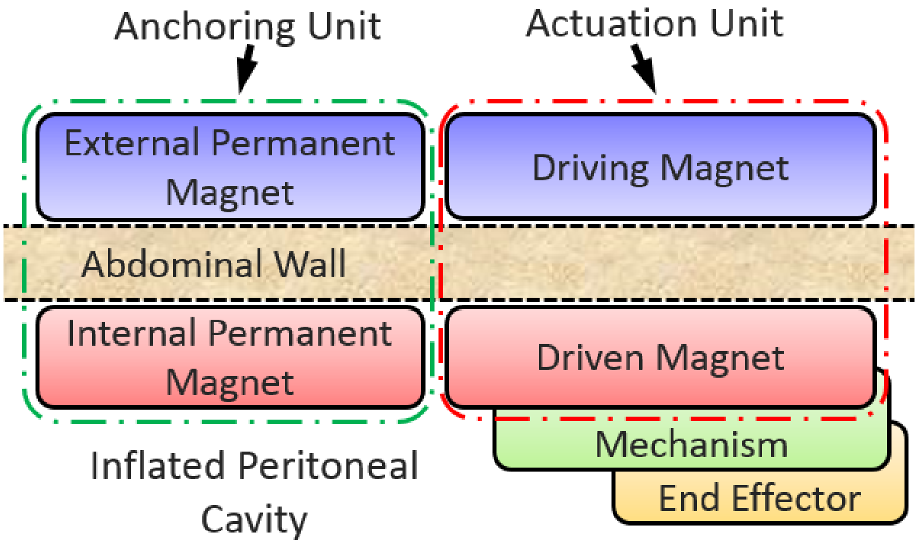

Figure III.2: Functional representation of a LMA-based robotic instrument coupled across the abdominal wall.

abdominal tissue. Having the EPM driven by a robotic arm would provide a better precision of movement, however, the dynamic interaction with the abdominal wall will always introduce unreliability in the control loop. Therefore, the best use of this approach may be gross positioning before starting a procedure, i.e. when high precision and repeatability of movements are not a stringent requirement.

Surgical tool design has severe size constraints for the modules that are to be introduced into the abdomen (i.e. outer diameter smaller than 12mm). Thus, to achieve higher forces and torques the best option is to move the actuators outside the patients body and use the largest magnets possible on board the surgical devices. Through controlled motion of the external magnets, one or more DOF can be transmitted over the LMA to the internal manipulators. Thanks to this approach, the only components that are required on board the manipulator, to achieve controlled motion, are the permanent magnets embedded in a properly designed mechanism.

An actuation mechanism based on the LMA concept can be seen as a modular structure, composed by a number of magnetic couples, each of them having one magnet inside and one outside the abdomen, with each couple carrying out a different function as shown in Fig. III.2. In more specific terms, the system is comprised of:

- AnU, composed of an external and an internal permanent magnet (EPM and IPM, respectively), whose function is to provide an anchoring force to the internal magnetic instrument during the surgical procedure.

- AcU, composed of an external driving EPM and an internal driven IPM. The external driving EPM is connected to a motor and can be actuated independently, causing the actuation of the respective internal driven magnet, coupled across the abdominal wall. The internal driven magnet can be used to actuate one or more DOFs of the internal module by cable or rigid link transmission.

Focusing on the AcU, a further dichotomy can be established by considering two different types of driving architectures, two example of AcUs enragements is described in Fig. III.3. In simplistic terms, these two actuation architectures can be described as follows:

- tLMA, where the external driving magnet is translated along a horizontal direction on a parallel plane to the abdominal wall. The external driving magnet, while translating, drags the internal driven magnet. Horizontal force at the IPM can be used to actuate a DOF of the internal module.

- rLMA, where the external driving magnet is rotated about its main axis. The driven magnets will rotate accordingly, trying to minimize the phase shift. Considering a cable winding up on the IPM shaft, the torque available at the IPM can be used to actuate an internal DOF.

A clear design advantage of the rLMA over the tLMA consists in the much larger workspace, since the actuating cable can be wound on a reel, while in the tLMA, the range is limited by the length of the slider the driven IPM is travelling on. On the other hand, the quantity of rotary motion for a rLMA could be adjusted as the design needs.

These are the main reasons behind the decision of pursuing the rLMA concept by analyzing the magnetic coupling from a static physics point of view to a dynamic and control theory point of view. This aims to achieve a controlled rotary motion of the driven unit by rotation of external driving magnets about their own axis. The remote rotary motion transmitted at the internal driven magnets can provide actuation to a mechanism or a joint connected by cable, rigid or hybrid transmission. The rLMA is more closely related to magnetic gears [77]. In tables III.2 and III.3 are reported the available torque generated by a couple of cylindrical permanent magnets diametrical magnetized and commercial DC motors respectively.

Previous work in the field of magnetic gears for industrial applications suggests that a coaxial concentric topology with radial coupling (i.e., driving and driven magnetic systems mounted one inside the other as in [75]) would enable a more efficient power transmission than a coupling, where the gears are rotating on parallel axes. This is due to a more homogeneous distribution of the attractive force around the main axis of each gear, as all the pole pairs are simultaneously involved in the transmission of mechanical power [76]. However, in the proposed application, this approach is unfeasible as the abdominal wall stands in between the driving and the driven units decreasing drastically the magnetic transmission's power. A possible solution is then to adopt a parallel-axis radial coupling across the tissue, with the associated challenge of an asymmetric attracting force and the related vibrations.

As regards the number of pole pairs, a magnetic coupling based on single-dipole magnets allows maximization of the volume of the magnetic material contributing to the torque transfer. Therefore, a parallel-axis radial coupling with single-dipole magnets seems to be the best solution for transmitting mechanical power to a device deep inside the human body. This approach was adopted in [118] for driving an implantable telescopic rod to correct skeletal deformities. While this work reported an interesting medical application, it did not address the challenges of achieving a servo control of the magnetic coupling.

This dissertation presents the extension of the methods proposed for the servo control of coaxial magnetic gears [119] to a parallel-axis radial coupling with single-dipole magnets.

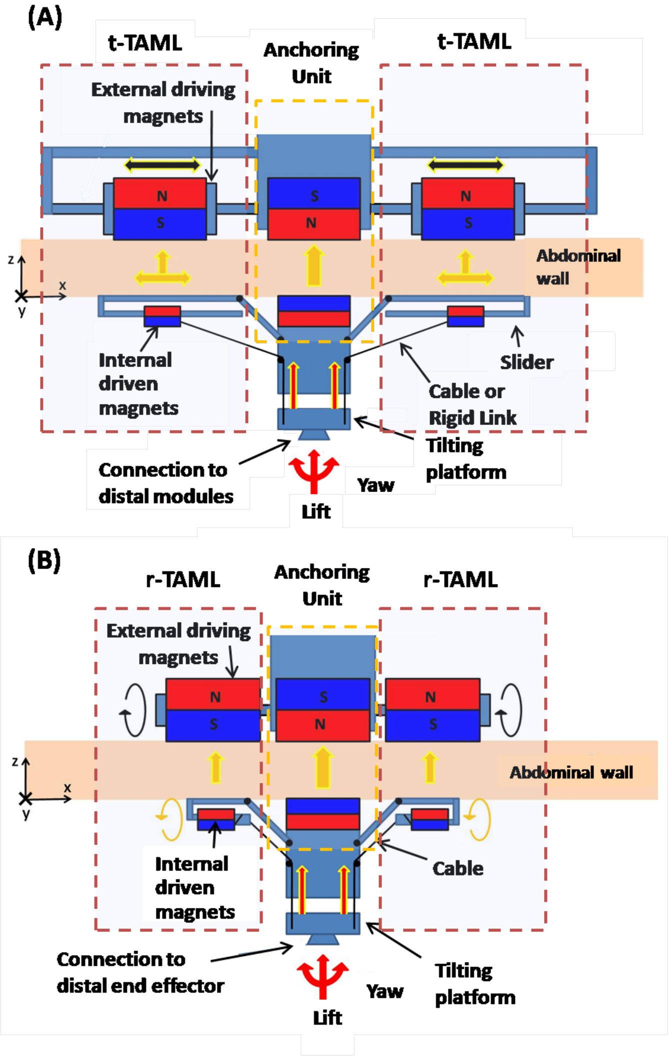

Figure III.3: Two examples of combining LMA units to obtain EE's DOFs: (A) Combination of an anchoring unit and two tLMA units. (B) Combination of an anchoring unit and two rLMA units. In both combinations showed in the examples, two actuation units can operate asymmetrically achieving yaw of the platform. Lift can be obtained by a symmetric operation, while push is possible only in the example (A), because rigid transmission allow push and pull.

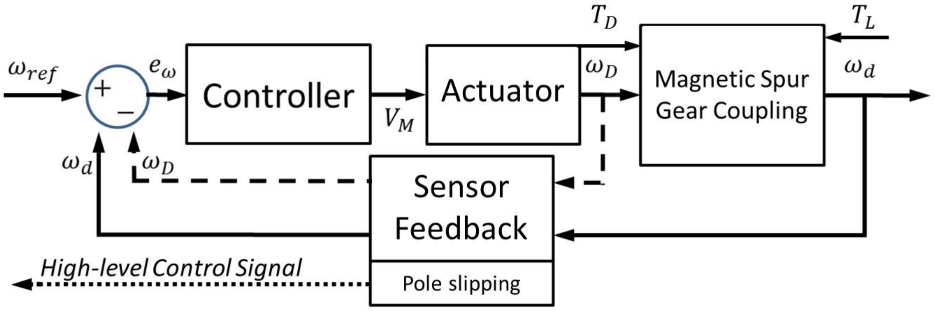

Figure III.4: Block diagram for the closed-loop control of a LMA actuation unit.

Generalization of the approach to the case where the driving and the driven magnets are asymmetrical (i.e., different in volume and/or magnetization), and where the intermagnetic distance h between them can vary within a certain range is addressed. The dynamics model of the rLMA actuation unit, quantification of the amount of the transmittable mechanical power and investigation of alternatives for closing the control loop strategy are also addressed.

III.2 Technical Contribution: Speed control of a magnetic spur gear

As represented in in Fig. III.4, the closed-loop control diagram for a single LMA actuation unit is composed of the magnetic spur gear coupling as in [77], the actuator rotating the driving magnet, the sensors measuring the feedback parameters, and the controller driving the actuator.

III.2.1 Controlling a rotational Local Magnetic Actuation Unit

Since the proposed LMA actuation strategy is intended to replace an onboard high speed/low torque rotational actuator, we aim to control the angular velocity at the load. As feedback parameter, we investigate the use of either the driving or the driven magnet angular velocity, ω_D or ω_d, respectively. This value is compared with the desired velocity ω_{ref}, and the error e_ω is fed to the controller that generates the appropriate voltage input V_M to the actuator. The external actuator imposes a torque T_D at an angular velocity ω_D to the magnetic gear system. The mechanical power is transferred to the driven magnet via magnetic coupling, to overcome the load torque T_L, which is seen as a disturbance to the system. As we use single-dipole magnets, the speed ratio between the driving and the driven magnets equals one. The proposed approach can be extended to multiple-dipole magnets by explicitly considering the ratio between the driven pole pairs and the driving pole pairs, as in [119]. The sensor feedback block measures in real time ω_D and ω_d, and detects if the system has entered the pole-slipping regime – the regime inherent to magnetic gears

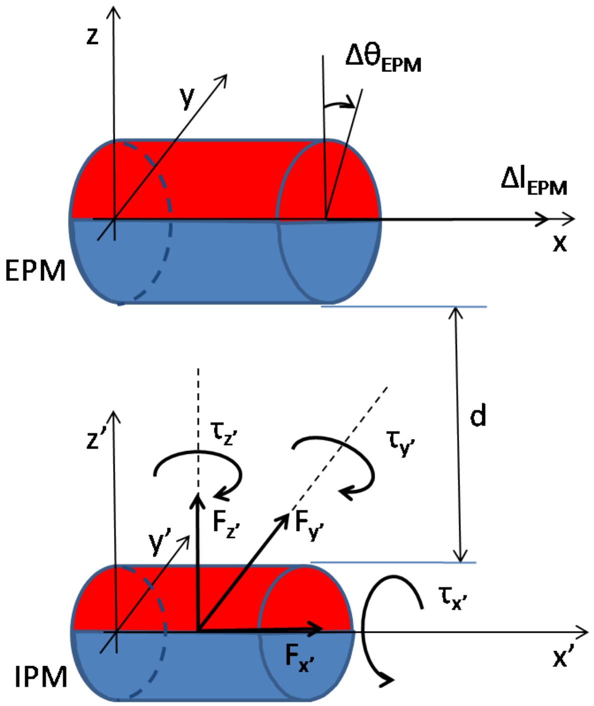

Figure III.5: Schematic representation of EPM and IPM for a typical LMA unit. The EPM is a cube in the anchoring and in the tLMA units and a cylinder in the rLMA unit.

where control is lost due to torque overload [119], or excessive driving magnet acceleration that induces inertial reaction forces on the driven magnet [120]. A warning signal can be transmitted to a high level controller in case of pole slipping. As suggested in [119], the coupling can be re-engaged by forcing ω_D at zero for a short period before being reset to the original speed command input.

III.2.2 Static Analysis of the Magnetic Spur Gear Coupling

A first piece of information toward the design of a rLMA-based device consists in predicting the maximum anchoring and actuation forces that are available at the IPM, given the main features of the magnetic link. At this point, a static model was developed as a first step toward establishing a complete modeling framework to describe this novel approach to mechanical power transfer.

Assuming that the environment does not contain ferromagnetic materials which are not included in the model, it is possible to apply the principle of superposition [90] to extend static magnetic modelling predictions to more complex magnetic configurations, as the ones represented in Fig. III.5.

Input parameters to the developed static model are the type of magnetization (i.e.

strength and direction), geometrical features of the magnets, distance between them, and the kind of motion of the driving magnet. The model provides the attraction force between the two magnets, i.e. the anchoring force for the IPM, and force and torque at the driven magnet in response to a translation or rotation of the driving magnet. The model is built upon the theories and the methods used in the analysis of steady currents, permanent magnets and magnetic circuits [90]. Referring to Fig. 3, the force E.1 and the torque E.2 at the IPM can be expressed as:

$$F = \oint_S j_m \times B_{ext} ds \tag{III.1}$$

$$T = \oint_S r \times (j_m \times B_{ext}) ds \tag{III.2}$$

where j_m is the equivalent surface current density on the IPM, r is the IPM radius, while B_ext is the rotating magnetic field E.3 induced by the EPM, which can be obtained by the magnetic charge model as:

$$B_ext(x) = -\frac{\mu_0}{4\pi} \oint_S \nabla \frac{M_E PM(x')\hat{n}}{\mid \mathbf{x} - \mathbf{x'} \mid} ds' \tag{III.3}$$

where $\mathbf{x}$ is the observation point, $\mathbf{x'}$ is the source point and $M_E PM$ is the EPM magnetization. This equation, obtained by applying the free-space Greens function, analytically describes the spatial components of the field generated by a magnetic source. In our case the source is the EPM and the observation point is the IPM. IPM features are modeled by j_m intended as the infinitesimal element of current flowing on the surface element ds. To quantify j_m E.4, we can apply:

$$j_m = \mathbf{M}_{IPM} \hat{n} \tag{III.4}$$

where $\hat{n}$ is the unit vector normal to ds, while M_{IPM} IPM is the IPM magnetization vector. Force and torque at the IPM can be computed using MatLab (MathWorks) to numerically solve the above equations with the FEM.

The actuation unit is based on the concept of magnetic spur gears [77] and is composed of two diametrically magnetized ring-shape magnetic dipoles, the EDM and the IDM, that are free to rotate about parallel axes. Referring to Fig. III.6.a, we define M$_D$ and M$_d$ as the magnetization vectors of the EDM and the IDM, θ_D and θ_d as the angular coordinates of M$_D$ and M$_d$, and d as the shortest distance between the external surfaces of the EDM and the IDM. In general, we assume d as coincident with the separation distance between the rLMA and the external controller. The difference between the two angular coordinates determines the actuation unit angular displacement $\Delta\theta = \theta_D + \theta_d$. The opposite orientation of the y and y' axes in Fig. III.6.a was adopted to emphasize that a clockwise rotation of the EDM induces an anti-clockwise rotation of the IDM.

As presented in Fig. III.6.b, the torque T$_{act}$ transferred from the EDM to the IDM is a function of $\Delta\theta$ [121–123] as follows:

$$T_{act}(\Delta\theta) = T_{max}\sin(\Delta\theta) \tag{III.5}$$

where $T_{\max}$ is the maximum torque that can be transmitted over the coupling. T$_{max}$ depends on the volume and magnetization strength of both EDM and IDM, and on their separation distance d. If $|\Delta\theta|$ exceeds $\pi/2$, the magnetic coupling enters a pole-slipping regime, resulting in a consequential loss of control, as explained by [124].

The magnetic coupling between EDM and IDM also generates a vertical attraction force between the two magnets. This force, referred to as F$_{act}$, contributes to supporting the retracted tissue by working in synergy with F$_{anc}$. As presented in Fig. III.6.c, F$_{act}$ can be formulated as a trigonometric function of θ_D, thus obtaining:

$$F_{act}(\theta_D) = \frac{F_v + F_h}{2} + \frac{F_v - F_h}{2}\cos(2\theta_D) \tag{III.6}$$

where F$_v$ and F$_h$ are the maximum and minimum values of F$_{act}$, corresponding to the vertical and the horizontal arrangements of the actuation magnets. As T$_{max}$, the values of F$_v$ and F$_h$ depend on the volume and magnetization strength of both the EDM and the IDM, and on their separation distance d. In addition, F$_v$ and F$_h$ are functions of $\Delta\theta$. While the plot in Fig. III.6.c considers $\Delta\theta = 0$.

Given the two selected magnets, we ran a set of FEM simulations to predict T$_{max}$, F$_v$, and F$_h$ as functions of d. In estimating F$_v$ and F$_h$, we assumed that $\Delta\theta = 0$. In the FEM simulations, we used a mesh with more than 3,500,000 elements and we varied d from 2 cm to 6 cm in 0.2 cm increments. Simulation results and exponential regressions fitting the data are reported in Fig. III.7.a for T$_{max}$ and in Fig. III.7.b for F$_v$ and F$_h$.

From Fig. III.7.a, it is interesting to observe that if compared to EM motors having a volume similar to the IDM [125,126], the torque available for driving a mechanism is larger as long as d remains below 5 cm.

Considering that the speed ratio from the EDM to the IDM is 1:1, the overall mechanical power that can be provided to a mechanism inside the abdominal cavity mainly depends on the speed of the external motor spinning the EDM. As the size is not a primary constraint in selecting the external actuator, a fast motor that is powerful enough to spin the EDM can

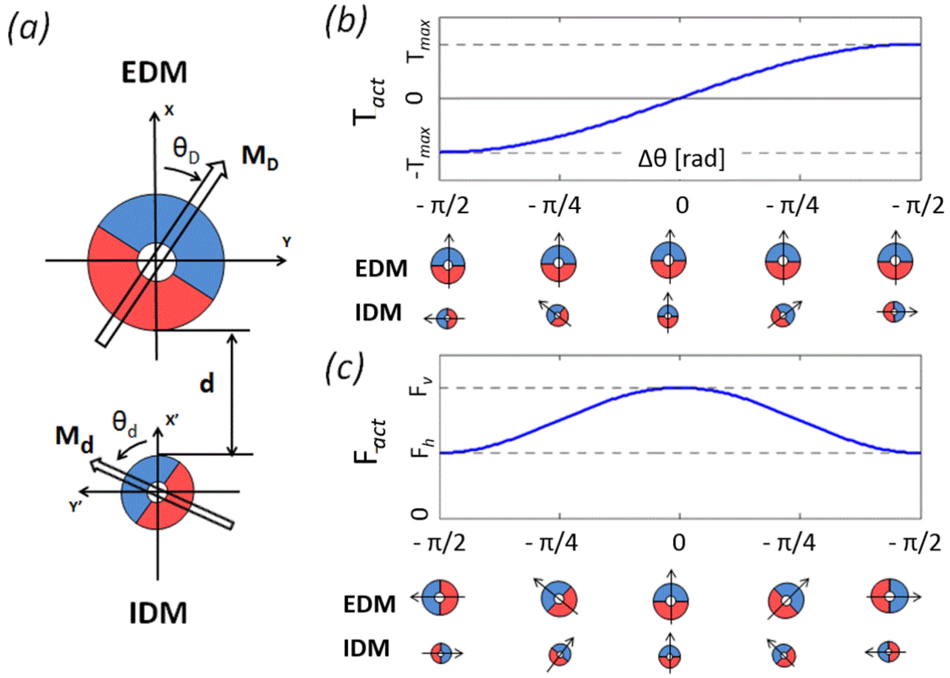

Figure III.6: (a) Schematic cross-section of the EDM and IDM composing the actuation unit. (b) Torque transferred from the EDM to the IDM as a function of the angular displacement between EDM and IDM. The cross-section view of the actuation unit is reported below the plot. (c) Vertical attraction force generated by the actuation unit as the magnets rotate. This plot assumes $\Delta\theta = 0$. The cross section view of the actuation unit is reported below the plot.

easily overcome the mechanical power that can be delivered by an embedded EM motor, constrained in size to fit a 12-mm surgical port.

III.2.3 Dynamic Analysis of the Magnetic Coupling

A schematic diagram of the LMA actuation unit that is analyzed in this study is represented in Fig. III.8. The magnetic couple is composed of two cylindrical permanent magnets diametrically magnetized, having magnetization M_D and M_d for the driving and the driven magnets, respectively. We assume that the two magnets have a single dipole each, and we consider the general case where the two magnets are different in diameter and length.

An important assumption of our model is that the two magnets are lying on two parallel axes (i.e., z and z'), spaced by a separation distance h'. Note that we define h' as the distance between the two axes, and h as the separation between the outer surfaces of the two magnets, as represented in Fig. III.8.a. Referring either to h or h' is equivalent, as

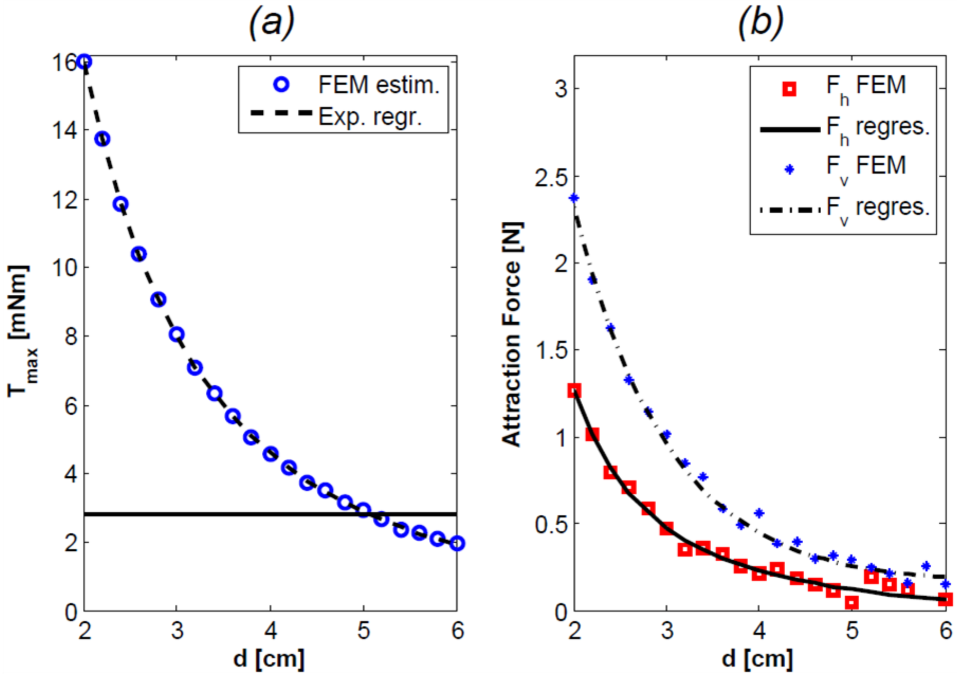

Figure III.7: (a)T_{max} and its exponential regression at different separation distances, the solid horizontal line represents the average nominal torque for commercially available EM motors that would fit a volume similar to the IDM. (b)$F_v and F_h$ and their exponential regressions at different separation distances, assuming $\Delta\theta = 0$. The selected IDM was 9.52mm in outside diameter (OD), 2.38 mm in internal diameter (ID), and 9.52 mm in length (L). It was made out of NdFeB, with a relative magnetic permeability of 1.05, and a magnetization grade of N42 (1.32 T magnetic remanence). The EDM was 25.4 mm in OD, 6.32 mm in ID, 25.4 mm in L, and presented the same magnetic features as the IDM.

the difference in their values is constant. We also assume that abdominal tissue does not influence the magnetic coupling [127].

We define J_D and J_d as the equivalent inertia at the driving and at the driven magnet side, respectively, while θ_D and θ_d are the angular coordinates of M_D and M_d as represented in Fig. III.8.b. The angular displacement of the drive train is denoted with $\Delta\theta = \pi - (|\theta_D| + |\theta_d|)$. As represented in Fig. III.8.a, the directions of rotation for the two magnets are opposite (i.e., a counterclockwise rotation of the driving magnet induces a clockwise rotation of the driven one).

The magnetic spur gear pair can be analytically described for different h by modifying the equivalent model for a two-inertia mechanical system [128]. In conventional two-inertia servo-drive systems, the interconnecting drive shaft has a linear torsional stiffness K – unit of Nm/rad – that stays constant within the operating range. Therefore, the torque T_C

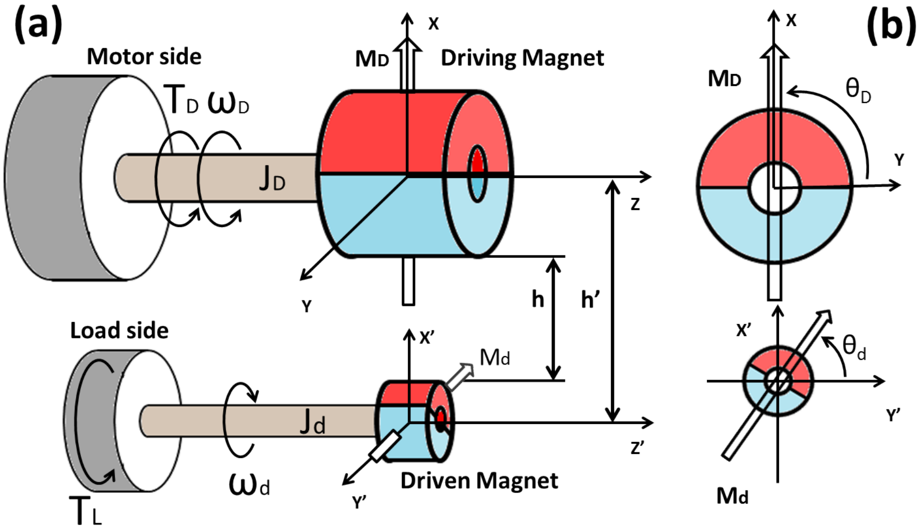

Figure III.8: Schematic overview (a) and lateral cross section (b) of the LMA actuation unit based on two diametrical magnetized cylindrical magnets.

transmitted by the prime mover to the load is a linear function of the angular displacement at the drive shaft. As introduced in [129], the torque transmitted across a radial magnetic coupling is not constant with $\Delta\theta$ and can be described by a nonlinear trigonometric function:

$$T_C(\Delta\theta) = T_G \sin(\Delta\theta), \tag{III.7}$$

where T_G is the maximum gear torque that can be transmitted over the magnetic coupling. The value of T_G depends on the volume and magnetization strength of the magnets and on their separation distance h. In case the driving and the driven magnets differ in terms of volume or magnetization, the cross-coupling due to the magnetic field becomes asymmetrical and two separate nonlinear torque transfer functions must be considered:

$$T_C^{Dd}(\Delta\theta, h) = T_G^{Dd}(h) \sin(\Delta\theta) \tag{III.8}$$

$$T_C^{dD}(\Delta\theta, h) = T_G^{dD}(h) \sin(\Delta\theta) \tag{III.9}$$

where Eq. III.8 refers to the torque transferred from the driving to the driven magnet, while Eq. III.9 refers to the torque transferred in the opposite direction.

The numerical values of T_G^{Dd} and T_G^{dD} at different h can be obtained by the static analysis

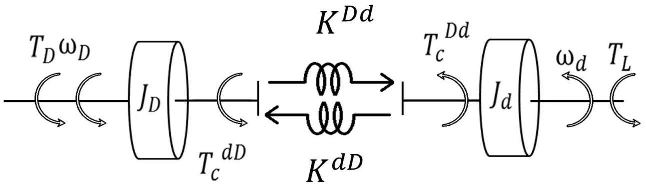

Figure III.9: Equivalent model of a magnetic spur gear pair with asymmetrical magnets.

and the FEM integration described in [114]. For a given magnetic gear pair considered at $\Delta\theta = \pi/2$, $T_G^{Dd}(h)$ and $T_G^{dD}(h)$ can be well approximated by exponential fits.

Referring to the equivalent model represented in Fig. III.9, the dynamic behavior of the LMA actuation unit can be described by the following system of equations:

$$J_D \frac{d^2\theta_D}{dt^2} = T_D - T_C^{dD}(\Delta\theta, h) \tag{III.10}$$

$$J_d \frac{d^2\theta_d}{dt^2} = T_C^{Dd}(\Delta\theta, h) - T_L. \tag{III.11}$$

The trigonometric expressions of T_C^{Dd} and T_C^{dD} can be linearized about $\Delta\theta = 0$ in the range $|\Delta\theta| < \pi/2$, assuming

$$T_C^{Dd}(\Delta\theta, h) \simeq K^{Dd}(h)\Delta\theta = \frac{2}{\pi}\tilde{T}_G^{Dd}(h)\Delta\theta, \tag{III.12}$$

$$T_C^{dD}(\Delta\theta, h) \simeq K^{dD}(h)\Delta\theta = \frac{2}{\pi}\tilde{T}_G^{dD}(h)\Delta\theta, \tag{III.13}$$

where $\tilde{T}_G^{Dd}(h)$ and $\tilde{T}_G^{dD}(h)$ are the exponential fits for $T_G^{Dd}(h)$ and $T_G^{dD}(h)$, respectively.

Beyond $|\Delta\theta| < \pi/2$ of angular displacement, the magnetic coupling enters a pole-slipping regime [119, 130], resulting in a consequential loss of control. This typically happens when the torque T_L required by the load overcomes the maximum value of torque that can be transmitted over the magnetic coupling, $T_G^{Dd}(h)$. For a reliable control of the driven magnet, pole slipping must be prevented. This can be accomplished by monitoring in real time $\Delta\theta$ with the method suggested in the next subsection.

The block diagram representing the open-loop system – shown in Fig. III.10 – can be derived by combining Eqs. III.10-III.13. In no-load conditions, the transfer functions relating the driving torque to the driving and the driven angular velocities are given by

$$\frac{\omega_D}{T_D} = \frac{s^2 + \frac{K^{Dd}}{J_d}}{J_D s(s^2 + \frac{K^{Dd}J_D + K^{dD}J_d}{J_D J_d})} = \frac{s^2 + \omega_a^2}{J_D s(s^2 + \omega_0^2)} \tag{III.14}$$

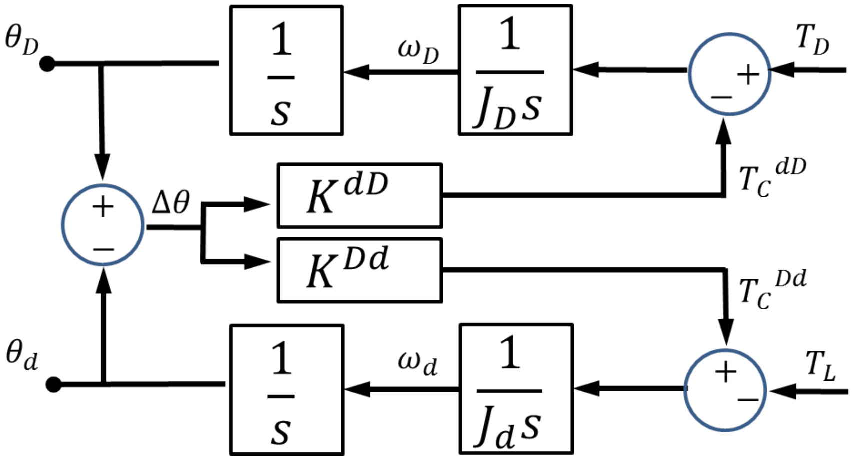

Figure III.10: Block diagram of the open-loop magnetic gear system.

$$\frac{\omega_d}{T_D} = \frac{K^{Dd}}{J_d J_D s} \frac{1}{s^2 + \frac{K^{Dd} J_D + K^{dD} J_d}{J_D J_d}} = \frac{K^{Dd}}{J_d J_D s(s^2 + \omega_0^2)} \tag{III.15}$$

where the antiresonant ω_a and the resonant ω_0 frequencies are, respectively, given by

$$\omega_a = \sqrt{\frac{K^{Dd}}{J_d}}, \qquad \omega_0 = \sqrt{\frac{K^{Dd} J_D + K^{dD} J_d}{J_D J_d}}. \tag{III.16}$$

The dynamic model validation consist of two stages of trials. The first step of validation focused on assessing the sensor feedback strategy, as this was used for all the experiments that follow. In particular, we compared ω_D as measured by the encoder with the value estimated. This test was performed for ω_D= [500, 700, 900, 1100, 1300, 1500] rpm, showing an average error of 7.28 ± 2.82 rpm. We can reasonably assume a similar uncertainty in reconstructing ω_d and $\Delta\omega$.

The second step consisted of validating the dynamic model of the magnetic gear coupling for different separation distances h, driving angular velocities ω_D, and applying load torques T_L. A single experiment consisted of increasing T_L, while driving the external magnet at a constant speed ω_D and maintaining a fixed intermagnetic distance h. As soon as the system entered in the pole-slipping regime, the experiment was ended. The intermagnetic distance h was varied from 2 cm to 7 cm in steps increments of 1 cm, while ω_D was increased from 500 rpm to 1500 rpm in steps increments of 200 rpm. The motor-side closed-loop control was adopted to guarantee a constant ω_D, as T_L was increased. Once a trial was started, the platform increased the voltage driving the hysteresis brake in 0.15 V increments every 0.2 s, resulting in an exponential increase of T_L over time. The event of pole slipping was detected by monitoring θ_d as measured by the sensor-side MFS. In particular, when θ_d was stalling around a limited number of angular positions, the algorithm assumed that the system was entered in the pole-slipping regime. In that case, the motor was stopped, the hysteresis brake was released, and the trial was considered over.

For each experiment, the data recorded for θ_D, θ_d, and T_D were used together with platform-specific parameters (i.e., J_D, J_d, $\tilde{T}_G^{Dd}$, $\tilde{T}_G^{dD}$) to estimate T_L. The dynamic model for T_L was derived by combining Eq. III.10 and Eq. III.11 and integrating over time, thus obtaining

$$T_L(t) = J_d \Delta\theta(t)\left(\frac{1}{\Delta t^2} + \frac{2}{\pi}\frac{\tilde{T}_G^{dD}}{J_D} + \frac{2}{\pi}\frac{\tilde{T}_G^{Dd}}{J_d}\right) - \frac{J_d}{J_D} T_D(t). \tag{III.17}$$

The reference value for T_L was obtained by measuring the current drained by the hysteresis brake and deriving the torque applied to the driven magnet from its calibration curve.

A typical plot for a single experiment at h=4 cm and ω_D=1000 rpm is represented in Fig. III.11. Here, three different regimes can be observed. In unloaded conditions, angular oscillations at the driven magnet were induced by the low inertia, combined with the non-linear elastic coupling of the magnetic link. In this regime, reconstruction of T_L by the model was noisy. As T_L increased, the amplitude of oscillations decreased significantly, and the model allowed for a reliable real-time estimation of the load torque. As expected, the system entered the pole-slipping regime as T_L overcame the maximum value of torque that can be transmitted over the magnetic coupling.

Five experiments were repeated for each combination of h and ω_D, and the estimation errors were averaged. The mean relative errors in estimating T_L at different velocities and intermagnetic distances are reported in Table III.1. Over the entire range of distances and velocities tested, the mean relative error was $7.1 \pm 2.3\%$, while the mean absolute error was 0.18 ± 0.06 mNm. All of these values are related to the loaded regime of operation. It is interesting to note a larger error at intermediate distances that is due to the effect of the resonant and antiresonant peaks in the open-loop transfer functions.

III.2.4 Sensor Feedback

Previous work on magnetic gear servo control [119, 120] focused on motor-side sensing, as load-side feedback sensors may be prohibitive to use in certain applications, such as off-shore wind turbines or all-electric automotive power trains. In case of surgical instruments, the constraints introduced by embedding feedback sensors on the load side are mainly related to sterilization and tethering. As for sterilization, low-temperature techniques can be adopted, in case the sensors cannot withstand the high temperature commonly used for

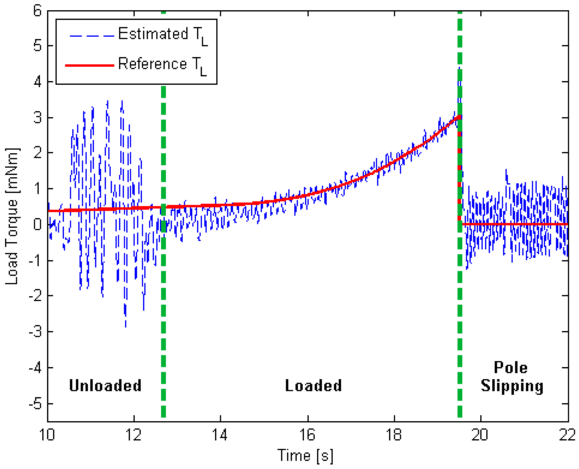

Figure III.11: Comparison between the estimated and the reference load torque for h=4 cm and ω_D=1000 rpm. The unloaded, loaded and pole-slipping regimes are highlighted by the dashed vertical lines.

	ω_D [rpm]					
h	500	700	900	1100	1300	1500
2 cm	9.4%	14.7%	5.7%	8.5%	7.9%	8.8%
3 cm	13.8%	8.1%	9.4%	6.4%	8.4%	3.1%
4 cm	9.6%	12.1%	10.9%	8.4%	8.3%	8.2%
5 cm	9.2%	13.4%	5.8%	7.6%	6.7%	7.9%
6 cm	8.7%	3.7%	4.0%	3.9%	4.1%	3.8%
7 cm	5.7%	3.1%	3.4%	3.8%	4.0%	5.5%

Table III.1: Mean relative errors in T_L estimation at different velocities and intermagnetic distances within the loaded regime.

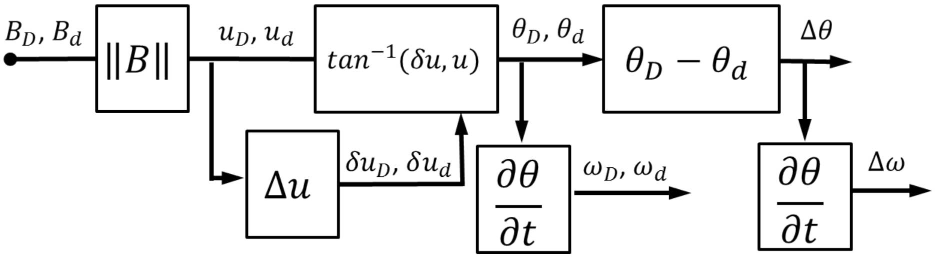

Figure III.12: Angular position (θ_D and θ_d), angular speed (ω_D and ω_d), angular displacement of the drive train ($\Delta\theta$), and its time derivative ($\Delta\omega$) are obtained through direct measurement of the magnetic field (B_D and B_d) generated by the driving and the driven magnets along the vertical direction.

steam sterilization (i.e., 132°C). Regarding tethering, a wired connection would be the most reliable option to acquire the data from the on-board sensors. This may be an advantage in terms of usability, as it can facilitate the retrieval of the instrument from the abdominal cavity once the surgery is over.

In this work, we investigate both motor-side and load-side sensing strategies by taking advantage of a pair of magnetic field sensors MFS. The motor-side sensor is placed next to the driving magnet, whereas the load-side sensor is placed close to the driven magnet.

The block diagram in Fig. III.12 shows how the signals acquired by the two MFS are used to derive the driving and the driven magnet angular positions, θ_D and θ_d, the angular velocities, ω_D and ω_d, the angular displacement of the drive train, $\Delta\theta$, and its time derivative, $\Delta\omega$. Referring to Fig. III.8, the component along x of the magnetic field generated by the driving magnet, B_D, is acquired by the motor-side MFS, while the load-side MFS acquires the component along $-x'$ of the magnetic field generated by the driven magnet, B_d. As the two magnets spin, B_D and B_d can be described by two cosine functions [114]. The magnetic field values are normalized, obtaining u_D or u_d, and the angular derivatives δu_D and δu_d are calculated. The inverse of the tangent function is applied to (u_D, δu_D) and to (u_d, δu_d) to derive θ_D and θ_d, respectively. Angular velocities ω_D and ω_d are then obtained by the time derivative of θ_D and θ_d, respectively.

III.2.5 Close-Loop Control on Motor Side

The motor-side closed-loop control is designed to work within a range of intermagnetic separation distances h from 2 cm to 7 cm. Therefore the controllers parameters are chosen in order to ensure controllability in the range of analysis which includes population range of abdominal thickness.

When a motor-side control strategy is adopted, the driven part of the actuator may

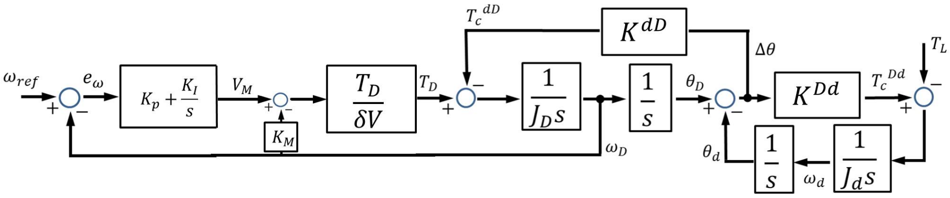

Figure III.13: Motor-side speed control system with PI controller.

be seen as a disturbance. In our approach, similar to [119, 128], we explicitly consider the effect of coupling in the control loop and, we adopt a standard Proportional-Integral (PI) controller fed with the motor-side angular velocity ω_D. The block diagram of the closed-loop system is shown in Fig. III.13. In this figure, K_p is the proportional feedback coefficient, while K_I is the integral feedback coefficient.

The closed-loop transfer function from the reference input to the motor speed is given by

$$\frac{\omega_D}{\omega_{ref}} = \frac{\frac{(K_I+K_p s)}{s}\,\frac{\frac{T_D}{\delta V}\,\frac{s^2+\omega_a^2}{J_D s(s^2+\omega_0^2)}}{1+\frac{T_D}{\delta V}\,\frac{s^2+\omega_a^2}{J_D s(s^2+\omega_0^2)}K_M}}{1+\frac{(K_I+K_p s)}{s}\,\frac{\frac{T_D}{\delta V}\,\frac{s^2+\omega_a^2}{J_D s(s^2+\omega_0^2)}}{1+\frac{T_D}{\delta V}\,\frac{s^2+\omega_a^2}{J_D s(s^2+\omega_0^2)}K_M}}. \qquad \text{(III.18)}$$

III.2.6 Close-loop Control on Load Side

The load-side closed-loop control is designed to work within a range of intermagnetic separation distances h from 2 cm to 7 cm. Therefore the controllers parameters are chosen in order to ensure controllability in the range of analysis which includes population range of abdominal thickness.

An alternative technique consists of closing the control loop on the load-side angular speed ω_d. This approach allows for a direct tracking of the system performance at the load, but may introduce system instabilities due to two imaginary poles in the open-loop transfer function (Eq. III.15). Therefore, we apply a custom controller with arbitrary placement of three poles and two zeroes to stabilize the system. Root locus analysis is used for the placement of controller singularities. In particular, two complex conjugates zeros are placed at higher frequencies and two complex conjugates poles are placed at lower frequencies to provide lag compensation. This allows reduction of steady state error and resonant peaks, thus increasing system stability. In addition, a pole is placed in the origin of the root locus to attenuate oscillations. The controller transfer function from the error e_ω to the motor

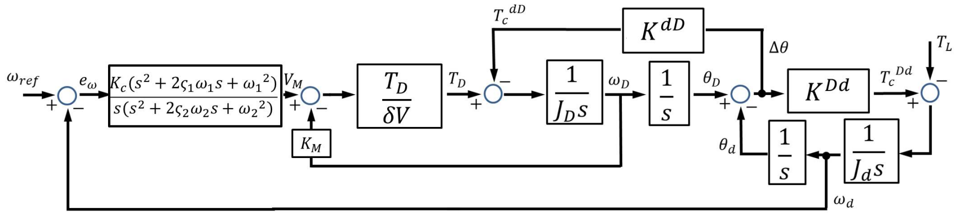

Figure III.14: Load-side speed control system with the custom controller fed by ω_d.

voltage input V_M is:

$$\frac{V_M}{e_\omega} = \frac{K_c(s^2+2\zeta_1\omega_1 s+\omega_1^2)}{s(s^2+2\zeta_2\omega_1 s+\omega_2^2)} \tag{III.19}$$

where K_c is the gain of the closed-loop controller, ω_1 and ω_2 represent natural angular frequencies, and ζ_1 and ζ_2 denote damping coefficients.

The block diagram for the load-side speed control is shown in Fig. III.14.

The closed-loop transfer function from the reference input to the load speed is given by

$$\frac{\omega_d}{\omega_{ref}} = \frac{\frac{K_c(s^2+2\zeta_1\omega_1 s+\omega_1^2)}{s(s^2+2\zeta_2\omega_1 s+\omega_2^2)}\frac{\frac{T_D}{\delta V}\frac{K_{Dd}}{s}\frac{1}{s^2+\omega_0^2}}{1+\frac{T_D}{\delta V}\frac{K_{Dd}}{s}\frac{1}{s^2+\omega_0^2}K_M}}{1+\frac{K_c(s^2+2\zeta_1\omega_1 s+\omega_1^2)}{s(s^2+2\zeta_2\omega_1 s+\omega_2^2)}\frac{\frac{T_D}{\delta V}\frac{K_{Dd}}{s}\frac{1}{s^2+\omega_0^2}}{1+\frac{T_D}{\delta V}\frac{K_{Dd}}{s}\frac{1}{s^2+\omega_0^2}K_M}}. \tag{III.20}$$

III.2.7 Control Strategies Comparison and Performances

Once the dynamic model was experimentally validated, we studied how variations in h were affecting the harmonic behavior of the two open-loop transfer functions in Eq. III.14 and Eq. III.15. Therefore, we plotted the two Bode diagrams for six discrete values of h (i.e., $h = [2, 3, 4, 5, 6, 7]$ cm). From the amplitude plots in Fig. III.15.a, we can observe that both the resonant and the antiresonant peaks in the motor-side transfer function migrate to lower frequencies as h increases, spanning less than a decade. In particular, ω_0=156 rad/s at h=2 cm, decreasing to ω_0=45 rad/s at h=7 cm. A similar behavior can be observed for the resonant peaks in the load-side transfer function, the amplitude of which is plotted in Fig. III.15.b. From the two Bode amplitude plots, it is relevant to emphasize that the singularities of the system and the range of their migration as h changes from 2 cm to 7 cm are within the interval of angular velocities investigated in this work (i.e., 500 rpm corresponds to 52 rad/s, while 1500 rpm corresponds to 157 rad/s). In determining the parameters for the two closed-loop controllers, we optimized the system response for h = [2...7] cm (i.e., the condition in which singularities occur at lower frequencies) and we

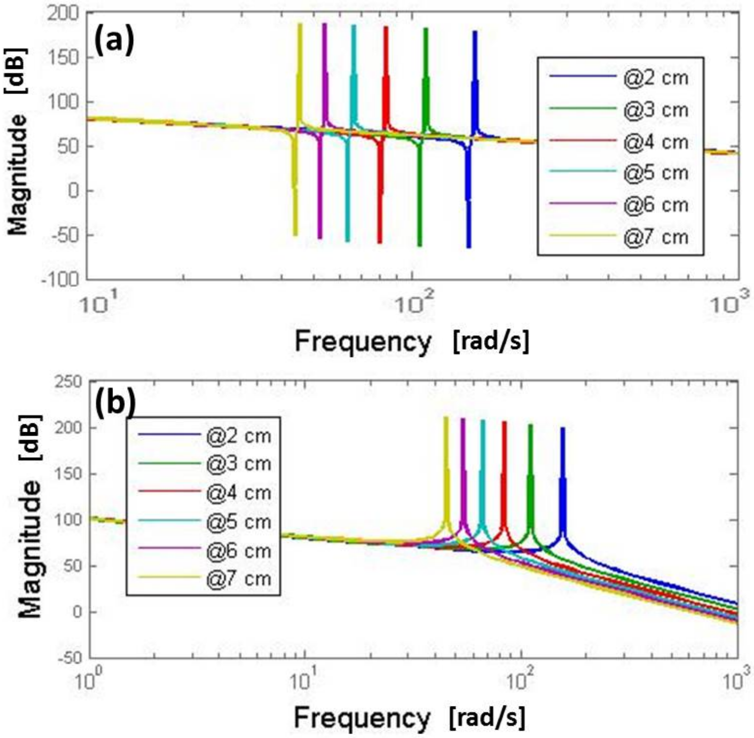

Figure III.15: Bode amplitude diagrams for the motor-side (a) and load-side (b) open-loop transfer functions for six discrete values of h (i.e., $h = [2, 3, 4, 5, 6, 7]$ cm).

experimentally investigated whether this choice could guarantee controllability in the entire range of h tested.

The Proportional and Integral coefficients for the motor-side closed-loop control were determined via the PID Tuning function of the Control System Toolbox (MATLAB, MathWorks, USA), obtaining K_P=52.42×10^{-3} V·s/rad and K_I=5.90 V/rad. Simulated step responses for $h = [2, 3, 4, 5, 6, 7]$ cm are reported in Fig. III.16.a, showing an overshoot that ranges from 11.4% to 10.8% and a settling time from 100 ms to 180 ms.

As regards the load-side control strategy, the parameters for the custom controller were also tuned for the range of analysis ($h \in [2, 7]$ cm), resulting in the following constants K_c=3.4×10^3V/rad, ω_1=1.6×10^{-4} rad/s, ω_2=5.5×10^{-6} rad/s, ζ_1=0.68, and ζ_2=1. Simulated step responses for $h = [2, 3, 4, 5, 6, 7]$ cm are reported in Fig. III.16.b, showing no relevant overshoot and a settling time of 200 ms for all the distances investigated.

A comparison between the simulated and the experimental step response is reported in

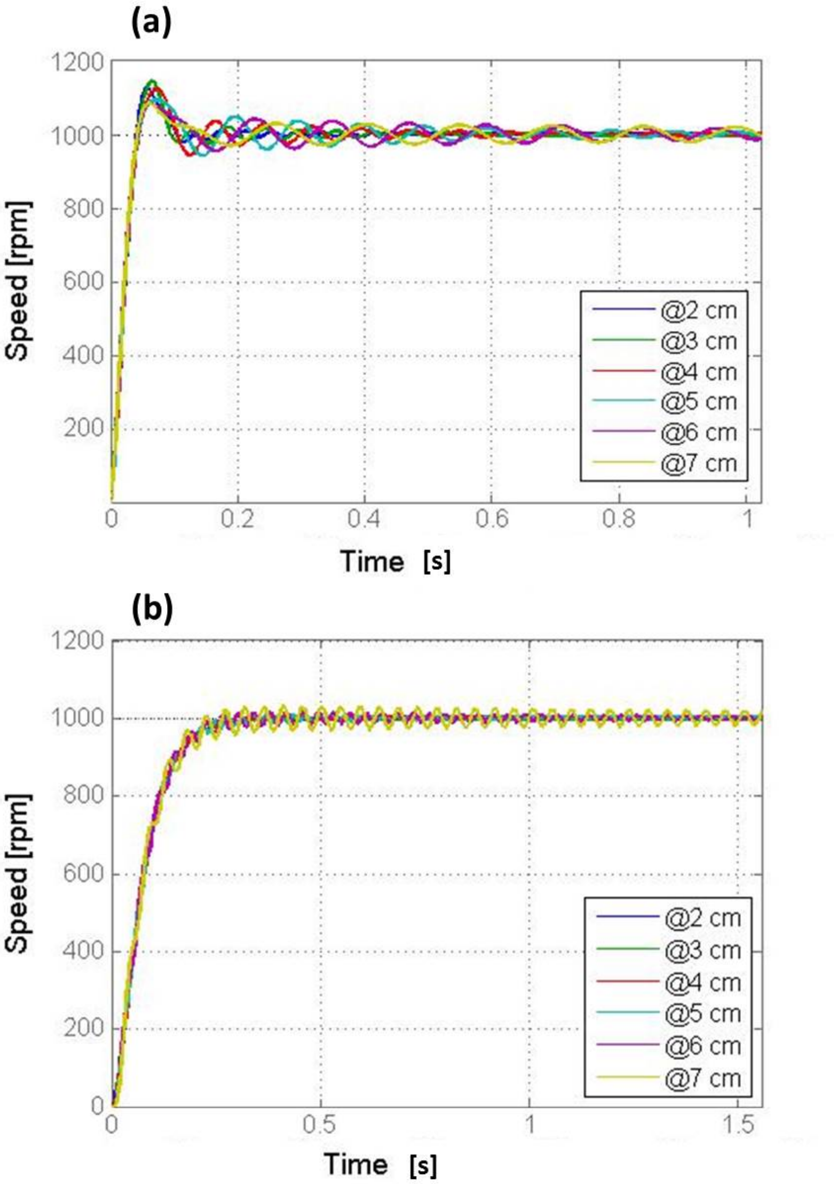

Figure III.16: Simulated step response for the motor-side (a) and load-side (b) closed-loop control for six discrete values of h (i.e., $h = [2, 3, 4, 5, 6, 7]$ cm).

Fig. III.17.a for the motor-side closed-loop control, and in Fig. III.17.b for load-side closed-loop control. Experiments were performed with ω_{ref}=1000 rpm at h=4 cm in unloaded conditions, and both ω_D and ω_d were recorded. The video showing the experimental set-up and the step response trials is attached as multimedia extension 1.

As regards the step response for the motor-side closed-loop control in Fig. III.17.a, the measured ω_D and ω_d presented an overshoot of 11.2% and 11.6%, respectively. These results were comparable with the overshoot obtained in the simulated response. Concerning the steady state, ω_D presented an average value of 998±23 rpm, while the average ω_d was 1032±32 rpm. As expected, no significant overshoot was observed in the load-side closed-loop control step response (III.16.b) and the settling time of ω_d was comparable with the model predictions. The average regime value was 990±18 rpm for ω_D, and 1006±30 rpm for ω_d.

By comparing the results, we can observe that the load-side controller allowed achievement of a more precise regulation of the average ω_d than the motor-side approach. Both controllers showed a ripple in the regulated speed of about 3% of the regime value. This effect was mainly due to the absence of a load connected to the driven magnet, as the system was working in the unloaded regime.

The presence of a load torque applied at the gear train induces variations in the parameters of the system, as it affects the equivalent inertia at the driven shaft. In particular, system characteristics such as the resonant and antiresonant frequencies are both influenced by variations in J_d. The experimental trials reported in this subsection aim to assess both closed-loop control strategies under different loading conditions.

First, a set of speed step responses were measured by setting T_L at 20%, 50%, and 80% of $\tilde{T}_G^{Dd}(h)$. The trials were performed by imposing ω_{ref}=1000 rpm at h=4 cm, and the results for the motor-side closed-loop control are reported in Fig. III.18. The steady-state error for ω_d adopting the motor-side closed-loop control was 22±18 rpm for T_L at 20% of $\tilde{T}_G^{Dd}$ (Fig. III.18.a), 21±19 rpm for T_L at 50% of $\tilde{T}_G^{Dd}$ (Fig. III.18.b), and 3±40 rpm for T_L at 80% of $\tilde{T}_G^{Dd}$ (Fig. III.18.c). When adopting the load-side closed-loop control, the steady-state error for ω_d was 2±3 rpm for T_L at 20% of $\tilde{T}_G^{Dd}$ (Fig. III.18.d), 1±6 rpm for T_L at 50% of $\tilde{T}_G^{Dd}$ (Fig. III.18.e), and 0.3±13 rpm for T_L at 80% of $\tilde{T}_G^{Dd}$ (Fig. III.18.f).

From the results reported in Fig. III.18, we can observe that the load-side control strategy was more effective in forcing the system to reach the desired ω_{ref}, although an overshoot of 8% of the steady state appeared as the load was applied. The load-side closed-loop control step response presented a ripple for ω_d within the 1% of the steady state value, while the motor-side closed-loop control showed a ripple up to 4%. From the plots, we can

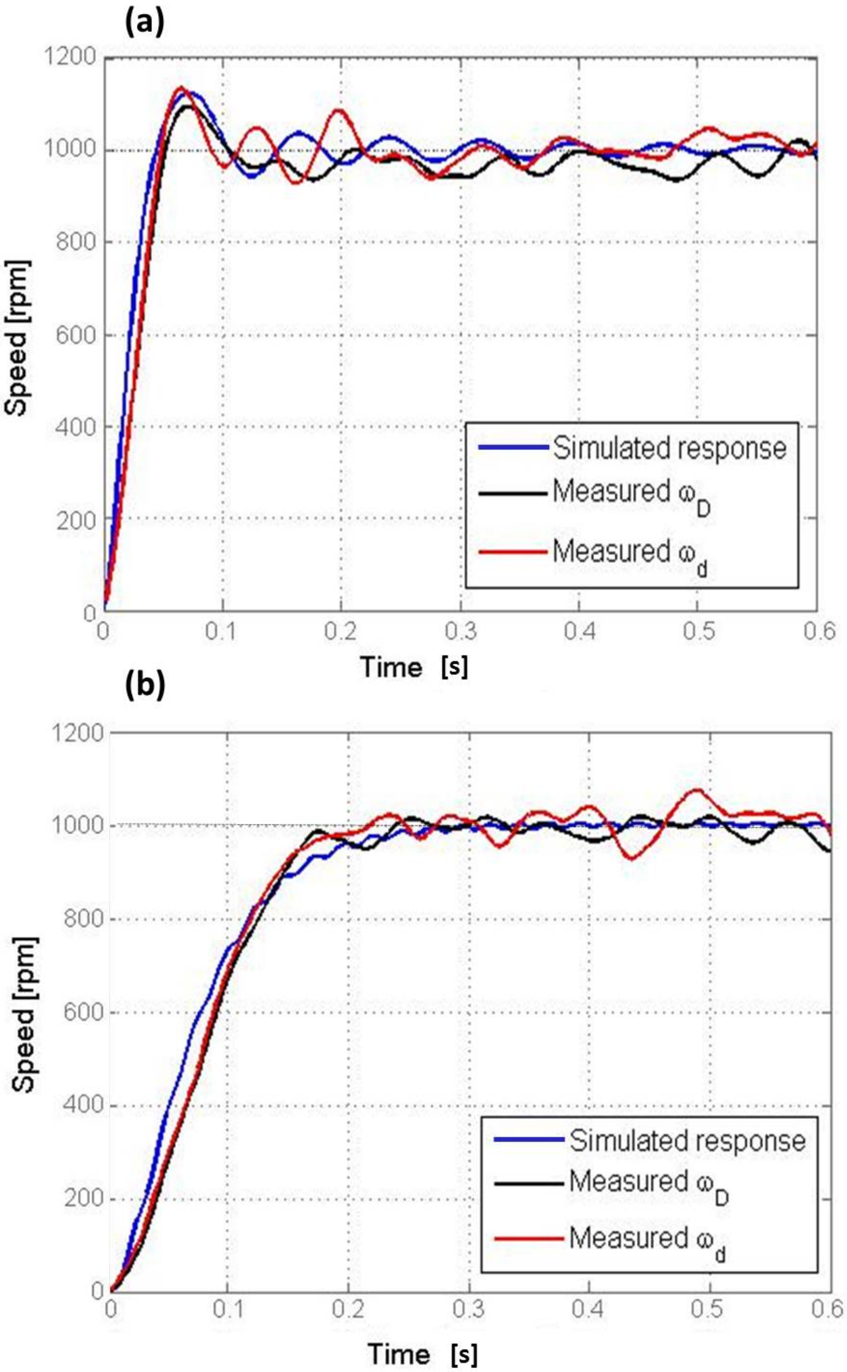

Figure III.17: (a) Simulated and experimental step response at h=4 cm for motor-side closed-loop control. Both the measured ω_D and ω_d are reported in the figure. (b) Simulated and experimental step response at h=4 cm for load-side closed-loop control. Both the measured ω_D and ω_d are reported in the figure.

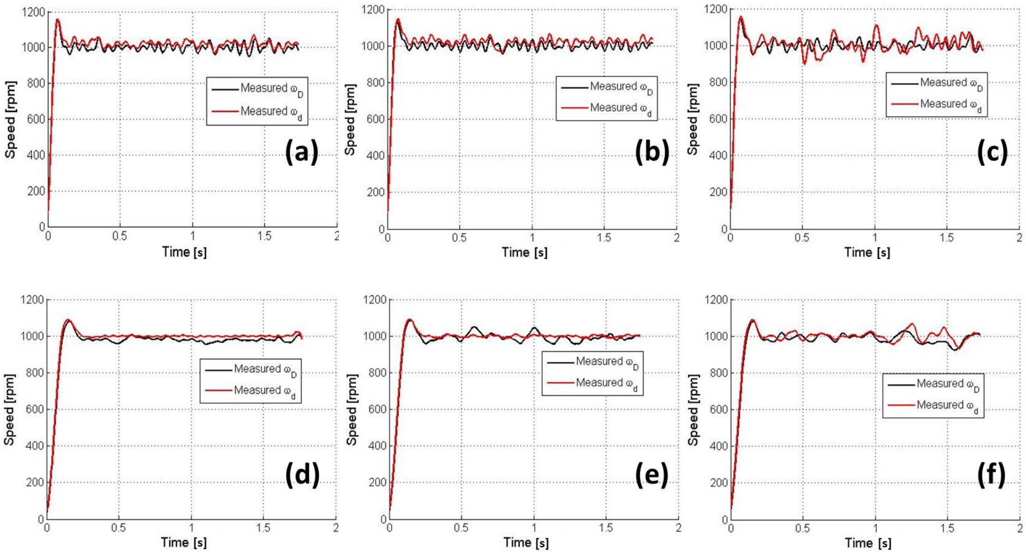

Figure III.18: Experimental step responses for motor-side closed-loop control (a, b, c) and load-side closed-loop control (d, e, f) with T_L at 20% (a, d), 50% (b, e), and 80% (c, f) of $\tilde{T}_G^{Dd}$. Experiments were performed at h=4 cm imposing a ω_{ref}=1000 rpm. Each plot shows the measured values for both ω_D and ω_d.

observe that both strategies showed an increase in the ripple with the applied T_L, as the system was moving towards the pole-slipping regime.

Load rejection experiments were then performed for both the control strategies at h=4 cm, and the results obtained are represented in Fig. III.19. The reference speed ω_{ref} was set to 1500 rpm, while T_L was initially set to 28% of $\tilde{T}_G^{Dd}$, then increased up to 85% of $\tilde{T}_G^{Dd}$ for about 2.5 seconds before resetting it to the initial value. While the load was at the 85% of $\tilde{T}_G^{Dd}$, the average error and the ripple for ω_d were 6±31 rpm for the motor-side closed-loop control (Fig. III.19.a), and 3±12 rpm for the load-side closed-loop control (Fig. III.19.b).

Both control strategies allowed rejection of the effect of a load variation without pole slipping. By analyzing in more detail Fig. III.19.a, we can observe residual damped oscillations in ω_d for more than one second after applying the variation in the load. These oscillations are due to the non-linear torsional spring behavior of the coupling, and are further amplified by the effect of an inertia ratio well below the unit [131] (i.e., in the proposed drive train, modeled as a two-inertia system, the inertia ratio in unloaded conditions is J_d/J_D=0.056). As shown in Fig. III.19.b, the custom controller implemented for the load-side strategy, providing a lag compensation, was effective in eliminating these oscillations in ω_d by modulating ω_D.

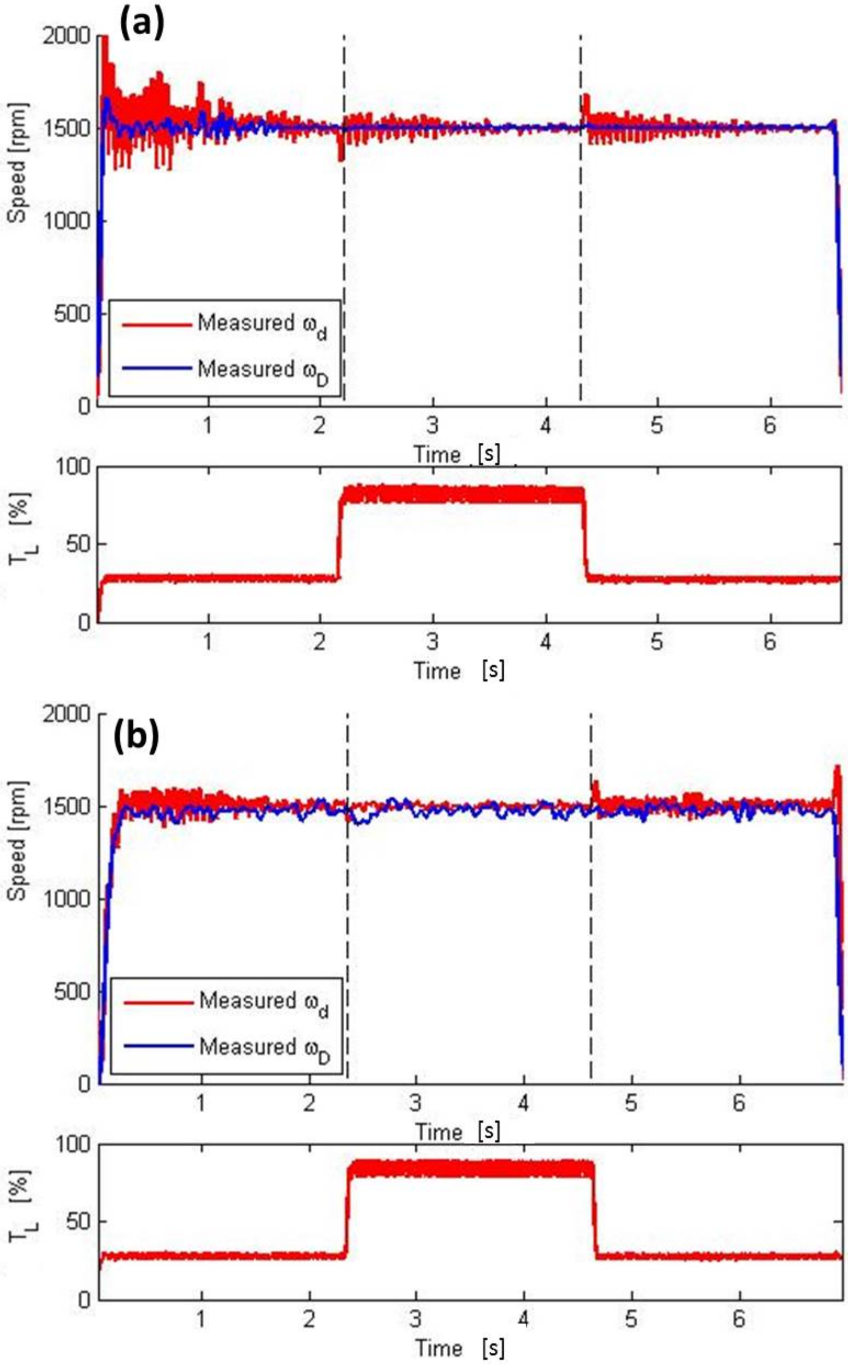

Figure III.19: Experimental load rejection responses for motor-side closed-loop control (a) and load-side closed-loop control (b). The profile of T_L, moving from 28% of $\tilde{T}_G^{Dd}$ to 85% of $\tilde{T}_G^{Dd}$ and back to its initial value, is represented below the speed plot. Experiments were performed at h=4 cm setting ω_{ref}=1500 rpm. Each plot shows the measured values for both ω_d and ω_D and the trend of the applied load torque.

A final test was performed to evaluate the mechanical power that can be transmitted by an LMA actuation unit at different intermagnetic distances. Using the motor-side closed-loop control, the maximum torque at the load T_L^{max} before entering the pole-slipping regime was experimentally measured for ω_{ref} ranging from 600 rpm to 1700 rpm at different separation distances (i.e., $h = [2, 3, 4, 5, 6, 7]$ cm). Each trial was repeated 10 times and the results are reported in Fig. III.20.a.

As expected from the harmonic analysis, we can identify in Fig. III.20.a the effect of the resonant peaks of the system shifting to lower frequencies as h increases. For rotational speeds that are not in the range of the resonant peaks, the torque transferred is constant, as expected, considering that the magnetic coupling has a 1:1 gear ratio. Therefore, as long as the torque required by the load does not bring the system into the pole-slipping regime, the amount of mechanical power that can be transferred mainly depends on the performance of the external motor (i.e., the faster the external motor, the larger the amount of mechanical power transmitted to the load).

The same test was repeated for the load-side closed-loop control and the results are reported in Fig. III.20.b. By comparing the plots in Fig. III.20.a and Fig. III.20.b, we can conclude that the load-side controller enables a larger torque to be transmitted before entering the pole-slipping regime. In particular, an average value of 1.5 mNm can be transferred at 7 cm, increasing up to 13.5 mNm as the separation distance is reduced down to 2 cm. In addition, the effect of the resonant peaks is less evident when using the load-side closed-loop control, which provides a value of T_L^{max} that is almost constant with ω_{ref} for h larger than 3 cm.

In analyzing the overall performance that an LMA actuation unit can achieve, we consider adopting the load-side closed-loop control as it provided a better performance when compared to the motor-side approach. In Fig. III.21 and Table III.2, we compare the maximum torque that can be transferred at different intermagnetic distances – same data as Fig. III.20.b – with the theoretical limit provided by FEM estimation. With the proposed dynamic modeling and control strategy, we are able to transfer an average of 86.2% of the theoretical value of maximum torque. This deviation is due to the adoption of a linear model for T_C^{Dd} and T_C^{dD} in Eqs. III.12 and III.13, respectively. For large angular displacements, which are expected, as the load torque brings the system towards the pole-slipping regime, a linear model in Eqs. III.12 and III.13 is far from being accurate and needs to be replaced by a non-linear equivalent.

From Fig. III.21, it is also interesting to observe that the standard deviation in T_L^{max} is larger at smaller distances. This may be explained by considering other magnetic effects

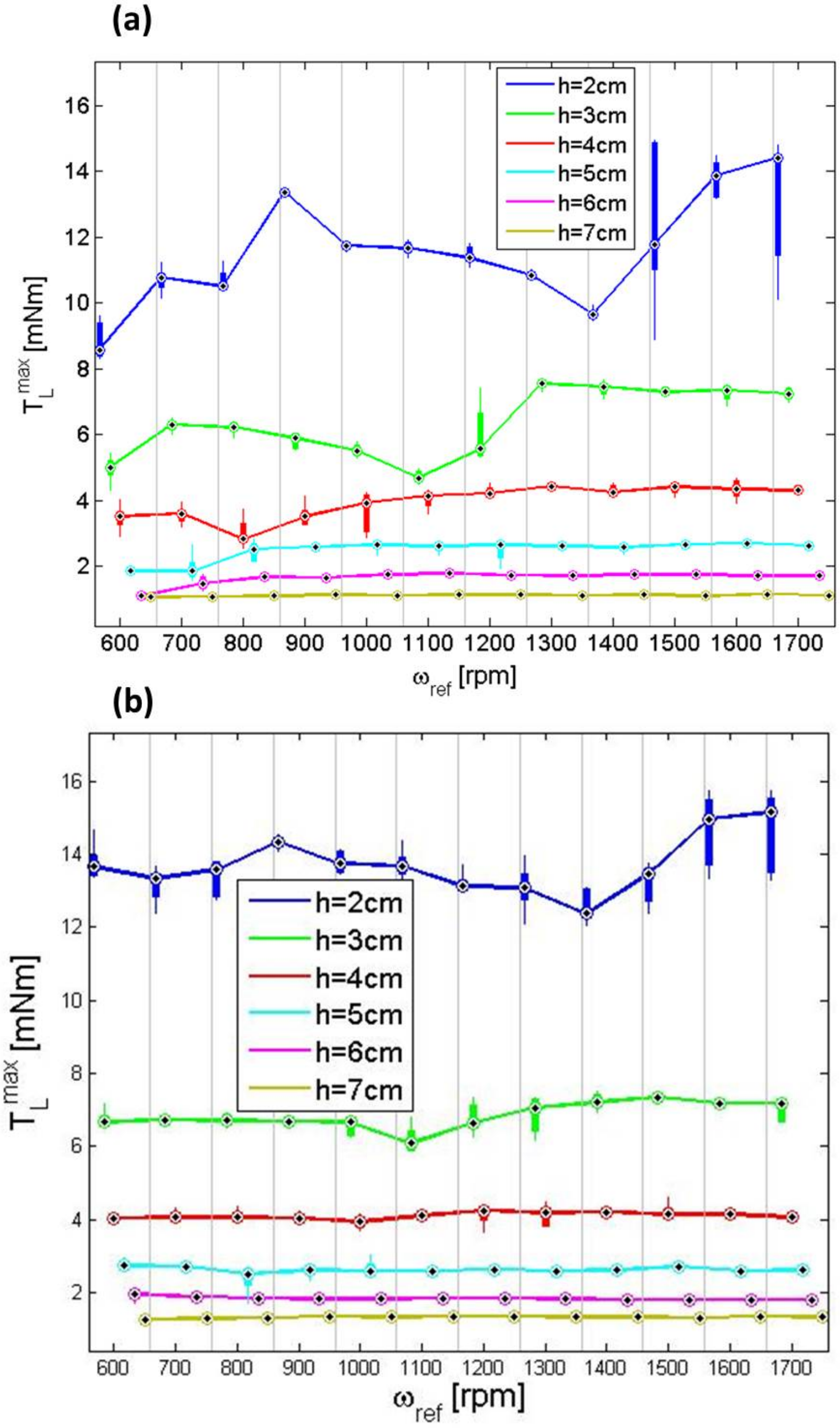

Figure III.20: Maximum torque at the load before entering the pole-slipping regime, measured using the motor-side (a) and the load-side (b) controller at different speeds and separation distances. Each data point is the result of ten independent trials.

	Distance $[cm]$					
MAX Torque [mNm]	2	3	4	5	6	7
Model $\tilde{T}_G^{Dd}(h)$	15.95	8.01	4.58	2.90	1.96	1.38
Experiment T_L^{max}	13.63	6.82	3.98	2.52	1.68	1.20
Efficiency %	85.4	85.2	87.0	86.8	85.5	87.3

Table III.2: Expected amount of torque transmitted, $\tilde{T}_G^{Dd}$, experimental amount of torque transmitted using the load-side closed-loop control, T_L^{max}, and efficiency defined as percentage of the theoretical amount of torque transmitted at different intermagnetic distances.

Model	Diameter	Length	Max Speed	Stall Torque	Reference
Namiki-SBL04	4mm	13.8mm	7000rpm	0.13mNm	[133]
Faulhaber-1016	10mm	16mm	18400rpm	0.87mNm	[134]
Faulhaber-1024	10mm	24mm	14700rpm	2.89mNm	[135]
Maxon-DCX10L	10mm	25mm	12000rpm	5.42mNm	[136]
Faulhaber-1219	12mm	19mm	16200rpm	0.96mNm	[137]
Faulhaber-1224	12mm	24mm	13800rpm	3.62mNm	[138]
Precision-NC110	12mm	12.5mm	10000rpm	0.50mNm	[139]
Precision-MC112	12mm	20mm	9500rpm	1.50mNm	[140]
Namiki-SCL12	12.5mm	32mm	13750rpm	3.71mNm	[141]

Table III.3: Off-the-shelf EM Motors comparable with the size of the driven magnet used in this work.

that are present in the system, but have not been included in the dynamic model, such as the vertical attraction force between the driving and the driven magnets that varies as the magnets spin [132].

As previously mentioned, an LMA actuation unit can be used instead of an onboard EM motor for driving a DOF of a laparoscopic robot. For the sake of comparison, in Table III.3 we listed off-the-shelf EM motors that have a diameter comparable with the driven magnet used in this study.

Thanks to a speed ratio equals one, the maximum speed that can be achieved at the driven shaft with the LMA approach corresponds to the maximum speed of the external EM motor. As the external motor is not as constrained in size as a motor to be embedded on board, a faster actuator than those listed in Table III.3 can be adopted. As for the

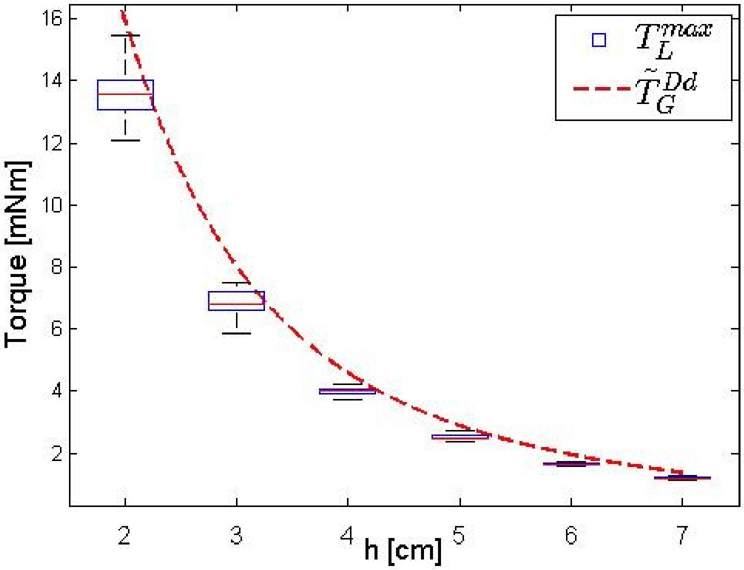

Figure III.21: Maximum torque at the load before entering the pole-slipping regime as a function of the intermagnetic distance. Theoretical value, $\tilde{T}_G^{Dd}$, and experimental data obtained by using the load-side closed-loop control, T_L^{max}.

stall torque, we can assume for the LMA approach the values of $T_L^{max}(h)$ reported in Table III.2. As represented in Fig. III.20.b, we can consider the stall torque to be constant as the speed increases. Considering that the driven magnet used in this study was 9.5 mm in both diameter and length, we can conclude that the LMA approach can provide a volumetric power density that is well above any of the motors listed in Table III.3 at any of the intermagnetic distances investigated.

Finally, it is worth to mention that the wired connection required to transmit sensor data from the instrument in the load-side control strategy can be easily replaced by a battery-operated wireless link [142] without increasing dramatically the size of the surgical tool.

III.3 Design contribution

III.3.1 1 DOF Laparoscopic Tissue Retractor Based on LMA

Method Overview: Given the above clinical considerations, we propose the LMA-based tissue retractor schematically presented in Fig. III.22.d and referred to as Laparoscopic Tissue Retractor LMA-based (LapR-LMA).

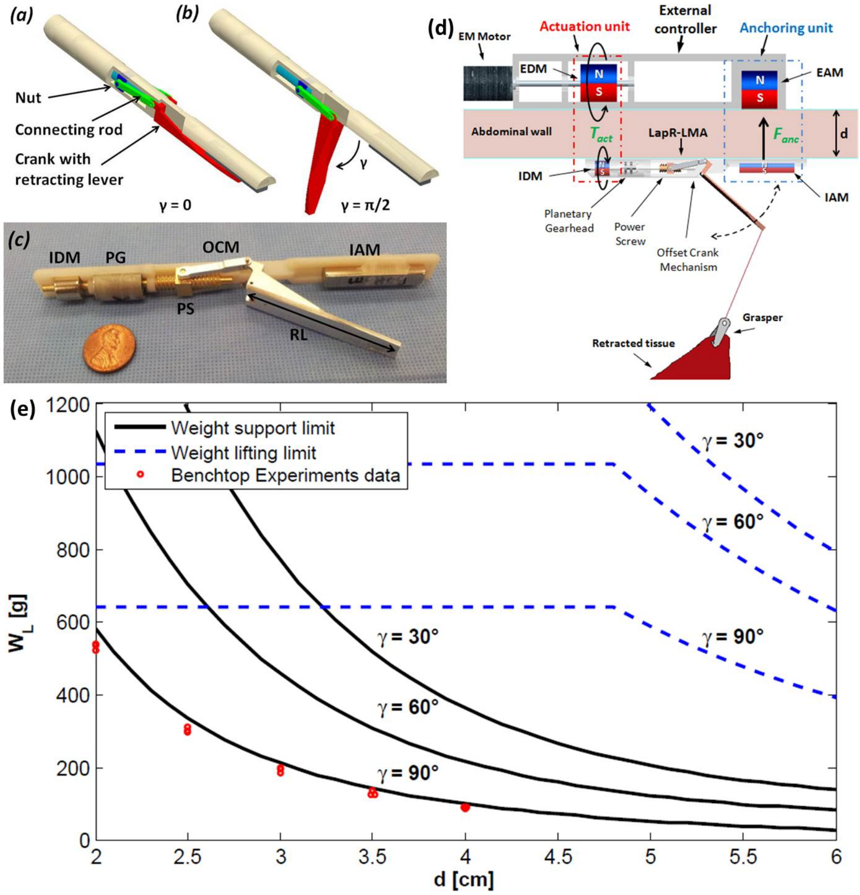

Figure III.22: Perspective rendering of the assembled LapR-LMA in the closed (γ=0) configuration (a) and in the open ($\gamma= \pi/2$) configuration (b). (c) The LapR-LMA prototype, where part of the outer shell was removed to shows the internal components. (d) Schematic representation of the LapR-LMA and the external controller components. (e) Maximum weight that can be lifted by operating the LapR-LMA (dashed line), and maximum weight that can be statically supported by the LapR-LMA (solid line). Both weight limitations are plotted as functions of the intermagnetic distance and the opening angle of the retracting lever. The measurements obtained during benchtop experiments are presented as single data points.

While the AnU is mainly responsible for gross positioning and for supporting both the device and the retracted tissue, the AcU is designed to transmit mechanical power from the external EM motor to the mechanism inside the LapR-LMA.

The spinning motion of the IDM is fed to a custom mechanical train, which has been designed to maximize the lifting force at the grasper and to fit the size constraints specified in the previous section. In particular, the IDM is connected to a three-stage planetary gearhead (PG), which rotates a power screw (PS) actuating an offset crank mechanism (OCM). The OCM controls the angular position of a retracting lever. In order to assess the proposed design, we connected a crocodile grasper to the lever via an inextensible wire. As proposed by Padilla et al. [4], the surgeon can clamp the grasper on the target tissue with standard laparoscopic forces. The specific application should require an atraumatic grasper, a suction cup [19] or a fan-shaped end effector [3] instead.

As presented in Fig. III.22.a,b,c, the mechanical train components are arranged around a thick extrusion in the core of the device. This feature guarantees structural resistance for the LapR-LMA. The fabricated prototype, presented in Fig. III.22.c, is 154 mm long, 12.5 mm in diameter, and weights 39.16 g.

Results & Discussions

Once the main components of the LapR-LMA were designed, two simple models were developed to predict the overall performance.

A first mathematical model aimed at providing an estimation of the tissue lifting performance of the device from the torque that can be transmitted over the magnetic coupling and the efficiencies of the single sub-modules. This model can also be used to predict the angular displacement $\Delta\theta$ corresponding to the weight at the gripper.

The second model we developed was a free body diagram of the LapR-LMA. This can be used to predict how much weight can be supported by the magnetic attraction force provided by both the AnU and the AcU.

Assuming no power losses due to internal friction, the weight W_L [g] that can be lifted up as the rotation of the EPM is activated can be predicted as follows:

$$W_L < \begin{cases} \frac{10^3}{9.8}\frac{(T_{act}GR_{pg}\eta_{pg}\beta_{ps}\eta_{ps})}{RL}\Gamma(\gamma), if T_{act} < \frac{T_{safe}}{GR_{pg}\eta_{pg}} \\ \frac{10^3}{9.8}\frac{(T_{safe}\beta_{ps}\eta_{ps})}{RL}\Gamma(\gamma), if T_{act} > \frac{T_{safe}}{GR_{pg}\eta_{pg}} \end{cases} \tag{III.21}$$

As represented by dashed blue lines in Fig. III.22.e, W_L is constant with d, as long as T_{act} exceeds the safe tooth-loading regime of the PG. In this working regime - which covers the entire range of d from 2 cm to 4 cm specified in section 2 - the overall efficiency of the mechanical train is 42.78%. In most of this region, the angular displacement $\Delta\theta$ stays below $\pi/18$ (i.e., 10), therefore we can assume $\Delta\theta^{max} = \pi/18$.

To predict the weight that can be supported by the LapR-LMA at different d and γ, we studied the free-body diagram of the device. The model considers F_{anc}, the weight force acting on the LapR-LMA, denoted with F_{lap}, and the force F_W required to lift the weight W_L at the gripper. The model also considers F_{act}, but scaled for $\Delta\theta^{max} = \pi/18$. In case of $|\Delta\theta| < \pi/18$, we estimated via FEM simulation a variation of F_h and F_v below 2.7% of the values. Further explanation are presented in Section G.

The condition for a stable anchoring can then be expressed by considering the rotational equilibrium in A (device extreme of the AnU side), as:

$$F_W < \frac{F_{Anc} \cdot AB + F_{act} \cdot AD - F_{lap} \cdot AX}{AC} \tag{III.22}$$

where F_{lap} is the force required to lift the LapR-LMA and X is the position of the LapR-LMA center of mass. This stability condition is plotted with solid black lines in Fig. III.22.e, showing the maximum weight W_L that can be supported by the LapR-LMA as a function of d and γ. Also in this case, the performance improves as γ goes from $\pi/2$ to 0, since the point of application of F_W moves closer to the pivoting point. By plotting together the tissue lifting and the tissue support models, as in Fig. III.22.e, we can derive the operative range for the LapR-LMA as the area below the minimum value of W_L that can be supported and lifted at the same time.

The main goal of this experiment was to confirm the operative range of the LapR-LMA. The external controller was affixed to a vertical adjustable slider and coupled with the LapR-LMA through a rigid plastic surface. The weight was connected to the lever - starting at $\gamma = \pi/2$ - via an inextensible wire. Then, the external EM motor was activated with a step command at a speed of 1,700 rpm. The maximum value of weight that was successfully lifted up was 500 g at d=2cm intermagnetic distance. This test was performed three times for each intermagnetic distance ranging from 2 cm to 4 cm, with 0.5 cm increments, and the results are presented in Fig. III.22.e.

Considering the geometrical features of the LapR-LMA and the values of the anchoring forces within the operative range, the pressure exerted by the device on the abdominal wall always stays below 30.7 kPa, thus satisfying the condition on safety [143].

III.3.2 4 DOFs LMA-based surgical robotic manipulator design

The design presented in Section H aims to develop a surgical manipulator for MIS able to perform surgical tasks combining mechanical power transmission based on LMA and cable-driven actuation of a novel design of spherical parallel wrist.

Method Overview:

This robotic manipulator features an LMA-actuated 4 DoF cable-driven spherical wrist, which is schematically represented in Fig.III.23.A and referred to as Multi Degree Of Freedom LMA-based (MultiDOF-LMA). The MultiDOF-LMA design has three AcU and an AnU. Each AcU provides the mechanical power to actuate one DOF of the wrist through a pair of antagonistic cable drive. The anchoring unit provides for the gross positioning, support, and through its ability to translate, also provides the actuation of the tilt angle (θ_1) DOF of the MultiDOF-LMA.

The AcU consists in a couple of diametrically magnetized magnets – the EDM and the IDM – designed to transmit mechanical power from the external motor to the mechanism embedded inside each of the Transmission Modules (TM)1-3. The gear transmission inside the TM amplifies the torque delivered by the IDM to the antagonistic-cables attachment. Each TM is equipped with a planetary gear train (1:16 gear ratio), a set of spur gears (1:14 gear ratio) and a cable reel (2.5 mm radius). The two antagonistic-cables lines are connected with the reel and rolled-up by lengths S_1, S_2 and S_3, respectively, for each actuated DOF of the spherical wrist. Each TM is connected to the link 1 of the manipulator through flexible pipes hosting each pair of antagonistic cables.

The AnU consists of a pair of axial magnetized permanent magnets. The External Anchoring Magnets (EAMs) are connected to each other by motorized linear slide. The EAMs are magnetically coupled with the Internal Anchoring Magnets (IAMs) generating the forces to support the MultiDOF-LMA during operation by offering two points of contact with the abdominal wall. For a typical abdominal surgery procedure, we considered a cubic workspace of $50X50X50mm^3$ side located 10 to 15 cm below the insufflated abdominal wall. The AnU also provides the actuation of joint 1 (J_1) to orient the manipulator tip along the direction of interest.

The MultiDOF-LMA design has a novel configuration for a 3 DoF cable-driven parallel wrist with no kinematic singularity in the joint limited workspace and decoupled cables actuation. The spherical wrist, showed in Fig. III.23.B, features a simple design with a parallel configuration. It is composed by a U-joint followed by a helical actuated serial joint [144]. The U-joint provides the parallel actuation of the tip along the axes $\mathbf{x}_0$ and $\mathbf{y}_0$ in a range of $\pm 60^o$ with respect to the wrist frame coordinate system. The ends of the two pairs of antagonistic cables are connected to the U-joint output link (UOL) and spaced by 90^o to each other. The helical actuated joint is composed by two cylindrical links, H_1 and H_2, one on top of the other, where H_1 can freely rotate relative to H_2. The helically actuated joint is mounted on top of the UOL and provides the tip rotation about $\mathbf{z}_2$ of the UOL coordinate system. The antagonistic cables are connected on the outer side of H_1 and helically rolled around H_1 and H_2, one clockwise and the other counterclockwise. This cable arrangement allows for a rotation of $\pm 180^o$ around $\mathbf{z}_2$ in either direction, depending on the cable that is remotely pulled.

On the tip of the manipulator, a cable-driven endoscopy flexible grasper could be attached to achieve the desired surgical tasks. The flexible grasper is inserted through the single abdominal access; it enters from the posterior of the MultiDOF-LMA and exits from the tip of the manipulator. The flexible grasper could be externally actuated to generate up to 40 N grasping forces [85].

Results & **Discussions** A prototype implementing the design described above has been fabricated and tested confirming the functionality of the novel cable-driven spherical wrist (Fig. III.23.C).The permanent magnets implementing both AcUs and AnUs have been tested and reported in [143]. Typical attraction forces are within the range of 1 N to 5 N, and actuating torque within 2 mNm to 8 mNm, considering a distance between the external and internal magnets below 6 cm.

The tilt angle θ_1 about J_1 achieved by the relative motion d between the EAMs is defined as following: $\theta_1 = cos^{-1}[(L-d)/(2l)]$, where L is the initial distance between the EAMs, and l is the length of both links 2 and 3. L_T is the whole length of the MultiDOF-LMA from J_1 to the tip. If the EAM is moved by d, the robotic tip reaches the distance h from the abdominal wall, such as: $h = L_T sin\{cos^{-1}[(L-d)/(2l)]\}$.

The two pairs of antagonistic cables connected at the U-joint actuate the angles θ_2 and θ_3, as shown in Fig. III.23.B. Each cable goes down along the U-joint structure passing through a needlepoint at the Cross Link Junction (CLJ). This cable constraint provides an even cable length variation during the U-joint actuation, thus decoupling the cables. The kinematic equation relating the antagonist cable displacements S_1, S_2 and the angles θ_2 and θ_3 is $\Delta S_1, l_2 = l_u - (l_u^2 + r_u^2)^{1/2} cos(tan^{-1}(r_u/l_u) + \theta_{2,3})$, where l_u is the UOL length and r_u is the UOL radius.

The antagonistic cables actuating the helical joint are connected on the outer side of H_1, controlling the rotational angle θ_4. The cables follow a helical path along the outer cylindrical surface of radius r and pitch $2\pi l_h$, where r is the helical joint radius and l_h is the length of both H_1 and H_2. The following parametric function describes the cable trajectory

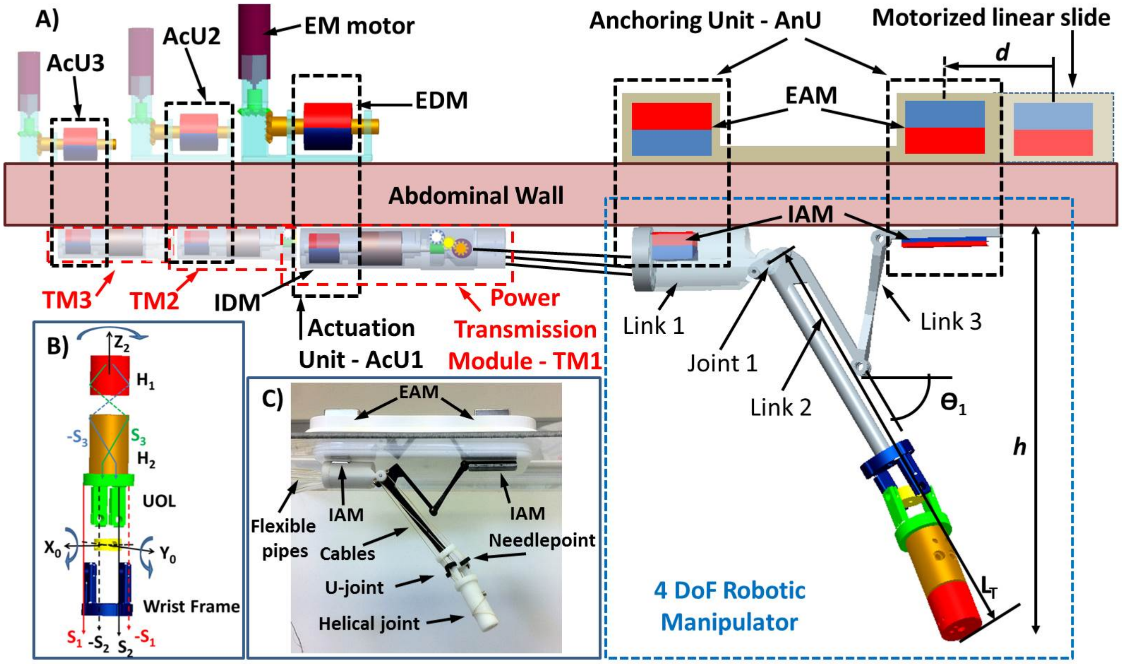

Figure III.23: Schematic view of the MultiDOF-LMA design (A), the spherical wrist schematic design (B) and the prototype implementation picture (C).

helically rolled along H_1 and $H_2 : t \rightarrow [rcos(t), rsin(t), l_h t/(2\pi)]$, where $t \in [0, 2\pi]$. In order to achieve $\theta_4 = \pm 180^o$, the cable displacement S_3 is actuated as follows: $\Delta S_3 = l_h/(\pi\theta_4)$. The cable decoupling is achieved by pushing the cable pair through the CLJ center hole. The estimated transmitted force at the tool tip, considering 2 mNm available torque at each AcU and a 50% of efficiency, is about 16 N for each direction of motion. The maximum estimated speed at the tool tip, considering the IDM rotating at 10000 rpm, is $58^o/s$, thus it covers the entire workspace for the U-joint in two seconds.

The fabricated prototype of the MultiDOF-LMA is presented in Fig. III.24, where Fig III.24.A represents the device configuration during introduction phase through the single port access, and Fig. III.24.B represents the deployed configuration during surgical operation. The device dimensions are: diameter of 15 mm, full length of 400 mm; the length of the actuation unit is 65 mm, and the manipulator is 130 mm long. Fig. III.25.A.B.C presents the AcU and the mechanical train: spur gears and planetary gears, which are fabricated in 6061 aluminum alloy through wire-cut Electrical Discharge Machining.

In conclusion the prototype has a diameter less than 15 mm allowing it to enter from a

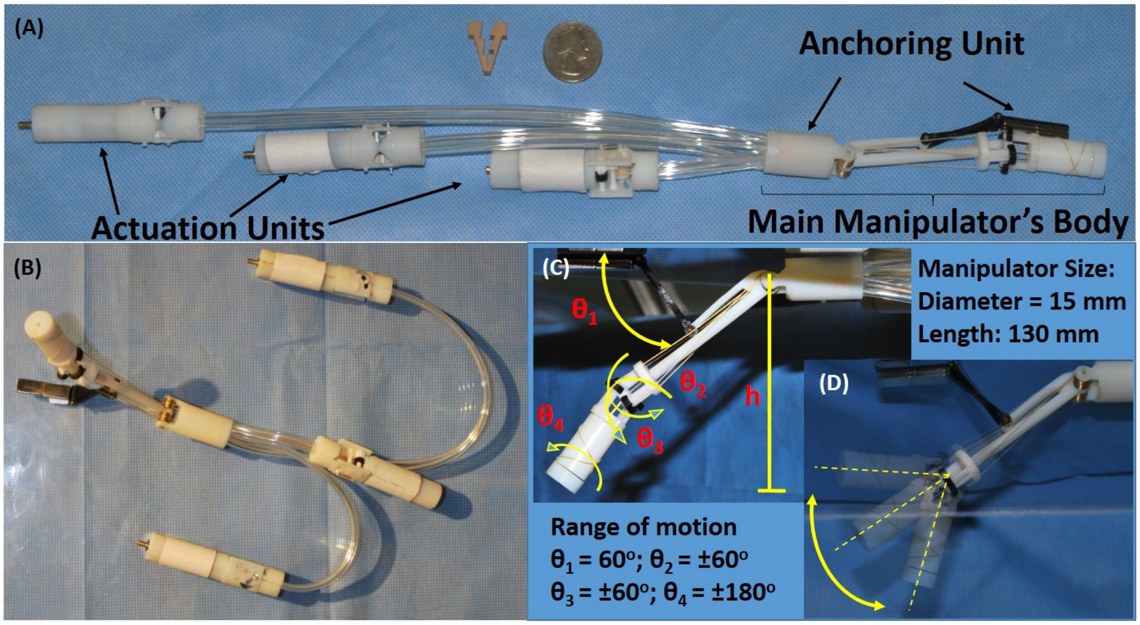

Figure III.24: (A)Configuration of the MultiDOF-LMA prototype during introduction phase through the single port access, and (B) is the deployed configuration of the device during surgical operation phase. (C) Prototype of the manipulator's body with representation of each DOF and (D) represents the mobility of one of the DOFs.

standard 15-mm trocar for MIS. The novel spherical wrist design is antagonistically cable-driven, has no kinematic singularity and presents cable decoupling. The proposed design paves the way for disposable low-cost implementation of robotic laparoscopic surgery.

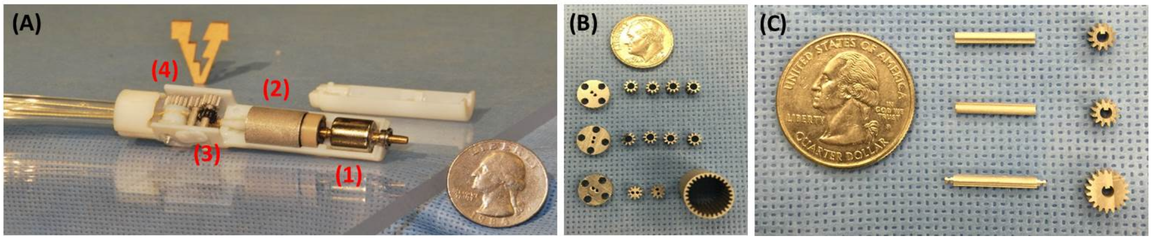

Figure III.25: (A) Actuation Unit, where the part of the outer shell was removed to show the internal components. (1) represents the embedded permanent magnet or the IDM. (2) Two stages planetary gear with transmission ratio of 1:16. (3) Worm gear system with gear ratio of 1:15. (4) Spur gear system (2:1) and pulley where the cables are connected. (B) Two stages planetary gear components and (B) spur gears components fabricated in wire-cut Electrical Discharge Machining.

Chapter IV

CONCLUSIONS AND FUTURE WORKS

IV.1 Conclusion: Magnetic Navigation and Pose Detection

This dissertation presents two novel approaches to detect, without line-of-sight and in real-time, the 6-DOF pose of a magnetic capsule endoscope, combining multiple sensor readings with finite element numerical solutions of the magnetic field generated by the magnetic source (EPM). These pose detection algorithms are compatible with magnetic manipulation and are optimized for a cylindrical EPM with axial magnetization. The sensing module is designed for wireless operation, and the algorithm has a computational time that allows real-time teleoperation. A third algorithm provides the estimation of the intermagnetic forces generated by the magnetic coupling of EPM and IPM embedded into the capsule. This algorithm is built on the same hardware of the previous localization systems. The hardware framework of the Magnetic Actuated Capsule (MaAC) is represented in Fig. II.5 of section II.3.1.1 and it is named FMSM. Table IV.1 summarizes the scientific contribution presented in this dissertation, where for each algorithm, main features and relative performances are presented. Table IV.2 presents the scientific contribution of this dissertation for what concern the design of wireless capsules, their relative medical application, performance evaluation and their reference in this manuscript.

The first localization approach provides an absolute estimation of capsule's pose expressed in 6 DOF as $\mathbf{p}_c = [x_c, y_c, z_c, \alpha, \beta, \gamma]^t$, where $\mathbf{p}_c$ is the capsule pose, which has the position expressed in cartesian coordinates and the orientation in Euler angles. This algorithm is able to provide an average error below 5 mm in position detection, and below 19° for angular motion within a spherical workspace of 15 cm in radius, centered on the EPM. The method validation, quantitative results and hardware description are detailed in Appendix A and its application to wireless tissue palpation is presented in Appendix B.

While this study advances the field of magnetic localization, a number of challenges still remain for future research. The detection of γ, the capsule rotation about the vertical axis of the world frame, could be estimated by adopting an IMU sensor with embedded accelerometer and gyroscope. This approach has been pursued for the second algorithm of magnetic pose detection proposed in this dissertation.

The second localization approach provides an iterative estimation of capsule's pose expressed in 6 DOF as $\mathbf{p}_c = [x_c, y_c, z_c, \alpha, \beta, \gamma]^t$, where $\mathbf{p}_c$ is the capsule pose, which has the

Algorithm's Features & Performances

Algorithm Typology:	Absolute Magnetic Pose Detection	Iterative Magnetic Pose Detection	Absolute Magnetic Force Feedback
Magnetic Locomotion Compatibility:	yes	yes	yes
Initialization Required:	no	yes	no
Real-Time:	yes	yes	yes
Refresh Rate:	50 Hz	1000 Hz	3000 Hz
Precision:	5 mm	6 mm	50 mN
Workspace:	30x30x30 cm	30x30x30 cm	30x30x30 cm
DOF:	5 (Appendix B); 6 (Appendices A, D)	6 (Appendix C)	1 (Appendix D)
Sensors Required:	3 or 6 MFSs, inclinometer	3 or 6 MFSs, IMU	4 MFSs

Table IV.1: Features and performances of the algorithms proposed in this dissertation.

Capsule Design and Result Evaluation

Wireless Capsule's Task:	Absolute Capsule's Magnetic Pose Detection	Fast Iterative Capsule's Magnetic Pose Detection	Inter-Magnetic Force Measurement
Medical Application:	a) Real-time tracking for WCE compatible with magnetic navigation; b) Tumor margin detection by using wireless device during MIS (combined with contact pressure measurements)	Real-time tracking of WCE during magnetic navigation	Resistance force and magnetic attraction force monitoring during magnetic navigation of WCE (combined with capsule's pose information)
Performance Evaluation:	yes	yes	yes
Scientific Contribution:	Absolute localization enabling magnetic navigation control	Iterative localization enabling magnetic navigation control	Real-time Inter-magnetic force monitoring
Manuscript Reference:	Appendices A, B, D	Appendix C	Appendix D

Table IV.2: Scientific and medical contribution presented in this dissertation.

position expressed in cartesian coordinates and the orientation in Euler angles. The algorithm is looping at 1 KHz refresh rate, by applying iterative methods based on magnetic filed properties and WCE spatial orientation. The investigated method establishes the feasibility of applying a non-linear interpolation method based on Kronecker product, which provides the formulation of an analytic expression of the magnetic field within the workspace of analysis. Then, by applying iterative Jacobian-based method upon the non-linear interpolation, we demonstrate the 6 DOF capsule pose estimation from magnetic field and inertial readings of magnetic actuated WCE. The proposed approach uses the same hardware of the previous localization system, but the sensors readings from onboard magnetic field sensors and inertial sensors are used to estimate the change in capsule pose with respect to the external magnetic field source, whose position and orientation are known.

Validation was performed by simulation and then by experimental trials. The source of magnetic field adopted was a cylindrical axially-magnetized permanent magnet and the workspace investigated was a cube space of 30-cm side with the magnetic field source in the middle of the workspace. With the proposed selection of orthogonal basis, the MDR was estimated through the simulation with a relative error below 5% within the workspace. Spiral capsule motions within the workspace were simulated to verify position change estimation, achieving a sub-millimeter localization accuracy. Then, the wireless experimental platform, composed by a magnetic actuated WCE and a robotically manipulated permanent magnet, was used to assess the iterative magnetic localization. Five stages of experimental trials was performed to show the steady-state behavior, the position initialization error sensitivity, and the uniformly acceleration linear motion between WCE and EPM. Finally, the overall pose localization behavior was assessed with an average error of 6 mm on both the radial and axial components, 5^o average error for θ and an average error of 3^o for α, β and γ capsule orientation angles.

This mathematical method for localization allows 1 ms refresh rate, an order of magnitude below than what reported in previous works, thus allowing a fast closed-loop control strategy for WCE magnetic manipulation within the specifics above mentioned. The method validation, quantitative results and hardware description are detailed in Appendix C.

The non-linear nature of the magnetic field generated by a specific permanent magnet shape could be analysed in order to simplify the order of mathematical complexity involved to analytically obtain the magnetic field direct relationship. The mathematical simplification altogether with the modal matrices representation of polynomial bases and Fourier harmonic basis, provides an invertible magnetic field and the analytic expression used for the WCE pose localization.

If comparing the simulation results and the experimental trials, the average error for the radial and the axial components are increasing from the sub-millimetric to 6 mm average error. This can be due to the noise in the measurement and to the limited sensor accuracy.

The intermagnetic force detection algorithm altogether with the absolute localization, allow us to introduce, for the first time, a wireless real-time platform for the *in vivo* measurement of the resistant force that a magnetically-driven capsule must overcome to move inside the GI tract. The platform takes advantage of a wireless capsule, magnetically coupled with an EPM, and is able to provide the real-time profile of both the intermagnetic force and capsule pose. The direct measurements of capsule pose, intermagnetic force and capsule acceleration are used to derive the dynamic profile of the resistant force opposing magnetic attraction.

The platform was assessed via three-tier validation. First, the intermagnetic force and capsule position estimation was assessed with a dedicated benchtop trial using a robotic manipulator as a benchmark for position and a commercial load cell as reference for the intermagnetic force. The average error in estimating the force and the position was less than 0.1 N and 10 mm, respectively. A second benchtop experiment was then performed to validate the dynamic reconstruction of $\mathbf{F}_r$ from the intermagnetic force and capsule motion estimation, using in this case a spring as reference for $\mathbf{F}_r$. The platform was able to estimate the spring constant with a relative error of 5.45%. Finally, the platform was assessed *in vivo* in a porcine colon model, where $\mathbf{F}_r$ was successfully measured. The method validation, quantitative results and hardware description are detailed in Appendix D.

While a statistically relevant study of the resistant forces of the porcine intestine was outside the scope of this study, this platform can be applied to more extensive biomechanical studies in the future (i.e., different segments of the GI tract can be investigated, and the force required to move with or against peristalsis can be measured). This would provide a quantitative understanding of resistant properties of the GI tract, paving the way for improved realistic biomechanical models.

Real-time knowledge of both the intermagnetic force and capsule motion profile can be used for robotic-guided capsule endoscopy. To the best of our knowledge, none of the platforms proposed thus far for magnetic control of endoscopic capsules [27, 30, 68, 108, 113, 145, 146] implements a real-time tracking of capsule position and intermagnetic force. Integrating the methods proposed in this work in a platform such as the one reported in [147] would enable ”closed-loop control” of magnetic locomotion, by adjusting, in real-time, the external source of the magnetic field to optimize the coupling with the capsule at any given point in time.

IV.2 Conclusion: Local Magnetic Actuation

Magnetic fields can be harnessed to transfer controllable mechanical power from outside the patient's body to a surgical instrument within the body. Combining magnetic units with different functions, i.e. anchoring or actuation, it is possible to design surgical robots that do not require motors on board, nor take up port space during the procedure.

Given the constraints in diameter and volume of a MIS instrument, the proposed approach enables the transfer of a larger amount of mechanical power than what is possible to achieve by embedding typical electromechanical actuators on board. At the same time, due to magnetic coupled devices, triangulation is enhanced and also invasiveness is reduced. In table IV.3 are summarized the technical contributions, performances and medical applications presented in this dissertation, whereas in table IV.4 the design contributions are reported.

As previously mentioned, an actuation mechanism based on the LMA can be seen as a composition of single units, mixed depending upon the specific needs. The developed static model touched on in Section III.1, and detailed in Appendix E is able to provide a reliable prediction of maximum values of forces and torques at the IPM for each single couple of magnets. By applying the principle of superposition, this simple model is able to provide an estimation about LMA peak capabilities.

It is worth mentioning that the rLMA provides an actuation force which is almost double that of the tLMA. Additionally, the tLMA requires the IPM to travel on a linear track to provide actuation, thus imposing severe limitations in terms of space constraints. As previously mentioned, the main advantage for the tLMA over the rLMA is the possibility to achieve a push-pull actuation.

An example of application of the magnetic force and torque model to a complete LMA design is detailed in Appendix E, where the magnetic model description and simulation results are presented. The reported results and discussion represent an encouraging first step towards the design of a more optimized LMA solution.

In this dissertation, it is also demonstrated the feasibility of controlling a parallel-axis radial coupling with asymmetrical single-dipole magnets within a range of intermagnetic separation distances compatible with the abdominal thickness in humans. This particular kind of magnetic coupling, referred as LMA unit, applying the magnetic spur gear concept, can be used in designing robotic surgical instruments to transfer mechanical power from the outside of the patient's body to an abdominal surgical instrument within. Given the constraints in diameter and volume for a surgical instrument, the proposed approach allows

LMA's Features & Performances

Unit Typology:	Actuation Unit	Anchoring Unit
DOF Typology:	Rotary	Translational
Magnetic Source:	Couple of cylindrical magnetized permanent magnets	Couple of axially magnetized permanent magnets
Theory Applied:	Magnetic Spur Gear	Magnetic Manipulation
Drawbacks:	Speed oscillations during rotation	Low precision during magnetic manipulation
Clinical Application:	Remote actuation of surgical instrument's DOFs	Device's gross positioning and support
Magnetic Torque/Force Model:	FEM model function of the driven magnet's angular position and intermagnetic distance	FEM model function of the intermagnetic distance vector
Max Torque/Force at 2 cm Intermagnetic Distance:	up to 14 mNm	up to 6 N
Max Torque/Force at 5 cm Intermagnetic Distance:	up to 3 mNm	up to 1 N
Static/Dynamic Model:	Appendix E and Appendix F	Appendix E and Appendix G
Control Strategy:	(a) PI closed on driving angular speed; (b) Custom controller closed on driven angular speed	Control strategy based on monoaxial intermagnetic distance tracking as in [148]
Feedback & Sensor Requirements:	Angular speed, 1 MFS	Intermagnetic distance, 1-3 MFSs

Table IV.3: LMA's actuation and anchoring unit features and performances.

Surgical Instrument Design Based on LMA Approach

MCR's Task:	Tissue Retractor	Surgical Manipulator
Medical Application:	Lift an organ	Orientate and support the final effector of the surgical instrument
DOF required:	1	4-6
Scientific Contribution:	Design, prototype implementation and experimental evaluation	Design, prototype implementation
Manuscript Reference:	Appendix G	Appendix H

Table IV.4: Design contribution presented in this dissertation.

the transmission of a larger amount of mechanical power than what is possible to achieve by embedding actuators on board.

The solution we propose for the servo control of an LMA actuation unit takes advantage of a dynamic model of the coupling, adapted from a two-inertia servo-drive system, and a sensing strategy based on Hall effect magnetic field sensors placed next to the driving and the driven magnets. In this study, we also compare two alternative approaches in closing the control loop. The first, referred to as motor-side closed-loop control, uses the angular velocity of the driving magnet as the feedback parameter and has the advantage of relying only on sensors placed on the motor-side of the coupling, thus outside the patient's body. The alternative approach, referred to as load-side closed-loop control, directly controls the angular velocity at the load and requires a Hall effect sensor to be placed inside the surgical instrument. The two approaches were assessed and compared in terms of step response, load rejection, and maximum torque that can be transmitted at different speeds and intermagnetic distances.

From the experimental results, we can conclude that the dynamic model we developed presented a relative error below 7.5% in estimating the load torque from the system parameters, while the sensing strategy based on Hall effect sensors has an average error below 1% in reconstructing the shaft speed. Concerning closed-loop control, both the strategies were effective in regulating the load speed with a relative error below 2% of the desired steady-state value. When comparing the two approaches, the load-side closed-loop control achieved a better performance, both in terms of steady-state error (below 0.2%) and ripple in the angular velocity (below 1%). In addition, the load-side closed-loop control allowed transmission of larger values of torque, showing – at the same time – less dependency from the angular velocity. The method validation, quantitative results and hardware description are detailed in Appendix F.

While this study should serve as background for the servo control of LMA-based DOFs in laparoscopic robots, a number of challenges still remain for future research.

A first direction of future work is improving the robustness of the control. As mentioned in Section F.4.5, a non-linear approach must be adopted to increase the amount of transmitted torque closer to its theoretical limit. Predictive control, suggested in [120] for coaxial magnetic gears, can be a viable solution. To reduce the oscillations in ω_d further, a digital notch-filter compensator, as suggested in [149], can be adopted. In addition, the model needs to be extended to a situation in which the two magnets spin on axes that are not fixed, nor parallel, as analyzed in [150]. Horizontal and vertical vibrations must be considered, as they will be present during laparoscopic surgery. Vertical attraction force between the driving and the driven magnets must be included in the model.

When designing an LMA-based surgical instrument as represented in Fig. F.1, the actuation module must provide controlled motion for a DOF, while the anchoring module should support the weight of the instrument and the vertical forces applied during tissue interaction. Overshoot in the speed at the driven magnet may occur in some conditions and must be taken into account when designing the mechanism that goes from the rotating shaft to the surgical end effector [132]. If the surgical robot needs more than one DOF, a number of LMA actuation modules will have to interact within the same confined space. Magnetic cross-coupling among LMA anchoring and actuation units may become an issue in this case. As the magnetic force and torque respectively decrease with the inverse of the fourth and third power of the intermagnetic distance, we plan to address this challenge by properly spacing the magnets on board the surgical instrument. Shielding with ferromagnetic or diamagnetic material can also be considered to address this problem. The model of the system would then be extended to include cross-coupling and to provide a tool for designing appropriate shielding between modules.

As previously discussed, the system can enter in the pole-slipping regime as a consequence of torque overload. As suggested in [119], the coupling can be re-engaged by stopping the motor rotation for a short period, and then resetting the input command. However, if the load is still above the maximum torque that can be transmitted, this strategy will be ineffective. A potential solution to this problem consists on controlling the vertical position of the external driving magnet, so that h can be reduced if a larger torque is required at the load. The intermagnetic distance can be tracked in real time by using the methods proposed in [148]. A different approach may be used to replace the driving unit with a set of coils that can generate a rotating magnetic field at the driven magnet. In this case, commutation control can be implemented to prevent the pole-slipping regime and maximize the transferred torque at any given time.

In Section III.3.1, we demonstrated the feasibility of using the LMA approach to design a tetherless laparoscopic tissue retractor. The same design steps presented in Appendix G (i.e., medical consideration and technical requirements related to magnetic coupling, magnetic modeling, selection of the magnets, interfacing between the IDM and the mechanical train, and modeling of the overall device performance) can be adopted to implement LMA-based surgical robots performing different and more complex tasks.

The LapR-LMA is 12.5 mm in diameter and can be laparoscopically introduced. If the abdominal wall thickness is about 2 cm, the LapR-LMA is able to retract more than ten times its own weight. Bench trials demonstrated that the designed mechanism is not backdrivable and guarantees accurate and controllable motion of the retraction lever in both directions. The mechanism is able to cover the full range of motion in about 20 seconds. While the motion is slower if compared with manual operation of a laparoscopic retractor, the surgeon has the ability to adjust precisely the degree of retraction achieved by the LapR-LMA.

In situations of overload, failure occurs in anchoring rather than actuation. If the anchoring failure occurs, the LapR-LMA needs to be recoupled with the external controller by the surgeon during the procedure. However, no failure was observed during the liver retraction experiment that was performed on a porcine model presenting an abdominal tissue thickness of 2 cm. The same experiment showed no abdominal wall tissue damage due to magnetic pinching.

While this study showed promising results, a number of challenges remain for future research.

Regarding LapR-LMA modeling, the maximum weight that can be lifted was overestimated by about 9%. This was mainly due to the assumption of no cross-coupling between the anchoring and the actuation units. Therefore, a more comprehensive model, capturing the interactions among all the magnets in the device, must be developed. Reducing the length of the device would improve maneuverability and provide better access to the surgical target, as observed during the *in vivo* trials.

As the main goal of this study was to assess the mechanical power transfer that can be achieved via the LMA approach, we did not focus extensively on the part of the device interacting with the tissue to be retracted. In particular, liver retraction was performed with traumatic graspers because of their availability. This is not applicable to a clinical case, where suction cups [151] or a fan-shaped end effector [115] must be used instead to prevent damaging the hepatic tissue. The current version of the LapR-LMA can be used whenever the retracted tissue must be removed at the end of the surgical procedure (e.g., cholecystectomy). While the current device is wireless, a thin tethered connection can be introduced to facilitate retrieval at the end of the procedure. Future studies involving surgeons will be devoted to assess and improve, if needed, the usability and the ergonomics of the device.

Finally, an intriguing direction of future research is to design an LMA-based surgical robot with multiple DOFs. Such a device would be able to achieve complex surgical tasks, such as surface scanning with an optical probe or even suturing. Combining a number of actuation units and one or more anchoring units in a device that can fit a laparoscopic access requires advanced modeling and, most likely, the use of shielding material [152] between units.

In Section III.3.2 is presented the design of the surgical manipulator called MultiDOF-LMA with 4-DOFs magnetically actuated by the LMA approach. This robotic manipulator features 3 DOF cable-driven spherical wrist, which is magnetically actuated by three magnetic spur gears. The MultiDOF-LMA design has three AcU and an AnU. Each AcU provides the mechanical power to actuate one DOF of the wrist through a pair of antagonistic cable drive. The anchoring unit provides support for the gross positioning, and also provides the actuation of the tilt angle (θ_1) of the MultiDOF-LMA thanks to its ability to translate.

A prototype implementing the design has been fabricated and tested confirming the functionality of the cable-driven spherical wrist (Fig. III.23.C). Typical attraction forces are within the range of 1 N to 5 N, and actuating torque within 2 mNm to 8 mNm, considering a distance between the external and internal magnets below 6 cm. The estimated transmitted force at the tool tip, considering 2 mNm available torque at each AcU and a 50% of efficiency, is about 16 N for each direction of motion. The maximum estimated speed at the tool tip, considering the IDM rotating at 10000 rpm, is $58^o/s$, thus it covers the entire workspace for the U-joint in two seconds.

The prototype has a diameter less than 15 mm, allowing it to enter from a standard 15-mm trocar for MIS. The novel spherical wrist design is antagonistically cable-driven, has no kinematic singularity and presents cable decoupling. Also the proposed design paves the way for disposable low-cost implementation of robotic laparoscopic surgery. The design description and evaluation are detailed in Appendix H. //

IV.3 Research Outcomes

This section reviews the candidate's publications during the period spent at Vanderbilt University. Currently, portions of the work presented in this dissertation have been published as following:

Journal Publications:

1. **C. Di Natali**, M. Beccani, N. Simaan, P. Valdastri, Jacobian-based Iterative Method For Magnetic Localization in Robotic Capsule Endoscopy, IEEE Transactions on Robotics,2015, submitted.

2. R. Caprara, K. L. Obstein, G. Scozzarro, **C. Di Natali**, M. Beccani, D. R. Morgan, P. Valdastri, A Platform for Gastric Cancer Screening in Low and Middle-Income Countries, IEEE Transactions on Biomedical Engineering, 2015, Vol. 62, N. 5, pp. 1324-1332.

3. **C. Di Natali**, J. Buzzi, N. Garbin, M. Beccani, P. Valdastri, Closed-Loop Control of Local Magnetic Actuation for Robotic Surgical Instruments, IEEE Transactions on Robotics, 2015, Vol 31, n. 1, pp 143-156.

4. N. Garbin, **C. Di Natali**, J. Buzzi, E. De Momi, P. Valdastri, Laparoscopic Tissue Retractor Based on Local Magnetic Actuation, Journal of Medical Devices, 2015, Vol. 9, 011005-1-10.

5. M. Beccani, **C. Di Natali**, N. E. Hall, C. E. Benjamin, C. S. Bell, and P. Valdastri, Wireless Tissue Palpation: head characterization to improve tumor detection in soft tissue, at Sensor & Actuators A: Physical, 2015, Vol. 223, pp. 180-190.

6. M. Beccani, E. Susilo, **C. Di Natali**, P. Valdastri, SMAC: A Modular Open Source Architecture for Medical Capsule Robots. Int J Adv Robot Syst, 2014, Vol. 11, N. 188, pp. 1-16.

7. **C. Di Natali**, M. Beccani, K. L. Obstein, and P. Valdastri, A wireless platform for in vivo measurement of resistance properties of the gastrointestinal tract. Physiological measurement, 2014, Vol. 35, no. 7, pp. 1197-1214.

8. **C. Di Natali**, M. Beccani, and P. Valdastri, Real-time pose detection for magnetic medical devices, Magnetics, IEEE Transactions on, 2013, Vol. 49, no. 7, pp. 3524-3527.

9. **C. Di Natali***, M. Beccani*, L. Sliker, J. Schoen, M. Rentschler, and P. Valdastri, Wireless tissue palpation for intraoperative detection of lumps in soft tissue, IEEE Trans. Bio-Med. Eng., vol. 61, no. 99, pp. 353-361, 2013. (* equally contributed to this work)

Conference Publications:

1. **C. Di Natali**, Ranzani, T., Simi, M., Menciassi, A., Valdastri, P. Trans-abdominal Active Magnetic Linkage for robotic surgery: Concept definition and model assessment. In Robotics and Automation (ICRA), 2012 IEEE International Conference on (pp. 695-700). IEEE.
2. **C. Di Natali**, M. Beccani, K. L. Obstein, and P. Valdastri, Wireless Real-Time Pose Detection for Magnetic Manipulated Endoscopic Capsules, Gastrointestinal Endoscopy, vol. 77, no. 5 Supplement, pp. Sa1622, 2013.
3. M. Beccani, **C. Di Natali**, M. Rentschler, and P. Valdastri, Wireless tissue palpation: Proof of concept for a single degree of freedom, in Robotics and Automation (ICRA), 2013 IEEE International Conference on, 2013, pp. 711-717.
4. X. Wang, **C. Di Natali**, M. Beccani, M. Kern, P. Valdastri, and M. Rentschler, Novel medical wired palpation device: A validation study of material properties, in Solid-State Sensors, Actuators and Microsystems (TRANSDUCERS EUROSENSORS XXVII), 2013 Transducers Eurosensors XXVII: The 17th International Conference on, June 2013, pp. 1653-1658.
5. M. Beccani, **C. Di Natali**, P. Valdastri, and K. L. Obstein, Restoring tactile perception in natural orifice transluminal endoscopic surgery (notes) through wireless tissue palpation, Gastrointestinal Endoscopy, vol. 77, no. 5 Supplement, pp. AB163-AB164, 2013.
6. M. Beccani, **C. Di Natali**, N. E. Hall, C. E. Benjamin, C. S. Bell, and P. Valdastri, Wireless Tissue Palpation: characterization of the probe head to improve detection of tumors in soft tissue, in Eurosensors 2014, Procedia Engineering, in press., 2014.
7. A. Mohammadi, D. Samsonas, **C. Di Natali**, P. Valdastriy, Y. Tan, D. Oetomo, Speed Control of Non-collocated Stator-Rotor Synchronous Motor with Application in Robotic Surgery, Asian Control Conference (ASCC), in press. 2015.

Abstract Publications:

1. **C. Di Natali**, M. Beccani, and P. Valdastri, Real-time pose detection for magnetic medical devices. 12th Joint Magnetism and Magnetics Materials (MMM) – Intermag Conference,, Jan 2012.
2. **C. Di Natali**, and P. Valdastri. "Surgical robotics and instrumentation." Surgery 245.3 (2012): 379-384. ISCAS, Best Paper Award.
3. C. Mitchell, M. Beccani, **C. Di Natali**, A. Benson, S. D. Herrell, P. Valdastri, Laparoscopic Wireless Palpation Probe: Feasibility of simulated tumor detection in a human prostate. 29th Annual Meeting Engineering and Urology Society, 2014, TOP 10 Abstract award.
4. A. Benson, M. Beccani, **C. Di Natali**, Ryan Pickens, S. D. Herrell, P. Valdastri, Laparoscopic Wireless Palpation Device: Preliminary Assessment of tissue stiffness measurement on elastic moduli, 31st WORLD CONGRESS of ENDOUROLOGY, 2013 Best Laparoscopic/Robotic, Paper Award
5. **C. Di Natali**, A. Mohammadi, D. Oetomo, P. Valdastri, Surgical Robotic Manipulator Based on Local Magnetic Actuation, ASME Journal of Medical Devices, in press.
6. A. Mohammadi, **C. Di Natali**, D. Samsonas, P. Valdastri, Ying Tan, D. Oetomo, Electromagnetically Controlled Actuators Across Abdominal Wall for Minimally Invasive Robotic Surgery, ASME Journal of Medical Devices, in press.
7. M. Beccani, **C. Di Natali**, C. Benjamin, P. Valdastri, A magnetic drug delivery capsule based on a coil actuation mechanism, Eurosensors 2015, Freiburg, Germany, submitted.

Awards:

1. **Best Paper Award**, ASME Student Mechanism & Robot Design Competition, Buffalo, NY, August 2014.
2. **Top 10 Abstract**, 29th Annual Meeting of the Engineering and Urology Section of the Endourological Society, May 2014.
3. **Recipient of the Olympus Best Laparoscopy/Robotic Paper Award**, 31st World Congress of Endourology, New Orleans, LA, October 2013.
4. **Recipient of Best Paper Award**, XVI Annual Conference of the International Society for Computer Aided Surgery (ISCAS), Pisa, Italy, June 2012.

5. **Best Paper Award**, Hamlyn Symposium on Medical Robotics, London, UK, June 2011.

PATENTS/PATENT APPLICATIONS (Co-inventor)

1. **C. Di Natali**, M. Beccani, K. Obstein, P. Valdastri, Real-time pose and magnetic force detection for a wireless magnetic capsule, U.S. Provisional Application No. 61/753,755 filed on January 17, 2013, converted to PCT/US2014/012086 on Jan 17, 2014.

2. R. Caprara, M. Beccani, **C. Di Natali**, G. Scozzarro, K. Obstein, P. Valdastri, Hydro-Jet Endoscopic Capsule and methods for gastric cancer screening in low resource settings, U.S. Provisional Application No. 62/048,105 filed on September 9th, 2014.

3. **C. Di Natali**, A. J. Herline, P. Valdastri, Local Magnetic Actuation, US Patent Application 13/893,611, priority date May 14, 2012.

4. M. Beccani, **C. Di Natali**, P. Valdastri, System and Method for Detecting Tissue Surface Properties, U.S. Patent Application No. US2014206953 and US2014081120 priority date September 14, 2012.

5. P. Valdastri, M. Simi, K. Obstein, **C. Di Natali**, M. Beccani, B. F. Smith, A Robotic Platform for an Increasing Compliance with Colorectal Cancer Screening, U.S. Provisional Application No. 10/548,399, Nov 11, 2011.

6. P. Valdastri, T. Ranzani, **C. Di Natali**, M. Simi, A. Menciassi, P. Dario, Robotic platform for mini-invasive surgery, PCT Patent Application WO2012164517, priority date May 31, 2011, converted to U.S. Provisional Application No. US2014358162 on Dec 4, 2014.

Appendices

Appendix A

REAL-TIME POSE DETECTION FOR MAGNETIC MEDICAL DEVICES

Christian Di Natali, Marco Beccani, Pietro Valdastri

From: IEEE Transactions on Magnetics, vol.49, no.7, pp.3524,3527,
Status: Published 2013

A.1 Abstract

Magnetic coupling is one of the few physical phenomena capable of transmitting motion across a physical barrier. In gastrointestinal endoscopy, remote magnetic manipulation has the potential to make screening less invasive and more acceptable, thus saving lives by early diagnoses and treatment. Closed-loop control of the magnetic device position is crucial for a safe and reliable operation. In order to implement closed-loop control, the pose (position and orientation) of the device must be available in real-time. This becomes challenging if magnetic coupling is achieved by permanent magnets, since the strong magnetic field required for manipulation interferes with current localization techniques. In this work, we present a novel real-time pose detection strategy that is compatible with magnetic manipulation based on permanent magnets. The localization algorithm combines multiple sensor readings with a pre-calculated magnetic field map. The proposed approach is able to provide an average error below 5 mm in position detection, and below 19° for angular motion within a spherical workspace of 15 cm in radius.

A.2 Introduction

The gastrointestinal (GI) tract is home to some of the most deadly human diseases. Today, flexible endoscopy allows for effective diagnosis and treatment through its different districts. However, this technique is not well perceived by patients due to the pain associated with the procedure and the frequent need for sedation. A more acceptable technique is wireless capsule endoscopy (WCE), introduced for the first time in 2000 and considered today the gold standard for diagnosis of small intestine diseases [49]. WCE entails the ingestion of a miniature pill-size camera that moves passively through the digestive system and enables visualization of the bowel without the need for intubation, insufflation, or sedation, thus offering an appealing alternative to flexible endoscopy.

Remote manipulation of capsule endoscopes has the potential to extend the reach of WCE to other GI districts, allowing the physician to have direct control of the camera viewpoint [49]. Among the different approaches proposed to achieve active locomotion, the use of magnetic fields to control the capsule pose (*i.e.*, position and orientation) has the advantage of preventing the need for onboard actuators, dedicated mechanisms, and energy. This approach is currently being pursued by the major commercial players in the field of GI endoscopy (*i.e.*, Olympus and Siemens in [30,153] and Given Imaging in [29]) and by several research group worldwide [49, 64, 154–157]. To achieve closed-loop control, the pose of the remote device must be determined in real-time and used in conjunction with the desired location or direction of motion specified by the user. Most of the localization techniques developed to date – mainly designed to track the capsule endoscope as it passively travels in the GI tract – are not compatible with magnetic manipulation due to electromagnetic interference [156]. A high-frequency alternating magnetic field, generated by pairs of Cartesian coils, can be used in conjunction with a resonating coil [158] or Hall Effect sensors [159] embedded in the capsule for localization during magnetic manipulation. This approach can provide sub-millimeter resolution, but is limited to three degrees of freedom (DOF).

A different strategy to achieve magnetic coupling is based on permanent magnets [28, 63, 64]. Compared to coils, permanent magnets can generate higher fields in a smaller form factor. In this case, the capsule can be localized by measuring the magnetic field generated by the external permanent magnet (EPM) at the capsule, taking advantage of onboard sensors [66]. This approach is adopted in [63] to achieve capsule localization in 5 DOF with an accuracy of 15 mm. Inertial sensing is used in conjunction with Hall effect sensors to localize an endoscopic capsule driven by a robotic EPM in [67]. This method achieves a 10 mm resolution on 3 DOF.

In this paper we propose a novel approach to detect in real-time the 6-DOF pose of a magnetic capsule endoscope. This method is compatible with magnetic manipulation and is optimized for a cylindrical EPM with axial magnetization.

A.3 Materials

A.3.1 Principle of Operation

The proposed method takes advantage of measuring the magnetic field generated by the EPM at the two ends of the capsule. Two Cartesian triplets of Hall Effect sensors are used to acquire the three components of the field (*i.e.*, $B'_{x1}, B'_{y1}, B'_{z1}, B'_{x2}, B'_{y2}, B'_{z2}$). The resulting $\overrightarrow{B'_1}$ and $\overrightarrow{B'_2}$ vectors are referred to the center of the capsule ($[x', y', z']$ reference frame represented in Fig. A.1). The inclination of the capsule (*i.e.*, α' and β' defined as pitch and yaw of $[x', y', z']$ with respect to the world reference frame $[x_w, y_w, z_w]$) is also recorded in real-time with an onboard triaxial accelerometer. Given these 8 real-time measurements, the proposed algorithm is able to provide the pose of the capsule in terms of the distance vector $\vec{d}$ and the three Euler's orientation angles (α, β, γ) referred to a Cartesian frame $[x, y, z]$ located at the center of the EPM. In case the EPM is mounted as the end effector of a robotic arm, as in [28, 63, 64], the transformation from $[x, y, z]$ to $[x_w, y_w, z_w]$ (and viceversa) can be easily obtained using the real-time data acquired from the robot encoders.

The method we developed is based on an iterative algorithm written in Matlab (Mathworks, Inc., USA). The first step consists in the calibration of the initial roll angle γ_0 as baseline. This is required because the roll γ is the only orientation angle that cannot be measured by the triaxial accelerometer. This calibration requires positioning the capsule with a known orientation for γ with respect to the EPM.

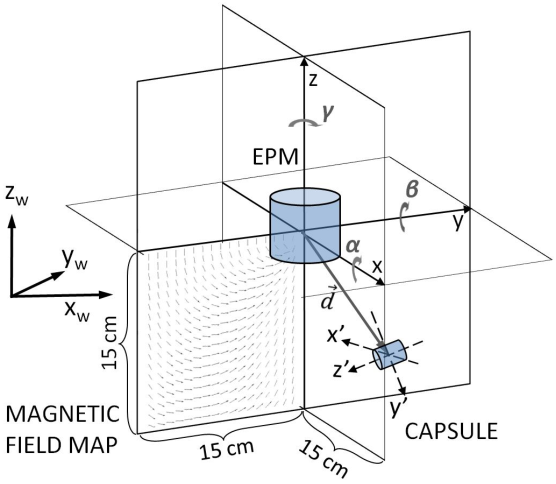

Figure A.1: Schematic view of the EPM and the capsule with the different reference frames used in the algorithm. A slice of the magnetic field map is represented in the lower left quadrant of the workspace.

The next steps are to acquire $\overrightarrow{B_1'}$ and $\overrightarrow{B_2'}$ from the onboard Hall Effect sensors, α' and β' from the accelerometer, and to express the magnetic field vectors with respect to $[x, y, z]$ by the following transformation:

$$\overrightarrow{B_i} = R^w R^w_{'} R^T_w \overrightarrow{B_i'} \qquad \text{with } i = 1,\, 2 \tag{A.1}$$

where R^w and its transpose R^T_w build the similarity transformation converting coordinates from $[x_w, y_w, z_w]$ to $[x, y, z]$, while the 3×3 rotation matrix $R_w^{'}$ is

$$R_w^{'} = \begin{bmatrix} c(\beta')c(\gamma) & c(\gamma)s(\alpha')s(\beta')-c(\alpha')s(\gamma) & s(\alpha')s(\gamma)+c(\alpha')c(\gamma)s(\beta') \\ c(\beta')s(\gamma) & c(\alpha')c(\gamma)-s(\gamma)s(\alpha')s(\beta') & s(\gamma)c(\alpha')s(\beta')-s(\alpha')c(\gamma) \\ -s(\beta') & c(\beta')s(\alpha') & c(\alpha')c(\beta') \end{bmatrix}$$

where $c(\cdot)$ and $s(\cdot)$ are cosine and sine trigonometric functions, $\alpha^{'}$ and $\beta^{'}$ are the pitch and yaw acquired by the triaxial accelerometer, while γ is equal to γ_0 for the first iteration. The angle γ is then generated by the algorithm for the following iterations.

The values of the magnetic field at the capsule are then used in conjunction with a pre-calculated numerical map of the magnetic field generated by the EPM. In this map, the magnetic field vectors are associated with the distance vector $\vec{d}$. A search is performed in the map to find the values of (d_x, d_y, d_z) related to the magnetic field vectors that are the closest to the measured values $\overrightarrow{B_1}$ and $\overrightarrow{B_2}$. The computational time and the precision of the proposed method strongly depend on the search function and the magnetic field map. In case an axially magnetized cylindrical permanent magnet is used as EPM, the magnetic field can be expressed in cylindrical coordinates. Therefore, the algorithm derives

$$\begin{cases} \overrightarrow{B_i^c} = B_{ri}\hat{r} + B_{zi}\hat{z} = \sqrt{(B_{xi}^2 + B_{yi}^2)}\hat{r} + B_{zi}\hat{z} \\ \theta_i = \arctan(\frac{B_{yi}}{B_{xi}}) \end{cases} \tag{A.2}$$

for $i = 1, 2$, where $B_{ri}\hat{r}$ is the radial component and $B_{zi}\hat{z}$ is axial component of $\overrightarrow{B_i^c}$. The azimuthal angle of the cylindrical coordinates is expressed by θ_i.

Magnetic models based upon the theories and the methods used in the analysis of steady currents, permanent magnets, and magnetic circuits [109, 160, 161] are applied to generate the field density map to cover a 30 cm × 30 cm × 30 cm workspace centered on the EPM. In particular, the Magnetic Current Model (MCM) allows for a numerical solution by finite element integration. The MCM for an axially magnetized cylindrical magnet is expressed as follows

$$\overrightarrow{B(p)} = \frac{\mu_0}{4\pi} \oint_{S^{''}} j_m(p^{''}) \times \frac{(p - p^{''})}{|p - p^{''}|^3} ds^{''} \tag{A.3}$$

where p indicates a generic point belonging to the workspace, $p^{''}$ is a point on the magnet surface, j_m is the equivalent surface current density, $S^{''}$ is the EPM integration surface, and μ_0 is the vacuum permeability constant. Expressing Eq. A.3 in cylindrical coordinates, the magnetic field becomes

$$\overrightarrow{B^c(p)} = K \int_L^0 \int_0^{2\pi} \frac{(R - r)\hat{z} + (z - z^{'})\hat{r}}{|R^2 + r^2 - 2rRc(\theta - \theta^{'}) + (z - z^{'})^2)|^{\frac{3}{2}}} d\theta^{'} dz^{'} \tag{A.4}$$

where r, θ, and z are the cylindrical coordinates of the generic point p, while R and L are the radius and the height of the EPM, respectively. The constant $K = \frac{\mu_0 M_s}{4\pi}$ accounts for the EPM magnetic remanence M_s.

Thanks to the cylindrical symmetry of the selected EPM, the value of $\overrightarrow{B^c}$ is only a function of r and z, since its θ component is zero (see Eq. A.4). This allows to simplify the magnetic field map to a single 15 cm × 30 cm slice. Also, since we can assume the capsule to be inside the body of a patient laying in the $z < 0$ space, the slice can be further reduced to a 15 cm × 15 cm domain, as represented in Fig. A.1. Each point belonging to this slice is expressed as a two component magnetic field vector $\overrightarrow{B^c(p)} = B_r(p)\hat{r} + B_z(p)\hat{z}$ with a univocal association to a point p in the domain. The values of the bi-dimensional map are calculated by applying Eq. A.4 to the specific EPM used in our platform with a spatial resolution of 0.2 mm. Of course, the resolution of the map is chosen as a trade-off between computational time and localization accuracy.

A sequential search is performed into the map to find (d_{ri}, d_{zi}) associated with the measured (B_{ri}, B_{zi}) for i=1, 2. The third cylindrical coordinate $d_{\theta i}$ can be calculated from the values of B_{yi} and B_{xi} by applying Eq. B.4. The position of the capsule center is then obtained by averaging $\vec{d_1}$ and $\vec{d_2}$. At this point, the capsule pose is fully identified with respect to $[x, y, z]$ and the algorithm restart from acquiring $\overrightarrow{B_1^{'}}$, $\overrightarrow{B_2^{'}}$, $\alpha^{'}$, and $\gamma^{'}$, this time adopting the actual γ in computing the $R_w^{'}$ matrix in Eq. D.11.

A.3.2 Platform Overview

The proposed method for capsule pose detection was assessed using the experimental platform represented in Fig. A.2.A. The platform consists of a robotic arm holding the EPM, and a capsule embedded with a permanent magnet and the localization module. The capsule is mounted on a gimbal (Fig. A.2.B), that allows 3 DOF rotations. Since the capsule is designed to operate inside the human body, thus in a loose environment, the gimbal allows to validate the algorithm without constraining the sensing module in a fixed orientation. An optical tracker (Micron Tracker, Claron Technology, Inc., USA) is used as reference system to measure the angular motion of the capsule.

The robotic arm (RV6SDL, Mitsubishi, Inc., Japan) has 6 DOF and a resolution of motion of 1 μm. The EPM is an off-the-shell cylindrical permanent magnet in NdFeB, with N52 axial magnetization, a remanance of 1.48 T, a diameter of 5 cm and a height of 5 cm (K&J Magnetics, Inc., USA). The permanent magnet embedded in the capsule has the same features as the EPM, but is 11 mm in diameter, and 11 mm in height. The magnetic coupling between the two magnets allows for an effective manipulation, as reported in [162].

The localization module is designed all around the onboard magnet in order to be easily integrated in a device operated by magnetic manipulation. The module consists of a digital triaxial accelerometer (LIS331DLH, STM, Switzerland) and six uniaxial Hall effect sensors (CYP15A, Chen Yang Technologies GmbH & Co. KG, Germany). The Hall Effect sensors

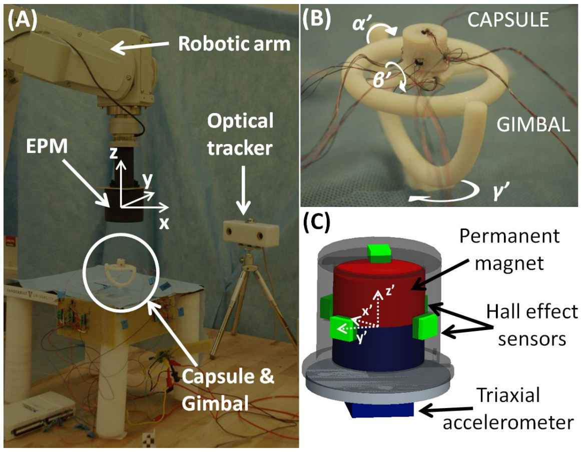

Figure A.2: Validation of the proposed pose detection method: (A) View of the platform; (B) Close view of the capsule and the gimbal; (C) Schematic view of the capsule.

were chosen with a large dynamic range (*i.e.*, from 0.1 μT to 2 T) to accommodate the offset due to the internal magnet (*i.e.*, about 10% of the dynamic range). As represented in Fig. A.2.C, the Hall Effect sensors were positioned along $[x', y', z']$ at the opposite sides of the capsule in order to maximize the separation between $\overrightarrow{B_1'}$ and $\overrightarrow{B_2'}$ readings. The separation distance for a couple of Hall Effect sensors laying on the same axis is 12 mm. The overall size of the localization module and the onboard magnet is 15 mm in diameter and 18 mm in height. Both gimbal and capsule were fabricated by rapid prototyping (OBJECT 30, Objet Ltd., Israel). Data are acquired from the Hall effect sensors and the accelerometer by an USB data acquisition board (DAQ 6211, National Instrument, Inc., USA) with a 16-bit resolution at each iteration of the algorithm. The sensor size, power consumption, and data output are compatible with wireless operation. In particular, a wireless microcontroller (*e.g.*, CC2530, Texas Instruments, Inc., USA) and a high resolution analog to digital converter (*e.g.*, ADS8320, Texas Instrument, Inc., USA) can be used to acquire the measurements at the same sampling rate and resolution, and send them to an external receiver by radiofrequency communication [162]. The algorithm is written in C++ and communicates in real-time with the data acquisition board and the robotic arm controller.

A.4 Experimental Validation and Results

In order to validate the proposed method, the robotic arm was programmed to move the EPM within the $z < 0$ portion of the workspace represented in Fig. A.1. Considering the capsule fixed to the gimbal at [x=0 cm, y=0 cm, z=-15 cm], the robot scanned a 30 cm × 30 cm area on the (x, y) plane at nine different vertical positions (*i.e.*, z varying from -8 cm to 0 cm in 1-cm steps). The benchmark for validation was provided by the robotic arm encoders (resolution of 1 μm) for $\vec{d}$, and by the optical tracker (resolution of 0.3°) for α, β, and γ.

Since the proposed method is based on magnetic field measurement, the error is expected to increase with the separation distance between the source of magnetic field and the position where it is measured. Therefore, the error in detecting capsule pose is reported in Fig. A.3 for three different values of $|\vec{d}|$ (*i.e.*, 10 cm, 12.5 cm, and 15 cm) within a typical range of operation for magnetic capsule endoscopes [28]. In particular, if the capsule is within 10 cm from the EPM, the average error and the standard deviation are -4.3 ± 2.1 mm for x, -4.5 ± 1.9 mm for y, -3.9 ± 1.8 mm for z, and $-12°\pm29°$ for γ. In case the capsule is within 15 cm from the EPM, the average error remains in the same range, but the standard deviation significantly increases. The error and standard deviation for $|\vec{d}| < 15$ cm are -3.4 ± 3.2 mm for x, -3.8 ± 6.2 mm for y, 3.4 ± 7.3 mm for z, and $-19°\pm50°$ for γ if the capsule is within 15 cm from the EPM. The angles α and β are measured by the accelerometer, therefore their error is not dependent on $|\vec{d}|$. The average error and the standard deviation for α and β are $-6°\pm18°$ and $3°\pm20°$, respectively.

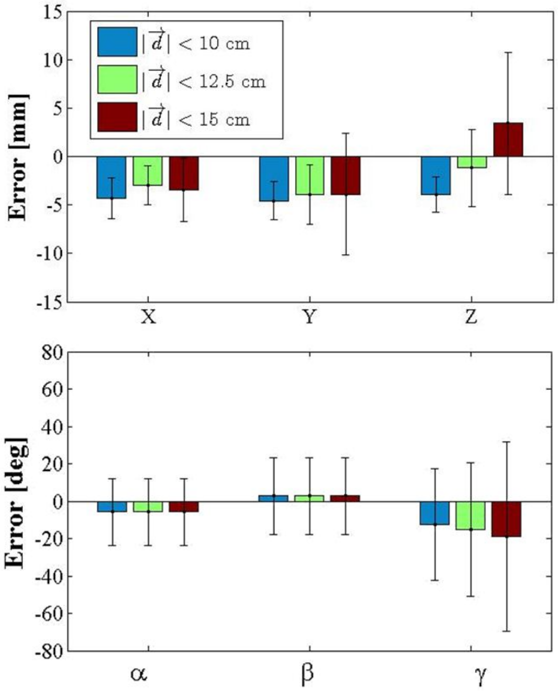

Figure A.3: Error bar plot for the proposed pose detection method in the six DOF, reported for three different values of $|\vec{d}|$. The bar height represents the average error, while the whiskers account for standard deviation.

Table A.1: Localization success rate for different $|\vec{d}|$

	$\lvert\vec{d}\rvert < 10\ cm$	$\lvert\vec{d}\rvert < 12.5\ cm$	$\lvert\vec{d}\rvert < 15\ cm$
Success Rate	82%	66%	48%
Total Measurements	4,000	12,500	26,000

For a more straightforward interpretation of results, it is possible to define the event of successful localization. A localization is successful if the capsule estimated position $\vec{d}$ is falling within a spherical volume centered in the capsule actual position and having a diameter of 11 mm, as current capsule endoscopes [49]. The success rates of the proposed algorithm related to the total number of measurements are reported in Table A.1 as a function of $|\vec{d}|$.

As regards computational time, a single instance of the algorithm takes 14 ms, while the search requires an average of 5 ms. These results are compatible with the closed-loop control cycle of the robotic arm controlling the EPM (*i.e.*, typically 20 ms).

A.5 Conclusion

In this paper we propose a novel approach to detect in real-time the 6-DOF pose of a magnetic capsule endoscope, combining multiple sensor readings with pre-calculated magnetic field values. This solution is compatible with magnetic manipulation and is optimized for a cylindrical EPM with axial magnetization. The sensing module is designed for wireless operation, and the algorithm has a computational time that allows real-time teleoperation. The proposed approach is able to provide an average error below 5 mm in position detection, and below 19° for angular motion within a spherical workspace of 15 cm in radius, centered on the EPM.

Future works will aim to improve angular accuracy by including magnetic field gradient computation. The localization module will be integrated in a wireless capsule. Then, the real-time pose detection algorithm will be used to achieve closed-loop control of capsule position by magnetic manipulation.

Appendix B

WIRELESS TISSUE PALPATION FOR INTRAOPERATIVE DETECTION OF LUMPS IN SOFT TISSUE

Marco Beccani, Christian Di Natali, Levin Sliker, Jonathan A. Schoen, Mark E.Rentschler, and Pietro Valdastri

From: IEEE Transactions on Biomedical Engineering, vol.61, no.2, pp.353,361,
Status: Published Feb. 2014

B.1 Abstract

In open surgery, identification of precise margins for curative tissue resection is performed by manual palpation. This is not the case for minimally invasive and robotic procedures, where tactile feedback is either distorted or not available. In this work, we introduce the concept of intraoperative wireless tissue palpation. The wireless palpation probe (WPP) is a cylindrical device (15 mm in diameter, 60 mm in length) that can be deployed through a trocar incision and directly controlled by the surgeon to create a volumetric stiffness distribution map of the region of interest. This map can then be used to guide tissue resection to minimize healthy tissue loss. Wireless operation prevents the need for a dedicated port and reduces the chance of instrument clashing in the operating field. The WPP is able to measure in real-time the indentation pressure with a sensitivity of 34 Pa, the indentation depth with an accuracy of 0.68 mm, and the probe position with a maximum error of 11.3 mm in a tridimensional workspace. The WPP was assessed on the benchtop in detecting the local stiffness of two different silicone tissue simulators (elastic modulus ranging from 45 kPa to 220 kPa), showing a maximum relative error below 5%. Then, *in vivo* trials were aimed to identify an agar-gel lump injected into a porcine liver and to assess the device usability within the frame of a laparoscopic procedure. The stiffness map created intraoperatively by the WPP was compared with a map generated *ex vivo* by a standard uniaxial material tester, showing less than 8% local stiffness error at the site of the lump.

B.2 Introduction

Minimally invasive surgery (MIS) drastically reduces patient trauma and recovery time when compared to open surgery. More than two million MIS procedures are performed annually in the United States alone [163]. Patient benefits, however, come with a price for surgeons in terms of constrained maneuverability of laparoscopic instruments and restricted field of view through the endoscopic camera. Force and tactile cues are commonly used in open surgery to identify tumor margins and vessels buried in soft tissue. In MIS, any haptic cue is severely compromised by the use of laparoscopic instruments due to friction against the surgical port (*i.e.*, trocar) and the fulcrum effect at the insertion point [164]. These shortcomings are amplified in robotic surgery, where the surgeon is physically removed from the bedside and haptic feedback is completely absent in the more than 2,000 Intuitive Surgical da Vinci platforms installed worldwide [165].

Tissue palpation is essential to effectively explore non-visible tissue and organ features, to identify buried structures (*e.g.*, nerves or blood vessels) that must be avoided during the surgical procedure, and to identify precise margins for curative tumor resections [166]. Achieving negative surgical margins is particularly relevant during partial nephrectomies [167] and hepatic surgeries [168] in order to minimize accidental damage to healthy tissue and to prevent organ failure, that would result in the urgent need for a transplant. Registration with pre-operative imaging – a standard practice for image guided surgery [169] – is not a viable option for soft tissues [166,170]. Therefore, surgeons currently rely on intraoperative ultrasonography (IOUS) for the evaluation of vascular anatomy, identification of known and occult lesions, and operative planning [171]. Recent studies confirm the utility of IOUS also in robotic procedures [167,168,172,173], even if several open issues still remain unaddressed. In particular, IOUS can only provide a vertical slice of tissue density, while a stiffness distribution map would better serve the need of tumor margin identification.

Restoring haptic sensations in MIS and robotic MIS has been an active research topic for more than two decades [174,175], with one of the first systems used in a human dating back to 1994 [176]. A relevant number of MIS instruments with force and/or tactile sensors have been developed to acquire *in vivo* data for tissue modeling and simulation [177–180], to improve the outcomes of the surgical procedure – preventing excessive forces from being applied to the tissues [164, 181–184], or to create stiffness distribution map by palpation [166,170,185–189].

However, MIS palpation instruments developed to date all present a rigid shaft and require a dedicated port. This increases the chance of tool clashing in the operating field and often requires an assistant to operate the palpation probe. A wireless device for uniaxial indentation of soft tissues was preliminary reported by the authors in [162]. Magnetic fields were proposed to indent the tissue and to reposition the probe while scanning the organ surface. This approach proved to be limited in terms of both safety and reliable positioning, due to the rapid variation of magnetic field strength with distance. Having a wireless device to be directly manipulated by the surgeon would dramatically improve

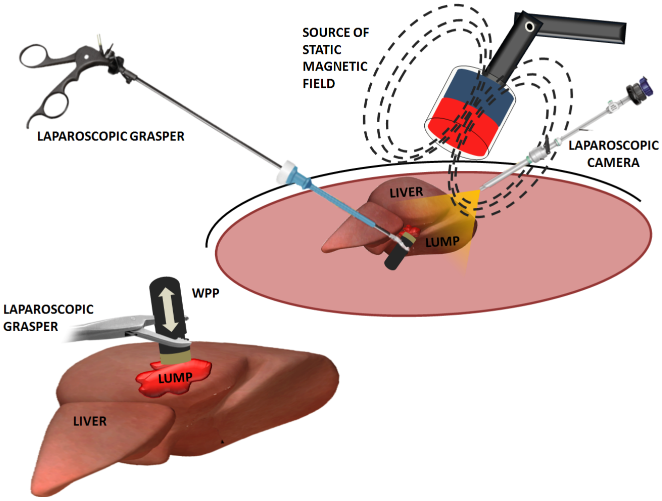

Figure B.1: Principle of operation for wireless tissue palpation using a wireless palpation probe (WPP).

maneuverability, autonomy, and precision, as illustrated by the soft-tethered IOUS probes presented in [167, 173].

In this paper we introduce for the first time an intraoperative wireless palpation probe (WPP) – schematically represented in Fig. B.1 – that can be deployed through a trocar incision and directly controlled by the surgeon to create a stiffness distribution map. Such a map can then be used to localize tumor margins during soft tissue surgery, thus improving intraoperative diagnostic and interventional decisions. Wireless operation prevents the need for a dedicated port and reduces the chance of instrument clashing in the operating field.

B.3 Materials

B.3.1 Principle of Operation

For indentation depths that are less than 10% of the organ thickness, it is possible to assume the tissue as linear elastic [166]. A volumetric stiffness map can then be created by estimating the local tissue stiffness $E(\mathbf{r})$ through the measurement of the indentation depth $\delta(\mathbf{r})$ and the tissue reaction pressure $P(\mathbf{r})$ at different positions $\mathbf{r}$ on the organ surface:

$$E(\mathbf{r}) \simeq \frac{P(\mathbf{r})}{\delta(\mathbf{r})}. \tag{B.1}$$

Referring to Fig. B.2, we can define (x, y, z) as the global Cartesian coordinate system, (x', y', z') as the reference frame at the external source of static magnetic field, and (x_w, y_w, z_w) as the coordinate system at the WPP. The origin O of (x, y, z) is coincident with the origin O' of (x', y', z'), while z_w is aligned with the main axis of the device. We

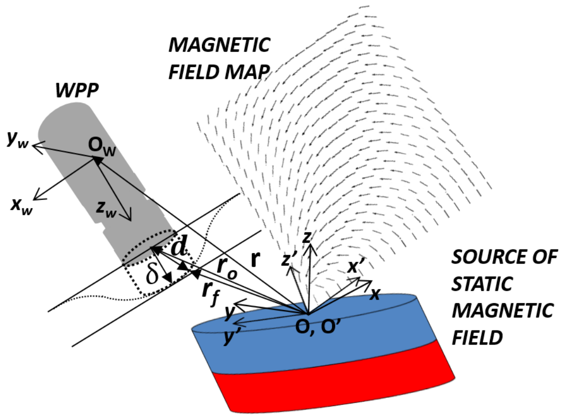

Figure B.2: The WPP during indentation and the external source of magnetic field with a slice of the magnetic field map. Vectors $\mathbf{r}_0$ and $\mathbf{r}_f$ represent the WPP position $\mathbf{r}$ at the beginning and at the end of the indentation. They are represented at the interface of WPP and tissue, rather than at O_w, for a better understanding of their physical meaning.

can assume the position vector $\mathbf{r}$ to identify the origin of (x_w, y_w, z_w) – noted as O_w – with respect to the global coordinate system (x, y, z). When the WPP is manipulated by the surgeon to palpate a tissue, its motion $\mathbf{d}$ is not constrained along z_w. Therefore, the following equation must be used to estimate the indentation depth $\delta(\mathbf{r})$:

$$\delta(\mathbf{r}) = \mathbf{d} \cdot \mathbf{z}_{w0} = (\mathbf{r}_f - \mathbf{r}_0) \cdot \mathbf{z}_{w0}, \tag{B.2}$$

where $\mathbf{r}_0$ and $\mathbf{r}_f$ are the WPP positions at the beginning and at the end of the indentation, respectively, while $\mathbf{z}_{w0}$ is the unit vector along z_w at the beginning of the indentation. In this approach, the beginning of the indentation is identified as the instant when the reading of the tissue reaction pressure $P(\mathbf{r})$ becomes significant. The end of each indentation is identified as the instant when $\delta(\mathbf{r})$ reaches the maximum value.

In our work, tissue reaction pressure is acquired by a barometric pressure sensor embedded in a silicone rubber at the probing surface of the WPP. This design is inspired by [110] and further details are provided in section B.3.2. A threshold value P_{th}, independent from $\mathbf{r}$, is defined by calibration and takes into account both bias and noise of the pressure sensor. A single indentation starts as $P(\mathbf{r}) > P_{th}$.

Real-time localization of the WPP serves two purposes. First, the position where indentation is taking place must be recorded in three degrees of freedom (DoF) in order to reconstruct the stiffness map. In this case, we assume the position $\mathbf{r}$ of each indentation to be coincident with WPP position as the indentation begins (*i.e.*, $\mathbf{r}_0$). A second goal for WPP tracking is to derive $\delta(\mathbf{r})$ as in Eq. B.2. In this case, real-time estimation of $\mathbf{r}$

and rotations of the WPP around x and y are required. Therefore, the WPP position and orientation in five DoF must be available in real-time. This is achieved by an on-board localization module, working in synergy with an external source of static magnetic field, as represented in Fig. B.1. The on-board module consists of three orthogonally mounted magnetic field sensors and a triaxial accelerometer (technical details are provided in section B.3.2). The accelerometer – used here as an inclinometer – provides WPP rotations around x and y. The WPP position vector $\mathbf{r}$ is derived from the magnetic field sensor readings, as suggested in [68]. In particular, the magnetic field vector $\mathbf{B}_w$ is measured at the WPP and rotated according to

$$\mathbf{B} = R^{'T} R^{w} R^{'} \mathbf{B}_w, \tag{B.3}$$

where R^w is the rotational matrix of the WPP reference frame with respect to the global Cartesian coordinate system, while $R^{'}$ is the rotational matrix of the reference frame at the external source of static magnetic field with respect to the global Cartesian coordinate system. The matrix R^w is obtained in real-time from the readings acquired by the inclinometer integrated in the WPP, while $R^{'}$ is derived from the data acquired by an inclinometer mounted on the external source of static magnetic field. Then, a search within a precalculated bi-dimensional magnetic field map is performed to find the WPP position $\mathbf{r}$ that would match with the actual magnetic field vector $\mathbf{B}$. The magnetic map associates each point $\mathbf{r}$ within the workspace – expressed in cylindrical coordinates (r_ρ, r_z) – to the related magnetic field intensity $\mathbf{B}$ – also expressed in cylindrical coordinates $(B_\rho,\ B_z)$ – with a spatial resolution of 0.2 mm. The third cylindrical coordinate r_θ can be calculated from the values of B_x and B_y by applying the following equation:

$$r_\theta = \arctan(\frac{B_y}{B_x}). \tag{B.4}$$

The effective localization workspace is a cylinder with a diameter of 35 cm and a length of 35 cm, centered on the static magnetic field source. The 5-DoF WPP coordinates derived by the algorithm are referenced to a Cartesian frame at the center of the workspace.

B.3.2 Wireless Palpation Probe Development

Both the method used to measure the indentation pressure and the solution for WPP localization are designed for wireless operation and can be implemented within a miniature device. The WPP prototype, represented in Fig. B.3, has a cylindrical shape (15 mm in diameter, 60 mm in length, 9.5 g total mass) with a grasping site close to the pressure sensor head. The cylindrical plastic shell – fabricated by rapid prototyping (OBJET 30, Objet Geometries Ltd, USA) – hosts a pressure sensing head, a localization module with a dedicated signal conditioning stage, a power regulation unit, a rechargeable battery, and a wireless microcontroller.

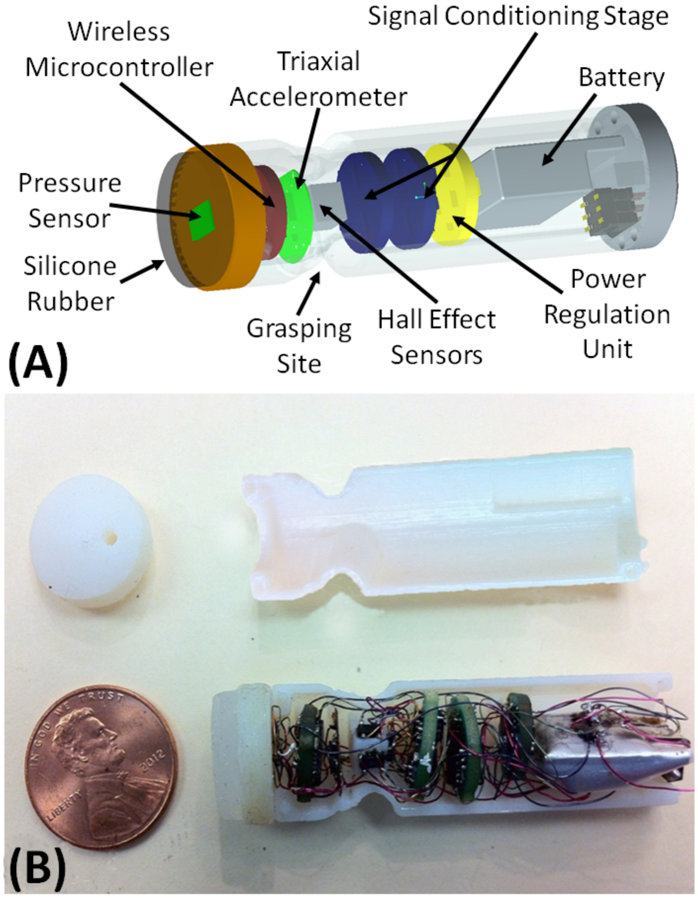

Figure B.3: (A) Schematic view and (B) picture of the wireless palpation probe. The signal conditioning stage, the triaxial accelerometer, the power regulation unit, and the wireless microcontroller are mounted on separate printed circuit boards (PCB) with a diameter of 9.9 mm. In particular, the signal conditioning stage was separated into two boards due to PCB area constraints.

The pressure sensing head – based on the design reported in [110] – consists of a barometric pressure sensor (MPL115A1, Freescale Semiconductors, USA) embedded in a 2.2 mm-thick silicone rubber layer (VytaFlex 20, Smooth On, USA). The bare barometric pressure sensor has a sensitivity of 0.5 kPa and a sensing range of 65 kPa for the atmospheric pressure.

The localization module includes three Hall effect sensors (CYP15A, ChenYang Technologies GmbH & Co. KG, Germany) and a 16 bit triaxial accelerometer with serial peripheral interface (SPI) (LIS331AL, STMicroelectronics, Switzerland). The Hall effect sensors are mounted on three orthogonal sides of a cubic structure, as represented in Fig. B.3. Their analog outputs are acquired by a signal conditioning stage. This stage consists of three instrumentation amplifiers (AD623, Analog Devices, USA) with a unity gain, three low-pass filters ($F_c = 30Hz$), and three 16 bit analog to digital converters (ADC) (ADS8320, Texas Instrument, USA) with SPI interface. The digitalized magnetic field signal has a sensitivity of 0.6 mT.

The power regulation unit embeds a low-dropout voltage regulator (LDO) (TPS73xx, Texas Instrument, USA), an operational amplifier (ADS8617, Analog Device, USA) used as voltage divider to provide the proper power supply to the signal conditioning stage and to monitor the battery level. A 50 mAh, 3.7 V rechargeable LiPo battery (Shenzhen Hondark Electronics Co., Ltd., China, 12 mm × 15 mm × 3 mm in size) is used as the onboard power supply source.

The data from the barometric pressure sensor, the accelerometer, and the magnetic field sensors are acquired by a wireless microcontroller (CC2530, Texas Instrument, USA) through the SPI interface at a clock frequency of 1 Mbit/s. Each dataset is then bounded into a 28 byte payload together with a progressive package indicator, a time stamp, the battery level, and two synchronization start and stop bytes. This payload is transmitted by the wireless microcontroller to an external transceiver over a 2.4 GHz carrier frequency. The external transceiver consists in a mirror wireless microcontroller (CC2530, Texas Instrument, USA) connected to the Universal Serial Bus (USB) port of a personal computer (PC) through a dedicated module (UM232R, FTDI, UK).

While the total time required to acquire a single dataset from all the sensors is 3.7 ms, the wireless data throughput runs at 44.8 kbit/s, resulting in a refresh time of 5 ms and a sampling rate of 200 Hz. The overhead allows to handle correctly the synchronization with the external transceiver.

In addition to the transceiver and the PC, the external platform includes the source of static magnetic field used for WPP tracking. The magnetic field is generated by an off-the-shelf cylindrical NdFeB permanent magnet mounted on an articulated three DoF friction clutch arm (Dectron, USA). The selected magnet has N52 axial magnetization, magnetic remanence of 1.48 T, is 50 mm in diameter and 50 mm in height, and has a mass of 772 g. These features allow for a localization workspace that extends 15 cm away from each side of the magnet. A triaxial accelerometer (LIS331AL, STMicroelectronics, Switzerland) is mounted on the magnet to measure its inclination and derive its rotation with respect to the global reference frame (x, y, z). Accelerometer data are fed directly to the PC through a secondary USB connection.

As concerns waterproofing of the WPP to operate during surgery, a layer of paraffin film (Parafilm, Sigma Aldrich, USA) was wrapped around the device. An additional layer of film was secured at the grasping site to enable a safe grip.

B.3.3 Communication Protocol and User Interface

The communication protocol provides robust operation, real-time data acquisition, and low power consumption. A sleep timer is used to wake up the WPP from a low power mode every 15 seconds. When active, the WPP tries to establish a wireless communication with the external transceiver. If this attempt fails, the WPP returns in sleep mode to save power. Once the wireless link is established, the WPP acquires a full dataset of sensor readings, transmits it to the external transceiver, and waits for an acknowledgement. If the acknowledgment is received, the WPP continues to acquire and send data. Otherwise, the WPP retries to transmit the same package. This attempt is repeated for two times, then the firmware forces the device to get a new dataset and updates the payload. In case of loss of the synchronization, the WPP auto-resets itself ready for a new acquisition. This protocol allows for a fail safe operation and prevents the need for a hard reset of the device, that would not be possible during surgery.

All the data received by the external transceiver are transmitted to the PC together with the Received Signal Strength Indicator (RSSI). The RSSI quantifies the quality of the wireless link. In case of a low RSSI, the user is warned to modify the position of the external transceiver to improve the wireless coupling.

A multi-thread C++ application running on the PC unbounds the data and shares them with a parallel application developed in Matlab (Mathworks, USA) via TCP-IP communication. Refresh rate for displayed data runs at 30 Hz.

The user interface is conceived to work in two different modalities: (1) creation of the volumetric stiffness map, (2) display of WPP position on the volumetric stiffness map. In the first modality, the surgeon grasps the WPP and creates the map by palpating the region of interest. In this case, the user interface displays in real-time the x, y, z coordinates of the WPP, a plot of the indentation pressure, and the numeric value of the indentation depth in case the indentation pressure has exceeded P_{th}. Visual indicators are provided to warn the user if the WPP is outside the localization workspace. Once the region of interest has been palpated with the desired spatial resolution, a command is provided by the user through the keyboard to create the volumetric stiffness map. Once the map is available, the user interface switches to the second modality, overlaying the real-time position of the WPP in a 3D space centered on the map. Under the assumption that the region palpated does not undergo substantial movements, the surgeon can manipulate the WPP as a cursor to identify the margins of a stiffer region buried underneath the tissue.

B.3.4 Wireless Palpation Probe Characterization

Before assessing the overall functionality of the proposed device, the single components were tested and characterized on the benchtop. In particular, the first step was to verify the localization unit algorithm to evaluate the WPP workspace, localization error, and any influence of surgical tool in the localization unit performance. Then, a load cell was adopted to calibrate the pressure sensor response. Finally, the WPP electronic performance was tested on bench to assess the battery lifetime and the wireless link reliability.

B.3.4.1 Localization

The device was mounted on the end effector of a six DoF industrial robot (RV6SDL, Mitsubishi Corp., Japan) which was used as a reference position system given its encoder feedback. Assuming the (x, y, z) global reference system centered on the external magnet and having z aligned with the main axis of the magnet, we characterized the localization on a grid of 3 by 3 points equally spaced by 50 mm along x and y directions at 3 different z coordinates (*i.e.*, 80 mm, 110 mm, and 140 mm). For each position, localization data were acquired from the robot encoders and the WPP algorithm. Onboard localization was repeated for each point with a disposable laparoscopic grasper (EndoGrasp 5 mm, Covidien, USA) closing its jaws at the grasping site. Then, the indentation depth error was estimated at each point of the grid by moving the robot end effector 3 mm along z in open air, thus emulating palpation. The average absolute errors were equal to 4.7 mm (±4.5 mm) for x, 4.1 mm (±5.8 mm) for y, and 4.5 mm (±2.2 mm) for z. The laparoscopic grasper increased the localization error to 9.8 mm (±5.1 mm) for x, 11.3 mm (±6.6 mm) for y, and 10.6 mm (±4.6 mm) for z. However, we observed that the contribution of the laparoscopic grasper does not vary substantially within the workspace, thus it can be assumed as a constant offset that factors out when reconstructing the stiffness map. The indentation depth average absolute error resulted in 0.68 mm (±0.44 mm).

B.3.4.2 Pressure Sensing Head

To calibrate and characterize the pressure sensing head response, a 6-DoF load cell (NANO17, ATI Industrial Automation, USA, resolution 1/160 N) was adopted as the force reference system [188]. The WPP was mounted as in the previous experiment, while the load cell was fixed on the benchtop. A 1-mm step motion pushing the WPP against the load cell was imposed. Speed of motion was 65 mm/s. After about 9 s, the same step was imposed in the opposite direction, releasing the load. From the experimental results – represented in Fig. B.4 – we can conclude that the silicone layer embedding the barometric

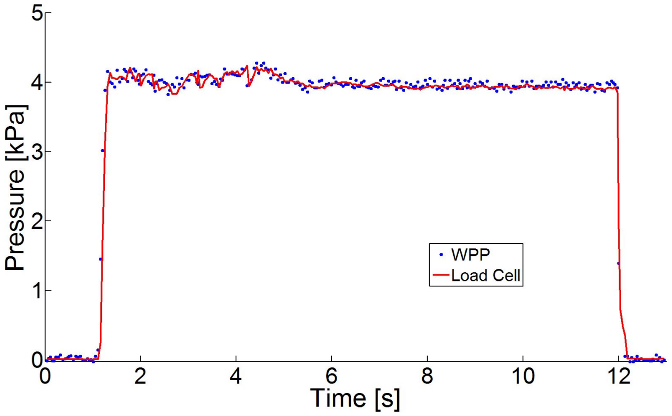

Figure B.4: Step response of the WPP pushing against a reference load cell.

pressure sensor does not introduce any relevant delay in the sensor response. An additional set of trials was performed by pushing the WPP against the load cell at a lower speed (*i.e.,* 3.12 mm/s), until the saturation of the barometric pressure sensor occurred. This test was repeated five times. The pressure sensing head showed a sensitivity of $P_s = 34$ Pa (*i.e.,* considering the probing area, this is equivalent to 5 g or 0.049 N), while saturation occurred at $P_{SAT} = 5$ kPa (*i.e.,* considering the probing area, this is equivalent to 730 g or 7.16 N). In light of a recent study [189] that reports tissue damage to the liver for a force exceeding 6 N – exerted by a probing area of the same size of the WPP – we can conclude that the pressure sensing range is adequate for this exploratory investigation. The threshold value P_{th} was therefore assumed as $P_{th} = P_{bias} + 2P_s$, where P_{bias} is the output value for the sensor when unloaded. This value for P_{th} allowed us to reliably identify the start of an indentation.

B.3.4.3 Electronics

As regards power consumption, a single 5 ms loop of data acquisition and wireless transmission drains an average of 33.3 mA with a peak of 41.6 mA. This translates in a battery lifetime of about 90 minutes when the WPP is in active mode. Average current consumption drops down to 3 mA when the WPP is in low power mode.

The data synchronization between the WPP and the external transceiver was tested in open air to estimate the robustness of the protocol. The firmware was ran for 36 consecutive hours without failures and was then stopped. The results included a package loss below 2% and an average RSSI of -13.5 dBm at a distance of 2 m between the WPP and the external trans-receiver. Complete loss of communication occurs as the RSSI drops below -88 dBm.

B.4 Wireless Palpation Probe Assessment

Experimental validation of the proposed platform consisted in two different trials. First, the effectiveness of the probe in identifying the local stiffness of a tissue simulator was assessed. Then, *in vivo* trials were aimed to identify agar-gel lumps injected into a porcine liver and to assess the device usability within the frame of a MIS procedure.

B.4.1 Assessment of Local Stiffness Identification

To estimate the ability of the WPP in detecting different local stiffnesses, two different synthetic tissue samples were fabricated combining two different ratios of liquid plastic and hardener (PVC Regular Liquid Plastic – Hardener, MF Manufacturing, USA – Sample 1: 1 to 10 ratio, resulting in an elastic modulus of 220 kPa; Sample 2: 1 to 2 ratio, resulting in an elastic module of 45 kPa). The samples were 30 mm thick with a lateral side of 75 mm. A traditional indenter was obtained mounting a 6-DoF load cell (MINI 45, ATI Industrial Automation, USA, resolution 1/16 N) at the end effector of the robotic manipulator used previously. A cylindrical probe with the same contact surface as the WPP was mounted on the distal side of the load cell to indent the sample. Then, the cylindrical probe was replaced with the WPP and the indentation was repeated acquiring both indentation pressure and depth from the wireless device. Five loading-unloading trials reaching an indentation depth of 2.6 mm were performed for each tissue sample and each method at a constant speed of 0.75 mm/s. The local stiffnesses measured with the traditional indenter were equal to $E_1 =$ 2.12 kPa/mm, $E_2 =$ 8.52 kPa/mm, while the results obtained with the WPP were $E_{1WPP} =$ 2.02 kPa/mm, $E_{2WPP} =$ 8.79 kPa/mm. Experimental plots obtained from a single loading are represented in Fig. B.5. Overall, the WPP was effective in detecting the local stiffness of different samples with an average relative error equal to 4.7% for sample 1 and 3% for sample 2.

B.4.2 In Vivo Validation

The feasibility of wireless tissue palpation was then assessed *in vivo* on an anastetized porcine model. The primary measure of interest was to acquire a volumetric stiffness map of a segment of the liver where agar-gel was injected to simulate a hepatic tumor. The map acquired *in vivo* by wireless palpation was then compared with a stiffness map obtained *post-mortem* within 12 hours after the procedure using a standard uniaxial material tester. Secondary measures of interest were the time to scan a liver segment by wireless palpation, WPP usability, instrument clashing, and operator workload. Reliability of the wireless link was also assessed.

The porcine surgery was performed at the University of Colorado Anschutz Medical Campus under IACUC protocol 87912(04)1D. A 57-kg female standard pig was used for

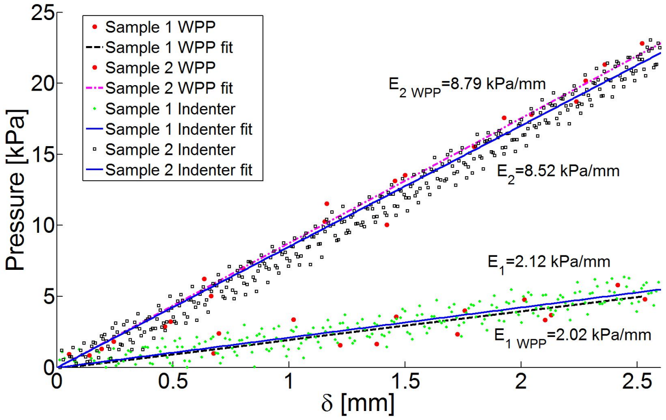

Figure B.5: Experimental data acquired by standard and wireless indentation for two different silicone samples. For this trial, relative errors in local stiffness identification were equal to 4.72% for sample 1 and 3.17% for sample 2.

this study. After intravenous sedation, a laparotomy was performed to access the liver. Similarly to the methods suggested in [170], 6 cc of Sigma Gelrite Gellan Gum (agar) was prepared in a 30:1 ratio of water to agar by weight, boiled, and injected into the right lateral segment of the liver, to approximately the mid-thickness of the organ. The midline incision was then sutured, and minimally invasive access was gained by one 5-mm (5 Versaport Plus, Covidien, Norwalk, CT, USA) and three 12-mm trocars (5-12 Versaport Plus, Covidien, Norwalk, CT, USA). The WPP was introduced in the abdominal cavity through one of the 12-mm trocar incisions before the placement of the port. The external source of magnetic field and the external transceiver were placed in the close vicinities of the right side of the animal, as represented in Fig. D.9.B. The surgeon used a standard laparoscopic grasper to operate the WPP under endoscopic guidance (see Fig. B.7). A lateral screen showed in real-time WPP position in three DoF, indentation pressure, and indentation depth (see Fig. D.9.A).

Once the right segment of the liver was identified, the surgeon palpated the organ in different positions, always targeting at least 3 mm as the indentation depth. To prevent localization artifacts, the surgeon verified that the liver was not moving during palpation and that adequate support was provided by the rib cage and the surrounding organs. Tissue stiffness was acquired on a total of 30 different points on the liver surface. This required about 5 minutes. The local stiffness map, represented in Fig. B.8, was then generated by the algorithm and displayed on the lateral screen, overlaying the current position of the WPP.

Immediately after euthanization, the liver was harvested from the animal for *ex vivo*

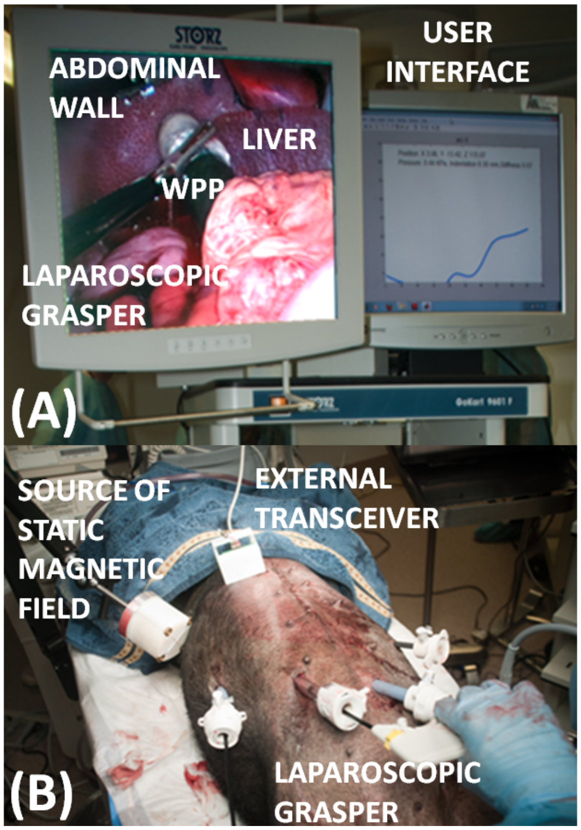

Figure B.6: Picture of the surgical setup during the *in vivo* trial. (A) Snapshot of the laparoscopic camera view and the user interface during the creation of the volumetric stiffness map. (B) Picture of the surgical field.

palpation tests using a standard uniaxial material testing system (MTS) (Insight 2 Electromechanical Testing System, MTS System Corporation, USA) to create a comparable stiffness map. The liver was placed in 0.9% phosphate buffered saline (PBS) solution immediately after excision and refrigerated until the *ex vivo* tests were performed. The liver was warmed to room temperature prior to testing. The organ was placed on a platform, marked with 28 pins and photographed from the top (Fig. B.9). The liver was indented with a cylindrical indenter probe (2 mm diameter) beside each pin location – to avoid palpating tissue that had been pricked by the pin. The test was performed following a standard tissue compressive property measurement method [190]. The tissue was hydrated throughout the tests by spraying PBS on the surface prior to each indentation. The testing room conditions were 23.5°C and 22% relative humidity (RH). A 2 N load cell (PN LCCA-118-75, MTS System Corporation, USA) with 1 mN resolution was used to measure the load exerted on the tissue by the indenter during each indentation. The probe was programmed to approach the

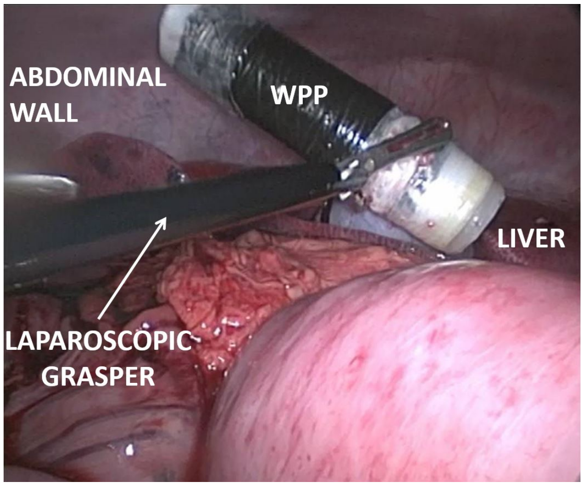

Figure B.7: Laparoscopic view of the WPP operated by the surgeon through a laparoscopic grasper during *in vivo* trials.

surface of the tissue at a low speed (0.1 mm/s) until a force threshold (2 mN) was reached. At that point, the probe advanced into the tissue at a rate of 1 mm/s to a depth of 3 mm to simulate the *in vivo* experiment. Force and indentation depth (10 μm resolution) data were collected at 100 Hz and analyzed with a customized program developed in Matlab. Following testing, the tissue was resected to verify that the agar did not dilute in the liver.

The force data were divided by the surface area of the cylindrical probe tip to obtain pressure. The local stiffness at each point was determined by computing the slope of a linear regression of the first 0.75 mm of the pressure-displacement curve. Force at depths larger than 0.75 mm were found to be too high due to the rigid platform that the liver was resting on and the relatively small liver thickness. This was not an issue *in vivo* as the liver was pressed against other organs or the rib cage. The stiffness values were assigned to pin locations and overlaid on the photograph of the liver to produce the stiffness map shown in Fig. B.9.

The two local stiffness maps were then compared with Matlab (grid area is equal to 1 mm^2 for both the maps). In particular, the maximum measured stiffness resulted in 10.0 kPa/mm with the MTS machine versus 10.8 kPa/mm with the WPP, corresponding to a 8% relative error. Then, the average pseudo stiffness of the three different areas A (36 mm^2), B (64 mm^2) and C (156 mm^2) centered on the maximum point were compared. Area A is a square sided 6 mm, area B is the frame with outer dimension 10 mm and inner dimension 6 mm, while the area C is the frame with outer dimension 16 mm and inner dimension 10 mm. The three areas are shown in both Fig. B.8 and Fig. B.9. The average stiffness was equal to $E_{A_{MTS}}$ = 9.64 kPa/mm and $E_{A_{WPP}}$ = 8.87 kPa/mm (average relative error

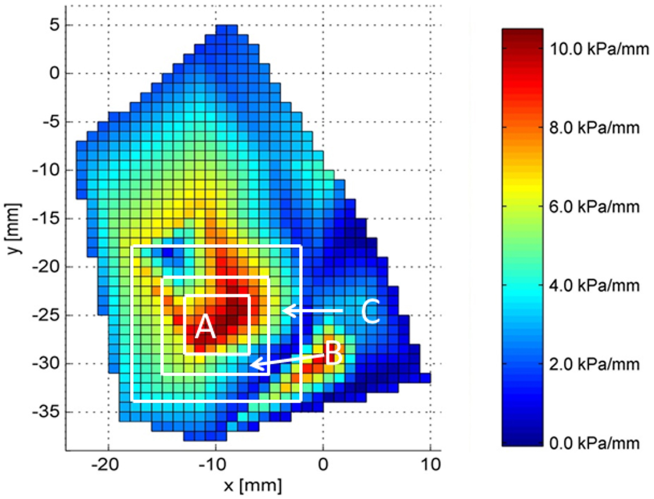

Figure B.8: Local stiffness map acquired *in vivo* for a 6 cc agar gel lump injected into the liver. Since the surface of the liver was almost flat in the palpated region, a bidimensional projection of the map is shown. The local stiffness values inside areas A, B, and C were compared with the *ex vivo* map represented in Fig. B.9.

7.96%), $E_{B_{MTS}} = 9.20$ kPa/mm and $E_{B_{WPP}} = 6.58$ kPa/mm (average relative error 28.5%) and $E_{C_{MTS}} = 8.64$ kPa/mm and $E_{C_{WPP}} = 4.82$ kPa/mm (average relative error 44.2%). Tissue stiffness slightly increased after euthanization and throughout the MTS testing due to the preservation and dehydration. However, the stiffness at the injection site remained constant to the *in vivo* conditions because the gel properties did not vary after explantation. This can help explain why the relative error increases with the distance from the maximum point which is nearby the injection site.

As concerns the qualitative measures of interest, no instrument clashing was reported. However, the length of the WPP limited the range of motion whenever the target of palpation was too close to the ribcage. The operator workload was minimal, since the surgeon was able to use a standard laparoscopic instrument to operate the WPP. Relevant learning occurred just at the beginning of the procedure, when the surgeon had to understand how strong to grasp the WPP to prevent slippage. This required about 20 minutes. After that, the surgeon was able to operate the WPP without losing the grip. The wireless link was always reliable, resulting in an average RSSI of -33.4 dBm with losses between 4.8% and 6.2% of the total packages. Battery operation was effective for the entire procedure.

It is worth mentioning that the surgeon noted that a tether tied to the WPP would help in the retrieval at the end of the procedure. A wired connection may also provide power to

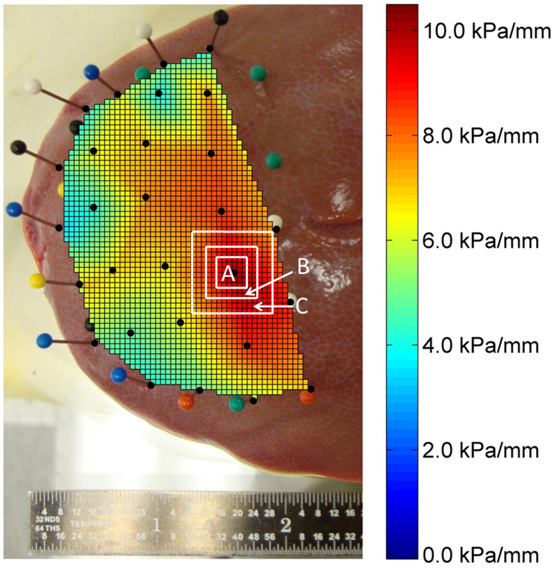

Figure B.9: Stiffness map obtained with a standard uniaxial MTS, overlayed on the right lateral segment of the explanted porcine liver. The local stiffness values inside areas A, B, and C were compared with the *in vivo* map represented in Fig. B.8.

the WPP instead of the battery, thus allowing for a reduction in size. On the other hand, a tether may limit WPP motion and get trapped in between instruments.

B.5 Conclusions and Future Work

This paper introduces for the first time the concept of wireless tissue palpation to localize tumor margins intraoperatively by creating a stiffness distribution map in real-time. The proposed wireless device is manipulated directly by the surgeon through a standard grasper, thus improving autonomy, precision, and maneuverability. Wireless operation effectively prevents instrument clashing and removes from the need of a dedicated access port. Preliminary *in vivo* results showed the feasibility of acquiring a stiffness map during a minimally invasive procedure. In the future, this map can be used to guide liver resection without sacrificing excess normal tissue and preventing postoperative organ failure.

While the indentation pressure is acquired by a sensor mounted on board, the position and the indentation depth measurements rely on an external source of static magnetic field. This imposes a constraint on the workspace, since magnetic field strength drops exponentially with distance. With the proposed platform, the workspace is a cylinder with a diameter of 35 cm and a length of 35 cm, centered on the source of static magnetic field. Considering that the abdominal wall thickness for severely obese patients (Body Mass Index ≤ 40 kg/m^2) is usually below 4 cm [117], the proposed platform is easily applicable to the vast majority of patients undergoing abdominal surgery. Nevertheless, if a larger workspace is required, either the source of magnetic field or the on-board magnetic field sensors can be adapted to meet the desired requirements.

As previously mentioned, motion of the organ during the creation of the map or poor background support for the tissue may result in localization artifacts. If this occurs, the surgeon needs to restart the acquisition of stiffness values. This issue is common for intraoperative palpation and can be addressed with appropriate surgical planning.

Next steps will consist of improving localization accuracy, [187] reducing the size of the WPP – to achieve a better maneuverability – and in demonstrating how the WPP can be used to assist liver resection in a series of *in vivo* trials. Blinded studies will be performed, where the operator is not aware of the location/number/stiffness of the buried lumps. In these studies, the effectiveness of the WPP approach will be compared with other forms of intraoperative palpation. Also, additional bench trials will be performed to quantify the efficacy of tumor identification with respect to size, depth, and relative stiffness of embedded lumps, following a protocol similar to [166] and performing CT scans of the region of interest as a benchmark for localization. The repeatability of the results will be quantified through statistical analysis. Non-linear stiffness modeling will be considered for the detection of deeper tumors. A triaxial force sensor [88, 191–193] may be used in the probing head of the WPP instead of a uniaxial pressure sensor. This would allow for studying more complex interactions with the tissue and to improve lump margin detection. Another relevant future step will be the optimization of the user interface. This will include a study on the most effective way to convey the acquired information to the surgeon, along the lines of the results reported in [187].

Appendix C

JACOBIAN-BASED ITERATIVE METHOD FOR MAGNETIC LOCALIZATION IN ROBOTIC CAPSULE ENDOSCOPY

Christian Di Natali, Marco Beccani, Nabil Simaan, Pietro Valdastri

From: IEEE Transactions on Robotics,
Status: Submitted

C.1 Abstract

The purpose of this study is to validate a Jacobian-based iterative method for real-time localization of magnetically controlled endoscopic capsules. The proposed approach applies finite element solutions to the magnetic field problem and least-squares interpolations to obtain closed-form and fast estimates of the magnetic field. By defining a closed-form expression for the Jacobian of the magnetic field relative to changes in the capsule pose, we are able to obtain an iterative localization at a faster computational time when compared with prior works, without suffering from the inaccuracies stemming from dipole assumptions.

The proposed approach was assessed via simulation and experimental trials, adopting a wireless capsule equipped with a permanent magnet, six magnetic field sensors, and an inertial measurement unit. The overall refresh rate, including sensor data acquisition and wireless communication, was 7 ms, thus enabling closed-loop control strategies for magnetic manipulation running faster than 100 Hz. The average localization error, expressed in cylindrical coordinates, was below 7 mm in both the radial and axial components, and 5^o in the azimuthal component. The average error for the capsule orientation angles, obtained by fusing gyroscope and inclinometer measurements, was below 5^o. Positional drift, robustness to initialization errors and positional lag were assessed as well, showing satisfactory results.

C.2 Introduction

Wireless capsule endoscopy (WCE) allows physicians to visualize internal organs for diagnosis and potentially for intervention. This paper focuses on creating a modeling and algorithmic framework for localization of magnetically actuated WCEs. All the existing platforms for remote magnetic manipulation of a WCE operate in open loop [49], i.e. the capsule pose (i.e., position and orientation) is not tracked and used for control feedback purposes. Position control of WCEs is typically based on the assumption that the permanent magnet inside the capsule aligns with the external magnetic field. Pose tracking of the WCE would allow the capsule to automatically optimize magnetic coupling to maintain effective magnetic actuation, enabling the user to detect if the capsule is not following the expected trajectory (i.e., the capsule is trapped within a tissue fold), and to take appropriate countermeasures for re-establishing an effective motion. An example of position closed-loop control for a magnetically manipulated WCE is presented in [33], where optical tracking with external cameras is adopted to localize the capsule. To apply these results in a clinical setting and move toward the closed-loop manipulation of magnetic WCE's position and orientation, online pose tracking without line-of-sight is crucial [32, 68].

Known methods for WCE pose tracking were designed largely for diagnostic purposes (i.e., to associate a lesion visualized by the capsule to its position inside the patient's body) [7,156,194,195], and are not compatible with magnetic manipulation due to electromagnetic interference with the external source of the driving field. Recently, a number of groups working on robotic magnetic manipulation of WCE began studying localization strategies that are compatible with magnetic manipulation. These works implement localization based on measuring the magnetic field at the WCE via magnetic field sensors. Generally, these works rely on absolute localization using simple dipole models (e.g. [196, 197]) or lookup tables based on finite element solutions to the exact magnetic field (e.g. [68, 198]). The simple dipole models provide limited localization performance when the WCE is close to the magnetic field source. They work best when the WCE workspace is far away from the driving magnet. However, to maximize the magnetic coupling, the WCE should ideally operate as close as possible to the driving magnet. The drawbacks of lookup table based localization are the slow refresh rate and large memory requirements.

The performance of current WCE localization algorithms provide modest localization accuracy within limited workspace. In [197], multiple measurements taken of the capsule moving along its main axis toward the external magnet allows the user to obtain the position in three degrees of freedom (DOF) with an error below 4 mm when the capsule is within 6 cm of an external magnet. Continuous rotation of the capsule by an external revolving magnetic field combined with on-board magnetic field sensing [196] allows detection of the capsule position and orientation with an average error of 11 mm and 11 degrees within the operative workspace. Real-time systems, such as [32, 68, 198], leverage sensor fusion (i.e., inertial and magnetic field sensing) and search within pre-compiled finite element magnetic maps. In particular, the method proposed in [198] achieves a refresh rate of 50 ms and a position error of 10 mm within a 12 cm workspace. Better performances are obtained in [32], where refresh rate goes down to 30 ms and the error drops below 6 mm within a 15 cm workspace. Finally, in our previous work [32], the sensor data acquisition and the localization algorithm required 6.5 ms and 16 ms per loop, respectively. One of the aims of our proposed new localization method is to decrease computational time, thus achieving both sensor acquisition and localization within 10 ms, allowing the implementation of a 100 Hz WCE manipulation closed-loop control.

In this paper, we validate our proposed algorithm on a WCE localization setup that includes an extracorporeal magnetic field source that manipulates an intracorporeal WCE. The localization strategy proposed herein aims to provide the change in pose of a WCE with respect to an external magnetic field source having known position and orientation. Using a similar approach to that used in [32, 68, 198], the capsule is henceforth assumed to be equipped with an inertial measurement unit (IMU) and six orthogonal magnetic field sensors.

The contribution of this paper stems from putting forward a new approach for WCE localization by using an iterative Jacobian-based method. To the best of our knowledge, iterative methods for WCE magnetic pose tracking have not been presented in prior works partly because a complete analytical solution for the magnetic field is not available. To overcome this challenge, we apply finite element solutions to the magnetic field problem and least-squares interpolations to obtain closed-form and fast estimates of the magnetic field. By defining a closed-form expression for the Jacobian of the magnetic field relative to changes in the WCE pose, we are able to obtain an iterative WCE localization method without suffering from the inaccuracies stemming from dipole assumptions and without the downside of a slow refresh rate.

C.3 Motivation and Clinical Context

The motivation behind this work stems from the field of gastroiontestinal (GI) endoscopy. The GI tract is home to many deadly diseases. Colorectal cancer alone is the third most common cancer in men and the second in women worldwide [43]. However, most GI diseases can be prevented or cured in a timely fashion if the diagnosis occurs at early stages. For this reason, GI screening is playing an increasingly important role in healthcare systems worldwide [44, 45]. The preferred method for GI screening is flexible endoscopy, which provides the physician with both diagnostic and therapeutic capabilities. Unfortunately, its application is sometimes limited due to its invasiveness, patient intolerance, and the need for sedation. These disadvantages are severe enough that a relevant portion of the population at risk forgo or avoid recommended screening [44].

During the past decade, WCE was established as a patient-friendly procedure for diagnosis of diseases in the small intestine [46]. Specific WCEs (11 mm in diameter, 31 mm in length) have been proposed for colon inspection, but have not reached the diagnostic accuracy of standard colonoscopy [47, 48]. One of the main limitations of commercially available WCEs is passive locomotion [49]. It is desirable for the endoscopist to be able to controllably maneuver the capsule rather than relying on peristalsis to drive it for adequate visualization of GI mucosa. For this reason, a relevant number of technical solutions have been recently proposed to provide WCE with active locomotion, the most promising being remote magnetic manipulation [2, 26–33].

The algorithms presented in this paper enable the WCE to be localized at a fast refresh rate (i.e., below 10 ms including sensor data acquisition) without the need for line-of-sight. This represents a relevant step toward closed-loop feedback control of magnetically actuated WCEs, where the magnet used for actuation is manipulated by a commercial robot having an average control rate of 100 Hz [28]. Real-time localization is crucial for reliable robotic manipulation and can prevent sudden failures of magnetic coupling between the source of the magnetic field and the WCE during the endoscopic procedure.

C.4 Method

C.4.1 Iterative Method for Magnetic Localization

Our localization approach is inspired by Jacobian-based methods (also known as resolved rates methods stemming from [96]). These methods are commonly used in robotics to solve systems of nonlinear equations subject to the limitations of first-order linearization. In this paper, we assume that the refresh rate for pose tracking is fast enough that only small movements of the WCE may occur between subsequent pose measurements.

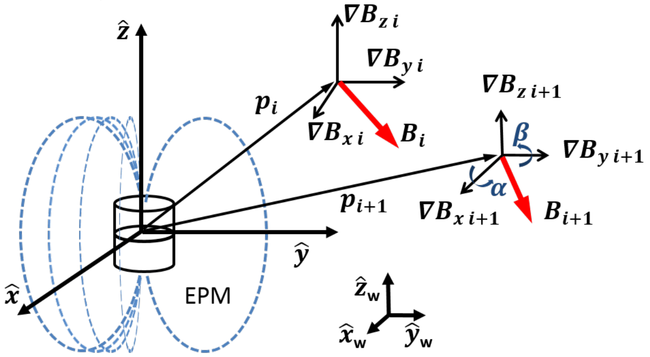

Figure C.1: Schematic representation of the source of magnetic field (External Permanent Magnet (EPM) in figure) and two sequential positions (i.e., $\mathbf{p}_i$ and $\mathbf{p}_{i+1}$) of the capsule to be localized. α and β are the capsule's orientational angles yaw and pitch.

In order to apply an iterative method to magnetic localization, we need to consider the magnetic field, generated by a known source, as the following time-invariant non-linear mathematical expression:

$$\mathbf{B}_i = f(\mathbf{p}_i) \qquad f(\mathbf{p}_i) : \mathbb{R}^3 \rightarrow \mathbb{R}^3. \tag{C.1}$$

This equation will be denoted as Magnetic Direct Relationship (MDR). Referring to Fig. F.9, the MDR associates the coordinates of a point outside the magnetic field source $\mathbf{p}_i = [x_i, y_i, z_i]^T$ to a corresponding vector function of magnetic field values $\mathbf{B}_i = [B_{ix}, B_{iy}, B_{iz}]^T$.

If the capsule position changes from $\mathbf{p}_i$ to $\mathbf{p}_{i+1}$ during a time increment Δt, the displacement $\Delta\mathbf{p}$ produces a change in the magnetic field measurements from $\mathbf{B}_i$ to $\mathbf{B}_{i+1}$ according to (C.1). The partial derivative of the magnetic field vector, $\frac{\partial}{\partial p}\mathbf{B}_i$, is given by:

$$\frac{\partial \mathbf{B}_i}{\partial \mathbf{p}} = \bigtriangledown_p f(\mathbf{p}_i) = \begin{bmatrix} \frac{\partial \mathbf{B}_x}{\partial p_x} & \frac{\partial \mathbf{B}_x}{\partial p_y} & \frac{\partial \mathbf{B}_x}{\partial p_z} \\ \frac{\partial \mathbf{B}_y}{\partial p_x} & \frac{\partial \mathbf{B}_y}{\partial p_y} & \frac{\partial \mathbf{B}_y}{\partial p_z} \\ \frac{\partial \mathbf{B}_z}{\partial p_x} & \frac{\partial \mathbf{B}_z}{\partial p_y} & \frac{\partial \mathbf{B}_z}{\partial p_z} \end{bmatrix}. \tag{C.2}$$

where $\bigtriangledown_p f(\mathbf{p}_i)$ designates the gradient of each scalar function in f with respect to $\mathbf{p}$. Using (C.2) in a first-order Taylor series approximation, we obtain:

$$\mathbf{B}_{i+1} = \mathbf{B}_i + \frac{\partial \mathbf{B}_i}{\partial \mathbf{p}}\Delta\mathbf{p} = \mathbf{B}_i + \bigtriangledown_p f(\mathbf{p}_i)\Delta\mathbf{p}. \tag{C.3}$$

The Magnetic Inverse Relationship (MIR), providing the current capsule position $\mathbf{p}_{i+1}$, can be derived by inverting (C.3):

$$\mathbf{p}_{i+1} = \mathbf{p}_i + \bigtriangledown_p f^{-1}(\mathbf{p}_i)\Delta\mathbf{B}_i. \tag{C.4}$$

Moving from differential to the finite difference iterative method, $\frac{\partial \mathbf{B}}{\partial p}\Delta\mathbf{p}$ is replaced by $\Delta\mathbf{B}_i$, where $\Delta\mathbf{B}_i$ is defined as $\Delta\mathbf{B}_i = (\mathbf{B}_{i+1} - \mathbf{B}_i)$. Also, according to [97], the gradient of a generic vectorial function, which is defined as $f(\mathbf{x}) : \mathbb{R}^n \to \mathbb{R}$, is the transpose of the Jacobian as: $\bigtriangledown_x f(\mathbf{x}) = (\mathbf{J}_x f(\mathbf{x}))^t$. Then, (C.4) becomes:

$$\mathbf{p}_{i+1} = \mathbf{p}_i + \mathbf{J}_p^{-1}\Delta\mathbf{B}_i, \tag{C.5}$$

where $\mathbf{J}_p^{-1}$ is the inverse of the Jacobian.

An explicit formulation of the MDR (C.1) can be obtained by finite element integration of magnetic field models, as suggested in [98], while a numerical estimate can be provided by a standard finite element method (FEM) software package, such as Comsol Multiphysics or ANSYS Maxwell. In the next subsections, we introduce a non-linear interpolation method for a data-set of magnetic field values related to the position $\mathbf{p}_i$. Then, the interpolation is used to provide an analytical expression of the MDR through modal representation, numerical algebra theory, and the Kronecker product. Finally, a first order resolved rates method using the Jacobian expression for the MIR is derived.

In Fig. C.2 is represented the proposed magnetic pose detection algorithm exploiting sensor fusion of magnetic field and inertial measurements. The magnetic field interpolation (also called magnetic field calibration) is achieved off-line, which leads to obtain the characteristic matrices $\mathbf{A}_r$ and $\mathbf{A}_z$. Once the interpolation is obtained the on-line algorithm takes as input the magnetic field, inertial measurements and the External Permanent Magnet (EPM) orientation, returning the capsule pose. The capsule position is referred to the EPM frame whereas the orientation expressed in Euler angles is relative to the world frame. The blocks DMR-IMR –which stand for Direct and Inverse Magnetic Relationship– and the Iterative Jacobian Method are presented in Section C.4.2, the three dimensional reconstruction is presented in Section C.4.3

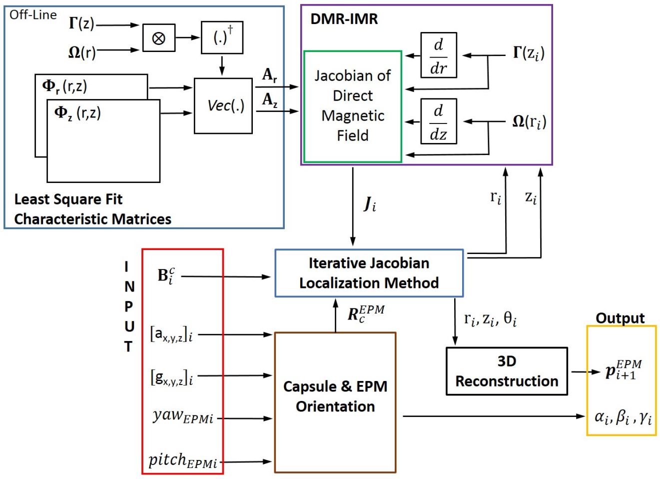

Figure C.2: Block diagram of the proposed iterative algorithm for WCE's pose detection. In the schematic are displayed system's input, output, Jacobian of the MDR, 3D reconstruction and the off-line least square fit calibration, which lead to the characteristic matrices $\mathbf{A}_r$ and $\mathbf{A}_z$.

C.4.2 Direct and Inverse Magnetic Relationship

The magnetic field of a cylindrical axially-magnetized permanent magnet exhibits cylindrical symmetry around its main axis ($\hat{\mathbf{z}}$) [90, 91]. If such a magnet is used as the external source of a magnetic field for capsule manipulation, as suggested in our previous work [32, 68], the localization can take advantage of the symmetry to reduce the computational burden. In particular, the three-dimensional position tracking problem can be reduced to two dimensions (2D). Then, once the position in 2D is obtained, the third coordinate can be derived by sensor fusion as explained in Section C.4.3.

As represented in Fig. C.3, the magnetic field is distributed around the main axis of symmetry of the EPM, $\hat{\mathbf{z}}$, while B_θ – angular component of the magnetic field along θ –

is null. The vector $\tilde{\mathbf{p}}_c = [r, \theta, z]^t$ represents a generic point on the loci of points, whose location satisfies the condition of having the same magnetic field $\mathbf{B}_c$. This set of points of the locus generates a circumference Υ (represented in Fig. C.3) that can be analytically described as $\Upsilon = [r, \theta, z] | r, z = const \in \mathbb{R}, \, and \; \theta \in 0 \rightarrow 2\pi$. We refer to $\tilde{\mathbf{p}}_c = [r, \theta, z]^t$ as the generic point on the loci, which is expressed in the three cylindrical coordinates, whereas $\mathbf{p}_c$ lies on the plane $\mathcal{H}$ and is obtained by applying a rotation about $\hat{\mathbf{z}}$ to $\tilde{\mathbf{p}}_c$. The plane $\mathcal{H}$ is defined as: $\mathcal{H} = \mathbb{R}^2 : \{(r, z) | r, z \in \mathbb{R} \; and \; \theta = 0\}$.

Considering the magnetic field applied on a generic point $\tilde{\mathbf{p}}_c$, its components are expressed as $\mathbf{B}_c = [B_r(r, z), B_\theta(r, z), B_z(r, z)]$, where $B_\theta(r, z) = 0$. Therefore, (C.1) could be furthermore simplified by defying the mathematical representation Ψ for the magnetic field $\mathbf{B}_c$. The magnetic field $\mathbf{B}_c$ is given by the two-dimensional transformation Ψ for any given point $\tilde{\mathbf{p}}_c$ around the magnetic field source, such as $\Psi : \tilde{\mathbf{p}}_c \rightarrow \mathbf{B}_c$. $B_r(r, z)$ and $B_z(r, z)$ are two scalar values representing the radial and the axial component of the magnetic field vector, which are functions of axial and radial spatial coordinates with respect to the center of the EPM.

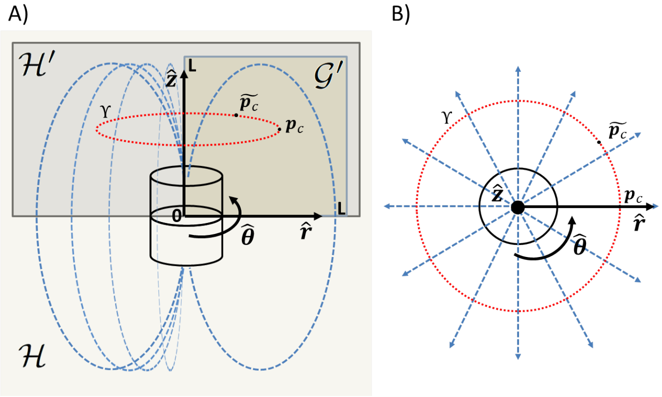

Figure C.3: Schematic view of the magnetic field distribution for a cylindrical axially-magnetized permanent magnet. (A) View of the $\mathcal{H}$ planes, its subset $\mathcal{H}'$ and the domain $\mathcal{G}'$, (B) shows the radial distribution of the magnetic field on the plane $[\hat{r}, \hat{\theta}]$.

The solution to the system of equations expressed by the transformation Ψ – in terms of both radial $B_r(r, z)$ and axial $B_z(r, z)$ magnetic field – is unique in the semi-domain $\mathcal{H}'$ defined as in Fig. C.3 (note that the semi-domain $\mathcal{H}'$ can be either related to the south or the north pole of the cylindrical axially-magnetized EPM). Then, we define a finite domain $\mathcal{G}'$, where the magnetic field radial component B_r is always positive. On the other hand, if considering the domain $\mathcal{H}$, the transformation Ψ leads to two solutions in diagonally opposite quadrants in Fig. C.3. Since the patient cannot be simultaneously above and below the magnet, we exclude one quadrant for practical implementation reasons. The region is a square plane having size L along $\hat{\mathbf{r}}$ and $\hat{\mathbf{z}}$, where the spatial transformation $f(\mathbf{p}_c)$ in (C.1) is simplified and solvable as

$$\begin{gathered}\Psi(\mathbf{p}_c) : \mathrm{I\!R}^2 \rightarrow \mathrm{I\!R}^2 \\ where : \mathbf{p}_c \in \mathcal{G}' : \mathcal{G}' = \{(r, z) \in [0, L]\}\end{gathered} . \tag{C.6}$$

The transformation $\Psi(\mathbf{p}_c)$ can be expressed by two scalar mathematical functions, each with two inputs. The two functions provide the magnetic field radial component as

$$B_r = \psi_r(r, z) : \mathrm{I\!R}^2 \rightarrow \mathrm{I\!R}, \tag{C.7}$$

and the magnetic field axial component as

$$B_z = \psi_z(r, z) : \mathrm{I\!R}^2 \rightarrow \mathrm{I\!R}. \tag{C.8}$$

The numerical solution of (C.7) and (C.8) can be obtained by either applying the Current Density Magnetic Model (CuDMM) or the Charge Density Magnetic Model (ChDMM), as demonstrated in [90, 91]. Then, the magnetic field values can be casted in two data matrices $\mathbf{\Phi}_r \in \mathrm{I\!R}^{m \times p}$ and $\mathbf{\Phi}_z \in \mathrm{I\!R}^{m \times p}$. These matrices represent the $m \times p$ magnetic field numerical solutions for any given position $\mathbf{p}_c$ within $\mathcal{G}'$, where m is the number of magnetic field measurements taken along the $\hat{\mathbf{r}}$ direction and p is the number of magnetic field measurements taken along $\hat{\mathbf{z}}$. The collection of numerical solutions $[\mathbf{\Phi}_r, \mathbf{\Phi}_z]^T$ of (C.7) and (C.8), are expressed as in (C.9) and (C.10).

$$\begin{gathered}\mathbf{\Phi}_r = [\Phi_{rij}(r_i, z_j)] \\ i \in \mathrm{I\!N} : [1 \leq i \geq m]; j \in \mathrm{I\!N} : [1 \leq j \geq p].\end{gathered} \tag{C.9}$$

$$\begin{gathered}\mathbf{\Phi}_z = [\Phi_{zij}(r_i, z_j)] \\ i \in \mathrm{I\!N} : [1 \leq i \geq m]; j \in \mathrm{I\!N} : [1 \leq j \geq p].\end{gathered} \tag{C.10}$$

where $\mathbf{\Phi}_{rij}$ and $\mathbf{\Phi}_{zij}$ are the magnetic field values at position (i, j), which could be generally expressed as $\mathbf{\Phi}_{ij}$. The single matrix element $\mathbf{\Phi}_{ij}$ can be approximated by applying the modal representation defined in [99–101] as

$$\begin{gathered}\mathbf{\Phi}_{ij} = \mathbf{B}_i(r, z) = \boldsymbol{\omega}(r)^T \mathbf{a}(z), \\ where : (\mathbf{a}, \boldsymbol{\omega}) \in \mathrm{I\!R}^n.\end{gathered} \tag{C.11}$$

The vector of the modal factors, $\mathbf{a}(z)$, can be expressed as

$$\begin{gathered}\mathbf{a}(z) = \mathbf{A}\boldsymbol{\gamma}(z), \\ where : (\mathbf{A}, \boldsymbol{\gamma}) \in \mathbb{R}^n.\end{gathered} \tag{C.12}$$

In this equation, $\mathbf{A}$ is the characteristic matrix of coefficients for the particular magnetic field shape, which together with the two orthogonal bases, $\boldsymbol{\omega} = \{\omega_0, \omega_1, ..., \omega_n\}$ and $\boldsymbol{\gamma} = \{\gamma_0, \gamma_1, ..., \gamma_q\}$, represents the interpolation functions that best numerically approximate the transformation $\mathbf{\Phi}_{ij}$ over the domain of interest [102]. Once the interpolation functions $\boldsymbol{\omega}$ and $\boldsymbol{\gamma}$ are chosen (Section C.6.1), and the characteristic matrices of coefficients $\mathbf{A}_r$ and $\mathbf{A}_z$ for radial and axial magnetic field respectively are derived, the interpolation problem can be easily solved. The best data-set interpolation is chosen by adopting the orthogonal function that minimizes the least square error between the reference measure $f(x)$ and the approximated value y^*, such as $||f(x) - y^*|| < \delta$. Examples of orthogonal functions investigated in this study include standard polynomial functions, Chebyshev polynomials [100, 101], Fourier harmonic basis [102, 103] and composition of these.

In the following paragraph, we describe how to derive the characteristic matrices of coefficients $\mathbf{A}_r$ and $\mathbf{A}_z$ for the algebraic equations system in (C.11) and (C.12) by using the following matrix representation, as suggested in [100, 101]:

$$\mathbf{\Phi} = \mathbf{\Omega}_{m\times n}\mathbf{A}_{n\times q}\mathbf{\Gamma}_{q\times p}, \tag{C.13}$$

where $\mathbf{\Phi}$ is either the MDR solutions of $\mathbf{\Phi}_r$ or $\mathbf{\Phi}_z$ within $r, z \in [0 \to L]$, while $\mathbf{\Omega}$ and $\mathbf{\Gamma}$ are the modal basis matrices and constitute the collection of n orthogonal basis for $\mathbf{\Omega}$ and q orthogonal basis for $\mathbf{\Gamma}$. Finally, m and p are the number of values estimated in the domain $r \in [0, L]$ and $z \in [0, L]$, respectively.

The solutions for $\mathbf{A}_r$ and $\mathbf{A}_z$ can be obtained by applying the Kronecker product theory as in [100, 101, 104], where the symbol $\otimes$ represents the Kronecker product of two matrices:

$$Vec(\mathbf{\Phi}) = [\mathbf{\Gamma}^T \otimes \mathbf{\Omega}]\, Vec(\mathbf{A}). \tag{C.14}$$

The result provided by the algebraic interpolation is the generic matrix of coefficients $\mathbf{A}$, which is given by

$$\begin{gathered}Vec(\mathbf{A}) = [\mathbf{\Gamma}^T \otimes \mathbf{\Omega}]^\dagger\, Vec(\mathbf{\Phi}), \\ where :\ Vec(\mathbf{A}) = [a_{11}...a_{n1}...a_{n2}...a_{np}]^T.\end{gathered} \tag{C.15}$$

Once the matrices $\mathbf{A}_r$ and $\mathbf{A}_z$ are known, the MDR, such as $\psi(z, y) : (z, y) \to (\Phi_{ij})$, is solved for any point within the domain $\mathcal{G}' = \{(r, z) \in [0, L]\}$.

Given the calibration matrices $\mathbf{A}_r$ and $\mathbf{A}_z$, and the orthogonal basis $\boldsymbol{\omega}(r)$ and $\boldsymbol{\gamma}(z)$, the system of equation expressed in (C.11) and (C.12) is completely determined. By differentiating $\boldsymbol{\omega}(r)$ and $\boldsymbol{\gamma}(z)$ in ∂r and ∂z, respectively, we can obtain the complete formulation of the MIR in (C.2). The following system of equations – expressed for the single solution $[\boldsymbol{\Phi}_r, \boldsymbol{\Phi}_z]^T$ – provides the ground to derive the Jacobian:

$$\begin{cases} \boldsymbol{\Phi}_r = \boldsymbol{\omega}(r)\mathbf{A}_r\boldsymbol{\gamma}(z) \\ \boldsymbol{\Phi}_z = \boldsymbol{\omega}(r)\mathbf{A}_z\boldsymbol{\gamma}(z) \end{cases} \tag{C.16}$$

Applying (C.2) to this system of equations, and deriving the partial derivatives of $\boldsymbol{\Phi} = [\boldsymbol{\Phi}_r, \boldsymbol{\Phi}_z]^T$ such as $\frac{\partial \boldsymbol{\Phi}_r}{\partial r}, \frac{\partial \boldsymbol{\Phi}_r}{\partial z}, \frac{\partial \boldsymbol{\Phi}_z}{\partial r}, \frac{\partial \boldsymbol{\Phi}_z}{\partial z}$, the gradient of $\boldsymbol{\Phi}$ becomes

$$\nabla\boldsymbol{\Phi} = \begin{cases} \nabla\boldsymbol{\Phi}_r = \frac{\partial(\boldsymbol{\omega}(r)\mathbf{A}_r\boldsymbol{\gamma}(z))}{\partial r} + \frac{\partial(\boldsymbol{\omega}(r)\mathbf{A}_r\boldsymbol{\gamma}(z))}{\partial z} \\ \nabla\boldsymbol{\Phi}_z = \frac{\partial(\boldsymbol{\omega}(r)\mathbf{A}_z\boldsymbol{\gamma}(z))}{\partial r} + \frac{(\partial\boldsymbol{\omega}(r)\mathbf{A}_z\boldsymbol{\gamma}(z))}{\partial z} \end{cases} \tag{C.17}$$

Considering that the derivatives of the constant coefficient matrices $\mathbf{A}_r$ and $\mathbf{A}_z$ are null, as well as $\frac{\partial\boldsymbol{\omega}(r)}{\partial z}$ and $\frac{\partial\boldsymbol{\gamma}(z)}{\partial z}$, (C.17) simplifies to:

$$\begin{aligned} \frac{\partial \boldsymbol{\Phi}_r}{\partial r} &= \frac{\partial\boldsymbol{\omega}(r)}{\partial r}\mathbf{A}_r\boldsymbol{\gamma}(z) \\ \frac{\partial \boldsymbol{\Phi}_r}{\partial z} &= \boldsymbol{\omega}(r)\mathbf{A}_r\frac{\partial\boldsymbol{\gamma}(z)}{\partial z} \\ \frac{\partial \boldsymbol{\Phi}_z}{\partial r} &= \frac{\partial\boldsymbol{\omega}(r)}{\partial r}\mathbf{A}_z\boldsymbol{\gamma}(z) \\ \frac{\partial \boldsymbol{\Phi}_z}{\partial z} &= \boldsymbol{\omega}(r)\mathbf{A}_z\frac{\partial\boldsymbol{\gamma}(z)}{\partial z} \end{aligned} \tag{C.18}$$

In order to obtain the expression of $\frac{\partial\boldsymbol{\omega}(r)}{\partial r}$ and $\frac{\partial\boldsymbol{\gamma}(z)}{\partial z}$, a derivation is applied to the vectors constituting the orthogonal basis $\omega(r), \gamma(z)$. This leads to the following expression for the Jacobian $\mathbf{J}_\Phi$:

$$\mathbf{J}_\Phi = \bigtriangledown_{\tilde{p}_c}\boldsymbol{\Phi}(r,z) = \begin{bmatrix} \frac{\partial\Phi_r}{\partial r} & \frac{\partial\Phi_r}{\partial z} \\ \frac{\partial\Phi_z}{\partial r} & \frac{\partial\Phi_z}{\partial z} \end{bmatrix} \tag{C.19}$$

Therefore, the magnetic field vector incremental difference $\Delta\mathbf{B}_i = [\Delta B_r, \Delta B_z]_i^T$ is given by

$$\Delta\mathbf{B}_i = \begin{bmatrix} \Delta B_r \\ \Delta B_z \end{bmatrix}_i = \mathbf{J}_\Phi\Delta\mathbf{p}_{ci} \tag{C.20}$$

This result can be used in (C.3) to estimate the magnetic field $\mathbf{B}_{i+1}$ by continuously updating $\Delta\mathbf{B}_i$ to the current magnetic field value:

$$\mathbf{B}_{i+1} = \mathbf{B}_i + \Delta\mathbf{B}_i = \mathbf{B}_i + \mathbf{J}_\Phi\Delta\mathbf{p}_{ci}. \tag{C.21}$$

In conclusion, the following equation shows the iterative method to localize the WCE, estimating the current position $\mathbf{p}_{ci+1} = [r_{i+1}, z_{i+1}]^T$ of the capsule as

$$\mathbf{p}_{ci+1} = \mathbf{p}_{ci} + \Delta\mathbf{p}_{ci} = \mathbf{p}_{ci} + \mathbf{J}_{\Phi}^{-1}\Delta\mathbf{B}_i, \tag{C.22}$$

where $\mathbf{J}^{-1}$ is the inverse of the Jacobian, which applies the least squares method of optimization to the solution [105]. The term $\Delta\mathbf{B}_i$ is the difference in magnetic field recorded from the previous measurement.

C.4.3 Three Dimensional Reconstruction

In order to track the WCE by applying the iterative algorithm, both the spatial orientation of the capsule and the external magnetic source pose must be known with respect to a common reference frame. The magnetic field vector $\mathbf{B}_c$ at the capsule position $\tilde{\mathbf{p}}_c$ – expressed in the capsule frame $[\hat{\mathbf{x}}_c, \hat{\mathbf{y}}_c, \hat{\mathbf{z}}_c]$ – is measured by the onboard sensors. This vector can be expressed in the EPM frame $[\hat{\mathbf{x}}, \hat{\mathbf{y}}, \hat{\mathbf{z}}]$ by applying the geometrical transformation $\mathbf{R}_c^{EPM}$, thus obtaining $\mathbf{B}$.

Then, considering Figs. F.9 and C.3, the magnetic field vector $\mathbf{B}$ is expressed in cylindrical coordinates from its cartesian coordinates, such as: $\mathbf{B} = [B_x, B_y, B_z]^T \rightarrow [B_r, B_z]^T$ *and* θ, where θ correspond to the azimuthal coordinate of the capsule position $\tilde{\mathbf{p}_c}$. The relationships that transform the magnetic field vector $\mathbf{B}_c = [B_x\hat{\mathbf{x}}, B_y\hat{\mathbf{y}}, B_z\hat{\mathbf{z}}]$ from cartesian to cylindrical coordinates are:

$$\begin{aligned} &\mathbf{B}_r = \sqrt{(B_x\hat{\mathbf{x}})^2 + (B_y\hat{\mathbf{y}})^2}\ \hat{\mathbf{r}} \\ &\mathbf{B}_z = B_z\hat{\mathbf{z}} \\ &\boldsymbol{\theta} = atan2(B_y, B_x)\hat{\boldsymbol{\theta}} \end{aligned} \tag{C.23}$$

where B_x, B_y, B_z are the cartesian components of the magnetic field vector $\mathbf{B}$ with respect to the EPM frame $[\hat{\mathbf{x}}, \hat{\mathbf{y}}, \hat{\mathbf{z}}]$. The axial and radial magnetic field components can be fed into the iterative algorithm, which derives the radial and axial coordinates of the capsule $\mathbf{p}_c = [p_r, p_z]$. These can be used in combination with $\boldsymbol{\theta}$ to derive the three cartesian coordinates as follows:

$$\begin{aligned} &\mathbf{p}_x = p_r cos(\theta)\hat{\mathbf{x}} \\ &\mathbf{p}_y = p_r sin(\theta)\hat{\mathbf{y}} \\ &\mathbf{p}_z = p_z\hat{\mathbf{z}} \end{aligned} \tag{C.24}$$

C.5 Capsule Orientation Algorithm

This section presents the algorithm used to detect the change in capsule orientation and to generate the rotational matrix $\mathbf{R}_c$ with respect to the global frame. This algorithm based on the fusion of inclinometer and gyroscope outputs is widely adopted in literature and is provided here for the sake of completeness. The capsule orientation knowledge is required in our magnetic localization approach in order to express the magnetic field vector $\mathbf{B}_c$ in the EPM frame.

Referring to Fig. F.9, the accelerometer can be used as an inclinometer to obtain the absolute values of the two orientational angles α and β [92]. The rotations about $\mathbf{x}_c$ and $\mathbf{y}_c$ are derived directly from the gravitational vector $\mathbf{g}$ projection mapped on the three orthogonal axes of the onboard accelerometer as

$$\begin{aligned} \boldsymbol{\alpha} &= atan2(a_y, \sqrt{a_x^2 + a_z^2}) \\ \boldsymbol{\beta} &= atan2(a_x, \sqrt{a_y^2 + a_z^2}) \end{aligned} \tag{C.25}$$

where a_x, a_y, a_z are the three accelerometer outputs.

A number of methods for inertial navigation can be adopted to estimate the third orientation angle $\boldsymbol{\gamma}$, which is the rotational angle along the gravitational vector $\mathbf{g}$. Examples span from fusing gyroscope and inclinometer measurements [93,94] to applying a quaternion-based algorithm to inertial data [95]. The approach we have adopted involves applying the axis-angle method for rotational matrices to the gyroscope outputs [199]. Briefly, it is possible to extract the rotation $\boldsymbol{\gamma}$ about the global axis $\mathbf{z}_w$ by building the rotational matrix $\Delta\mathbf{R}_c$ with respect to the moving frame attached to the capsule $[\hat{\mathbf{x}}_c, \hat{\mathbf{y}}_c, \hat{\mathbf{z}}_c]$. The instantaneous variations in capsule orientation can be derived from the gyroscope outputs as

$$\Delta\alpha_c = g_x \Delta t \qquad \Delta\beta_c = g_y \Delta t \qquad \Delta\gamma_c = g_z \Delta t \tag{C.26}$$

where $\Delta[\alpha_c, \beta_c, \gamma_c]$ are the instantaneous angle variations at the capsule moving frame within a measurement loop that lasts Δt. The instantaneous capsule rotational matrix $\Delta\mathbf{R}_c$ is then defined as

$$\Delta\mathbf{R}_c = \mathbf{R}_x(\Delta\alpha_c)\mathbf{R}_y(\Delta\beta_c)\mathbf{R}_z(\Delta\gamma_c) \tag{C.27}$$

where $\mathbf{R}_x, \mathbf{R}_y, \mathbf{R}_z$ are the rotational matrixes with respect to the $\mathbf{x}_c$, $\mathbf{y}_c$, and $\mathbf{z}_c$ axis, respectively. Then, the axial-angle representation of the rotational matrix $\Delta\mathbf{R}_c$ is derived, thus achieving the angle of rotation θ and the axis of rotation ω:

$$\begin{aligned} \theta &= arccos\left(\tfrac{trace(\Delta\mathbf{R}_c)-1}{2}\right) \\ \omega &= \tfrac{1}{2sin(\theta)} \textstyle\sum_{j=1}^{3} \left(\hat{\mathbf{e}}_{c_j,i} \times \hat{\mathbf{e}}_{c_j,i+1}\right) \end{aligned} \tag{C.28}$$

where $\hat{\mathbf{e}}_{c_j,i}$ and $\hat{\mathbf{e}}_{c_j,i+1}$ are the unit vectors of the capsule frame at the *i-th* and *(i+1)-th* iterations respectively. Finally, the axis-angle representation θ, ω must be reoriented according to the capsule orientation with respect to the global frame at the previous time step, $\mathbf{R}_c^{t-1}$. The third coordinate of the axial-angle representation corresponds to the capsule angle variation $\Delta\gamma$ about $\hat{\mathbf{z}}_w$. The capsule absolute orientation γ about the global axis $\hat{\mathbf{z}}_w$ is achieved by summation of $\Delta\gamma$ at each loop.

C.6 Simulation-Based Validation

The proposed approach was validated using a NdFeB cylindrical EPM with an axial N52-grade magnetization, a diameter of 5 cm, and a length of 5 cm. The size L of the squared domain $\mathcal{G}'$ was fixed at 15 cm. The reference values for the magnetic field in $\mathcal{G}'$ were obtained using Comsol Multiphysics, using a pitch of 0.2 mm for the mesh. The mathematical analysis and simulations were performed by using MATLAB, MathWorks Inc.

C.6.1 Magnetic Direct Relationship

Comsol Multiphysics was also used to create the 15 × 15 matrix $\mathbf{\Phi}_r$ and the 18 × 18 matrix $\mathbf{\Phi}_z$ relative to the radial and axial components of the magnetic field, respectively. These two matrices were interpolated by using two orthogonal bases $\boldsymbol{\omega} = \{\omega_0, \omega_1, ..., \omega_n\}$, $\boldsymbol{\gamma} = \{\gamma_0, \gamma_1, ..., \gamma_p\}$, chosen as the composition of a 12^{th} order Fourier Harmonic basis ($u = 12$) and a 5^{th} order polynomial basis ($v = 5$). The modal basis functions were chosen based on simulation of the approximation residue with the minimum number of terms that provide a relative error of less than 10% within a portion of at least 70% of the domain $\mathcal{G}'$. These modal functions are:

$$\begin{array}{l} \boldsymbol{\omega}(r) = \left[\begin{array}{cccccc} 1/2 & ... & \cos(\frac{\pi u r}{L}) & \sin(\frac{\pi u r}{L}) & ... & r^v \end{array} \right] \\ \boldsymbol{\gamma}(z) = \left[\begin{array}{cccccc} 1/2 & ... & \cos(\frac{\pi u z}{L}) & \sin(\frac{\pi u z}{L}) & ... & z^v \end{array} \right] \end{array}. \tag{C.29}$$

Both $\mathbf{A}_r$ and $\mathbf{A}_z$ were derived applying (C.15), thus obtaining 31 × 31 matrices. The interpolation was obtained by applying (C.11) and (C.12) to any radial and axial coordinate of the domain $\mathcal{G}'$. The interpolation error was evaluated by comparing the interpolated magnetic field with the reference values derived by Comsol Multiphysics. Given the position vector $\mathbf{p}_{ci} = [r, z]_i^T$ within $\mathcal{G}'$, Fig. C.4-a shows the module of the relative error for the radial magnetic field component, while Fig. C.4-b shows the module of the relative error for the axial component. Table C.1 reports the portions of $\mathcal{G}'$ where the interpolation error is below 1%, 5%, 10%, and 20% for both the axial and the radial component of the magnetic field. The radial component estimation presents a relative error below 10% for the 86% of the radial magnetic field map. The axial component estimation shows that the 70% of the axial

Table C.1: Portions of $\mathcal{G}'$ showing different levels of relative error in the interpolated magnetic field from the proposed method and the single magnetic dipole model.

Level of relative error	Radial Component	Axial Component
Below 1%	42%	30%
Below 5%	78%	61%
Below 10%	86%	70%
Below 20%	92%	79%
Magnetic dipole model		
Below 1%	12%	0.4%
Below 5%	63%	2%
Below 10%	81%	5%
Below 20%	90%	10%

magnetic field map presents a relative error below 10%. Whenever the value of magnetic field intensity is very small, or null, a small approximation noise leads to a high relative error, as it is shown in Fig. C.4. These results show an efficient estimation of both B_r and B_z, thus allowing the MDR to be analytically derived via (C.16).

Fig. C.5 shows the ratio of the relative error of the single dipole model to the relative error of our interpolation method where the relative error is calculated with respect to the reference values derived by Comsol Multiphysics. The blue regions –ratio between 0 and 1– of the maps correspond to a similar or better performance of interpolation for the dipole model comparing with the proposed method. The dark red regions correspond to ratio greater than 8. Table C.1 reports the portions of $\mathcal{G}'$ where the interpolation error of the dipole model is below 1%, 5%, 10%, and 20% for both the axial and the radial component of the magnetic field.

C.6.2 Magnetic Inverse Relationship

The pose detection iterative method based on (C.22) was assessed by simulating the capsule motion along a spiral path, starting from a central position in the map $\mathbf{p}_c \approx [0.09, 0.055]m$ and reaching a final diameter of 1 cm. Fig. C.6 shows the reference trajectory and its pose estimation. The color map represents the relative error of the radial coordinate. The estimation of the simulated capsule pose results in an axial coordinate relative error below 1%, with respect to its current position, for almost the entire simulation. The radial coordinate relative error is below 1% for the upper-right, lower-left and lower-right quadrants of the spiral path represented in Fig. C.6. The upper-left quadrant presents a relative error below 5%. The ellipsoid of localization uncertainty due to magnetic

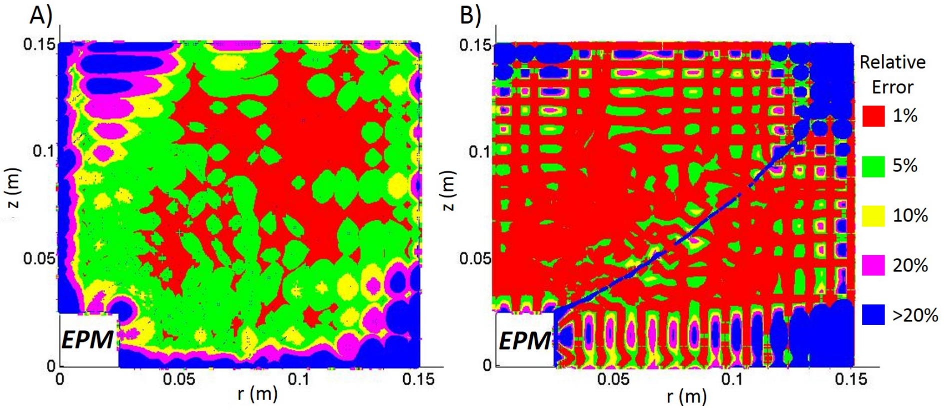

Figure C.4: Relative error for the radial (A) and axial (B) magnetic field estimated by the MDR within $\mathcal{G}'$.

field sensor noise is represented by the cyan ellipses. The magnetic field sensors noise for the measurements of B_r and B_z are ±0.08 and ±0.05 mT respectively. Overall, this simulation shows an average sub-millimeter localization accuracy for both the radial and axial component.

C.7 Experimental Assessment

C.7.1 Experimental Platform

C.7.1.1 Hardware

The experimental platform, represented in Fig. C.7.A, is composed of the WCE, the EPM, a robotic manipulator (RM), and a personal computer (PC) connected to a wireless transceiver via the universal serial bus (USB) port. The real-time algorithm runs on the PC and communicates with the capsule through a USB transceiver. The EPM is an NdFeB (magnetization N52, magnetic remanence 1.48 T) cylindrical permanent magnet with axial magnetization. The EPM diameter and length are both equal to 50 mm, while the mass is 772 g. A six-DOF robot (RV6SDL, Mitsubishi Corp., Japan) mounts at its end-effector the EPM. The robot is controlled in real time through a multi-thread C++ software application, which is described in section C.7.1.3. The manipulator is used to control and track the EPM position and orientation with respect to the global reference frame $[\hat{\mathbf{x}}_w, \hat{\mathbf{y}}_w, \hat{\mathbf{z}}_w]$, which is assumed to be superimposed on the manipulator ground frame $[\hat{\mathbf{x}}_0, \hat{\mathbf{y}}_0, \hat{\mathbf{z}}_0]$. The current EPM pose for the localization algorithm is derived from the robot end-effector pose, which is available at the application interface level with a resolution of $2{\times}10^{-2}$ mm in position and $1{\times}10^{-3}$ degree in orientation. The EPM orientation frame $[\hat{\mathbf{x}}, \hat{\mathbf{y}}, \hat{\mathbf{z}}]$ is an input for the localization algorithm (as described in section C.4.3), while the EPM pose, as acquired by the robot encoders, is used as a reference position for the experimental assessment. A

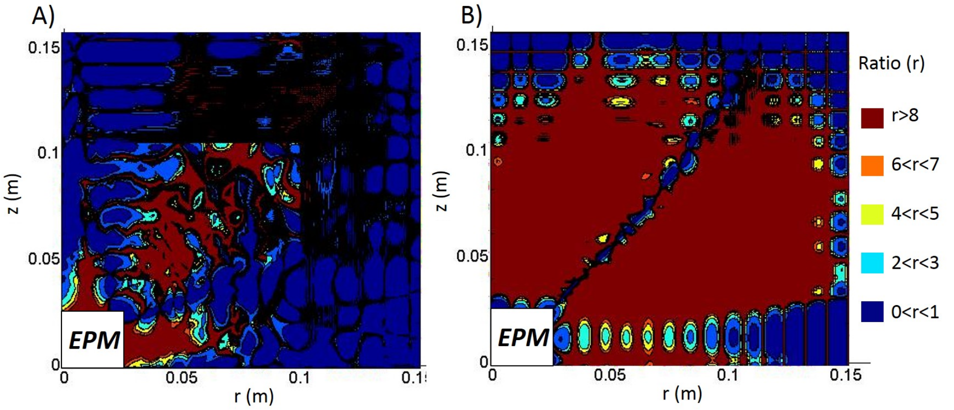

Figure C.5: The ratio of relative errors of the single dipole model to the interpolation model for the radial (A) and axial (B) magnetic field components. Black regions stem from visualization artifacts due to oscillations in the ratio from 3 to 8 times.

load cell (MINI 45, ATI Industrial Automation, USA), mounted in between the EPM and the RM, allows the EPM to be moved via admittance control for the general assessment described in Section C.7.2.3.

C.7.1.2 Wireless Capsule

The WCE, schematically represented in Fig. C.7.B, hosts the Force and Motion Sensing Module (FMSM), which was presented in [32], Wireless MicroController (WMC), and Power Supply (PS). The outer shell is fabricated in VeroWhite 3D printer material (OBJET 30, Stratasys, USA). The current prototype is 36 mm in length, 17.5 mm in diameter, and 15 g in mass. The capsule shell has four lateral wings that are used as a reference to achieve a precise alignment for the capsule frame $[\hat{\mathbf{x}}_c, \hat{\mathbf{y}}_c, \hat{\mathbf{z}}_c]$ during the calibration.

The FMSM is composed of six Magnetic Field Sensors (MFS, A1391, Allegro MicroSystems, USA), an Inertial Measurement Unit (IMU) embedding both an accelerometer and a gyroscope (LSM 330, STMicroelectronics, Switzerland), and an off-the-shelf NdFeB (N52) cylindrical magnet, which was axially magnetized with 1.48 T of magnetic remanence, 11 mm in diameter and 11 mm in height. The readings of the magnetic sensors integrated in the FMSM are acquired by the onboard 16-bit Analog to Digital Converter (ADC, AD7689, Analog Devices, Inc. USA). An acquisition cycle starts from sampling six analog inputs connected to the MFS outputs. Then, the six digitized values of acceleration and angular speed are received from the IMU. This dataset is acquired every 4.4 ms by the WMC (CC2530, Texas Instruments, USA) and used to build a 36-byte package together with the capsule status indicators (i.e., battery level, start/stop bytes). This package is then transmitted by the WMC to the external transceiver over a 2.4 GHz carrier frequency, with a refresh time of 6 ms (wireless data throughput 42.4 kbit/s), resulting in a sampling rate of

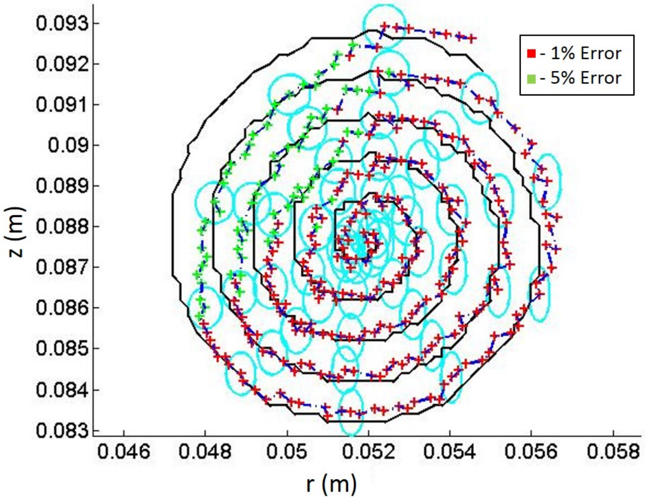

Figure C.6: Simulated motion of a capsule along a spiral trajectory in the center of $\mathcal{G}'$. The black line represents the reference trajectory, while the crossed line shows the capsule position estimated by applying the Jacobian-based iterative method. The cyan ellipses represent the ellipsoid of localization uncertainty due to magnetic field sensor noise. Colors in the crossed line express the relative error in position detection for the radial component.

166 Hz. The external transceiver is based on an identical WMC which communicates with the PC through a USB-serial converter (UM232R, FTDI, UK).

The power supply module embeds a low-dropout voltage regulator (LDO) (TPS73xx, Texas Instruments, USA) to provide a stable supply to both the FMSM and the communication module. In order to limit the current consumption when the device is not acquiring measurements, a digital output of the microcontroller can drive the SLEEP pin of all the MFS. This results in a current consumption which varies between 400 mA, when the microcontroller is in low power mode, and 20 mA when it is in IDLE mode with the radio active. Average current consumption rises to 48 mA during a single cycle of sensor data acquisition and wireless transmission. The power source used is a 50 mAh, 3.7 V rechargeable LiPo battery (Shenzhen Hondark Electronics Co., Ltd., China).

C.7.1.3 Software Architecture

A multi-thread C++ WIN32 application running on the PC unbundles the data and shares them with three other parallel threads. The first thread controls the robotic manipulator through a UDP/IP communication with a refresh rate of 140 Hz. It sends the desired pose to the robot controller and then receives the robot pose feedback. The second thread implements a digital Kalman filter for each of the six MFS and the six IMU outputs before running the iterative localization algorithm. The algorithm outputs the 6-DOF

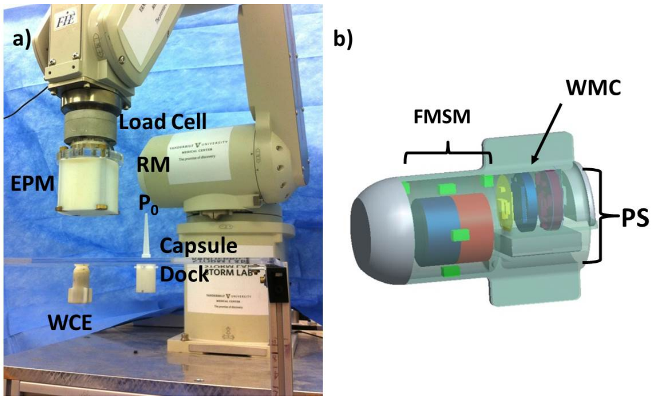

Figure C.7: Experimental platform: (A) Robotic Manipulator (RM) and External Permanent Magnet (EPM). (B) Visual rendering of the Wireless Capsule Endoscope (WCE) and its internal components, where FMSM is the Force and Motion Sensing Module, WMC is the Wireless MicroController and PS is the Power Supply.

capsule pose estimation $\mathbf{p} = [x, y, z, \alpha, \beta, \gamma]$ with respect to the EPM frame $[\hat{\mathbf{x}}, \hat{\mathbf{y}}, \hat{\mathbf{z}}]$. The third thread manages a TCP/IP communication with a MATLAB application (Mathworks, USA), which displays the localization algorithm estimation. The data transfer rate for the robot controller applications is 83 Hz. The refresh time for the capsule pose estimation $\mathbf{p}$ and the capsule wireless data transfer is 6.8 ms (refresh rate 150 Hz). Referring to Fig. C.8, the MATLAB application displays the capsule position and orientation $\mathbf{p} = [x, y, z, \alpha, \beta, \gamma]$ with respect to the EPM reference frame $[\hat{\mathbf{x}}, \hat{\mathbf{y}}, \hat{\mathbf{z}}]$ in real time (refresh every 30 ms) on a 3D plot. Current pose numerical values are also displayed.

C.7.2 Experiments and Results

C.7.2.1 Capsule orientation algorithm assessment

Because the localization method we propose also relies on real-time capsule orientation data, the first step in the experimental assessment consisted in validating the algorithm described in section C.5. In order to quantify the absolute error in capsule orientation, the WCE was rigidly attached to the end effector of the RM. The orientation of the WCE was varied within a range of $\pm 90^o$ about each of the three axes $[x_{EPM}, y_{EPM}, z_{EPM}]$ by adopting combined motions for a total of one minute. Inertial data acquired by the WCE were sent over the wireless link, while the orientation of the end effector, as measured by the RM built-in encoders, was adopted as a reference. The average orientation error was $3.4^o \pm 3.2^o$ for α, $3.7^o \pm 3.5^o$ for β, and $3.6^o \pm 2.6^o$ for γ.

A second experiment aimed to quantify the steady-state drift for the capsule orientation algorithm. This is particularly relevant for the estimation of γ, which, unlike α and β, is obtained by iterative integration. For this test, the WCE was locked into the capsule dock

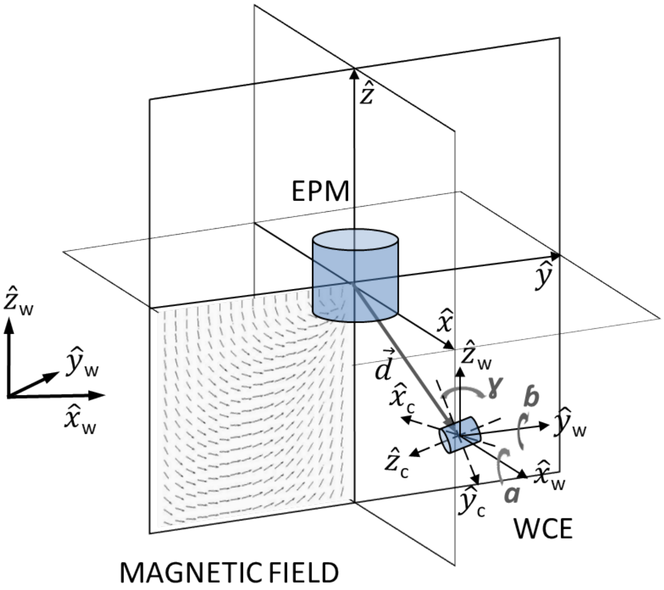

Figure C.8: Schematic representation of the global frame, EPM frame and capsule frame. The capsule orientation angles $[\alpha, \beta, \gamma]$ are shown with respect the global frame.

(see Fig. C.7 or the multimedia attachment 1) for 7.5 minutes while acquiring data and running the capsule orientation algorithm. The average error over the entire period was $0.34^o \pm 0.18^o$ for α, $0.27^o \pm 0.17^o$ for β, and $1.8^o \pm 1.1^o$ for γ, while the absolute error at the end of the 7.5 minutes was 0.5^o for α, 0.2^o for β, and 5.2^o for γ.

C.7.2.2 Steady state positional drift evaluation

This set of experiments, referred to as T01, was aimed at evaluating the localization algorithm behavior in steady conditions. Before the trials began, the iterative localization algorithm was initialized as shown in the multimedia attachment 1. The calibration consisted of three steps. First, the capsule was placed into the capsule dock, with a known position and orientation with respect to the global frame $[x_w, y_w, z_w]$. Then, the magnetic field sensors in the WCE were biased while maintaining the EPM outside the workspace. Finally, the EPM was moved to a reference position with respect to the WCE, and the relative distance between the EPM and the WCE, as derived by design, was used to initialize $\mathbf{p}(t = 0)$ (digitization phase in the multimedia attachment 1).

After the initial calibration, the EPM was moved to eight different positions within the workspace, while the WCE was maintained in the capsule dock. Each position was chosen to be at about 10 cm from the center of the workspace along both the radial and axial coordinate. The azimuth coordinate θ_{EPM} was changed from zero to 2π in $\pi/4$ steps. Each EPM position was maintained for one minute, while recording the localization data. The

Table C.2: Results of the steady state positional drift experiment (T01). For the eight trials, the radial and axial coordinates of the EPM were fixed to 80 mm and 130 mm, respectively. The azimuth coordinate θ_{EPM} is reported in the first column. Average radial and axial error for each trial are reported in the second and third column, respectively.

$\theta_{EPM}(^{o})$	T01-RE (mm)	T01-AR (mm)
0	0.3 ± 0.3	1.5 ± 0.5
45	1.5 ± 0.9	0.3 ± 0.3
90	7.2 ± 2.8	6.4 ± 3.3
135	4.4 ± 2.1	3.4 ± 1.6
180	0.5 ± 0.5	1.8 ± 0.8
225	5.1 ± 2.8	2.5 ± 1.2
270	3.7 ± 1.5	0.6 ± 0.2
315	0.5 ± 0.4	0.4 ± 0.3

results were compared to the reference EPM pose as derived by the RM encoders. Table C.2 reports the azimuth coordinate, the average radial error and the average axial error for each of the eight EPM positions.

For each trial, the relative error, the drift, and the residual measurement noise were statistically analysed while the system was not subjected to relative motion between the WCE and the EPM. The proposed localization method presented an average absolute and relative error for the radial component of $2.9 \pm 1.4mm$ and $1.85 \pm 2.1\%$, respectively. The average absolute and relative errors for the axial component were $2.1{\pm}1.0mm$ and $1.9{\pm}0.9\%$, respectively.

Typical trends for radial and axial component estimation are shown in Fig. C.9. During the trials, the pose estimation presented a drift due to the system noise and the iterative integration. However, the relative error was always below 5%. The residual measurement noise (Fig. C.9.d) had a gaussian distribution (Jarque-Bera normality test with h equal to 1 and p-value 0.1) with null average and a bandwidth below 0.5%, which remained constant for the entire duration of each trial. The magnetic field measurement noise fused with the IMU measurements did not affect the localization algorithm, thus resulting in a stable long-term behavior.

C.7.2.3 Robustness to initialization errors

This set of experiments, referred to as T02, was aimed at assessing the algorithm sensibility to errors in position initialization. These trials were performed by moving the EPM to the same eight positions used for T01, while maintaining the WCE fixed into the capsule dock. For each EPM position, four different tests were performed by adding an increasing error $\mathbf{e}$ to the initialization distance $\mathbf{p}(t = 0)$ as measured during calibration. In particular, the error $\mathbf{e}$ had a random direction in $\hat{\mathbf{r}}$ and $\hat{\mathbf{z}}$ and an increasing module (i.e., 1 mm, 5 mm, 10 mm, and 20 mm). As in T01, each test was one minute long.

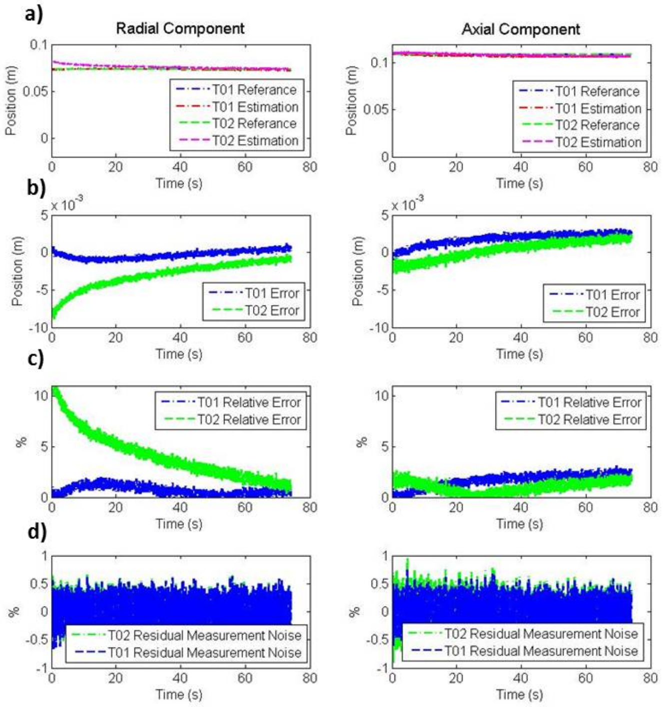

Figure C.9: Results for the steady state positional drift experiment (T01) and for the initialization error evaluation (T02) with an initialization error of $10mm$. Both T01 and T02 results are evaluated for the radial (left column) and the axial (right column) component. (a) Reference position vs. estimation. (b) Absolute positional errors. (c) Relative positional errors. (d) Residual measurement noise. The azimuth error is presented in Fig. C.12.

Considering all 32 tests performed, the average absolute and relative error for the radial component were $15.5 \pm 4.2mm$ and $19.5 \pm 6.0\%$, respectively. The axial component had an average absolute error of $13.6 \pm 3.9mm$ and an average relative error of $12.1 \pm 3.5\%$.

Typical trends for radial and axial component estimation affected by a 10 mm error in position initialization are shown in Fig. C.9. In this case, the absolute and the relative error (Fig. C.9.b and Fig. C.9.c, respectively) decreased within the duration of the trial, never exceeding 10% of the reference value. Interestingly, the localization algorithm was able to correct the initialization error with time. The residual measurement noise for both the radial and the axial component (Fig. C.9.d) presented the same behavior observed in T01 trials.

C.7.2.4 Robustness to positional lag

This set of trials aimed at evaluating the effect that a lag between the EPM and the WCE may have on the localization algorithm. In particular, our goal was to quantify the minimum value for the relative speed between the EPM and the WCE that would prevent the localization algorithm to converge. For reference, the typical endoscope absolute speed during a colonoscopy is in the order of 0.8 mm/s to 1.6 mm/s [50]. However, for magnetic capsule endoscopy, the relative EPM-WCE speed is ideally null, as the WCE should be following the EPM motion under the effect of magnetic coupling. This is true as long as the WCE is able to freely move inside the lumen.

After the initial calibration as described for T01, five trials were performed by moving the EPM at increasing speeds while collecting localization data. Like the previous experiments, the WCE was locked into the capsule dock. The EPM was initially positioned at 110 mm along the radial component and 110 mm along the axial component, and then moved by 200 mm along y_w at a constant acceleration. For the five trials, acceleration was set to $0.396, 0.793, 1.190, 1.587$, and $1.984\ \frac{m}{s^2}$, respectively. The multimedia extension 1 shows one of these trials, while the results for the experiment with $1.984\ \frac{m}{s^2}$ acceleration are reported in Fig. C.10. As expected, the EPM motion along y_w only affected the radial component of the localization algorithm, leaving the axial component almost unperturbed.

For this set of trials, the localization algorithm presented a relative error in the radial component of 10% for a relative speed of $0.221 \pm 0.046\ \frac{m}{s}$. This increased up to 20% for a relative speed of $0.335 \pm 0.050\ \frac{m}{s}$. The average absolute error in the radial component was $11.86 \pm 8.36mm$, with an average relative error of $16.3 \pm 10.2\%$. For the axial component, the average absolute error was $2.66 \pm 1.8mm$, with an average relative error of $2.3 \pm 1.6\%$.

Given these results, we can conclude that the algorithm is sensitive to the relative speed between the WCE and the EPM and the relative error exceeds 10% if the relative speed is greater than $0.2\frac{m}{s}$. As previously discussed, this speed is well above the values that we expect to experience during magnetic manipulation of a WCE.

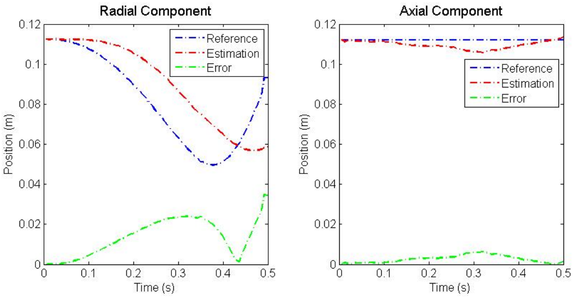

Figure C.10: Position estimation results during the positional lag trial with uniform acceleration of $1.984\ \frac{m}{s^2}$.

C.7.2.5 General assessment

The final experiment aimed at validating the localization algorithm for a generic trajectory of the EPM, with the WCE fixed into the capsule dock. After calibration, the EPM was moved via admittance control to form a three-dimensional loop within the workspace, starting from the initialization position $\mathbf{p}(t = 0)$. During this trial, the EPM coordinates spanned from about -10 cm to 10 cm along both $\hat{x}_w$ and $\hat{y}_w$ axes, and from 6 cm to 12 cm away from the WCE position along the $\hat{\mathbf{z}}_w$ axis.

For the entire trajectory, the proposed method of localization presented an average absolute error in the radial component of $6.2 \pm 4.4mm$ and an average relative error of $5.7 \pm 7.6\%$. The average absolute error for the axial component was $6.9 \pm 3.9mm$, with an average relative error of $7.0 \pm 4.9\%$. The average absolute error for the azimuth component $(\boldsymbol{\theta})$ was $5.4^o \pm 7.9^o$.

The trajectory (as reconstructed from the RM encoders) and its estimation are represented in Fig. C.11. Typical trends for the radial (r), the axial (z), and the azimuthal (θ) component estimations are shown in Fig. C.12.a,c,e, while the absolute and relative errors are reported in Fig. C.12.b,d,f. The azimuthal component presents a bigger absolute error when the radial component of the capsule position is approaching zero. This is due to error of misalignments between capsule end EPM, which generates erroneous output for the azimuthal component. Anyway this is not an issue since through the capsule's pose conversion from cylindrical to cartesian coordinates by apply C.24, leads to a small error since the radial component p_r is very small or equals to zero.

It is worth noting that the experimental assessment showed an error that is about one order of magnitude larger than what was observed by simulation. This is probably due to the noise introduced by the sensors and by the digitization process.

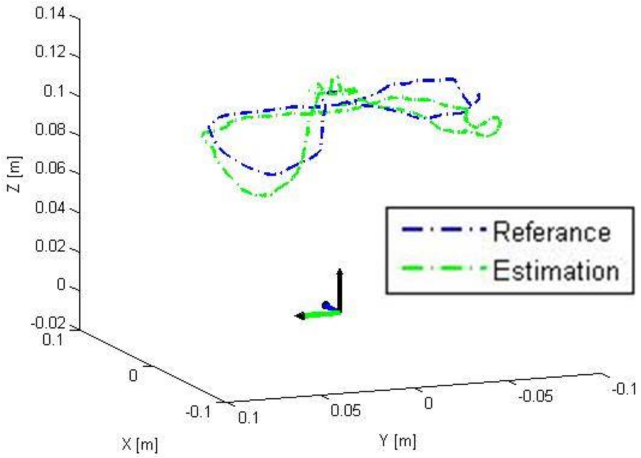

Figure C.11: Three-dimensional representation of the EPM trajectory and its estimation by the localization algorithm.

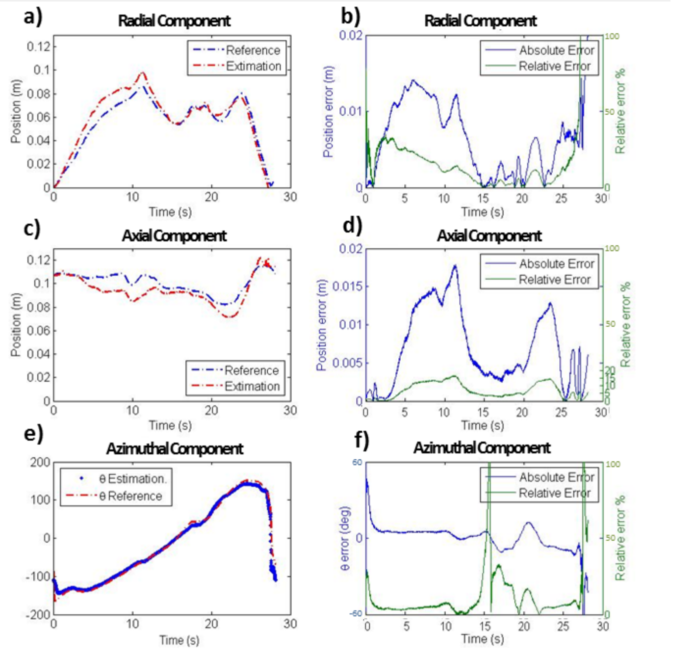

Figure C.12: Typical trends for the radial (a), the axial (c) and the azimuth (e) component during the final experiment, and related absolute and relative errors (b, d, and f, respectively).

Real-time operation of the localization algorithm for random motion of the WCE is shown in the multimedia extension 2. On the left side of the screen, the localization output is plotted in real-time showing the WCE and the EPM reference frames.

In the multimedia extension 3, the localization is performed while moving the EPM parallel to a plexiglass pipe placed at an angle with respect to the global frame. In this case, the WCE is free to move in the pipe under the effect of magnetic coupling. The distance between the EPM and the WCE is about 10 cm. The localization real-time output $\mathbf{p} = [x, y, z, \alpha, \beta, \gamma]$ and the EPM position are both superimposed to the video stream. This demonstrates the ability of the proposed localization algorithm to track the WCE in real-time during magnetic manipulation.

C.8 Conclusions

This paper was motivated by the limitations of existing magnetic localization algorithms in terms of computational time, precision, and compatibility with magnetic manipulation of endoscopic capsules. To overcome these limitations, we put forward a new method for real-time localization using fusion of inertial data with information from magnetic field sensors, combined with an iterative Jacobian-based approach. Our strategy uniquely applies a parametrization of the magnetic field using least squares interpolation over an exact finite element solution, thus overcoming the limitations of the simplistic dipole model. To achieve this parametrization, we used Kronecker products and a modal fitting to describe the magnetic field. To assist with real-time localization (which is paramount for solving a nonlinear inverse problem), we used the Jacobian of the magnetic field intensity relative to pose perturbations of the endoscopic capsule. This allowed the use of a local linearization approach that is similar to the resolved rates method for inverse kinematics of serial robots.

Our algorithm was evaluated by simulation and experiments. We investigated the robustness of our pose estimates of the wireless capsule to initialization errors. We also characterized the residual measurement noise and the effect of positional lag when the magnet driving the capsule was moving. Our results showed that, even though the proposed algorithm exhibits limitations of convergence for fast relative motions, the pose estimation of the magnetic capsule for clinically realistic speeds was effective and reliable. In particular, experimental results showed an average error (expressed in cylindrical coordinates) below 7 mm in both the radial and axial components, and 5^o in the azimuthal component. The average errors for the capsule orientation angles, obtained by fusing gyroscope and inclinometer measurements, were 0.3^o for α and β, and 5^o for γ. Overall, the relative error always remained below 10%. The proposed localization algorithm was able to run at a 1 ms refresh rate, an order of magnitude below what was reported in previous works. The overall refresh rate, including sensor data acquisition and wireless communication, was 7 ms, thus enabling closed-loop control strategies for WCE magnetic manipulation running faster than 100 Hz. Since the least square interpolation present some regions of the magnetic field domain $\mathcal{G}'$ where the relative error is greater than 20% in future applications the robot path planner can be instructed to follow the capsule and to enclose it in an optimal localization area to avoid these regions.

Drift – a common problem in integrative methods – may become an issue over time and affect the precision of localization. A possible solution is to integrate the proposed approach with an absolute localization technique working at a slower refresh rate, such as the strategy proposed in [32, 68]. Since the final goal is to localize the capsule during magnetic manipulation, the behaviour of the algorithm must be assessed with the capsule in motion, exploiting also inertial navigation system theory by applying extended Kalman filter [200,201]. The absolute localization algorithm can repeatedly provide initialization values to the integrative method, thus preventing the integration error from exceeding a desired value. Localization techniques fusing multiple sensor data having different resolutions and refresh rates, as proposed in [202–206] for SLAM applications, may also improve our approach.

In summary, the proposed localization strategy is compatible with magnetic manipulation of WCE, does not require clear line-of-sight, has a resolution that is finer than the capsule size, and a refresh rate that is adequate for real-time closed loop robotic control. This represents an enabling technology that can move us toward intelligent control of a WCE during an endoscopic procedure.

Appendix D

WIRELESS PLATFORM FOR MEASUREMENT OF RESISTANT PROPERTIES OF THE GI TRACT: A WIRELESS PLATFORM FOR *IN VIVO* MEASUREMENT OF RESISTANCE PROPERTIES OF THE GASTROINTESTINAL TRACT

Christian Di Natali, Marco Beccani, Keith L. Obstein, Pietro Valdastri.

From: Physiological Measurements, Vol. 35, pp. 11971214
Status: Published 2014

D.1 Abstract

Active locomotion of wireless capsule endoscopes has the potential to improve the diagnostic yield of this painless technique for the diagnosis of gastrointestinal tract disease. In order to design effective locomotion mechanisms, a quantitative measure of the propelling force required to effectively move a capsule inside the gastrointestinal tract is necessary.

In this study, we introduce a novel wireless platform that is able to measure the force opposing capsule motion, without perturbing the physiologic conditions with physical connections to the outside of the gastrointestinal tract. The platform takes advantage of a wireless capsule that is magnetically coupled with an external permanent magnet. A secondary contribution of this manuscript is to present a real-time method to estimate the axial magnetic force acting on a wireless capsule manipulated by an external magnetic field. In addition to the intermagnetic force, the platform provides real-time measurements of the capsule position, velocity, and acceleration.

The platform was assessed with benchtop trials within a workspace that extends 15 cm from each side of the external permanent magnet, showing average error in estimating the force and the position of less than 0.1 N and 10 mm, respectively. The platform was also able to estimate the dynamic behavior of a known resistant force with an error of 5.45%. Finally, an *in vivo* experiment on a porcine colon model validated the feasibility of measuring the resistant force in opposition to magnetic propulsion of a wireless capsule.

D.2 Introduction

The gastrointestinal (GI) tract is home to many deadly human diseases. Colorectal cancer (CRC) alone is the third most common cancer in men and the second in women worldwide [43]. However, most GI diseases can be prevented – or timely cured – if the diagnosis occurs at an early stage of development. For this reason, GI screening is playing an increasingly important role in healthcare systems worldwide [44, 45].

One method for GI screening that has quickly risen to become the preferred option is flexible endoscopy due to its ability to serve as both a diagnostic and therapeutic modality. Unfortunately, its application is sometimes limited due to its invasiveness, patient intolerance, and the need for sedation. These disadvantages are severe enough for some patients, that millions forgo or avoid recommended screening [44].

Over the past decade, wireless capsule endoscopy (WCE) established itself as a patient-friendly procedure for diagnosis of diseases in the small intestine [46]. Specific wireless capsule endoscopes have been proposed for colon inspection, but have not reached the diagnostic accuracy of standard colonoscopy [47,48]. One of the main limitations of commercially available capsule endoscopes is passive locomotion [49]. It is desirable for the endoscopist to be able to maneuver the camera arbitrarily rather than relying on peristalsis to drive the capsule for adequate visualization of GI mucosa. For this reason, a relevant number of technical solutions have been recently proposed to provide active locomotion to WCE, including walking [50] or crawling [51] capsules, remote magnetic manipulation [29, 30, 64, 146], and hybrid approaches [27, 207].

As mentioned in [208], the engineers designing active locomotion mechanisms for WCE would greatly benefit from having a quantitative measure of the propelling forces required to effectively move a capsule in the targeted GI segment. Several works have been published recently that address this scientific need. The proposed methods to measure resistant properties of the GI tract range from *ex vivo* trials performed with benchtop equipment [111, 113, 209, 210], to dedicated instrumentation that can acquire data *in vivo* during a surgical procedure [208, 211]; however, the main limitation to all of the proposed methods thus far has been that a wired connection is always used to perform the measurement. In [111], a capsule mock-up sliding inside an intestinal lumen is pulled by a load cell through a string, whereas a multi-lumen connection is used in [208] to operate the measurement device deployed in the small intestine of a living pig. Having a physical connection to the outside of the GI tract throughout the measurement has the potential to affect the readings and compromise the results integrity. Measuring the resistance properties of the GI tract with a wireless device would allow for preservation of physiological conditions – including the contribution of surrounding organs – and to obtain measurements that are closer to the actual forces that an active capsule endoscope must face in navigating the GI tract.

The main contribution of this paper is to present – for the first time – a wireless platform for the measurement of the resistant force that an active capsule must overcome in order to move inside the GI tract. The proposed platform is validated with benchtop trials and through an *in vivo* experiment using a porcine colon model. A secondary contribution of this paper is to present a real-time method to estimate the axial magnetic force acting on a wireless capsule manipulated by an external magnetic field. An extensive quantification of resistance properties of the different GI segments – outside the scope of this paper – can then be obtained by adopting the proposed methods. The same approach would also enable gathering reliable data for implementing realistic biomechanical models of the GI tract [112, 113, 212, 213].

D.3 Materials and Methods

D.3.1 Method Overview

A common method to measure the resistance properties of the intestine is to impose a motion to a capsule mock-up inside the lumen and to measure the associated force profile [111–113]. An equivalent approach, schematically represented in Fig. D.1, consists of imposing an increasing force $\mathbf{F}_a$ to the capsule and recording the motion profile to understand when the applied force $\mathbf{F}_a$ overcomes the resistant force $\mathbf{F}_r$. Referring to the instant when motion starts as t_0 and assuming a static equilibrium until that moment, the value $\mathbf{F}_a(\mathrm{t}_0)=\mathbf{F}_r(\mathrm{t}_0)$ quantifies the static resistant force that an active capsule must overcome to begin its motion. Then, as the motion builds up, driven by $\mathbf{F}_a$ increases, the system moves away from the equilibrium and the following equation can be used to describe its dynamics:

$$\mathbf{F}_{tot} = \mathbf{F}_a - \mathbf{F}_r = m\ddot{\mathbf{d}}, \tag{D.1}$$

where $\mathbf{d}$ is the position of the capsule center of mass O_c, while m is the capsule mass.

The platform described in this paper allows application of a force $\mathbf{F}_a$ to a capsule without the need for a tethered connection – thus preserving physiologic condition during *in vivo* measurements. This is achieved by leveraging magnetic coupling between an external permanent magnet (EPM) and a magnet embedded inside the capsule. The applied force $\mathbf{F}_a$, the position $\mathbf{d}$, and the acceleration $\ddot{\mathbf{d}}$ are measured wirelessly in real time with respect to a reference frame $\{\mathbf{x}_m, \mathbf{y}_m, \mathbf{z}_m\}$ on the EPM. While just $\mathbf{F}_a$ and $\ddot{\mathbf{d}}$ would be sufficient for a complete characterization of $\mathbf{F}_r$, real-time knowledge of $\mathbf{d}$ allows adjustment of the setup during *in vivo* trials and to record the distance traveled by the capsule for each measurement. In addition, the capsule velocity $\dot{\mathbf{d}}$ can be calculated as the first derivative of $\mathbf{d}$ to provide additional information about the motion profile. The methods for measuring all of the quantities mentioned will be described in the following sections of the paper.

The applied force $\mathbf{F}_a$ can be adjusted by controlling the position of the EPM. This can be achieved by a robotic manipulator, as proposed for benchtop validation in sections D.4.1

and D.4.2. Alternatively, the EPM position can be manually adjusted by an operator until the capsule starts its motion, as indicated by the real-time measurement of $\dot{\mathbf{d}}$ and $\ddot{\mathbf{d}}$. This approach was used for the *in vivo* validation of the platform, as further detailed in section D.4.3.

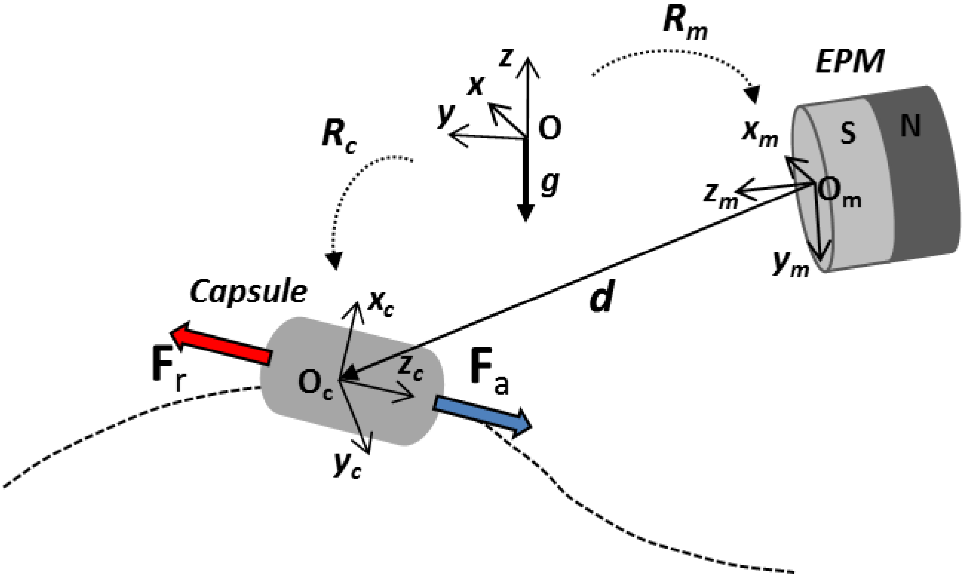

Figure D.1: Schematic representation of the principle of operation. The attraction force $\mathbf{F}_a$ is generated by magnetic coupling between an external permanent magnet (EPM) and a magnet embedded in the capsule. The intermagnetic force $\mathbf{F}_a$ and the capsule position $\mathbf{d}$ with respect to the EPM are recorded wirelessly in real time. $\mathbf{F}_r$ is the resistant force, $\mathbf{g}$ is the gravitational acceleration vector, R_c is the rotational matrix of the capsule reference frame with respect to the global Cartesian coordinate system, while R_m is the rotational matrix of the reference frame at the EPM with respect to the global Cartesian coordinate system.

D.3.2 Platform Overview

The platform is composed of a wireless capsule, the EPM, and a personal computer (PC) connected to a wireless transceiver via the universal serial bus (USB) port. The real-time algorithm runs on the PC and communicates with the capsule through the USB transceiver. The EPM is a NdFeB (magnetization N52, magnetic remanence 1.48 T) cylindrical permanent magnet with axial magnetization, as represented in Fig. D.1. The EPM diameter and length are both equal to 50 mm, while the mass is 772 g. A triaxial accelerometer (LIS331DL, STMicroelectronics, Switzerland) – used as inclinometer – is mounted on the EPM to provide pitch and yaw angles of $\{\mathbf{x}_m, \mathbf{y}_m, \mathbf{z}_m\}$ with respect to the global frame $\{\mathbf{x}, \mathbf{y}, \mathbf{z}\}$. These angles are used for the localization algorithm – as described in section D.3.3.2

– and fed directly to the PC through a 16-bit acquisition board (DAQ USB-6211, National Instruments, USA).

The wireless capsule, schematically represented in Fig. D.2, hosts a force and motion sensing module (FMSM), wireless communication, and power supply. Each of these modules are described in detail in the following subsections. The outer shell was fabricated in biocompatible material – polyether-ether-ketone, PEEK – by traditional machining. The current prototype is 60 mm in length, 18 mm in diameter, 21 g in mass. For comparison, the Given Imaging PillCam SB2 is 26 mm in length, 11 mm in diameter, 3.5 g in mass. Having a larger capsule for measuring resistance properties does not jeopardize the relevance of the results, as long as the animal model selected takes into account the appropriate scaling factors (i.e., diameter and size of human colon [214], diameter and size of porcine colon as a function of body weight [215], resistant properties of capsule endoscopes as a function of size, surface and diameter of the capsule [111, 212]).

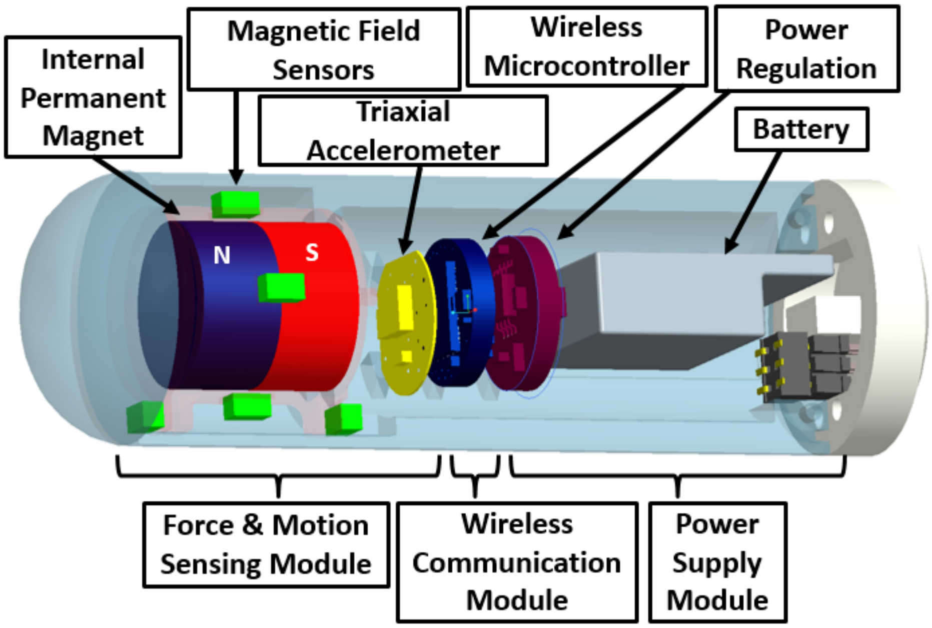

Figure D.2: Schematic view of the wireless capsule for measuring resistant properties of the GI tract.

D.3.3 Force and Motion Sensing Module

The FMSM hosts the internal permanent magnet (IPM) that couples with the EPM to generate the force $\mathbf{F}_a$ applied to the wireless capsule. The selected IPM is an off-the-shelf NdFeB (N52) cylindrical magnet axially magnetized with 1.48 T of magnetic remanence, 11 mm in diameter and 11 mm in height. This EPM-IPM couple generates an intermagnetic force of 1 N when the two magnets are separated by 8 cm and the axes $\mathbf{z}_c$ and $\mathbf{z}_m$ are aligned.

The FMSM is responsible for acquiring the real time sensor readings required to estimate $\mathbf{F}_a$, $\mathbf{d}$, and $\ddot{\mathbf{d}}$. The transducers embedded in the module are six linear magnetic field sensors (MFS) based on the Hall effect (A1391, Allegro Microsystems, USA) and a 16-bit digital triaxial accelerometer with serial peripheral interface (SPI) (LIS331DL, STMicroelectronics, Switzerland, sensitivity of 176.6 mm/s^2). As represented in Fig. D.3, the MFS are mounted two by two orthogonally around the IPM. Each MFS measures the component of the magnetic field $\mathbf{B}$ that is perpendicular to the IPM surface at the MFS location (i.e., referring to Fig. D.3, MFS$_i$ measures the component B$_i$ for i ranging from 1 to 6). Similarly to [106], the position of each MFS has been selected to minimize the constant bias in the reading due to the field generated by the IPM. This explains why the two MFS along the z$_c$ direction (MFS$_5$ and MFS$_6$) are placed at the edge of the IPM, rather than on its main axis. The bias from the IPM that still remains in each MFS output is treated as an offset and filtered out from the measurements. The MFS analog outputs are acquired by the 12-bit analog to digital converter (ADC) of the wireless microcontroller (CC2530, Texas Instruments, USA) integrated in the communication module. The digitized magnetic field signal results in a sensitivity of 64 μT.

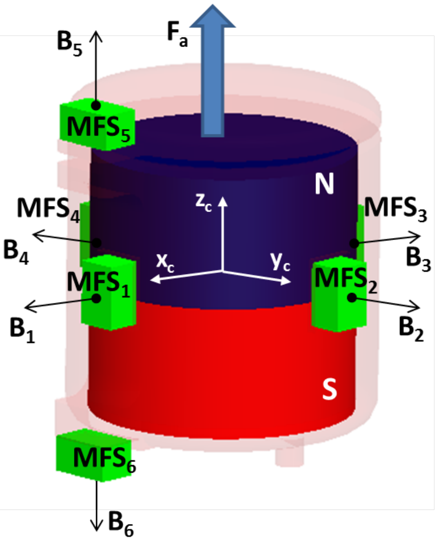

Figure D.3: Magnetic field sensor (MFS) position with respect to the internal permanent magnet.

D.3.3.1 Intermagnetic Force Estimation

The goal of this section is to describe a new method to estimate the intermagnetic force $\mathbf{F}_a$ acting on the main axis of the IPM (i.e., $\mathbf{z}_c$ in Fig. D.3) under the effect of an external magnetic field $\mathbf{B}_{ext}$. Current approaches either rely on the dipole-dipole magnetic field approximation [107] or finite element integration [108]. The first method provides an analytical expression of the magnetic field that is accurate at a certain distance from the magnetic field source. On the other hand, finite element integration allows the procurement of accurate results at the price of long computational times [108].

The method proposed in this study is based on the finite element integration of real-time sensor data. The analytical formulation derived in this subsection, can be used to estimate $\mathbf{F}_a$ in real time as a direct function of four MFS readings (i.e., MFS_1 to MFS_4) with low computational costs.

As described in [109], the magnetic force $\mathbf{F}$ acting on a permanent magnet under the effect of an external magnetic field $\mathbf{B}_{ext}$ can be expressed by applying the equivalent current magnetic model:

$$\mathbf{F} = \oint_S \mathbf{j}_m \times \mathbf{B}_{ext} \delta S, \tag{D.2}$$

where S is the IPM surface and $\mathbf{j}_m$ is the equivalent current surface density on the IPM. The current density $\mathbf{j}_m$ is derived from:

$$\mathbf{j}_m = \mathbf{M}_{IPM} \times \mathbf{n}, \tag{D.3}$$

where $\mathbf{M}_{IPM}$ is the IPM magnetization vector, having expression $B_r/\mu_0 \hat{\mathbf{z}}$ – with $\hat{\mathbf{z}}$ denoting the unit vector along $\mathbf{z}_c$, while $\mathbf{n}$ is the normal vector coming out from the IPM surface, as represented in Fig. D.4.A.

From Eq. D.3, it is possible to conclude that – given an axially magnetized cylindrical IPM, $\mathbf{j}_m$ only flows on the lateral surface. Therefore, the component of $\mathbf{B}_{ext}$ along $\hat{\mathbf{z}}$ does not contribute to the estimation of $\mathbf{F}$ through the equivalent current magnetic model (Eq. D.2).

In order to provide an analytical expression for Eq. D.2, it is possible to take advantage of the axial symmetry of our problem, thus dividing the cross-section of the IPM into four identical quadrants, as represented in Fig. D.4.A. Focusing on the u-th quadrant and defining θ as the angular coordinate (see Fig. D.4.B), it is possible to express the current density $\mathbf{j}_m$ as:

$$\mathbf{j}_m(\theta) = M_{IPM}[-sin(\theta)\hat{\mathbf{x}} + cos(\theta)\hat{\mathbf{y}}], \tag{D.4}$$

where $\hat{\mathbf{x}}$ and $\hat{\mathbf{y}}$ are the unit vectors along $\mathbf{x}_c$ and $\mathbf{y}_c$, respectively.

In the proposed capsule design, the magnetic field $\mathbf{B}_u$ is measured by the MFS$_u$ placed at $\theta = \pi/4$ in each quadrant and can be expressed as:

$$\mathbf{B}_u = B_u[cos(u\frac{\pi}{2} - \frac{\pi}{4})\hat{\mathbf{x}} + sin(u\frac{\pi}{2} - \frac{\pi}{4})\hat{\mathbf{y}}], \tag{D.5}$$

where B$_u$ is the numerical value recorded by MFS$_u$ and u ranges from 1 to 4.

Assuming that the magnetic field in each quadrant is coincident with the magnetic field $\mathbf{B}_u$, the surface integral in Eq. D.2 can be simplified in the following sum:

$$\mathbf{F} = \sum_{u=1}^{4}\sum_{\theta=0}^{\pi/2}(\mathbf{j}_m \times \mathbf{B}_u)\Delta S = \sum_{u=1}^{4} sgn[cos(u\frac{\pi}{2} - \frac{\pi}{4})]\sum_{\theta=0}^{\pi/2} f_u \Delta S \hat{\mathbf{z}}, \tag{D.6}$$

where sgn is the sign function, ΔS is the lateral surface of one quadrant of the IPM and is equal to $\pi/2rh$, in which r is the radius and h the height of IPM. f_u is the contribution to the module of the intermagnetic force acting on the u-th quadrant at a given θ and can be expressed as:

$$f_u = M_{IPM}\frac{B_u}{\sqrt{2}}(sin(\theta) + cos(\theta)). \tag{D.7}$$

Considering that

$$\sum_{\theta=0}^{\pi/2}[sin(\theta) + cos(\theta)] = \Theta = 1.27, \tag{D.8}$$

the analytical expression for the intermagnetic force becomes:

$$\mathbf{F} = \sum_{u=1}^{4} sgn[cos(u\frac{\pi}{2} - \frac{\pi}{4})]\frac{\Theta}{\sqrt{2}}M_{IPM}\frac{\pi}{2}rhB_u\hat{\mathbf{z}} \tag{D.9}$$

This simple equation can be used to get a fast estimate of the intermagnetic force $\mathbf{F}_a$ from the readings of MFS$_1$, MFS$_2$, MFS$_3$, MFS$_4$. Considering the computational platform described in section D.3.5, the time required to estimate the magnetic force is 0.18 ± 0.05 ms.

D.3.3.2 Capsule Motion Estimation

The information related to capsule motion that the proposed platform provides in real time are: (1) capsule acceleration $\ddot{\mathbf{d}}$, (2) indication that motion has started, and (3) capsule position $\mathbf{d}$ with respect to the EPM.

The capsule acceleration $\ddot{\mathbf{d}}$ is directly measured by the onboard triaxial accelerometer. The same sensor is also used to detect the instant when capsule motion begins. In particular,

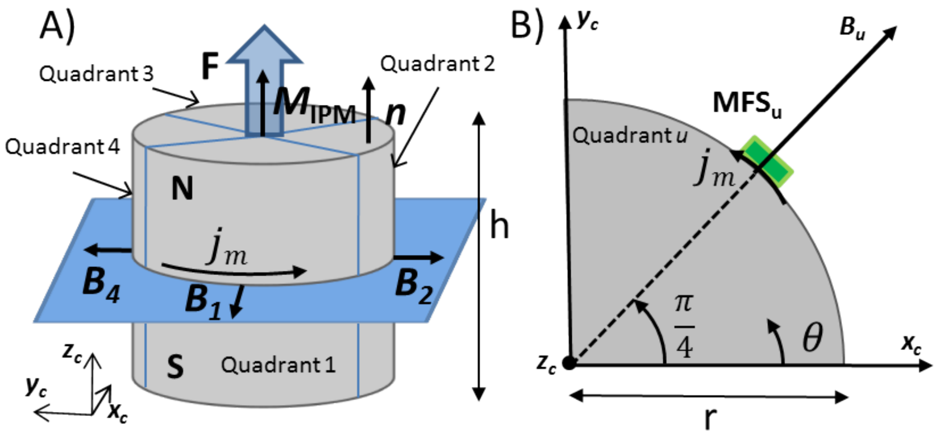

Figure D.4: (A) Lateral view of the IPM. (B) Schematic view of the i-th quadrant of the IPM.

it is possible to assume that the capsule begins moving whenever the following equation is satisfied:

$$\|\ddot{\mathbf{d}} - \mathbf{g}\| \geq T, \tag{D.10}$$

where $\mathbf{g}$ is the gravitational acceleration vector and T is a threshold set to 5% of $|\mathbf{g}|$ (i.e., 0.49 m/s^2). The threshold T was defined by experimental calibration to prevent false positives due to noise of the measurement or movements that were not related to capsule motion. Another method to confirm that the capsule is moving – probably better suited for *a posteriori* data interpretation – consists of analyzing the position $\mathbf{d}$ and the velocity $\dot{\mathbf{d}}$ profiles, both acquired by the proposed platform. This approach would allow for detection of motion profiles that begin without a sudden change in acceleration.

The methods and the algorithm used to solve the electromagnetic inverse problem (i.e., to estimate the capsule position $\mathbf{d}$ with respect to the EPM) by leveraging onboard sensor readings are reported in [68, 216]. Briefly, using an average of the measurements provide by MFSs lying on the same axis, the three components of the magnetic field vector $\mathbf{B}_{ext}$ are measured at the capsule center. The $\mathbf{B}_{ext}$ vector is then rotated according to

$$\mathbf{B}'_{ext} = R_m^T R_c R_m \mathbf{B}_{ext}, \tag{D.11}$$

where R_c is the rotational matrix of the capsule reference frame with respect to the global Cartesian coordinate system, while R_m is the rotational matrix of the reference frame at the EPM with respect to the global Cartesian coordinate system, as represented in Fig.

D.1. The matrix R_c is obtained in real time from the readings acquired by the inclinometer integrated in the capsule, while R_m is derived from the data acquired by the inclinometer mounted on the EPM.

Then, a search within a precalculated magnetic field map is performed to find the capsule position $\mathbf{d}$ that would match with the actual magnetic field vector $\mathbf{B}^{'}_{ext}$. The magnetic map – associating each point $\mathbf{d}$ within the workspace to the related magnetic field intensity $\mathbf{B}^{'}_{ext}$ – denotes the search space for the inverse localization procedure. The effective localization workspace – defined as the search space of potential capsule positions – extends 15 cm away from each side of the EPM. The only limitation of this localization method is that capsule or EPM orientation around the $\mathbf{z}$ axis of the global Cartesian coordinate system cannot be measured by the inclinometers used to generate R_c and R_m. This sets a constraint on the experimental procedure that the capsule and the EPM must lay on parallel vertical planes for the entire duration of the measurement. If taken into account when designing the measurement protocol, this constraint does not limit the effectiveness of the platform in acquiring reliable *in vivo* data on intestinal resistance properties, as demonstrated in section D.4.3.

The capsule velocity and acceleration can be estimated as the first and second time derivative of $\mathbf{d}$, respectively. However, direct measurement of $\ddot{\mathbf{d}}$ from the accelerometer provides better accuracy, as briefly discussed in section D.4.1. Considering the computational platform described in section D.3.5, the time required to estimate the capsule position with respect the magnetic source is 16 ± 2.5 ms.

D.3.4 Communication and Power Supply Modules

The readings of the sensors integrated in the FMSM are acquired by the onboard wireless microcontroller. An acquisition cycle starts from sampling seven analog inputs – six connected to the MFS outputs, and one to the battery for monitoring the charge status. Then, the three digitized values of acceleration are received from the 128 kbyte/s SPI bus connected to the onboard accelerometer. This dataset is acquired every 4.4 ms by the microcontroller and used to build a 32-byte package together with the wireless signal strength indicator, the battery level, an incremental package number identifier, and the start/stop bytes. This package is then transmitted by the wireless microcontroller to the external transceiver over a 2.4 GHz carrier frequency, with a refresh time of 6 ms (wireless data throughput 42.4 kbit/s), resulting in sampling rate of 166 Hz. The external transceiver is based on an identical microcontroller (CC2530, Texas Instruments, USA) which communicates with the PC through a USB-serial converter (UM232R, FTDI, UK).

The power supply module embeds a low-dropout voltage regulator (LDO) (TPS73xx, Texas Instruments, USA) to provide a stable supply to both FPMS and communication modules. In order to limit the current consumption when the device is not acquiring measurements, a digital output of the microcontroller can drive the SLEEP pin of all the MFS. This results in a current consumption which varies between 400 μA, when the microcontroller is in low power mode, and 20 mA when it is in IDLE mode with the radio active. Average current consumption rises to 48 mA during a single cycle of sensor data acquisition and wireless transmission. The power source used is a 50 mAh, 3.7 V rechargeable LiPo battery (Shenzhen Hondark Electronics Co., Ltd., China, 12 mm × 15 mm × 3 mm in size).

D.3.5 User Interface

A multi-thread C++ WIN32 application running on the PC unbundles the data and shares them via TCP-IP communication with a second application (developed in MATLAB, Mathworks, USA), which runs in parallel to implement the estimation algorithms and the user interface. The data transfer rate between the two applications is 30 Hz, while the refresh time for capsule position $\mathbf{d}$, acceleration $\ddot{\mathbf{d}}$, and intermagnetic force $\mathbf{F}_a$ is 50 ms (refresh rate 20 Hz). Two real-time plots are displayed on the main screen, as represented on the right side of Fig. D.5. The applied intermagnetic force $\mathbf{F}_a$ is shown on the left as a function of time, while the position and orientation of the capsule reference frame $\{\mathbf{x}_c, \mathbf{y}_c, \mathbf{z}_c\}$ with respect to the EPM reference frame $\{\mathbf{x}_m, \mathbf{y}_m, \mathbf{z}_m\}$ are displayed in real time on the right side. Numerical values for capsule position $\mathbf{d}$ and velocity $\dot{\mathbf{d}}$ are also shown, together with the most current values of the battery voltage and the wireless signal strength indicator. Capsule velocity $\dot{\mathbf{d}}$ is filtered by applying a 5-element moving average. A visual indicator alerts the user every time that motion starts, in agreement with Eq. D.10. The user interface also allows the user to set the initial bias for the measurement and to record the data in a spreadsheet file.

D.4 Platform Assessment

D.4.1 Validation of Intermagnetic Force and Capsule Position Estimation

The setup used to assess the intermagnetic force and capsule position estimation is represented in Fig. D.5. The wireless capsule was mounted on a rigid support connected to a six-axis load cell (NANO17, ATI Industrial Automation, USA, resolution 1/160 N). The load cell output was assumed as reference for $\mathbf{F}_a$ measurement. The EPM was mounted at the end effector of a six-degree of freedom robotic manipulator (RV6SDL, Mitsubishi Corp., Japan). The robotic arm allowed the EPM to move inside the workspace instead of the capsule, providing a reference for the EPM-capsule separation vector $\mathbf{d}$ via the built-in encoders (resolution of 1 μm). A second six-axis load cell (MINI 45, ATI Industrial Automation, USA, resolution 1/16 N) was placed in between the EPM and the robotic arm. This load cell was used as shared control input [217] to impose the desired EPM trajectories during the validation. The capsule and the EPM reference frame orientations are shown in Fig. D.5, together with the position of the external inclinometer.

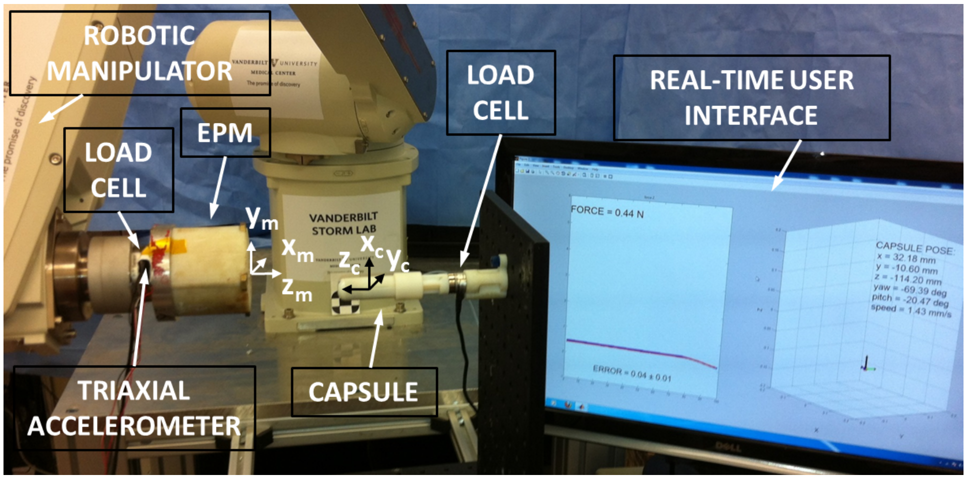

Figure D.5: Experimental setup used to assess the intermagnetic force and capsule position estimation.

A total of 20 trials were performed by moving the EPM inside a workspace defined as $\{x_c \in [0cm..15cm], y_c \in [-15cm..15cm], z_c \in [0cm..15cm]\}$. The space with $\mathbf{x}_c$ negative was not considered, since it is not accessible for the EPM during *in vivo* trials. For each measurement, the EPM was moved along the $\mathbf{z}_c$ axis from 15 cm to 5 cm away from the capsule and back. The EPM position along the $\mathbf{x}_c$ and $\mathbf{y}_c$ axes was varied randomly by the operator for each trial. Rotations of the EPM around $\mathbf{y}_m$ were avoided to satisfy the constraint mentioned in section D.3.3.2. The estimated modules of $\mathbf{F}_a$ and $\mathbf{d}$ are plotted in Fig. D.6 together with the module of the EPM position, as derived from the manipulator encoders, and the module of the force along $\mathbf{z}_c$, as measured by the load cell connected to the capsule. These plots are related to a part of a trial where the EPM was moved mainly along the $\mathbf{z}_c$ axis for about 9 cm.

The data recorded during the 20 trials were statistically analyzed to derive the average error and the standard deviation of both $\mathbf{F}_a$ and $\mathbf{d}$ within the entire workspace. The proposed method presented an average error of 0.079 ± 0.049 N in estimating the intermagnetic force $\mathbf{F}_a$. As regard to capsule position $\mathbf{d}$, the average estimation error was 3.34 ± 2.23 mm for the x component, 4.12 ± 2.88 mm for the y component, and 6.45 ± 4.84 mm for z component. Given these results, it is possible to estimate how the uncertainty in position would propagate to the acceleration if this is calculated as the second time derivative of $\mathbf{d}$.

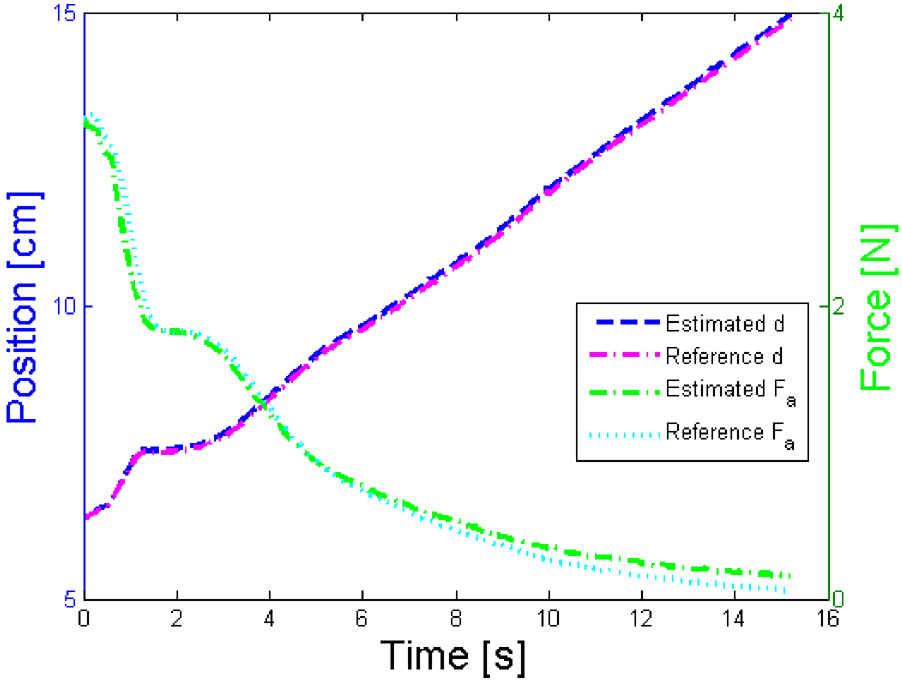

Figure D.6: Modules of the estimated force $\mathbf{F}_a$, the reference force along $\mathbf{z}_c$, the estimated position $\mathbf{d}$, and the reference position as measured by the robotic manipulator encoders for part of a trial where the EPM was moved mainly along the $\mathbf{z}_c$ axis (i.e., from {x$_c$=8 mm, y$_c$=-10 mm, z$_c$=62 mm} to {x$_c$=8 mm, y$_c$=-5 mm, z$_c$=148 mm}.

By applying the Kline-McClintock method [218], the uncertainty of $\ddot{\mathbf{d}}$ as a derived measurement from $\mathbf{d}$ would be in the order of 0.6 m/s^2, thus demonstrating that the $\ddot{\mathbf{d}}$ is more reliably quantified by the onboard accelerometer.

D.4.2 Validation of Resistant Force Estimation

The goal of this experiment was to assess the entire platform in reconstructing a known resistant force applied to the capsule. As represented in Fig. D.7, the capsule was connected to a support frame through a two-element metallic spring (180-A W.B., Jones Spring CO, Inc.) with a nominal elastic constant k of 192.6 N/m. The EPM – mounted on the robotic manipulator – was approached to the capsule from the opposite side of the spring in steps of 2 mm, until the magnetic force did not overcome the elastic force and the capsule started accelerating towards the EPM. Foam placed on top of the EPM prevented damaging the capsule. Spring elongation Δx was measured by real-time image analysis. This approach allowed an estimation of the capsule motion profile that was independent and one order of magnitude more accurate than the method proposed in section D.3.3.2. In particular, an optical tracker was implemented by acquiring and elaborating images from a USB camera

(MacAlly MegaCam 2.0 Megapixel, 30 fps with 1600×1200 pixel resolution) to track the position of a marker painted on the capsule. Calibration of the tracker consisted of finding the spatial resolution in terms of mm/pixel and defining the image window where the capsule would move during the experiment. Overall accuracy and sampling rate for Δx as measured by optical tracking was 0.15 mm and 35 ms, respectively.

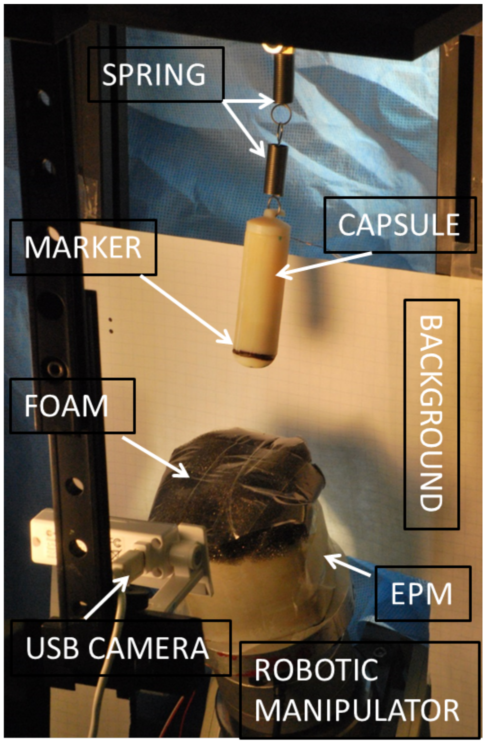

Figure D.7: Experimental setup used to validate the reconstruction of a known resistant force.

The plot in Fig. D.8.A shows with a blue solid line the module of the estimated resistant force $|\mathbf{F}_r^{est}| = |\mathbf{F}_a - m\ddot{\mathbf{d}}|$, where $\mathbf{F}_a$ is obtained with the method described in section D.3.3.1, m is the mass of the capsule, and $\ddot{\mathbf{d}}$ is measured by the onboard accelerometer. On the same plot, the dashed green line represents the reference for the module of the resistant force, obtained by $|\mathbf{F}_r| = k\Delta x$, where k is the nominal constant of the spring and Δx is the spring elongation as measured by the optical tracker. The dashed vertical line indicates the instant when the EPM was moved towards the capsule by 2 mm, but the magnetic force was not enough to overcome the elastic force. The solid vertical line indicates a second 2-mm motion of the EPM towards the capsule. This event is almost coincident with the start of capsule motion as detected by Eq. D.10.

Focusing on the data acquired during the elongation phase of the spring, Fig. D.7.B shows $|\mathbf{F}_r^{est}|$ (solid blue line) as a function of the capsule position $|\mathbf{d}|$, as estimated by the method described in section D.3.3.2. On the same figure, the reference $|\mathbf{F}_r|$ (dashed green line) is plotted as a function of the capsule position measured by the optical tracker. Since the capsule was moving in a straight line, we can assume that the variation in position corresponds to the spring elongation. Therefore, the slope of the solid blue line provides an estimation of the spring constant. Such an estimation is 203.1 N/m, thus showing a 5.45% deviation from the nominal value.

D.4.3 In Vivo Validation

The feasibility of measuring resistant forces in the large intestine with the proposed wireless platform was then assessed *in vivo* on an anesthetized porcine model. The primary measure of interest was to acquire the static resistant force that a magnetically-driven capsule must overcome to begin its motion in a living colon. The dynamic behavior of the resistant force was also recorded, together with the position profile, as the capsule was moving toward the EPM under the effect of magnetic attraction.

Secondary measures of interest were the time to complete a single measurement, platform usability, assessment of the workspace, and robustness of the measurement with respect to electromagnetic interference. Reliability of the wireless link was also assessed.

The porcine surgery was performed at Vanderbilt University under IACUC protocol M/13/003. A 41-kg female Yorkshire swine was used for this study. After intravenous sedation, a laparotomy was performed to access the abdominal cavity. Then, the wireless capsule was inserted into a segment of the colon by intestinal ostomy, as represented in Fig. D.9.A. The colon segment was straightened and sutured to the abdominal wall along the sagittal plane (two sutures spaces approximately 180 degree apart along the same circular segment) to prevent the capsule from dragging the tissue as it moved. The other end of the segment was left unconstrained, so that the capsule was subjected to both circular and longitudinal muscle contraction. The length of the straightened segment was approximately 15 cm, thus allowing the capsule enough room to travel forward. A surgical marker was used to label 15 cm distal from the point of the suture. The midline incision was then sutured and the external transceiver was positioned on the porcine abdomen. As shown in Fig. D.9.B, the EPM was placed parallel to the sagittal plane of the animal body, so that it would lie on the same vertical plane as the capsule and the straightened segment of large intestine. This satisfies the constraint defined in section D.3.3.2 for a correct estimation of capsule motion profile. The acquisition software and the user interface were started, so that the user holding the EPM was able to see in real time both the intermagnetic force and the position and orientation of the capsule with respect to the EPM. The user interface also warned the user if the EPM and the capsule were both within the measurement workspace. Then, the operator moved the EPM closer to the capsule in steps of approximately 5 mm, until the user interface signaled that the capsule was starting to move. This process was repeated for ten times on the same segment of large intestine, always forcing the capsule to travel away from the anus. At the end of each measurement, the midline incision was opened and the capsule was moved backward to its starting position. For each trial, the platform recorded the intermagnetic force $\mathbf{F}_a$, the EPM-capsule separation distance $\mathbf{d}$, the capsule acceleration $\ddot{\mathbf{d}}$, and the time t_0 when the motion started as indicated by Eq. D.10. From these data, the algorithm calculated the resistant force $\mathbf{F}_r$ and the capsule velocity $\dot{\mathbf{d}}$. During data analysis, the capsule velocity was used to confirm that the capsule was moving.

Two of the ten trials were excluded as the capsule did not accelerate fast enough to satisfy the trigger condition. The mean static resistant force $\mathbf{F}_r(t_0)$ recorded from the remaining eight trials was 0.21 N with a standard deviation of 0.06 N. The order of magnitude of this result agrees with previous literature data [112, 219].

A plot of the modules of $\mathbf{F}_r$ and $\mathbf{d}$ for one trial is shown in Fig. D.10. The adjustment in position of the EPM before the capsule started moving can be identified at the beginning of the two curves (dashed vertical line), where the position profile suddenly decreases and the force increases. The increase in the estimated $\mathbf{F}_r$ as the capsule moves towards the EPM can be explained by the exponential increase in the magnetic force, combined with the capsule decelerating at the end of the colon segment, where the tissue in between the capsule and the EPM prevents any further motion. The profiles reported in Fig. D.10 suggest that the capsule was already moving before the platform detected its motion. However, before t_0, the acceleration was not strong enough to satisfy the condition in Eq. D.10. As suggested in section D.3.3.2, position $\mathbf{d}$ and velocity $\dot{\mathbf{d}}$ profiles can be analyzed to have a more sensitive condition for detecting the instant when capsule motion starts.

The time to complete a single measurement was 5 ± 1 minutes, from the moment that the EPM was introduced into the workspace to the instant when the capsule was placed back in the starting position. Thanks to the information available to the operator in real time, the platform was easy to use in all trials, and the protocol was performed without any need for adjustment. The workspace was confirmed to extend 15 cm away from each side of the EPM, and the effect of electromagnetic interference due to the equipment present in the operating room was negligible. The wireless link was reliable for about the 98% of data transmissions and battery operation was effective for the entire procedure. The *in vivo* experiment was one hour and fifteen minutes long.

D.5 Conclusions and Future Work

This manuscript introduces for the first time a wireless real-time platform for the *in vivo* measurement of the resistant force that a magnetically-driven capsule must overcome to move inside the GI tract. The platform takes advantage of a wireless capsule, magnetically coupled with an EPM, and is able to provide the real-time profile of both the intermagnetic force and capsule acceleration. The EPM-capsule separation vector and the capsule velocity are also estimated in real time, as well as the instant when the capsule starts moving under the effect of the external magnetic field. This information is used to derive the dynamic profile of the resistant force opposing magnetic attraction.

The platform was assessed via three-tier validation. First, the intermagnetic force and capsule position estimation was assessed with a dedicated benchtop trial using a robotic manipulator as a benchmark for position and a commercial load cell as reference for the intermagnetic force. The average error in estimating the force and the position was less than 0.1 N and 10 mm, respectively. A second benchtop experiment was then performed to validate the dynamic reconstruction of $\mathbf{F}_r$ from the intermagnetic force and capsule motion estimation, using in this case a spring as reference for $\mathbf{F}_r$. The platform was able to estimate the spring constant with a relative error of 5.45%. Finally, the platform was assessed *in vivo* in a porcine colon model, where $\mathbf{F}_r$ was successfully measured.

While a statistically relevant study of the resistant forces of the porcine intestine was outside the scope of this study, this platform can be applied to more extensive biomechanical studies in the future (i.e., different segments of the GI tract can be investigated, and the force required to move with or against peristalsis can be measured). This would provide a quantitative understanding of resistant properties of the GI tract, paving the way for improved realistic biomechanical models.

Future improvements to the platform will aim to reduce the capsule size, extend the localization workspace, improve the localization accuracy, and add the sixth degree of freedom (i.e., rotation of the capsule about the $\mathbf{z}$ axis of the Global Cartesian coordinate system) to the localization algorithm. A promising approach of this direction consists in adopting the methods described in [220–222] for forward modeling and inverse localization of electric currents and magnetic fields in the GI tract.

Real-time knowledge of both the intermagnetic force and capsule motion profile can be used for robotic-guided capsule endoscopy. To the best of our knowledge, none of the platforms proposed thus far for magnetic control of endoscopic capsules [27, 30, 68, 108, 113, 145, 146] implements a real-time tracking of capsule position and intermagnetic force. Integrating the methods proposed in this work in a platform such as the one reported in [147] would enable ”closed-loop control” of magnetic locomotion, by adjusting in real time the external source of the magnetic field to optimize the coupling with the capsule at any given point in time. Insufflation techniques such as the one proposed by the authors in [147, 223] would then prevent the magnetic capsule from becoming stuck along the way during the endoscopic examination.

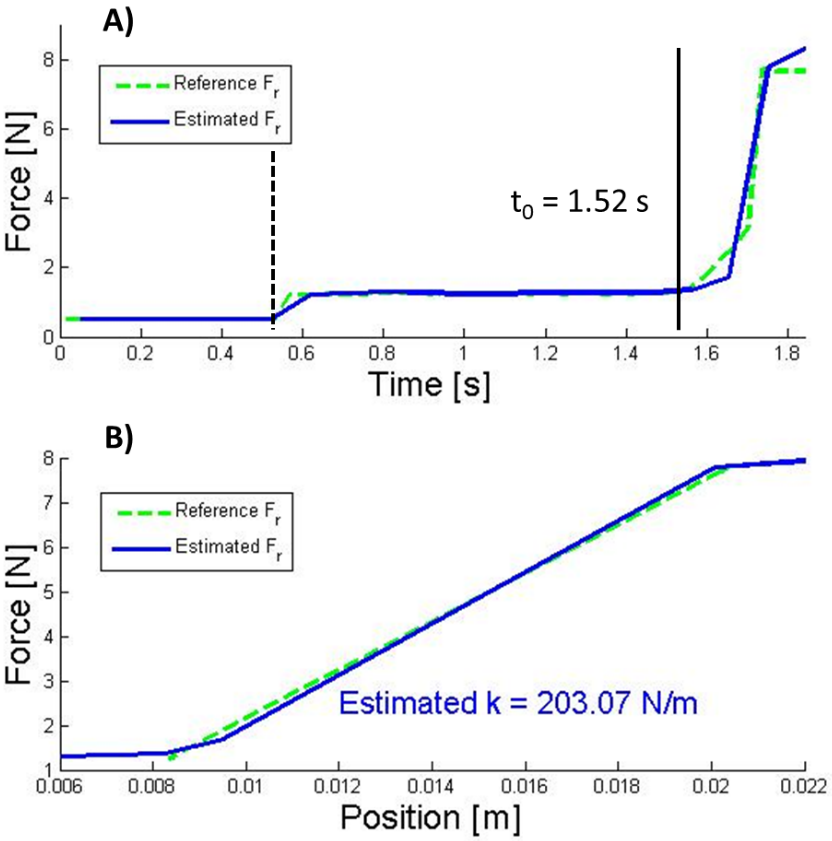

Figure D.8: (A) Time variation of the modules of the resistant force estimated with the proposed method (solid blue line) and reference (dashed green line). The dashed vertical line indicates the instant when the EPM was moved towards the capsule by 2 mm, but the the magnetic force was not enough to overcome the elastic force. The solid vertical line indicates a second 2-mm motion of the EPM towards the capsule. This event is almost coincident with the start of capsule motion as detected by Eq. D.10. (B) Modules of the resistant force estimated with the proposed method (solid blue line) and reference (dashed green line) plotted as a function of capsule position.

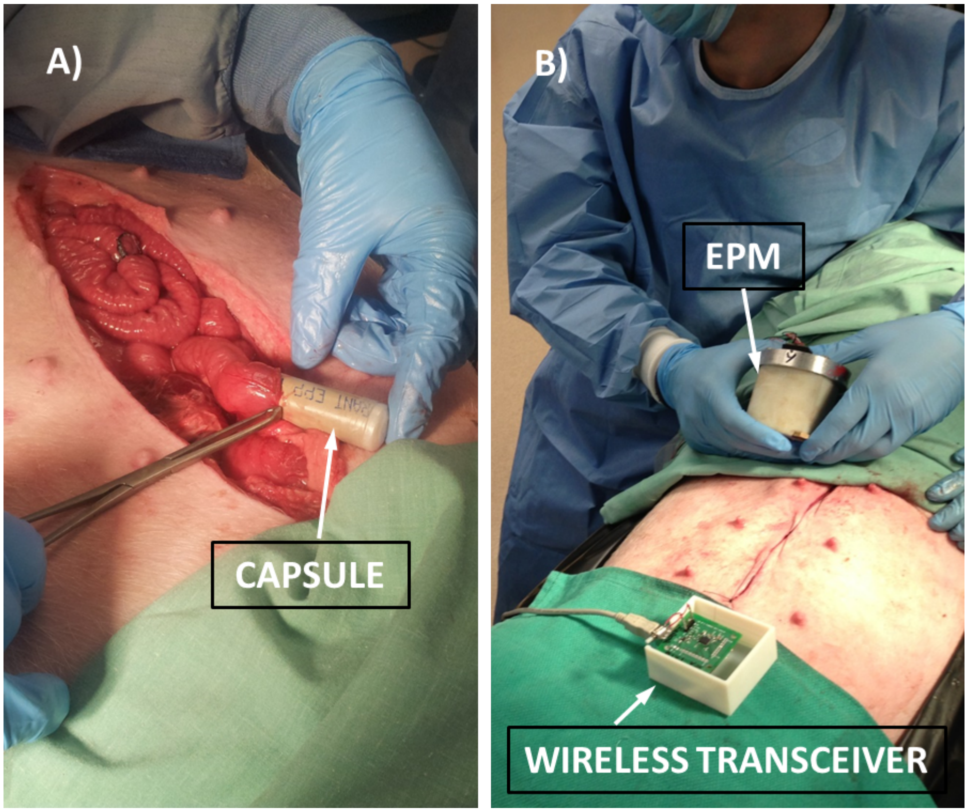

Figure D.9: Photograph of the operative setup during the *in vivo* trial. (A) The wireless capsule being introduced in the porcine large intestine. (B) The surgical field during measurement.

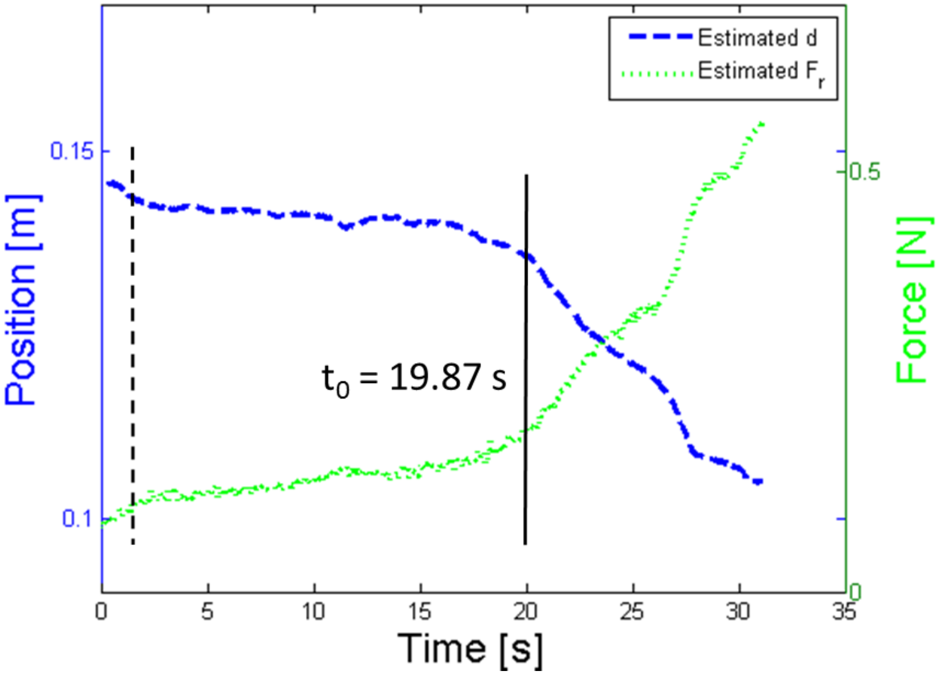

Figure D.10: Plot of the modules of $\mathbf{F}_r$ and $\mathbf{d}$ acquired during the *in vivo* trial. The dashed vertical line indicates the instant when the EPM was moved closer to the capsule, while the solid vertical line indicates the instant when capsule motion started.

Appendix E

TRANS-ABDOMINAL ACTIVE MAGNETIC LINKAGE FOR ROBOTIC SURGERY: CONCEPT DEFINITION AND MODEL ASSESSMENT

C. Di Natali, T. Ranzani, M. Simi, A. Menciassi, P. Valdastri

From: IEEE International Conference on Robotics and Automation (ICRA), pg 695–700
Status: 2012

E.1 Abstract

The novel concept of Trans-abdominal Active Magnetic Linkage for laparoendoscopic single site surgery has the potential to enable the deployment of a bimanual robotic platform trough a single laparoscopic incision. The main advantage of this approach consists in shifting the actuators outside the body of the patient, while transmitting a controlled robotic motion by magnetic field across the abdomen without the need for dedicated incisions. An actuation mechanism based on this approach can be comprised of multiple anchoring and actuation units, mixed depending upon the specific needs. A static model providing anchoring and actuation forces and torques available at the internal side of the magnetic link was developed to provide a tool to navigate among the many possibilities of such an open ended design approach. The model was assessed through bench top experiments, showing a maximum relative error of 4% on force predictions. An example of a single degree of freedom manipulator actuated with the proposed concept and compatible with a 12-mm access port is able to provide an anchoring force of 3.82 N and an actuation force of 2.95 N.

E.2 Introduction

Robotic surgery is currently a popular, widely accepted clinical practice, thanks to the large scale use of the Intuitive Surgical's Da Vinci platform [165]. The next generation of surgical robots should guarantee the same dexterity and performance, while reducing access trauma. A promising approach in this direction is represented by robotic platforms specifically developed for (or adapted to) laparoendoscopic single site (LESS) surgery [34, 39, 85, 224]. Actuation for the several degrees of freedom (DoFs) may be external, by means of cables [34, 85], internal, using on-board motors [224], or hybrid [39]. In these cases, the mechanical continuity of the kinematic chain constrains the workspace to the proximity of the insertion point. Having the single components of the platform, i.e. at least 2 manipulators and one camera, magnetically linked across the abdominal wall as in [115], would greatly enhance both freedom of operation and triangulation. However,

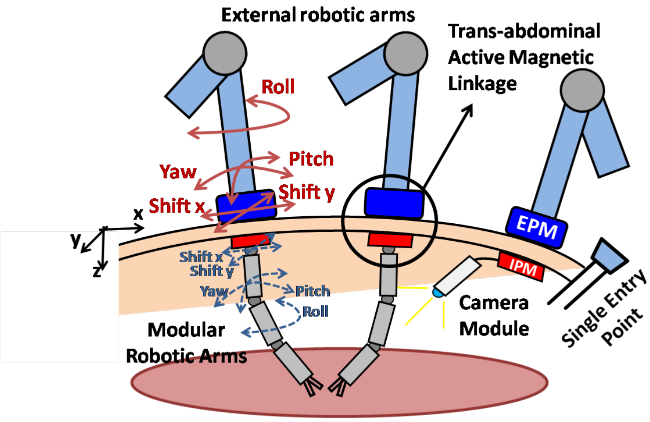

Figure E.1: Concept of a magnetically actuated surgical platform. On the left are shown the several DoF that can be obtained by simple magnetic coupling.

in the previous works, robotic manipulators based on this kind of approach were always actuated by on-board electromagnetic motors [1, 115]. Assuming that the available power (torque x velocity) in such an actuator scales with mass and volume, the motors that can fit a tiny single incision, as desirable in LESS, have very limited performance. This limits the effectiveness of the platforms proposed in [1,115,225] for real-time teleoperation of a surgical task. Larger, more powerful motors can be used at the price of enlarging the access port [39]. For that reason, a novel kind of robotic actuation is desirable to achieve a concrete step ahead in robotic surgery. In particular, moving the actuators outside of the body, but still taking advantage of the reduced access trauma guaranteed by a trans-abdominal magnetic coupling, would provide dexterity, while preventing the need for powerful on-board motors.

A first step, and straightforward approach, towards meeting this goal can be realized by mounting permanent magnets to the end effectors (EE) of industrial robotic arms. As represented in Fig. G.1, two manipulators and one camera can be introduced into the abdomen by a single incision, as demonstrated in [115], and each can be coupled with an external magnet held by a robotic arm. If the EE and the internal modules are properly designed, up to 5 degrees of freedom (DoF) can be transmitted by moving the external permanent magnet (EPM). Referring to the left arm in Fig. G.1, roll and X Y translation will work against the friction of the internal module on the abdominal wall, while pitch and yaw must counteract the elasticity of the abdominal tissue. Having the EPM driven by a robotic arm would provide a better precision of movement, however, the dynamic interaction with the abdominal wall will always introduce unreliability in the control loop. Therefore, the best use of this approach may be gross positioning before starting a procedure, i.e. when high precision and repeatability of movements are not a stringent requirement.

A step forward in terms of robotic control was introduced in [226], where a laparoscopic camera with a controlled tilt was presented. In that case, an on-board motor was rotating a permanent magnet, thus changing in real time the trans-abdominal magnetic coupling. Once the camera was set in place by manual operation of the EPM, the tilt was activated, thus obtaining a span of 80^o with a resolution of 0.01^o. One of the main advantages of this approach, referred as Trans-abdominal Active Magnetic Linkage (TAML), consists of the possibility of actuating a DoF without manual operation of the EPM, thus enhancing stability of motion and repeatability.

Having severe size constraints for the modules that are to be introduced into the abdomen (i.e. outer diameter smaller than 12mm) does not allow for a stronger motor to be used on-board. Thus, to achieve higher forces and torques the best option is to move the actuators outside the patient's body and use the largest magnets possible on board the surgical devices.

Through controlled motion of the external magnets, one or more DoF can be transmitted over the TAML to the internal manipulators. Thanks to this approach, the only components that are required on board the manipulator to achieve controlled motion are the permanent magnets embedded in a properly designed mechanism.

In this paper we better detail the TAML actuation concept and we present and validate a static model for the TAML. The model is then used to predict the performances that can be achieved by the single modules composing a TAML operated DoF. Given the modularity of TAML components and the different mix in terms of performance that can be achieved with them, the model represents a first fundamental step in assessing the effective potential of the TAML approach for a less invasive robotic surgery.

E.3 Principle of Operation

An actuation mechanism based on the TAML concept can be seen as a modular structure, composed by a number of magnetic couples, each having one magnet inside and one outside the abdomen, with each couple carrying out a different function. In more specific terms, the system is comprised of:

- *Anchoring unit*, composed of an external and an internal permanent magnet (EPM and IPM, respectively), whose function is to provide an anchoring force to the internal magnetic instrument during the surgical procedure.

- *Actuation unit*, composed of an external driving EPM and an internal driven IPM. The external driving EPM is connected to a motor and can be actuated independently, causing the actuation of the respective internal driven magnet, coupled across the

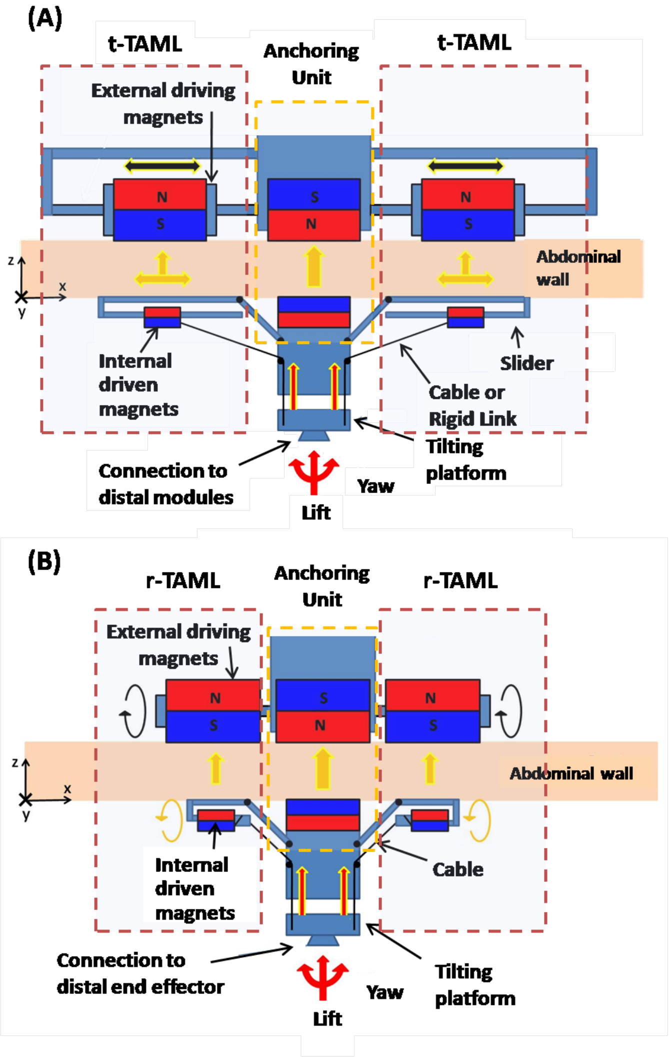

Figure E.2: Two examples of combining TAML units to obtain 2 DoF: (A) Combination of an anchoring unit and two t-TAML units; (B) Combination of an anchoring unit and two r-TAML units.

abdominal wall. The internal driven magnet can be used to actuate one or more DoFs of the internal module by cable or rigid link transmission.

Focusing on the actuation unit, a further dichotomy can be established by considering two different types of driving architectures. In simplistic terms, these two actuation architectures can be described as follows:

- *translational-TAML (t-TAML)*, where the external driving magnet is translated along a horizontal direction on a parallel plane to the abdominal wall. The external driving magnet, while translating, drags the internal driven magnet. Horizontal force at the IPM can be used to actuate a DoF of the internal module.
- *rotational-TAML (r-TAML),* where the external driving magnet is rotated about its main axis. The driven magnets will rotate accordingly, trying to minimize the phase shift. Considering a cable winding up on the IPM shaft, the torque available at the IPM can be used to actuate an internal DoF.

The TAML concept can be realized in practice by mixing a number of constitutive elements. Two examples of combining one anchoring and two actuation units to achieve 2 DoF are represented in Fig. G.2.a and G.2.b for t-TAML and r-TAML, respectively. In particular, through asymmetric operation of the two actuation units it is possible to achieve yaw of the platform. Lift can be obtained by a symmetric operation, while push is possible only in the case of t-TAML with rigid link transmission from the IPM to the platform. A clear design advantage of the r-TAML over the t-TAML consists in the much larger workspace, since the actuating cable can be wound on a reel, while in the t-TAML, the range is limited by the length of the slider the driven IPM is travelling on.

Of course, a proper mechanism (e.g. umbrella-like) will be required to deploy the concepts represented in Fig. 2a and 2b through a surgical port. On the other hand, before designing such a complex mechanism, a clear idea of the optimal mix of TAML units and the overall performance must be available. Given the many variations possible, a reliable model would provide the best way to select the most promising configuration before investing resources in the fabrication of a concept.

In particular, having a model which is able to predict the anchoring force for a specific anchoring unit and the force available at the IPM for a specific actuation unit, given EPM and IPM distance and features (strength and orientation of magnetization and geometry), would benefit designers by allowing for prediction of the overall performance of a TAML modular design through superposition. Such a model is introduced, assessed and used for predictions in the following sections.

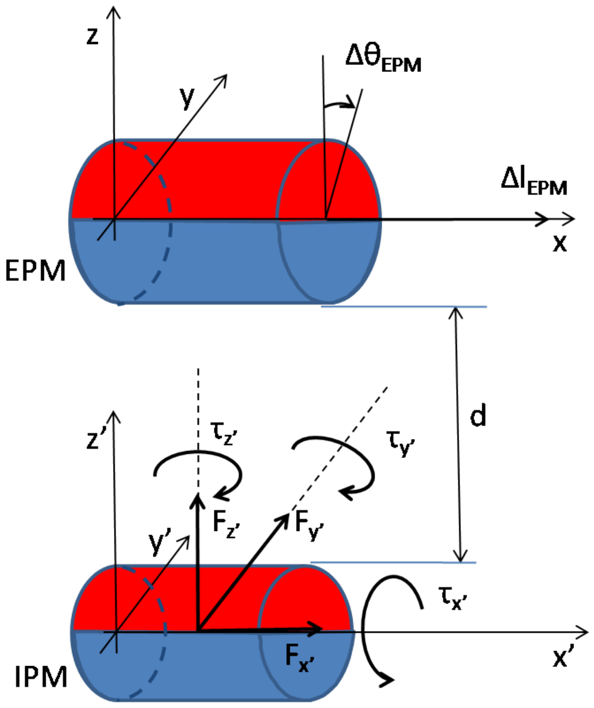

Figure E.3: Schematic representation of EPM and IPM for a typical TAML unit. The EPM is a cube in the anchoring and in the t-TAML units and a cylinder in the r-TAML unit.

E.4 Modeling

A first piece of information toward the design of a TAML device consists in predicting the maximum anchoring and actuation forces that are available at the IPM, given the main features of the magnetic link. To this end, a static model was developed as a first step toward establishing a complete modeling framework to describe this novel approach to mechanical power transfer. Since relative permeability of off-the-shelf NdFeB permanent magnets is approximately equal to the permeability of air ($\mu_r\tilde{1}$) and assuming that the environment does not contain ferromagnetic materials which are not included in the model, it is possible to apply the principle of superposition [90] to extend static model predictions to more complex magnetic configurations, as the ones represented in Fig. G.2. Additional steps in modeling should then address the dynamical behavior, so to enable closed-loop control, and the real-time interactions with the abdominal tissue, which are affecting the distance between EPM and IPM at any given time.

Input parameters to the developed static model are the type of magnetization (i.e. strength and direction), geometrical features of the magnets, distance between them, and the kind of motion of the driving magnet. The model provides the attraction force between the two magnets, i.e. the anchoring force for the IPM, and force and torque at the driven magnet in response to a translation or rotation of the driving magnet. The model is built upon the theories and the methods used in the analysis of steady currents, permanent magnets and magnetic circuits [90]. Referring to Fig. G.3, the force E.1 and the torque E.2 at the IPM can be expressed as:

$$F = \oint_S j_m \times B_{ext} ds \tag{E.1}$$

$$T = \oint_S r \times (j_m \times B_{ext}) ds \tag{E.2}$$

where j_m is the equivalent surface current density on the IPM, r is the IPM radius, while B_ext is the rotating magnetic field E.3 induced by the EPM, which can be obtained by the magnetic charge model as:

$$B_ext(x) = -\frac{\mu_0}{4\pi} \oint_S \nabla \frac{M_EPM(x')\hat{n}}{\mid \mathbf{x} - \mathbf{x'} \mid} ds' \tag{E.3}$$

where $\mathbf{x}$ is the observation point, $\mathbf{x'}$ is the source point and M_EPM is the EPM magnetization. This equation, obtained by applying the free-space Greens function, analytically describes the spatial components of the field generated by a magnetic source. In our case the source is the EPM and the observation point is the IPM. IPM features are modeled by

j_m intended as the infinitesimal element of current flowing on the surface element ds. To quantify j_m E.4, we can apply:

$$j_m = \mathbf{M}_{IPM}\hat{n} \tag{E.4}$$

where n is the unit vector normal to ds, while $\overrightarrow{M}_{IPM}$ is the IPM magnetization vector. Force and torque at the IPM can be computed using MatLab (MathWorks) to numerically solve the above equations with the Finite Element Method (FEM). In order to predict attraction force and actuation forces on the IPM for the different TAML units, the model was applied to three different scenarios. The same kinds of trials were then replicated as bench top experiments to assess model predictions. The only constraint that was considered in selecting the magnets was the possibility to introduce the internal part of the unit through a 12-mm surgical trocar (5-12 Vesaport Plus, Covidien, Norwalk, CT, USA).

Predicting the attraction force $F_{z'}$ available at the IPM for the anchoring unit was the goal of the first simulation. In this case, a cubic N42 magnet with a size of 30 mm and magnetized along the Z axis was selected as EPM. A N52 cylindrical magnet with a radius of 6 mm, a length of 13 mm, with the main axis laying on X' and magnetized along Z' was used as IPM. EPM and IPM were separated by a distance, d, of 30mm. This distance corresponds to the average thickness of the abdominal wall upon insufflation [225]. The static model provided an estimation for $F_{z'}$, being all the other components of force and torque on the IPM equal to zero.

The main objective for the second test was to quantify the horizontal force $F_{x'}$ available at the IPM for the t-TAML unit. The same EPM and IPM described for the anchoring force trial, still spaced by 30 mm, were used. The EPM was moved along the X axis in steps of Δl_{EPM}=1 mm, starting from a position where both EPM and IPM centers were laying on the same coordinate on the X axis, until reaching a 100 mm final displacement. The static model provided an estimation of the three components of force and torque acting on the IPM at each step.

The last test was designed to estimate the x' component of the torque, $\tau_{x'}$, at the IPM for a r-TAML unit. In this case, a N42 cylindrical driving magnet with a radius of 9.5 mm, a length of 19 mm, with its main axis laying on X and magnetized along Z was selected as EPM. The same IPM and EPM/IPM distance used for the previous simulations were also adopted in this case. The EPM was rotated about the X axis in steps of $\Delta\theta_{EPM}$=0.5^o, from 0^o to 180^o and the three components of force and torque at the IPM were predicted for each step.

It is worth mentioning that all the cylindrical magnets assumed as IPM were modeled

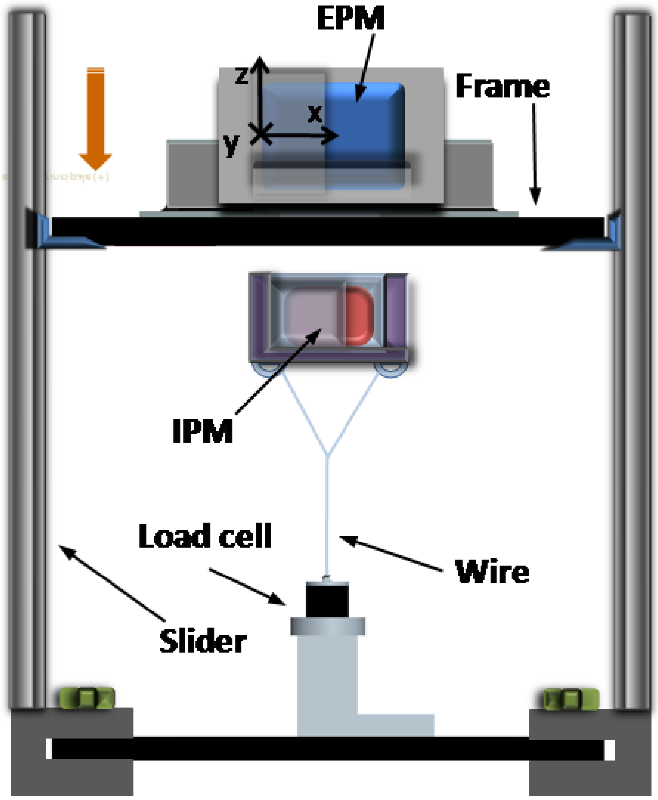

Figure E.4: Configuration of the bench test used to evaluate the anchoring force.

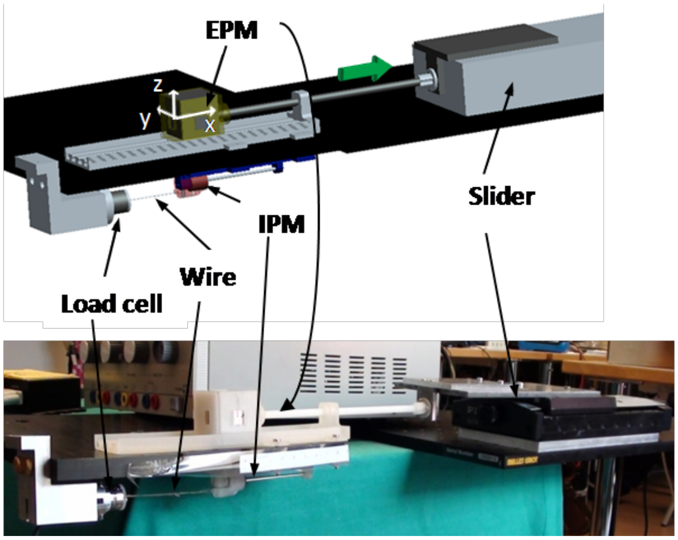

Figure E.5: Experimental data and model prediction for the force $F_{x'}$ available at the IPM for the t-TAML unit.

with a coaxial hollow cylindrical space of 1.5-mm radius to host a shaft for guidance in their final design. Similarly, the EPM used in the r-TAML simulation was modeled with a 3-mm radius coaxial cylinder hole.

The used meshing consisted of about 10,000 elements with a maximum element size fixed to 1/26 of the maximum geometric feature.

E.5 Experimental Assessment

A first step in assessing the model was to verify the predicted magnetic field for a single magnet alone. Magnets having the same features as the ones modeled were acquired from K&J Magnetics, USA. A magnetometer (Kosvaha 5, Wuntronic GmbH, Germany) was used to measure the field surrounding each magnet at a distance of ±30 mm on the Z axis and the data were compared with the model. The maximum error between the model and the experimental data was 0.14 mT on a full range going from -18 mT to 18mT. This translates to a 0.4 % error when compared to a single-magnet model prediction.

The simulations described in the previous section were then validated by three specific bench top experiments, each replicating the EPM/IPM modeled interaction. Force data was acquired using a 6-axis load cell (NANO 17, ATI, USA). During the design of the bench-top experiments particular care was given to preventing interferences to the EPM/IPM magnetic coupling from ferromagnetic materials. Therefore, components that may cause interferences with the magnetic field were placed far enough from EPM/IPM to have a negligible effect.

A first bench top experiment, represented in Fig. G.4, was designed to assess the first simulation. The IPM was connected to the load cell by an inextensible cable and the EPM lowered by a vertical slider down to an EPM/IPM vertical distance of 30 mm. This simple test was repeated five times, in order to bias undesired interferences on the measurements. The offset due to the weight of the IPM was taken into account in comparing modeled data with experimental results. The model predicted an $\mathrm{F}_{z'}$ of 1.63 N, while the average experimental value was 1.70 N. Therefore, the model provides an underestimation of the attraction force with an error of 4%.

A second bench-top experiment was developed to measure the actuating force $\mathrm{F}_{x'}$ available at the IPM for the t-TAML unit. As represented in Fig. G.5, a linear stage (M-410CG, PI, Karlsruhe, Germany) was used to move the EPM along the X direction for 100 mm at a constant speed of 1 mm/s. The IPM, located 30 mm away from the EPM, was connected to the load cell along the X' axis by an inextensible wire, in order to quantify $\mathrm{F}_{x'}$. Model prediction for $\mathrm{F}_{x'}$ and 5 plots acquired during the experiment are reported in Fig. G.6. Considering the specific application, the most important value to be predicted is the peak force, since this will be a performance parameter for the design of the robot. The initial part of the plot will also play a fundamental role, but at a later stage, i.e. when control of the TAML actuator will be implemented. At that stage, a dynamic model will be required for proper closed loop control. From Fig. G.6 we can observe that the peak for $\mathrm{F}_{x'}$ is obtained for Δl_{EPM}=19 mm. Average experimental value for the peak $\mathrm{F}_{x'}$ is 1.10 N, while the model predicted 1.09 N. This translates to a 1.5% relative error. The average error on the initial part of the curve is 11%. This is mainly due to the friction experienced by the IPM travelling on the slide.

Finally, a bench top experiment was designed to assess the model in predicting r-TAML unit performance, as represented in Fig. G.7. The EPM was mounted on a 3-mm radius shaft and connected to a motor (Faulhaber 2342 DC motor) rotating at 0.1 rad/s, while the IPM was mounted on a 1.5-mm radius shaft, winding a cable connected to the load cell. EPM/IPM distance was 30 mm also in this case. The torque around X', $\tau_{x'}$, available at the end effector, scaled by the shaft radius r_{shaft}, is plotted in Fig. G.8 as a function of $\Delta\theta_{EPM}$ for both model prediction and five experimental trials. In this case the peak for $\tau_{x'}$ is achieved at $\Delta\theta_{EPM}$=90^o. After that, control on the IPM is lost due to inversion of polarity. The average peak force available at the IPM shaft was 3.44 N from the experiment, while its predicted value was 3.36 N. This results in an average error for the peak force of 2.3%. The average error in model prediction during the initial part of the plot was on the order of 17% and it was mainly due to cable which was not inextensible as expected.

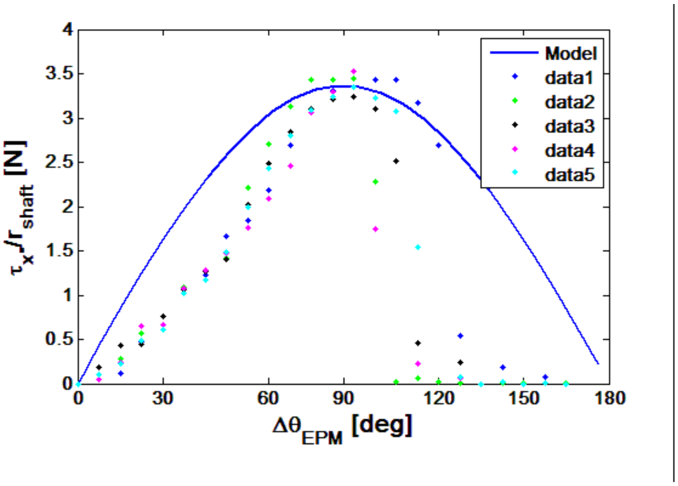

Figure E.6: Experimental data and model prediction for the force $F_{x'}$ available at the IPM for the t-TAML unit.

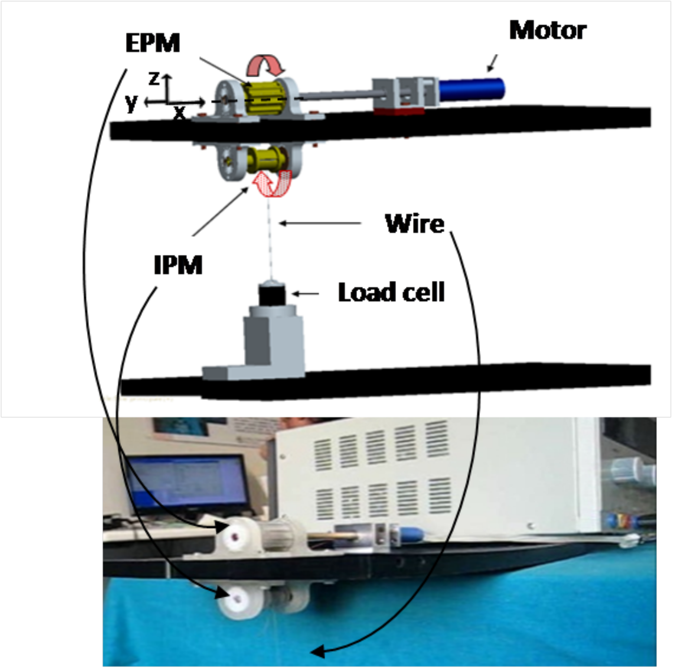

Figure E.7: Bench test developed to evaluate the actuating torque $\tau_{x'}$ for the r-TAML unit.

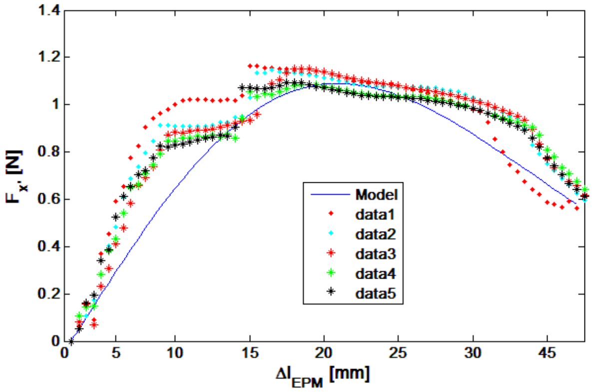

Figure E.8: Experimental data and model prediction for the torque $\tau_{x'}$ scaled by the shaft radius r_{shaft}, as a function of $\Delta\theta_{EPM}$, defined as the angle displacement between magnets' magnetization direction. This is the force available at the IPM for the r-TAML unit.

E.6 Discussion and Conclusion

As previously mentioned, an actuation mechanism based on the TAML can be seen as a composition of single units, mixed depending upon the specific needs. The developed static model is able to provide a reliable prediction of maximum values of forces and torques at the IPM for each single couple of magnets. By applying the principle of superposition, this simple model is able to provide an estimation about TAML peak capabilities. On the other hand, substantial deviations were observed for force and torque in the rising phase toward the regime value. These deviations are due to the simple nature of the static model and to the low level of ideality in the experimental setup. A more precise model is therefore required to move the next step toward dynamical performance prediction and closed loop control.

It is worth mentioning that the r-TAML provides an actuation force which is almost double that of the t-TAML. Additionally, the t-TAML requires the IPM to travel on a linear track to provide actuation, thus imposing severe limitations in terms of space constraints. As previously mentioned, the main advantage for the t-TAML over the r-TAML is the possibility to achieve a push-pull actuation.

As an example of applying the model to a complete TAML design, it is possible to consider the concept represented in Fig. G.9. In this case a r-TAML unit is used in between 2 anchoring units for the cable actuation of a single DoF (J1). If the same IPMs considered for the simulations are used, this manipulator can be introduced through a 12-mm trocar in a straight configuration and moved to the desired position by magnetic dragging. Once in place, the r-TAML unit can be used to actuate the J1 DoF, avoiding any manual motion of the external magnets. Assuming for each unit the same magnetic features used for simulations and bench top assessment and an abdominal tissue thickness of 30 mm, an anchoring force of 3.8 N and an actuating force of 2.9 N can be achieved. These values are derived by applying the superposition of the models of each single unit in a combined simulation. It is interesting to note that the total anchoring force is about the sum of the $F_{z'}$ contributions coming from the two anchoring units (i.e. 1.7 N each) and a 0.4 N contribution coming from the actuation unit. Concerning the actuation force, the value expected from a single r-TAML unit (i.e. 3.44 N) is reduced by the presence of the two anchoring units. Despite being below the 5 N usually considered as the maximum force exerted on the tip of a surgical instrument [227], these results represent an encouraging first step towards the design of a more optimized TAML solution.

Concerning safety, a recent study [228] reported that abdominal wall tolerated a maximum pressure of 7.78 psi even when compressed across a distance of 0.9 cm, thus supporting the further clinical development of the proposed approach.

In addition to estimates of force and torque available at the IPM, the developed model can be used in a "backward" mode, where the input are the desired force and torque value at the IPM, IPM features and EPM/IPM distance, while the output are EPM features. This "backward" mode can be useful for estimating the feasibility of applying the TAML concept to obese patients. For example, the same performance for the design represented in Fig. 9 can be achieved by using EPMs 6 times larger in lateral dimensions in a case where the abdominal tissue thickness is increased to 15 cm. Of course, different kinds of motions for the driving magnet can be devised, resulting in different and, possibly, better performances. Next steps will consist of developing a dynamical model, accounting for inertia, tissue interaction and time variant magnetic effects for each TAML unit to be used in closed loop control of a robotic device.

While a complete bimanual platform for LESS surgical robotics may be considered as the long-term goal of this work, to be pursued by more focused research efforts once the TAML feasibility is assessed, any progress achieved in TAML design and modeling may have an impact on simpler surgical and endoscopic tools, such as magnetic endoscopes or tissue retractors.

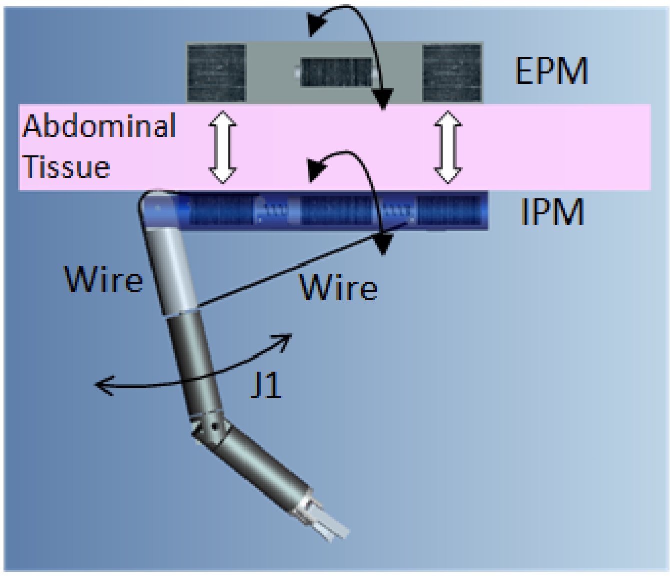

Figure E.9: A possible design implementation combining 2 anchoring units and one r-TAML to operate a single DoF.

Appendix F

CLOSED-LOOP CONTROL OF LOCAL MAGNETIC ACTUATION FOR ROBOTIC SURGICAL INSTRUMENTS

Christian Di Natali, Jacopo Buzzi, Nicoló Garbin, Marco Beccani, and Pietro Valdastri

From: IEEE Transactions on Robotics,
Status: Accepted

F.1 Abstract

We propose Local Magnetic Actuation (LMA) as approach to robotic actuation for surgical instruments. An LMA actuation unit consists of a pair of diametrically magnetized single-dipole cylindrical magnets, working as magnetic gears across the abdominal wall. In this study, we developed a dynamic model for an LMA actuation unit by extending the theory proposed for coaxial magnetic gears. The dynamic model was used for closed-loop control, and two alternative strategies – using either the angular velocity at the motor or at the load as feedback parameter – were compared. The amount of mechanical power that can be transferred across the abdominal wall at different intermagnetic distances was also investigated.

The proposed dynamic model presented a relative error below 7.5% in estimating the load torque from the system parameters. Both the strategies proposed for closed-loop control were effective in regulating the load speed with a relative error below 2% of the desired steady-state value. However, the load-side closed-loop control approach was more precise and allowed the system to transmit larger values of torque, showing, at the same time, less dependency from the angular velocity. In particular, an average value of 1.5 mNm can be transferred at 7 cm, increasing up to 13.5 mNm as the separation distance is reduced down to 2 cm.

Given the constraints in diameter and volume for a surgical instrument, the proposed approach allows for transferring a larger amount of mechanical power than what would be possible to achieve by embedding commercial DC motors.

F.2 Introduction

Magnetic coupling is one of the few physical phenomena capable of transmitting actuation forces across a physical barrier. This ability enables an entirely new paradigm for robotic instruments in minimally invasive surgery (MIS).

In [114], the authors introduced the concept of Local Magnetic Actuation (LMA), where mechanical power is transferred across the abdominal wall by magnetic coupling to drive a degree of freedom (DoF) of a laparoscopic robot. This approach prevents the need for embedded actuators and wired connections. As represented in Fig. F.1, each LMA-based device is composed of at least one anchoring unit, plus an actuation unit per independent DoF. The anchoring unit is composed of an external and an internal permanent magnet, and its function is to support the instrument during surgery. The actuation unit is composed of an external driving permanent magnet and an internal driven permanent magnet. The driving magnet is connected to a motor and can be actuated independently, causing the actuation of the respective driven magnet, coupled across the abdominal wall. The driven magnet is used to actuate, through a mechanism, one DoF of the laparoscopic robot.

A possible implementation of LMA was proposed in [229], with two diametrically magnetized cylindrical permanent magnets working as magnetic spur gears across the abdominal wall. In this case, the external driving magnet in the actuation unit is axially rotated by a motor and the driven magnet rotates accordingly. The mechanical power – in terms of rotational speed and load torque – transferred on the driven magnet can then be used to actuate a mechanism instead of an embedded motor. Considering that the diameter of laparoscopic instruments is constrained by the inner lumen of the surgical port (typically 5 mm to 12 mm), electromagnetic (EM) motors embedded into a robotic device for MIS must be small. As the available mechanical power at EM motors scales with mass and volume, the LMA approach take advantage of larger and more powerful motors – placed outside the body of the patient – than what would be possible to embed inside a laparoscopic robot. The mechanical continuity is also broken by using magnets coupled across the abdominal tissue overcoming workspace constraints and lack of triangulation due to cable-driven robots.

While magnetic anchoring was discussed in [114] and the theoretical feasibility of driving a laparoscopic tool was shown in [229] via a static analysis, in this paper we focus on dynamic modeling and closed-loop control of a single LMA-actuated DoF. In addition, we investigate the amount of mechanical power that can be transferred across the abdominal wall at different intermagnetic distances, and we compare the results with EM motors having a size similar to the internal driven magnet.

F.2.1 Clinical Motivation

Robotic surgery is currently a popular, widely accepted clinical practice, as demonstrated by the over 2,800 Intuitive Surgical da Vinci platforms installed worldwide as of September 2013 [165]. Despite the wide availability of the da Vinci, robotics has yet to become the gold standard tool for general surgery, due its higher invasiveness compared with the laparoscopic approach [230]. The next generation of surgical robots should therefore

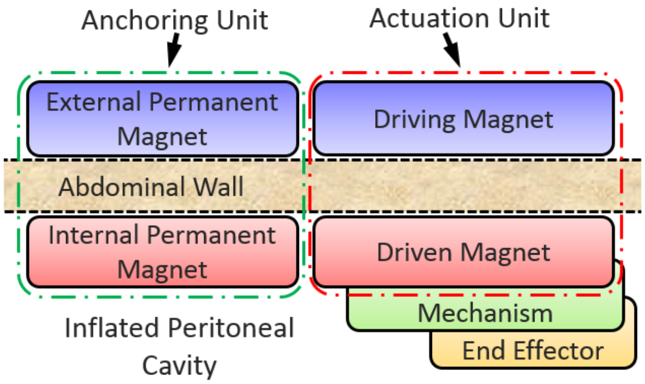

Figure F.1: Functional representation of a LMA-based robotic instrument coupled across the abdominal wall.

aim to guarantee the same dexterity and performance as current robots, while reducing the access trauma.

A promising approach in this direction is represented by robotic platforms specifically developed for (or adapted to) Laparo-Endoscopic Single Site (LESS) surgery [34–39]. Actuation for the several DoF may be external, by means of cables or rigid connection [34,35]; internal, using on-board motors [36–38]; or hybrid [39]. In any case, the mechanical continuity of the kinematic chain constrains the workspace proximally at the insertion point.

Having the surgical instruments and the laparoscopic camera magnetically coupled across the abdominal wall would greatly enhance both freedom of operation and triangulation (i.e., the triangular positioning of the camera and surgical instruments in laparoscopy which mimics the positioning of the human head and arms [3]). Fully insertable magnetic surgical instruments were first proposed in [40]. These instruments are able to enter the abdominal cavity through the same single incision, without taking up port space during the operation. Each single surgical instrument is coupled with an independent external handheld magnet. The main drawback of this approach is in the low dexterity and poor motion accuracy due to manual operation of the external magnets [231]. To overcome this limitation, magnetic coupling can be used mainly for gross positioning, while on-board EM motors can be adopted for providing fine motion of the surgical end effector [38, 231, 232]. As previously mentioned, however, the on-board actuators that can fit through a single tiny incision are very limited in power and do not allow the performance of surgical tasks such as lifting an organ or following in real-time the surgeon's movements at the master interface. Larger, more powerful motors can be used at the expense of enlarging the access port [39], hence increasing the trauma for the patient.

With the LMA approach we propose, the constraint on the diameter of the laparoscopic instrument only affects the size of the internal driven magnet, while all the mechanical power provided by a large EM motor – placed outside the patient – can be leveraged for actuating the internal mechanism [229].

F.2.2 Technical Contribution

Tetherless transmission of mechanical power between magnetic field generators outside of the body and instruments within the body is gaining momentum in the surgical robotics community, as shown by the increasing number of platforms to drive wireless capsule endoscopes [29, 30, 146, 150, 233, 234]. A similar approach to what is discussed in this paper has recently been proposed in [42], where a magnetic resonance scanner generates the driving magnetic field, imposing the rotation of a small ferromagnetic body around an axis. The mechanical power transferred with this approach is used to drive one DoF of a needle injection robot. While this approach recalls the principle of operation of EM motors – with an external source generating a rotating magnetic field and an internal rotor following it – the LMA is more closely related to magnetic gears [77].

Previous work in the field of magnetic gears for industrial applications suggests that a coaxial concentric topology with radial coupling (i.e., driving and driven magnetic systems mounted one inside the other as in [75]) would enable a more efficient power transmission than a coupling where the gears are rotating on parallel axes. This is due to a more homogeneous distribution of the attractive force around the main axis of each gear, as all the pole pairs are simultaneously involved in the transmission of mechanical power [76]. However, in the proposed application, this approach is unfeasible as the abdominal wall stands in between the driving and the driven units. A possible solution is then to adopt a parallel-axis radial coupling across the tissue, with the associated challenge of an asymmetric attracting force and the related vibrations.

As regards the number of pole pairs, a magnetic coupling based on single-dipole magnets allows maximization of the volume of the magnetic material contributing to the torque transfer. Therefore, a parallel-axis radial coupling with single-dipole magnets seems to be the best solution for transmitting mechanical power to a device deep inside the human body. This approach was adopted in [118] for driving an implantable telescopic rod to correct skeletal deformities. While this work reported an interesting medical application, it did not address the challenges of achieving a servo control of the magnetic coupling.

In this study, we extend the methods proposed for the servo control of coaxial magnetic gears [119] to a parallel-axis radial coupling with single-dipole magnets. We generalize the approach to the case where the driving and the driven magnets are asymmetrical (i.e., different in volume and/or magnetization), and where the intermagnetic distance h between

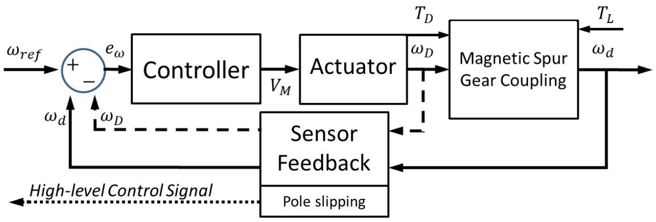

Figure F.2: Block diagram for the closed-loop control of a LMA actuation unit.

them can vary within a certain range. In particular, assuming that the average abdominal tissue thickness upon insufflation for a population that includes obese patients (body mass index > 30 kg/m^2) is 4 cm [117], we focus our analysis on h ranging from 2 cm to 7 cm. Within this range, we model the dynamics of the LMA actuation unit, quantify the amount of mechanical power that can be transferred, and investigate two alternative strategies for closing the control loop. The first strategy leverages the motor-side velocity as feedback parameter, as suggested in [119] for the servo control of coaxial magnetic gears. The alternative approach consists of using the load-side velocity acquired via magnetic field sensing.

F.3 Controlling a LMA Actuation Unit

As represented in in Fig. F.2, the closed-loop control diagram for a single LMA actuation unit is composed of the magnetic spur gear coupling, the actuator rotating the driving magnet, the sensors measuring the feedback parameters, and the controller driving the actuator.

Since the proposed LMA actuation strategy is intended to replace an onboard high speed/low torque rotational actuator, we aim to control the angular velocity at the load. As feedback parameter, we investigate the use of either the driving or the driven magnet angular velocity, ω_D or ω_d, respectively. This value is compared with the desired velocity ω_{ref}, and the error e_ω is fed to the controller that generates the appropriate voltage input V_M to the actuator. The external actuator imposes a torque T_D at an angular velocity ω_D to the magnetic gear system. The mechanical power is transferred to the driven magnet via magnetic coupling, to overcome the load torque T_L, which is seen as a disturbance to the system. As we use single-dipole magnets, the speed ratio between the driving and the driven magnets equals one. The proposed approach can be extended to multiple-dipole magnets by explicitly considering the ratio between the driven pole pairs and the driving pole pairs, as in [119]. The sensor feedback block measures in real time ω_D and ω_d, and detects if the system has entered the pole-slipping regime – the regime inherent to magnetic gears where control is lost due to torque overload [119], or excessive driving magnet acceleration that induces inertial reaction forces on the driven magnet [120]. A warning signal can be transmitted to a high level controller in case of pole slipping. As suggested in [119], the coupling can be re-engaged by forcing ω_D at zero for a short period before being reset to the original speed command input.

Within this section, we first derive the open-loop dynamic model of the magnetic gear coupling (Section F.3.1), then we describe the actuator model and the sensor feedback strategy (Section F.3.2), and we conclude by proposing two alternative strategies to close the control loop (Section F.3.3).

F.3.1 Dynamic Model of the Magnetic Gear Coupling

A schematic diagram of the LMA actuation unit that is analyzed in this study is represented in Fig. F.3. The magnetic couple is composed of two cylindrical permanent magnets diametrically magnetized, having magnetization M_D and M_d for the driving and the driven magnets, respectively. While we assume the two magnets having a single dipole each, we consider the general case where the two magnets are different in diameter and length.

An important assumption of our model is that the two magnets are lying on two parallel axes (i.e., z and z'), spaced by a separation distance h'. Note that we define h' as the distance between the two axes, and h as the separation between the outer surfaces of the two magnets, as represented in Fig. F.3.a. Referring either to h or h' is equivalent, as the difference in their values is constant. We also assume that abdominal tissue does not influence the magnetic coupling [127].

We define J_D and J_d as the equivalent inertia at the driving and at the driven magnet side, respectively, while θ_D and θ_d are the angular coordinates of M_D and M_d as represented in Fig. F.3.b. The angular displacement of the drive train is denoted with $\Delta\theta = \pi - (|\theta_D| + |\theta_d|)$. As represented in Fig. F.3.a, the directions of rotation for the two magnets are opposite (i.e., a counterclockwise rotation of the driving magnet induces a clockwise rotation of the driven one).

The magnetic spur gear pair can be analytically described for different h by modifying the equivalent model for a two-inertia mechanical system [128]. In conventional two-inertia servo-drive systems, the interconnecting drive shaft has a linear torsional stiffness K – unit of Nm/rad – that stays constant within the operating range. Therefore, the torque T_C transmitted by the prime mover to the load is a linear function of the angular displacement at the drive shaft. As introduced in [129], the torque transmitted across a radial magnetic coupling is not constant with $\Delta\theta$ and can be described by a nonlinear trigonometric function:

$$T_C(\Delta\theta) = T_G \sin(\Delta\theta), \tag{F.1}$$

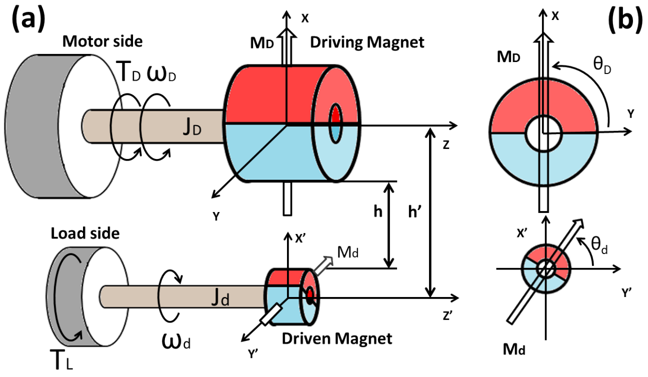

Figure F.3: Schematic overview (a) and lateral cross section (b) of the LMA actuation unit based on two diametrical magnetized cylindrical magnets.

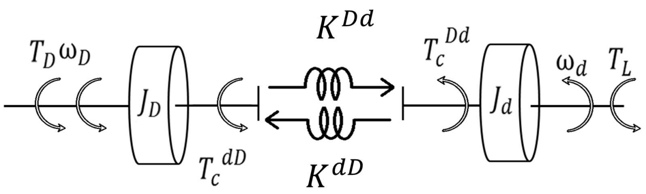

Figure F.4: Equivalent model of a magnetic spur gear pair with asymmetrical magnets.

where T_G is the maximum gear torque that can be transmitted over the magnetic coupling. The value of T_G depends on the volume and magnetization strength of the magnets and on their separation distance h. In case the driving and the driven magnets differ in terms of volume or magnetization, the cross-coupling due to the magnetic field becomes asymmetrical and two separate nonlinear torque transfer functions must be considered:

$$T_C^{Dd}(\Delta\theta, h) = T_G^{Dd}(h)\sin(\Delta\theta) \tag{F.2}$$

$$T_C^{dD}(\Delta\theta, h) = T_G^{dD}(h)\sin(\Delta\theta) \tag{F.3}$$

where Eq. F.2 refers to the torque transferred from the driving to the driven magnet, while Eq. F.3 refers to the torque transferred in the opposite direction.

The numerical values of T_G^{Dd} and T_G^{dD} at different h can be obtained by the static analysis and the finite element method (FEM) integration described in [114]. For a given magnetic gear pair considered at $\Delta\theta = \pi/2$, $T_G^{Dd}(h)$ and $T_G^{dD}(h)$ can be well approximated by exponential fits.

Referring to the equivalent model represented in Fig. F.4, the dynamic behavior of the

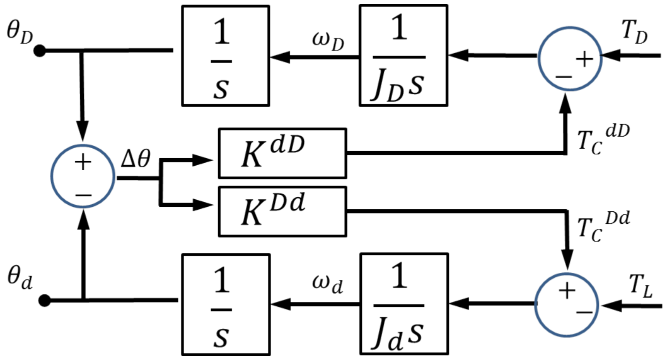

Figure F.5: Block diagram of the open-loop magnetic gear system.

LMA actuation unit can be described by the following system of equations:

$$J_D \frac{d^2\theta_D}{dt^2} = T_D - T_C^{dD}(\Delta\theta, h) \tag{F.4}$$

$$J_d \frac{d^2\theta_d}{dt^2} = T_C^{Dd}(\Delta\theta, h) - T_L. \tag{F.5}$$

The trigonometric expressions of T_C^{Dd} and T_C^{dD} can be linearized about $\Delta\theta = 0$ in the range $|\Delta\theta| < \pi/2$, assuming

$$T_C^{Dd}(\Delta\theta, h) \simeq K^{Dd}(h)\Delta\theta = \frac{2}{\pi}\tilde{T}_G^{Dd}(h)\Delta\theta, \tag{F.6}$$

$$T_C^{dD}(\Delta\theta, h) \simeq K^{dD}(h)\Delta\theta = \frac{2}{\pi}\tilde{T}_G^{dD}(h)\Delta\theta, \tag{F.7}$$

where $\tilde{T}_G^{Dd}(h)$ and $\tilde{T}_G^{dD}(h)$ are the exponential fits for $T_G^{Dd}(h)$ and $T_G^{dD}(h)$, respectively.

Beyond $|\Delta\theta| < \pi/2$ of angular displacement, the magnetic coupling enters a pole-slipping regime [119, 130], resulting in a consequential loss of control. This typically happens when the torque T_L required by the load overcomes the maximum value of torque that can be transmitted over the magnetic coupling, $T_G^{Dd}(h)$. For a reliable control of the driven magnet, pole slipping must be prevented. This can be accomplished by monitoring in real time $\Delta\theta$ with the method suggested in the next subsection.

The block diagram representing the open-loop system – shown in Fig. F.5 – can be derived by combining Eqs. F.4-F.7. In no-load conditions, the transfer functions relating the driving torque to the driving and the driven angular velocities are given by

$$\frac{\omega_D}{T_D} = \frac{s^2 + \frac{K^{Dd}}{J_d}}{J_D s(s^2 + \frac{K^{Dd}J_D + K^{dD}J_d}{J_D J_d})} = \frac{s^2 + \omega_a^2}{J_D s(s^2 + \omega_0^2)} \tag{F.8}$$

$$\frac{\omega_d}{T_D} = \frac{K^{Dd}}{J_d J_D s} \frac{1}{s^2 + \frac{K^{Dd} J_D + K^{dD} J_d}{J_D J_d}} = \frac{K^{Dd}}{J_d J_D s(s^2 + \omega_0^2)} \tag{F.9}$$

where the antiresonant ω_a and the resonant ω_0 frequencies are, respectively, given by

$$\omega_a = \sqrt{\frac{K^{Dd}}{J_d}}, \qquad \omega_0 = \sqrt{\frac{K^{Dd} J_D + K^{dD} J_d}{J_D J_d}}. \tag{F.10}$$

F.3.2 Actuator Model and Sensor Feedback

F.3.2.1 Actuator Model

In this work, we use an EM Direct Current (DC) motor with current monitoring to drive the external magnet in the LMA actuation unit. The motor dynamic model – schematically represented in Fig. F.6 – considers

$$V_M = K_M \omega_D + R_{tot} i_M + L \frac{d}{dt} i_M \tag{F.11}$$

where V_M is the voltage applied to the motor, K_M is the electromotive force constant scaled by the gear ratio of the motor gearbox, i_M is the current, and L is the motor inductance. The term R_{tot} includes both the motor and the current monitor resistances, R_M and R_{cur} respectively.

The motor torque T_D, fed to the magnetic gear system, is derived by monitoring the motor current as

$$T_D = K_{Tq} i_M \tag{F.12}$$

where K_{Tq} is the motor torque constant.

Defining δV as $\delta V = V_M - K_M \omega_D$, the transfer function relating the motor torque T_D to δV in the Laplace domain is

$$\frac{T_D}{\delta V} = \frac{K_{Tq}}{L(R_{tot}/L + s)}. \tag{F.13}$$

F.3.2.2 Sensor Feedback

Previous work on magnetic gear servo control [119, 120] focused on motor-side sensing, as load-side feedback sensors may be prohibitive to use in certain applications, such as off-shore wind turbines or all-electric automotive power trains. In case of surgical instruments, the constraints introduced by embedding feedback sensors on the load side are mainly related to sterilization and tethering. As for sterilization, low-temperature techniques can be adopted, in case the sensors cannot withstand the high temperature commonly used for steam sterilization (i.e., 132°C). Regarding tethering, a wired connection would be the most

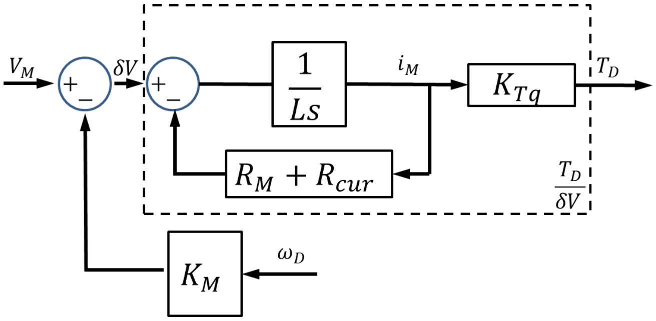

Figure F.6: Dynamic model of the EM DC motor with current monitoring.

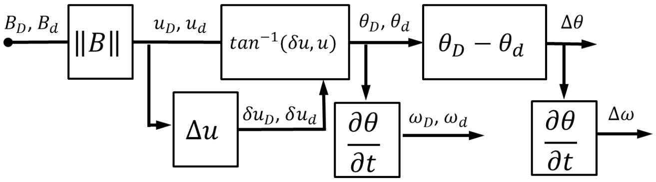

Figure F.7: Angular position (θ_D and θ_d), angular speed (ω_D and ω_d), angular displacement of the drive train ($\Delta\theta$), and its time derivative ($\Delta\omega$) are obtained through direct measurement of the magnetic field (B_D and B_d) generated by the driving and the driven magnets along the vertical direction.

reliable option to acquire the data from the on-board sensors. This may be an advantage in terms of usability, as it can facilitate the retrieval of the instrument from the abdominal cavity once the surgery is over.

In this work, we investigate both motor-side and load-side sensing strategies by taking advantage of a pair of magnetic field sensors (MFS). The motor-side sensor is placed next to the driving magnet, whereas the load-side sensor is placed close to the driven magnet (for the physical implementation, refer to section F.4.1).

The block diagram in Fig. F.7 shows how the signals acquired by the two MFS are used to derive the driving and the driven magnet angular positions, θ_D and θ_d, the angular velocities, ω_D and ω_d, the angular displacement of the drive train, $\Delta\theta$, and its time derivative, $\Delta\omega$. Referring to Fig. F.3, the component along x of the magnetic field generated by the driving magnet, B_D, is acquired by the motor-side MFS, while the load-side MFS acquires the component along $-x'$ of the magnetic field generated by the driven magnet, B_d. As the two magnets spin, B_D and B_d can be described by two cosine functions [114]. The magnetic field values are normalized, obtaining u_D or u_d, and the angular derivatives δu_D and δu_d are calculated. The inverse of the tangent function is applied to (u_D, δu_D) and to (u_d, δu_d) to derive θ_D and θ_d, respectively. Angular velocities ω_D and ω_d are then obtained by the time derivative of θ_D and θ_d, respectively.

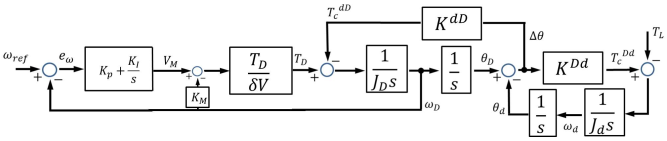

Figure F.8: Motor-side speed control system with PI controller.

F.3.3 Closing the Control Loop

Having both motor-side and load-side sensing available, we investigate and compare two alternative strategies to achieve closed-loop control of the angular velocity ω_{ref}. Both controllers are designed to work within a range of intermagnetic separation distances h from 2 cm to 7 cm. Therefore the controllers parameters are chosen in order to ensure controllability in the range of analysis which includes population range of abdominal thickness.

F.3.3.1 Motor-side Closed-Loop Control

When a motor-side control strategy is adopted, the driven part of the actuator may be seen as a disturbance. In our approach, similar to [119, 128], we explicitly consider the effect of coupling in the control loop and, we adopt a standard Proportional-Integral (PI) controller fed with the motor-side angular velocity ω_D. The block diagram of the closed-loop system is shown in Fig. F.8. In this figure, K_p is the proportional feedback coefficient, while K_I is the integral feedback coefficient.

The closed-loop transfer function from the reference input to the motor speed is given by

$$\frac{\omega_D}{\omega_{ref}} = \frac{\frac{(K_I+K_p s)}{s}\,\frac{\frac{T_D}{\delta V}\frac{s^2+\omega_a^2}{J_D s(s^2+\omega_0^2)}}{1+\frac{T_D}{\delta V}\frac{s^2+\omega_a^2}{J_D s(s^2+\omega_0^2)}K_M}}{1+\frac{(K_I+K_p s)}{s}\,\frac{\frac{T_D}{\delta V}\frac{s^2+\omega_a^2}{J_D s(s^2+\omega_0^2)}}{1+\frac{T_D}{\delta V}\frac{s^2+\omega_a^2}{J_D s(s^2+\omega_0^2)}K_M}}. \qquad \text{(F.14)}$$

F.3.3.2 Load-side Closed-Loop Control

An alternative technique consists of closing the control loop on the load-side angular speed ω_d. This approach allows for a direct tracking of the system performance at the load, but may introduce system instabilities due to two imaginary poles in the open-loop transfer function (Eq. F.9). Therefore, we apply a custom controller with arbitrary placement of three poles and two zeroes to stabilize the system. Root locus analysis is used for the placement of controller singularities. In particular, two complex conjugates zeros are placed at higher frequencies and two complex conjugates poles are placed at lower frequencies to provide lag compensation. This allows reduction of steady state error and resonant peaks, thus increasing system stability. In addition, a pole is placed in the origin of the root locus

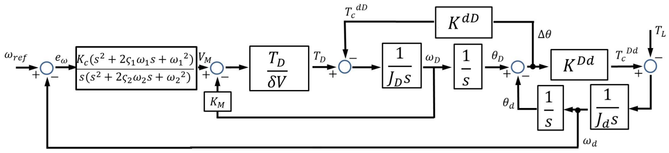

Figure F.9: Load-side speed control system with the custom controller fed by ω_d.

to attenuate oscillations. The controller transfer function from the error e_ω to the motor voltage input V_M is:

$$\frac{V_M}{e_\omega} = \frac{K_c(s^2 + 2\zeta_1\omega_1 s + \omega_1^2)}{s(s^2 + 2\zeta_2\omega_1 s + \omega_2^2)} \tag{F.15}$$

where K_c is the gain of the closed-loop controller, ω_1 and ω_2 represent natural angular frequencies, and ζ_1 and ζ_2 denote damping coefficients.

The block diagram for the load-side speed control is shown in Fig. F.9.

The closed-loop transfer function from the reference input to the load speed is given by

$$\frac{\omega_d}{\omega_{ref}} = \frac{\frac{K_c(s^2+2\zeta_1\omega_1 s+\omega_1^2)}{s(s^2+2\zeta_2\omega_1 s+\omega_2^2)} \frac{\frac{T_D}{\delta V}\frac{K_{Dd}}{s}\frac{1}{s^2+\omega_0^2}}{1+\frac{T_D}{\delta V}\frac{K_{Dd}}{s}\frac{1}{s^2+\omega_0^2}K_M}}{1+\frac{K_c(s^2+2\zeta_1\omega_1 s+\omega_1^2)}{s(s^2+2\zeta_2\omega_1 s+\omega_2^2)} \frac{\frac{T_D}{\delta V}\frac{K_{Dd}}{s}\frac{1}{s^2+\omega_0^2}}{1+\frac{T_D}{\delta V}\frac{K_{Dd}}{s}\frac{1}{s^2+\omega_0^2}K_M}}. \tag{F.16}$$

F.4 Model Validation and Experimental Assessment

F.4.1 Experimental Platform

The experimental platform designed to validate the LMA control is represented in Fig. F.10. An EM DC motor was used to spin the driving magnet, whereas the driven magnet was connected to a hysteresis brake. The motor-side assembly was mounted on a vertical slide that allowed adjustment of the intermagnetic distance h.

The DC motor (2342-024CR, Faulhaber, Germany) has a nominal voltage of 24 V, embeds a 1:3.7 planetary gearhead, and can provide a maximum torque of 60 mNm at a maximum speed of 1900 rpm. A two-channel optical encoder (HEDS 5500, Avago Technologies, USA) with 96 counts per revolution was connected to the motor and provided the reference for assessing the feedback strategy described in section F.3.2.

The driving magnet (K&J Magnetics, Inc., Pennsylvania, USA) is made of NdFeB and has a cylindrical shape (25.4 mm in both diameter and length) with diametrical magnetization (N42 grade, 1.32 T in magnetic remanence). The driven magnet has the same features, but smaller dimensions (9.5 mm in both diameter and length). The diameter of the driven magnet was selected to fit a laparoscopic device that can enter the abdominal

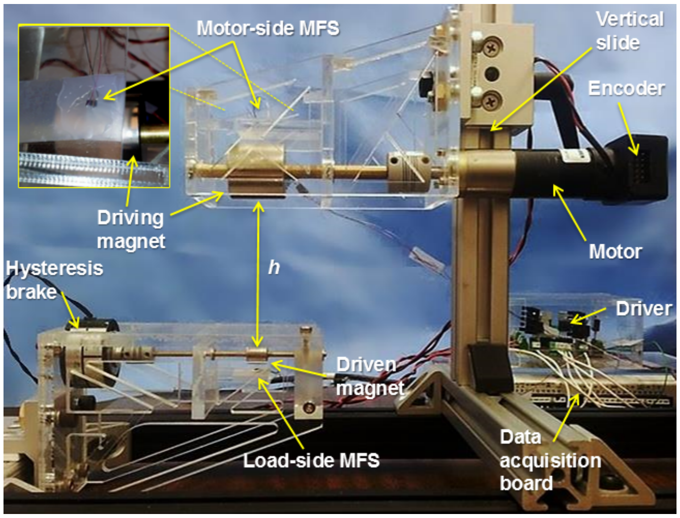

Figure F.10: Picture of the experimental platform. The upper left inset shows the placement of the MFS next to the driving magnet.

cavity through a 12 mm surgical port. Given the selected pair of magnets, T_G^{Dd} and T_G^{dD} for h ranging from 2 cm to 7 cm were estimated by FEM integration (COMSOL Multiphysics, USA). Two two-term exponential models were used to fit the FEM data, obtaining

$$\tilde{T}_G^{dD}(h) = 222e^{-169h} + 63e^{-51h}[mNm] \tag{F.17}$$

$$\tilde{T}_G^{Dd}(h) = 78e^{-105h} + 12e^{-31h}[mNm] \tag{F.18}$$

where h has the unit of meters. The fitting functions were obtained with the Curve Fitting Toolbox (MatLab, Mathworks, USA), by setting the confidence level at 98%. The two fitting functions are represented together with the FEM estimations in Fig. F.11.

The hysteresis brake (H3, Placid Industries, USA) was used to impose on the driven magnet a controllable T_L. Two MFS (CY-P15A, ChenYang Technologies, Germany) were placed next to the driving and the driven magnets for monitoring in real time their angular displacement via the algorithm described in Section F.3.2. Data from each sensor was acquired using three electrical wires (i.e., data, ground, and voltage supply) having a diameter of 0.1 mm. The maximum absolute temperature rating for the selected MFS is $[-100; 180]$°C, thus allowing steam sterilization.

The motor-side and the load-side inertias of the experimental platform resulted in J_D=8.9×10^{-6}kg·m^2 and J_d=0.46×10^{-6}kg·m^2, respectively.

A data acquisition board (DAQ USB-6211, National Instruments, USA) was used to collect the data from the MFS at 500 Hz and to control both the motor and the hysteresis

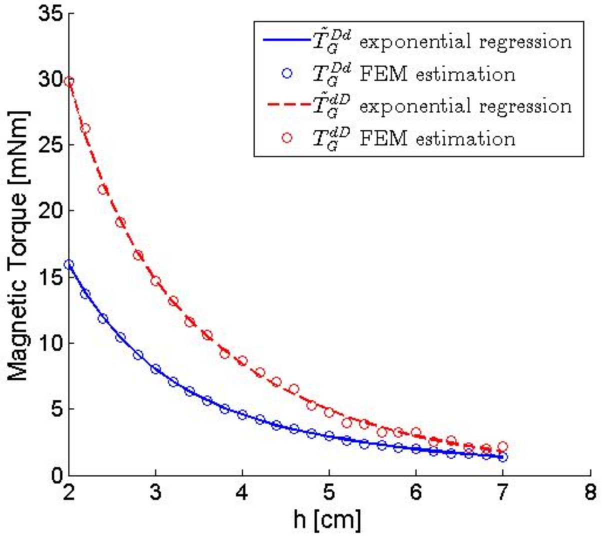

Figure F.11: FEM estimations of the maximum transmissible torque functions and their exponential fittings for different intermagnetic distances.

brake via a custom driver. Regarding the operation of the motor, the current drained is monitored across a 10 Ω buffered resistor R_{cur}. The hysteresis brake was also controlled in voltage, while the drained current was monitored via a second buffered resistor. The user interface, developed in C++, allowed the user to select one of the two control strategies, and to set ω_{ref} up to 1900 rpm and T_L from 0.5 mNm to 25 mNm.

F.4.2 Dynamic Model Validation

The first step of validation focused on assessing the sensor feedback strategy reported in section F.3.2, as this was used for all the experiments that follow. In particular, we compared ω_D as measured by the encoder with the value estimated by implementing the algorithm in Fig. F.7. This test was performed for ω_D= [500, 700, 900, 1100, 1300, 1500] rpm, showing an average error of 7.28 ± 2.82 rpm. We can reasonably assume a similar uncertainty in reconstructing ω_d and $\Delta\omega$.

The next step consisted of validating the dynamic model of the magnetic gear coupling for different separation distances h, driving angular velocities ω_D, and applying load torques T_L. A single experiment consisted of increasing T_L, while driving the external magnet at a constant speed ω_D and maintaining a fixed intermagnetic distance h. As soon as the system entered in the pole-slipping regime, the experiment was ended. The intermagnetic distance h was varied from 2 cm to 7 cm in steps increments of 1 cm, while ω_D was increased from 500 rpm to 1500 rpm in steps increments of 200 rpm. The motor-side closed-loop control described in section F.3.3.1 was adopted to guarantee a constant ω_D, as T_L was increased.

Once a trial was started, the platform increased the voltage driving the hysteresis brake in 0.15 V increments every 0.2 s, resulting in an exponential increase of T_L over time. The event of pole slipping was detected by monitoring θ_d as measured by the sensor-side MFS. In particular, when θ_d was stalling around a limited number of angular positions, the algorithm assumed that the system was entered in the pole-slipping regime. In that case, the motor was stopped, the hysteresis brake was released, and the trial was considered over.

For each experiment, the data recorded for θ_D, θ_d, and T_D were used together with platform-specific parameters (i.e., J_D, J_d, $\tilde{T}_G^{Dd}$, $\tilde{T}_G^{dD}$) to estimate T_L. The dynamic model for T_L was derived by combining Eq. F.4 and Eq. F.5 and integrating over time, thus obtaining

$$T_L(t) = J_d \Delta\theta(t)(\frac{1}{\Delta t^2} + \frac{2}{\pi}\frac{\tilde{T}_G^{dD}}{J_D} + \frac{2}{\pi}\frac{\tilde{T}_G^{Dd}}{J_d}) - \frac{J_d}{J_D} T_D(t). \tag{F.19}$$

The reference value for T_L was obtained by measuring the current drained by the hysteresis brake and deriving the torque applied to the driven magnet from its calibration curve.

A typical plot for a single experiment at h=4 cm and ω_D=1000 rpm is represented in Fig. F.12. Here, three different regimes can be observed. In unloaded conditions, angular oscillations at the driven magnet were induced by the low inertia, combined with the non-linear elastic coupling of the magnetic link. In this regime, reconstruction of T_L by the model was noisy. As T_L increased, the amplitude of oscillations decreased significantly, and the model allowed for a reliable real-time estimation of the load torque. As expected, the system entered the pole-slipping regime as T_L overcame the maximum value of torque that can be transmitted over the magnetic coupling.

Five experiments were repeated for each combination of h and ω_D, and the estimation errors were averaged. The mean relative errors in estimating T_L at different velocities and intermagnetic distances are reported in Table F.1. Over the entire range of distances and velocities tested, the mean relative error was $7.1 \pm 2.3\%$, while the mean absolute error was 0.18 ± 0.06 mNm. All of these values are related to the loaded regime of operation. It is interesting to note a larger error at intermediate distances that is due to the effect of the resonant and antiresonant peaks in the open-loop transfer functions (see next subsection).

F.4.3 Closed-Loop Control Validation

Once the dynamic model was experimentally validated, we studied how variations in h were affecting the harmonic behavior of the two open-loop transfer functions in Eq. F.8 and Eq. F.9. Therefore, we plotted the two Bode diagrams for six discrete values of h (i.e., $h = [2, 3, 4, 5, 6, 7]$ cm). From the amplitude plots in Fig. F.13.a, we can observe that both the resonant and the antiresonant peaks in the motor-side transfer function migrate to

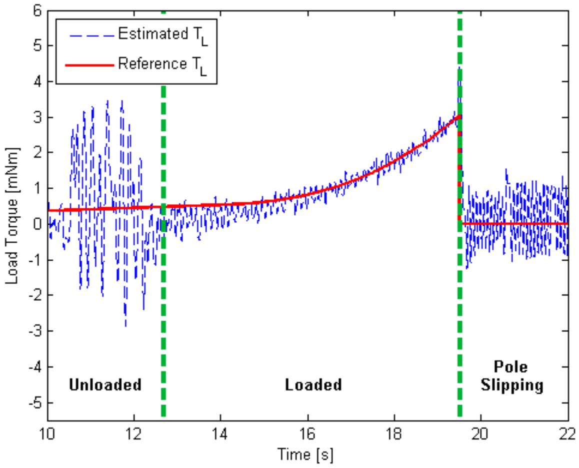

Figure F.12: Comparison between the estimated and the reference load torque for h=4 cm and ω_D=1000 rpm. The unloaded, loaded and pole-slipping regimes are highlighted by the dashed vertical lines.

	ω_D [rpm]					
h	500	700	900	1100	1300	1500
2 cm	9.4%	14.7%	5.7%	8.5%	7.9%	8.8%
3 cm	13.8%	8.1%	9.4%	6.4%	8.4%	3.1%
4 cm	9.6%	12.1%	10.9%	8.4%	8.3%	8.2%
5 cm	9.2%	13.4%	5.8%	7.6%	6.7%	7.9%
6 cm	8.7%	3.7%	4.0%	3.9%	4.1%	3.8%
7 cm	5.7%	3.1%	3.4%	3.8%	4.0%	5.5%

Table F.1: Mean relative errors in T_L estimation at different velocities and intermagnetic distances within the loaded regime.

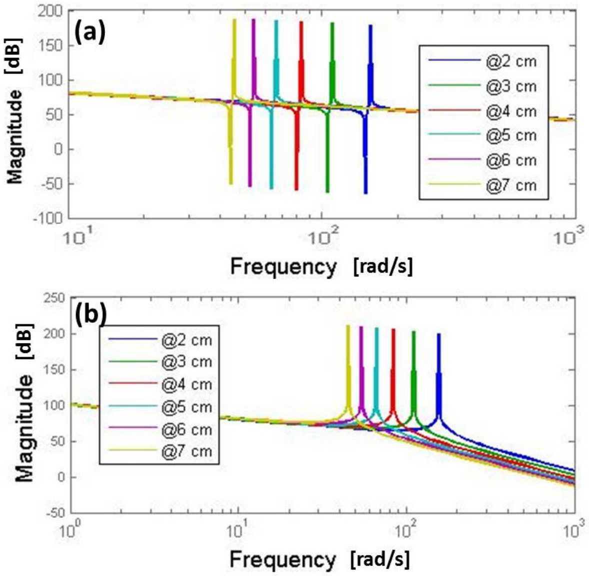

Figure F.13: Bode amplitude diagrams for the motor-side (a) and load-side (b) open-loop transfer functions for six discrete values of h (i.e., $h = [2, 3, 4, 5, 6, 7]$ cm).

lower frequencies as h increases, spanning less than a decade. In particular, ω_0=156 rad/s at h=2 cm, decreasing to ω_0=45 rad/s at h=7 cm. A similar behavior can be observed for the resonant peaks in the load-side transfer function, the amplitude of which is plotted in Fig. F.13.b. From the two Bode amplitude plots, it is relevant to emphasize that the singularities of the system and the range of their migration as h changes from 2 cm to 7 cm are within the interval of angular velocities investigated in this work (i.e., 500 rpm corresponds to 52 rad/s, while 1500 rpm corresponds to 157 rad/s). In determining the parameters for the two closed-loop controllers, we optimized the system response for h = [2...7] cm (i.e., the condition in which singularities occur at lower frequencies) and we experimentally investigated whether this choice could guarantee controllability in the entire range of h tested.

The Proportional and Integral coefficients for the motor-side closed-loop control were determined via the PID Tuning function of the Control System Toolbox (MATLAB, MathWorks, USA), obtaining K_P=52.42×10^{-3} V·s/rad and K_I=5.90 V/rad. Simulated step responses for $h = [2, 3, 4, 5, 6, 7]$ cm are reported in Fig. F.14.a, showing an overshoot that ranges from 11.4% to 10.8% and a settling time from 100 ms to 180 ms.

As regards the load-side control strategy, the parameters for the custom controller were also tuned for the range of analysis ($h \in [2, 7]$ cm), resulting in the following constants

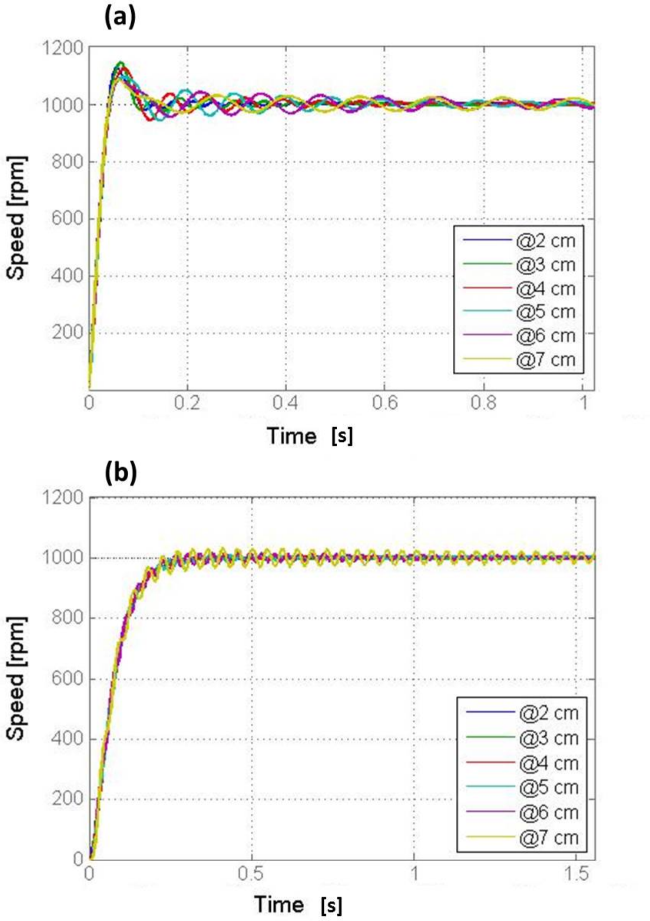

Figure F.14: Simulated step response for the motor-side (a) and load-side (b) closed-loop control for six discrete values of h (i.e., $h = [2, 3, 4, 5, 6, 7]$ cm).

K_c=3.4×10^3V/rad, ω_1=1.6×10^{-4} rad/s, ω_2=5.5×10^{-6} rad/s, ζ_1=0.68, and ζ_2=1. Simulated step responses for $h = [2, 3, 4, 5, 6, 7]$ cm are reported in Fig. F.14.b, showing no relevant overshoot and a settling time of 200 ms for all the distances investigated.

A comparison between the simulated and the experimental step response is reported in Fig. F.15.a for the motor-side closed-loop control, and in Fig. F.15.b for load-side closed-loop control. Experiments were performed with ω_{ref}=1000 rpm at h=4 cm in unloaded conditions, and both ω_D and ω_d were recorded. The video showing the experimental set-up and the step response trials is attached as multimedia extension 1.

As regards the step response for the motor-side closed-loop control in Fig. F.15.a, the measured ω_D and ω_d presented an overshoot of 11.2% and 11.6%, respectively. These results were comparable with the overshoot obtained in the simulated response. Concerning the steady state, ω_D presented an average value of 998±23 rpm, while the average ω_d was 1032±32 rpm. As expected, no significant overshoot was observed in the load-side closed-loop control step response (F.14.b) and the settling time of ω_d was comparable with the model predictions. The average regime value was 990±18 rpm for ω_D, and 1006±30 rpm for ω_d.

By comparing the results, we can observe that the load-side controller allowed achievement of a more precise regulation of the average ω_d than the motor-side approach. Both controllers showed a ripple in the regulated speed of about 3% of the regime value. This effect was mainly due to the absence of a load connected to the driven magnet, as the system was working in the unloaded regime.

F.4.4 Load Rejection and Torque Transmission

The presence of a load torque applied at the gear train induces variations in the parameters of the system, as it affects the equivalent inertia at the driven shaft. In particular, system characteristics such as the resonant and antiresonant frequencies are both influenced by variations in J_d. The experimental trials reported in this subsection aim to assess both closed-loop control strategies under different loading conditions.

First, a set of speed step responses were measured by setting T_L at 20%, 50%, and 80% of $\tilde{T}_G^{Dd}(h)$. The trials were performed by imposing ω_{ref}=1000 rpm at h=4 cm, and the results for the motor-side closed-loop control are reported in Fig. F.16. The steady-state error for ω_d adopting the motor-side closed-loop control was 22±18 rpm for T_L at 20% of $\tilde{T}_G^{Dd}$ (Fig. F.16.a), 21±19 rpm for T_L at 50% of $\tilde{T}_G^{Dd}$ (Fig. F.16.b), and 3±40 rpm for T_L at 80% of $\tilde{T}_G^{Dd}$ (Fig. F.16.c). When adopting the load-side closed-loop control, the steady-state error for ω_d was 2±3 rpm for T_L at 20% of $\tilde{T}_G^{Dd}$ (Fig. F.16.d), 1±6 rpm for T_L at 50% of $\tilde{T}_G^{Dd}$ (Fig. F.16.e), and 0.3±13 rpm for T_L at 80% of $\tilde{T}_G^{Dd}$ (Fig. F.16.f).

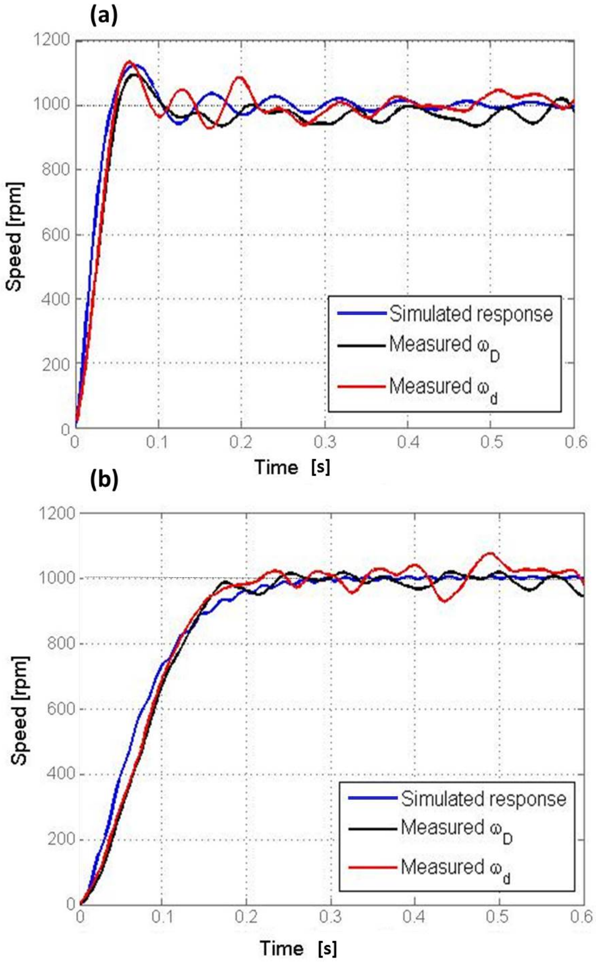

Figure F.15: (a) Simulated and experimental step response at h=4 cm for motor-side closed-loop control. Both the measured ω_D and ω_d are reported in the figure. (b) Simulated and experimental step response at h=4 cm for load-side closed-loop control. Both the measured ω_D and ω_d are reported in the figure.

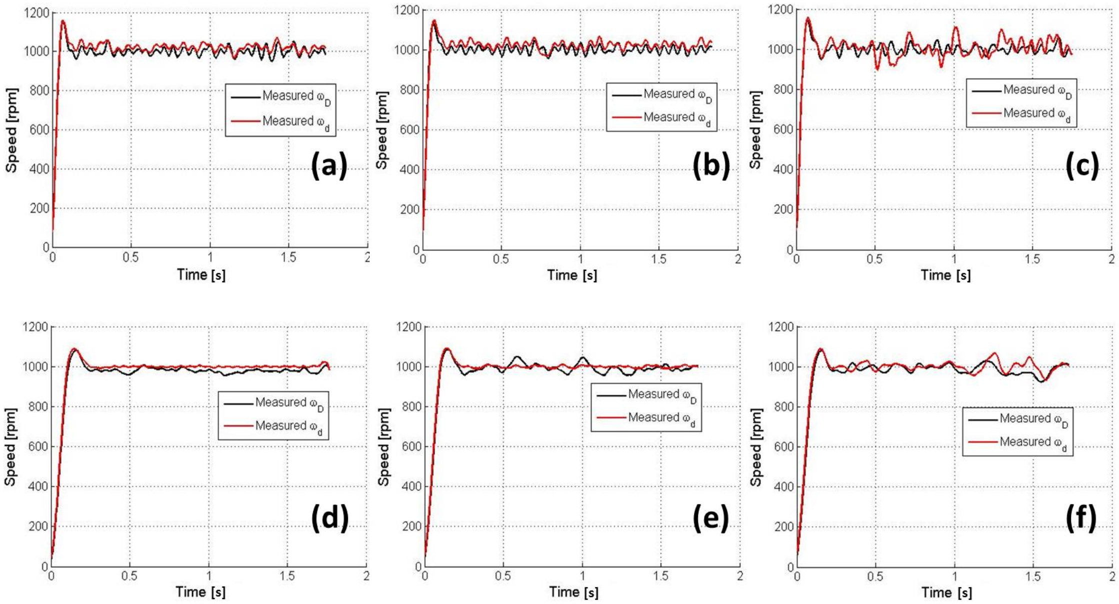

Figure F.16: Experimental step responses for motor-side closed-loop control (a, b, c) and load-side closed-loop control (d, e, f) with T_L at 20% (a, d), 50% (b, e), and 80% (c, f) of $\tilde{T}_G^{Dd}$. Experiments were performed at h=4 cm imposing a ω_{ref}=1000 rpm. Each plot shows the measured values for both ω_D and ω_d.

From the results reported in Fig. F.16, we can observe that the load-side control strategy was more effective in forcing the system to reach the desired ω_{ref}, although an overshoot of 8% of the steady state appeared as the load was applied. The load-side closed-loop control step response presented a ripple for ω_d within the 1% of the steady state value, while the motor-side closed-loop control showed a ripple up to 4%. From the plots, we can observe that both strategies showed an increase in the ripple with the applied T_L, as the system was moving towards the pole-slipping regime.

Load rejection experiments were then performed for both the control strategies at h=4 cm, and the results obtained are represented in Fig. F.17. The reference speed ω_{ref} was set to 1500 rpm, while T_L was initially set to 28% of $\tilde{T}_G^{Dd}$, then increased up to 85% of $\tilde{T}_G^{Dd}$ for about 2.5 seconds before resetting it to the initial value. While the load was at the 85% of $\tilde{T}_G^{Dd}$, the average error and the ripple for ω_d were 6±31 rpm for the motor-side closed-loop control (Fig. F.17.a), and 3±12 rpm for the load-side closed-loop control (Fig. F.17.b).

Both control strategies allowed rejection of the effect of a load variation without pole slipping. By analyzing in more detail Fig. F.17.a, we can observe residual damped oscillations in ω_d for more than one second after the variation in the load is applied. These oscillations are due to the non-linear torsional spring behavior of the coupling, and are further amplified by the effect of an inertia ratio well below the unit [131] (i.e., in the proposed drive train, modeled as a two-inertia system, the inertia ratio in unloaded conditions is J_d/J_D=0.056). As shown in Fig. F.17.b, the custom controller implemented for the load-side strategy, providing a lag compensation, was effective in eliminating these oscillations in ω_d by modulating ω_D.

A final test was performed to evaluate the mechanical power that can be transmitted by an LMA actuation unit at different intermagnetic distances. Using the motor-side closed-loop control, the maximum torque at the load T_L^{max} before entering the pole-slipping regime was experimentally measured for ω_{ref} ranging from 600 rpm to 1700 rpm at different separation distances (i.e., $h = [2, 3, 4, 5, 6, 7]$ cm). Each trial was repeated 10 times and the results are reported in Fig. F.18.a.

As expected from the harmonic analysis, we can identify in Fig. F.18.a the effect of the resonant peaks of the system shifting to lower frequencies as h increases. For rotational speeds that are not in the range of the resonant peaks, the torque transferred is constant, as expected considering that the magnetic coupling has a 1:1 gear ratio. Therefore, as long as the torque required by the load does not bring the system into the pole-slipping regime, the amount of mechanical power that can be transferred mainly depends on the performance of the external motor (i.e., the faster the external motor, the larger the amount of mechanical power transmitted to the load).

The same test was repeated for the load-side closed-loop control and the results are reported in Fig. F.18.b. By comparing the plots in Fig. F.18.a and Fig. F.18.b, we can conclude that the load-side controller enables a larger torque to be transmitted before entering the pole-slipping regime. In particular, an average value of 1.5 mNm can be transferred at 7 cm, increasing up to 13.5 mNm as the separation distance is reduced down to 2 cm. In addition, the effect of the resonant peaks is less evident when using the load-side closed-loop control, which provides a value of T_L^{max} that is almost constant with ω_{ref} for h larger than 3 cm.

F.4.5 Performance Evaluation of LMA

In analyzing the overall performance that an LMA actuation unit can achieve, we consider adopting the load-side closed-loop control as it provided a better performance when compared to the motor-side approach. In Fig. F.19 and Table F.2, we compare the maximum torque that can be transferred at different intermagnetic distances – same data as Fig. F.18.b – with the theoretical limit provided by FEM estimation. With the proposed dynamic modeling and control strategy, we are able to transfer an average of 86.2% of the

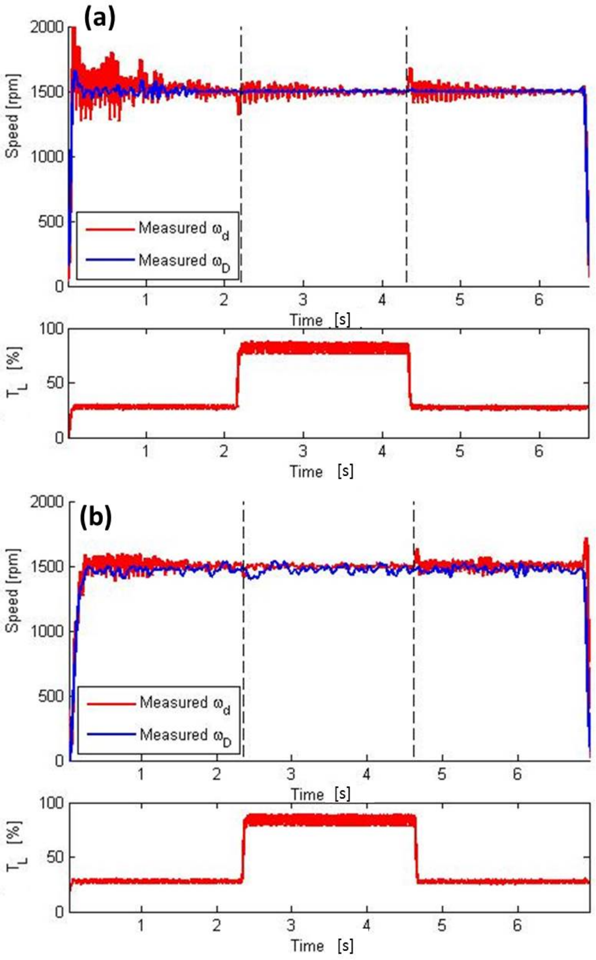

Figure F.17: Experimental load rejection responses for motor-side closed-loop control (a) and load-side closed-loop control (b). The profile of T_L, moving from 28% of $\tilde{T}_G^{Dd}$ to 85% of $\tilde{T}_G^{Dd}$ and back to its initial value, is represented below the speed plot. Experiments were performed at h=4 cm setting ω_{ref}=1500 rpm. Each plot shows the measured values for both ω_d and ω_D and the trend of the applied load torque.

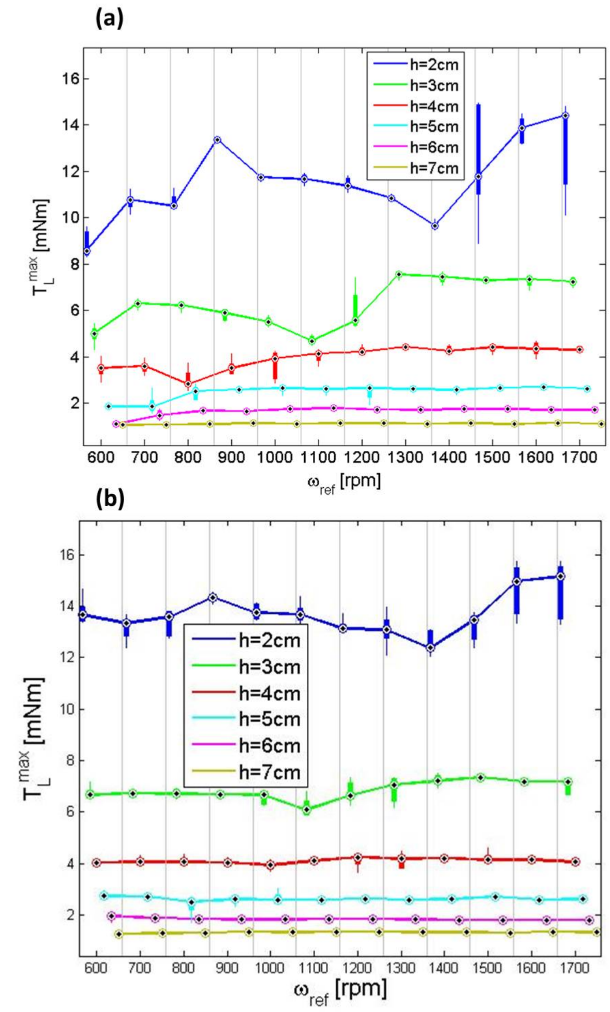

Figure F.18: Maximum torque at the load before entering the pole-slipping regime, measured using the motor-side (a) and the load-side (b) controller at different speeds and separation distances. Each data point is the result of ten independent trials.

	Distance $[cm]$					
MAX Torque [mNm]	2	3	4	5	6	7
Model $\tilde{T}_G^{Dd}(h)$	15.95	8.01	4.58	2.90	1.96	1.38
Experiment T_L^{max}	13.63	6.82	3.98	2.52	1.68	1.20
Efficiency %	85.4	85.2	87.0	86.8	85.5	87.3

Table F.2: Expected amount of torque transmitted, $\tilde{T}_G^{Dd}$, experimental amount of torque transmitted using the load-side closed-loop control, T_L^{max}, and efficiency defined as percentage of the theoretical amount of torque transmitted at different intermagnetic distances.

theoretical value of maximum torque. This deviation is due to the adoption of a linear model for T_C^{Dd} and T_C^{dD} in Eqs. F.6 and F.7, respectively. For large angular displacements, which are expected as the load torque brings the system towards the pole-slipping regime, a linear model in Eqs. F.6 and F.7 is far from being accurate and needs to be replaced by a non-linear equivalent.

From Fig. F.19, it is also interesting to observe that the standard deviation in T_L^{max} is larger at smaller distances. This may be explained by considering other magnetic effects that are present in the system, but have not been included in the dynamic model, such as the vertical attraction force between the driving and the driven magnets that varies as the magnets spin [132].

As previously mentioned, an LMA actuation unit can be used instead of an onboard EM motor for driving a DoF of a laparoscopic robot. For the sake of comparison, in Table F.3 we listed off-the-shelf EM motors that have a diameter comparable with the driven magnet used in this study.

Thanks to a speed ratio equals one, the maximum speed that can be achieved at the driven shaft with the LMA approach corresponds to the maximum speed of the external EM motor. As the external motor is not as constrained in size as a motor to be embedded on board, a faster actuator than those listed in Table F.3 can be adopted. As for the stall torque, we can assume for the LMA approach the values of $T_L^{max}(h)$ reported in Table F.2. As represented in Fig. F.18.b, we can consider the stall torque to be constant as the speed increases. Considering that the driven magnet used in this study was 9.5 mm in both diameter and length, we can conclude that the LMA approach can provide a

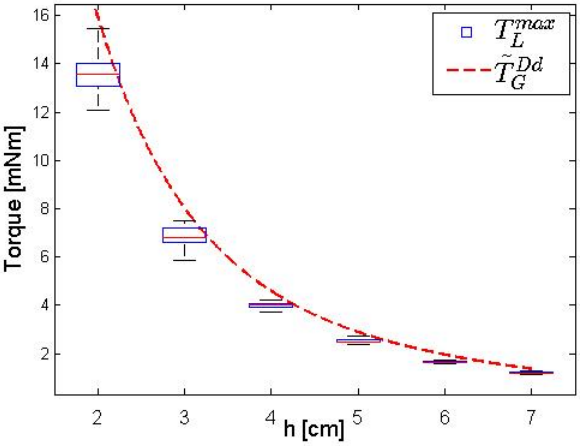

Figure F.19: Maximum torque at the load before entering the pole-slipping regime as a function of the intermagnetic distance. Theoretical value, $\tilde{T}_G^{Dd}$, and experimental data obtained by using the load-side closed-loop control, T_L^{max}.

Model	Diameter	Length	Max Speed	Stall Torque	Reference
Namiki-SBL04	4mm	13.8mm	7000rpm	0.13mNm	[133]
Faulhaber-1016	10mm	16mm	18400rpm	0.87mNm	[134]
Faulhaber-1024	10mm	24mm	14700rpm	2.89mNm	[135]
Maxon-DCX10L	10mm	25mm	12000rpm	5.42mNm	[136]
Faulhaber-1219	12mm	19mm	16200rpm	0.96mNm	[137]
Faulhaber-1224	12mm	24mm	13800rpm	3.62mNm	[138]
Precision-NC110	12mm	12.5mm	10000rpm	0.50mNm	[139]
Precision-MC112	12mm	20mm	9500rpm	1.50mNm	[140]
Namiki-SCL12	12.5mm	32mm	13750rpm	3.71mNm	[141]

Table F.3: Off-the-shelf EM Motors comparable with the size of the driven magnet used in this work.

volumetric power density that is well above any of the motors listed in Table F.3 at any of the intermagnetic distances investigated.

Finally, it is worth mentioning that the wired connection required to transmit sensor data from the instrument in the load-side control strategy can be easily replaced by a battery-operated wireless link [142] without increasing dramatically the size of the surgical tool.

F.5 Conclusions and Future Work

In this work, we demonstrated the feasibility of controlling a parallel-axis radial coupling with asymmetrical single-dipole magnets within a range of intermagnetic separation distances compatible with the abdominal thickness in humans. This particular kind of magnetic coupling, referred as LMA actuation unit, can be used in designing robotic surgical instruments to transfer mechanical power from outside the body of a patient to a laparoscopic instrument within. Given the constraints in diameter and volume for a surgical instrument, the proposed approach allows for transferring a larger amount of mechanical power than what is possible to achieve by embedding actuators on board.

The solution we propose for the servo control of an LMA actuation unit takes advantage of a dynamic model of the coupling, adapted from a two-inertia servo-drive system, and a sensing strategy based on Hall effect magnetic field sensors placed next to the driving and the driven magnets. In this study, we also compare two alternative approaches in closing the control loop. The first, referred to as motor-side closed-loop control, uses the angular velocity of the driving magnet as the feedback parameter and has the advantage of relying only on sensors placed on the motor-side of the coupling, thus outside the patient's body. The alternative approach, referred to as load-side closed-loop control, directly controls the angular velocity at the load and requires a Hall effect sensor to be placed inside the surgical instrument. The two approaches were assessed and compared in terms of step response, load rejection, and maximum torque that can be transmitted at different speeds and intermagnetic distances.

From the experimental results, we can conclude that the dynamic model we developed presented a relative error below 7.5% in estimating the load torque from the system parameters, while the sensing strategy based on Hall effect sensors had an average error below 1% in reconstructing the shaft speed. Concerning closed-loop control, both the strategies were effective in regulating the load speed with a relative error below 2% of the desired steady-state value. When comparing the two approaches, the load-side closed-loop control achieved a better performance, both in terms of steady-state error (below 0.2%) and ripple in the angular velocity (below 1%). In addition, the load-side closed-loop control allowed transmission of larger values of torque, showing – at the same time – less dependency from the angular velocity.

While this study should serve as the background for the servo control of LMA-based DoFs in laparoscopic robots, a number of challenges still remain for future research.

A first direction of future work is improving the robustness of the control. As mentioned in Section F.4.5, a non-linear approach must be adopted to increase the amount of transmitted torque closer to its theoretical limit. Predictive control, suggested in [120] for coaxial magnetic gears, can be a viable solution. To reduce the oscillations in ω_d further, a digital notch-filter compensator, as suggested in [149], can be adopted. In addition, the model needs to be extended to a situation in which the two magnets spin on axes that are not fixed, nor parallel, as analyzed in [150]. Horizontal and vertical vibrations must be considered, as they will be present during laparoscopic surgery. Vertical attraction force between the driving and the driven magnets must be included in the model.

When designing an LMA-based surgical instrument as represented in Fig. F.1, the actuation module must provide controlled motion for a DoF, while the anchoring module should support the weight of the instrument and the vertical forces applied during tissue interaction. Overshoot in the speed at the driven magnet may occur in some conditions and must be taken into account when designing the mechanism that goes from the rotating shaft to the surgical end effector [132]. If the surgical robot needs more than one DoF, a number of LMA actuation modules will have to interact within the same confined space. Magnetic cross-coupling among LMA anchoring and actuation units may become an issue in this case. As the magnetic force and torque respectively decrease with the inverse of the fourth and third power of the intermagnetic distance, we plan to address this challenge by properly spacing the magnets on board the surgical instrument. Shielding with ferromagnetic or diamagnetic material can also be considered to address this problem. The model of the system would then be extended to include cross-coupling and to provide a tool for designing appropriate shielding between modules.

As discussed in Section F.3, the system can enter in the pole-slipping regime as a consequence of torque overload. As suggested in [119], the coupling can be re-engaged by stopping the motor rotation for a short period, and then resetting the input command. However, if the load is still above the maximum torque that can be transmitted, this strategy will be ineffective. A potential solution to this problem consists of controlling the vertical position of the external driving magnet, so that h can be reduced if a larger torque is required at the load. The intermagnetic distance can be tracked in real time by using the methods proposed in [148]. A different approach may be to replace the driving unit with a set of coils that can generate a rotating magnetic field at the driven magnet. In this case, commutation control can be implemented to prevent the pole-slipping regime and maximize the transferred torque at any given time.

F.6 Appendix: Appendix of Multimedia Extensions

The multimedia extension page is found at http://www.ieeexplore.org

Extension	Type	Description
1	Video	Step response of both motor and load side closed-loop controls

Appendix G

LAPAROSCOPIC TISSUE RETRACTOR BASED ON LOCAL MAGNETIC ACTUATION

Nicolo Garbin, Christian Di Natali, Jacopo Buzzi, Elena De Momi, Pietro Valdastri.

From: Journal of Medical Devices, vol.9, no.1,
Status: Published 2015

G.1 Abstract

Magnetic instruments for laparoscopic surgery have the potential to enhance triangulation and reduce invasiveness, as they can be rearranged inside the abdominal cavity and do not need a dedicated port during the procedure. Onboard actuators can be used to achieve a controlled and repeatable motion at the interface with the tissue. However, actuators that can fit through a single laparoscopic incision are very limited in power and do not allow performance of surgical tasks such as lifting an organ. In this study, we present a tissue retractor based on local magnetic actuation (LMA). This approach combines two pairs of magnets, one providing anchoring and the other transferring motion to an internal mechanism connected to a retracting lever. Design requirements were derived from clinical considerations, while finite element simulations and static modeling were used to select the permanent magnets, set the mechanism parameters, and predict the lifting and supporting capabilities of the tissue retractor. A three-tier validation was performed to assess the functionality of the device. First, the retracting performance was investigated via a benchtop experiment, by connecting an increasing load to the lever until failure occurred, and repeating this test for different intermagnetic distances. Then, the feasibility of liver resection was studied with an ex vivo experiment, using porcine hepatic tissue. Finally, the usability and the safety of the device were tested in vivo on an anesthetized porcine model. The developed retractor is 154mm long, 12.5mm in diameter, and weights 39.16 g. When abdominal wall thickness is 2 cm, the retractor is able to lift more than ten times its own weight. The model is able to predict the performance with a relative error of 9.066±0.52%. Liver retraction trials demonstrate that the device can be inserted via laparoscopic access, does not require a dedicated port, and can perform organ retraction. The main limitation is the reduced mobility due to the length of the device. In designing robotic instrument for laparoscopic surgery, LMA can enable the transfer of a larger amount of mechanical power than what is possible to achieve by embedding actuators on board. This study shows the feasibility of

implementing a tissue retractor based on this approach and provides an illustration of the main steps that should be followed in designing a LMA laparoscopic instrument.

Nomenclature

- LMA - Local Magnetic Actuation
- EAM - External Anchoring Magnet
- IAM - Internal Anchoring Magnet
- EDM - External Driver Magnet
- IDM - Internal Driven Magnet
- LapR-LMA Laparoscopic Retractor based on LMA
- PG - Planetary Gearhead
- GR - Gear Ratio
- PS - Power Screw
- OCM - Offset Crank Mechanism
- RL - Retracting Lever length

G.2 Introduction

Magnetic instrumentation for abdominal surgery was first introduced in 2007 [115] with the goal of achieving the same triangulation (i.e., the triangular positioning of the camera and surgical instruments in laparoscopy, which mimics the positioning of the human head and arms [228]) as traditional laparoscopy while significantly decreasing invasiveness. Fully insertable tools, magnetically coupled across the abdominal wall, do not take up port site space during the operation and can be introduced through a single standard laparoscopic port. By moving the external magnet around the patient's abdominal wall, the internal device can be steered to the task-appropriate location, thus achieving the desired triangulation without the need for multiple incisions.

Magnetic surgical instruments developed to date include cameras [115], retractors [235], dissectors [115], and cautery devices [40], with trials performed on animal and human models via single-incision access [4].

However, low dexterity and poor motion accuracy due to manual operation of the external controlling magnets have prevented so far the applicability of magnetic tools to complex surgical tasks, such as tissue manipulation or finely controllable tissue retraction.

A possible solution to the limited dexterity consists of embedding controllable actuators inside the magnetic instruments. The most common approach reported in literature is adopting electromagnetic (EM) motors [1, 236, 237]. Since the available mechanical power in this kind of actuator scales with mass and volume, the motors that can fit through a single tiny incision have very limited power and do not allow surgeons to perform surgical tasks such as lifting an organ, or to teleoperate the instrument tip in real-time.

An alternative approach is the tetherless transmission of mechanical power between magnetic field generators outside of the patient's body and instruments within the body. This can provide controlled motion without requiring on-board motors, as illustrated by [238] where the field generated by a Magnetic Resonance Imaging scanner was used to induce the rotation of a constrained small ferromagnetic body around the vertical axis. This rotating body was connected to a gearbox that controlled a needle injection robot. A similar approach was used in [239], where an external rotating field generated by a permanent magnet was used for driving an implanted telescopic rod to correct skeletal deformities.

In the past, we have proposed to apply a similar concept to abdominal surgery by introducing the Local Magnetic Actuation (LMA) approach [121, 240]. As presented in Fig. G.1, an LMA-based device is composed of at least one anchoring unit, plus an actuation unit per independent DOF that must be controlled. The anchoring unit is composed of an External and an Internal permanent Anchoring Magnet (EAM and IAM, respectively), and its function is to support the instrument during surgery. The actuation unit is composed of an External Driving and an Internal Driven Magnet (EDM and IDM, respectively). The EDM is axially rotated by a motor, thus causing the rotation of the IDM. The mechanical power - in terms of rotational speed and load torque - transferred to the IDM can then be used to actuate a mechanism instead of an embedded EM motor. The main advantage of this approach is that large and powerful motors can be used on the outside of the patient for transferring mechanical power to the inside of the abdomen via magnetic coupling.

In this work, we introduce the LapR-LMA for the first time, a laparoscopic tissue retractor based on the LMA approach. This device is composed only of mechanical parts – thus enabling autoclave sterilization – and can be used for controllably retracting an organ without the need for a dedicated incision or a motor on board. In addition to describing the LapR-LMA, this work provides an illustration of the design flow that should be adopted in developing and testing novel LMA-based laparoscopic instruments.

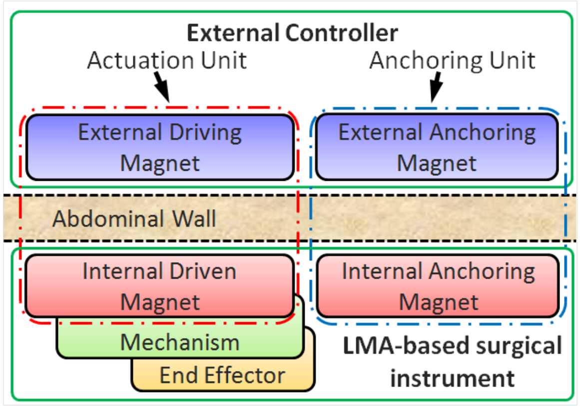

Figure G.1: An external controller is required to anchor and actuate an LMA-based surgical instrument. The anchoring unit supports the device because of the attraction force that the External Anchoring Magnet (EAM) generates on the Internal Anchoring Magnet (IAM). The magnetic coupling between the External Driving Magnet (EDM) and the Internal Driven Magnet (IDM) provides actuation. A mechanism connected to the IDM controls a DoF of the end effector.

G.3 Clinical Consideration

The design of an LMA-based laparoscopic instrument entails the development of both the external controller and the surgical tool. The main design specifications for the two parts of the system can be derived from the following clinical considerations.

Incision port: Laparoscopic surgery is usually performed by placing three to four trocars across the abdominal wall. The trocar with the largest inner diameter is usually dedicated to the endoscopic camera (i.e., 13 mm inner diameter for the Versaport V2, Covidien, USA). Assuming we use that port for insertion, we can consider 12.7 mm as the maximum outer diameter for an LMA-based instrument [237]. The limitation in diameter affects the design of all the components inside the surgical tool, including the internal magnets.

Abdominal thickness: Magnetic field strength decreases exponentially with the increase in the distance between the magnets outside the body of the patient and those inside. Therefore, abdominal thickness plays a fundamental role in the selection of the magnets - particularly external ones - since magnets inside the instrument are already constrained by the access port diameter. A value ranging from 20 mm to 40 mm upon insufflation can be assumed for abdominal tissue thickness to include overweight patients (body mass index up to 30 kg/m^2) [117].

Safety: Rare-earth permanent magnets can generate strong attraction forces, posing the risk of histological damage to the tissue in between the external and the internal magnets. A pressure of 46.7 kPa was reported by Best et al. [228] to be well tolerated in a porcine model. We will assume this value as the safety threshold not to be exceeded during the operation of the LMA-based instrument.

Sterilization: In order to permit cheap reprocessing, a reusable surgical instrument should be able to withstand the high temperature commonly used for steam sterilization (i.e., 132^oC). This disables the possibility of using electronics on board and requires the selection of special-grade permanent magnets.

Internal Workspace: Laparoendoscopic procedures are performed by insufflating the abdominal cavity, usually with carbon dioxide. As a general guideline for how long an insertable instrument should be, we can assume 275 mm as the maximum distance between the abdominal wall and the point of intervention, as reported by [241]. This provides an indication about the workspace that the instrument should be able to reach, as well as a limitation on the instrument length.

External Workspace: The external controller must be compact and easy to use for the surgeon, enabling the internal device gross positioning by magnetic dragging. Once the desired positioning is achieved, the controller should be locked in place while the LMA actuation unit is running.

Ease of use: In order to maximize the potential for future adoption, the surgical instrument must be easy to introduce in the abdominal cavity and the external controller must be intuitive to operate. Once the feasibility of the proposed approach is demonstrated, the input from surgeons becomes crucial in improving the ergonomics of the design.

While the considerations above can be applied to any LMA-based laparoscopic instrument, the following refer specifically to a tissue retractor.

Degrees of freedom: Tissue retraction requires one controllable DOF to either lift up or lower down the organ being manipulated. The DOF should not be backdrivable in order to maintain the tissue retracted while the surgeon is operating underneath. How fast an organ is retracted is not a relevant requirement, as long as the time is compatible with the surgical workflow.

Retracting force: A retracting force of at least 5 N can be assumed as the target force necessary at the retractor end effector [242]. This target value is typical for liver retraction and gallbladder exposure during cholecystectomy. The amount of force must be provided both dynamically, while the mechanism is operated to lift up the tissue, and statically, thus allowing the surgeons to operate underneath. Interestingly, insertable retractors that use embedded EM motors reported so far [236, 243] can only generate up to 1.53 N.

Interaction with the retracted tissue: If the tissue to be retracted is not going to be resected, the surgical tool must be gentle in interacting with it. Suction cups [151] or fan-shaped levers [115] can be adopted in this case. On the other hand, traumatic graspers (e.g., crocodile jaws) are a viable solution if the surgeon plans to remove the retracted tissue at the end of the procedure (e.g., cholecystectomy) [235].

G.4 Principle of Operation

Given the above clinical considerations, we propose the LMA-based tissue retractor schematically presented in Fig. G.2 and referred to as LapR-LMA.

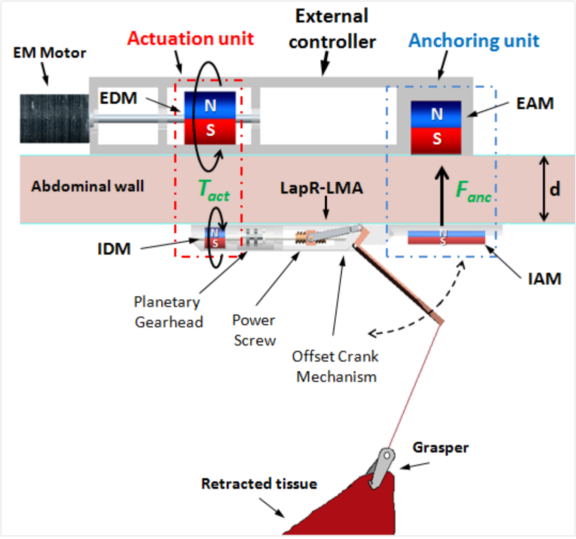

Figure G.2: Schematic representation of the LapR-LMA and the external controller components.

While the anchoring unit is mainly responsible for gross positioning and for supporting both the device and the retracted tissue, the actuation unit is designed to transmit mechanical power from the external EM motor to the mechanism inside the LapR-LMA.

The spinning motion of the IDM is fed to a custom mechanical train, which has been designed to maximize the lifting force at the grasper and to fit the size constraints specified in the previous section. In particular, the IDM is connected to a three-stage planetary gearhead (PG), which rotates a power screw (PS) actuating an offset crank mechanism (OCM). The OCM controls the angular position of a retracting lever. In order to assess the proposed design, we connected a crocodile grasper to the lever via an inextensible wire. As proposed by [235], the surgeon can clamp the grasper on the target tissue with standard laparoscopic forceps. Should the specific application require an atraumatic grasper, a suction cup [151] or a fan-shaped end effector [115] can be used instead.

G.5 Design of the LapR-LMA Platform

G.5.1 Magnetic Design

In modeling and designing both the anchoring and the actuation units, magnetic torques and forces were estimated via Finite Element Analysis (FEA) (COMSOL MULTIPHYSICS 4.3b, Sweden), by following the approach proposed and validated by [121]. In particular, FEA simulations were based on the theories and the methods used in the analysis of steady currents, permanent magnets and magnetic circuits [90].

In estimating the different contributions of the magnetic units, we assumed that the anchoring and the actuation units were spaced far enough to neglect cross-talking effects. The validity of this assumption was verified during the benchtop validation (section G.6.1). All the permanent magnets used in this work were purchased from K&J Magnetics, Inc, PA, USA.

G.5.1.1 Anchoring Unit

The LapR-LMA must have a cylindrical shape to enter a surgical port. Therefore, the space available for the IAM has a round cross-section. This would suggest using a cylindrical magnet. However, as reported by [244], square-section permanent magnets exert a stronger coupling than cylindrical magnets. Therefore, a 38 mm long permanent magnet, with a cross-section of 6.35 mm in side, was selected to fit inside the LapR-LMA. The permanent magnet was made out of Neodymium-Iron-Boron (NdFeB) with magnetization N52 oriented as in Fig. G.2 A cubic NdFeB magnet with a side of 25.4 mm and N52 magnetization (1.48 T magnetic remanence) was selected as EAM to achieve an adequate attraction force, F_{anc}, on the IAM within the intermagnetic separation range investigated in this work. Given the two selected anchoring magnets, F_{anc} was estimated via FEA simulation using a mesh with more than 3,500,000 elements, and by varying the intermagnetic separation distance d from 2 cm to 6 cm in 0.1 cm increments. It is worth mentioning that the investigated range is larger than what mentioned in section 2.B in order to improve the confidence of the results and obtain regressions that are more reliable. As presented in Fig. G.3, the data fits ($R^2 > 0.94$) a two term exponential.

G.5.1.2 Actuation Unit

The actuation unit is based on the concept of magnetic spur gears [245] and is composed of two diametrically magnetized ring-shape magnetic dipoles, the EDM and the IDM, that are free to rotate about parallel axes. Referring to Fig. G.4.a, we define M_D and $M_d$as the magnetization vectors of the EDM and the IDM, θ_D and θ_d as the angular coordinates of $M_D$and M_d, and d as the shortest distance between the external surfaces of the EDM and the IDM. In general, we assume d as coincident with the separation distance between the

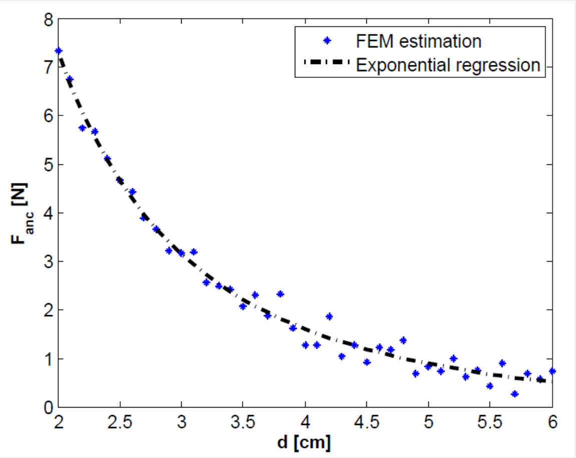

Figure G.3: FEA simulation and two term exponential fit for the magnetic attraction force at increasing intermagnetic separation distance.

LapR-LMA and the external controller. The difference between the two angular coordinates determines the actuation unit angular displacement $\Delta\theta = \theta_D - \theta_d$. The opposite orientation of the y and y' axes in Fig. G.4.a was adopted to emphasize that a clockwise rotation of the EDM induces an anti-clockwise rotation of the IDM.

As presented in Fig. G.4.b, the torque T$_{act}$ transferred from the EDM to the IDM is a function of $\Delta\theta$ [121–123] as follows:

$$T_{act}(\Delta\theta) = T_{max}\sin(\Delta\theta) \tag{G.1}$$

where T_{max} is the maximum torque that can be transmitted over the coupling. T$_{max}$ depends on the volume and magnetization strength of both EDM and IDM, and on their separation distance d. If $|\Delta\theta$— exceeds $\pi/2$, the magnetic coupling enters a pole-slipping regime, resulting in a consequential loss of control, as explained by [124]. In section G.5.3.1, we estimate the expected $\Delta\theta^{max}$ corresponding to the maximum load that the LapR-LMA is able to lift. Due to the mechanical advantage introduced by the three-stage mechanism described in the following section, $\Delta\theta^{max}$ remains far below the pole-slipping threshold. The magnetic coupling between EDM and IDM also generates a vertical attraction force between the two magnets. This force, referred to as F$_{act}$, contributes to supporting the retracted tissue by working in synergy with F$_{anc}$. As presented in Fig. G.4.c, F$_{act}$ can be formulated as a trigonometric function of θ_D, thus obtaining

$$F_{act}(\theta_D) = \frac{F_v + F_h}{2} + \frac{F_v - F_h}{2}\cos(2\theta_D) \tag{G.2}$$

where F_v and F_h are the maximum and minimum values of F_{act}, corresponding to the vertical and the horizontal arrangements of the actuation magnets. As T_{max}, the values of F_v and F_h depend on the volume and magnetization strength of both the EDM and the IDM, and on their separation distance d. In addition, F_v and F_h are functions of $\Delta\theta$. While the plot in Fig. G.4.c considers $\Delta\theta = 0$, in section G.5.3.2 we will comment on the variations of F_v and F_h within the range $|\Delta\theta| < \Delta\theta^{max}$.

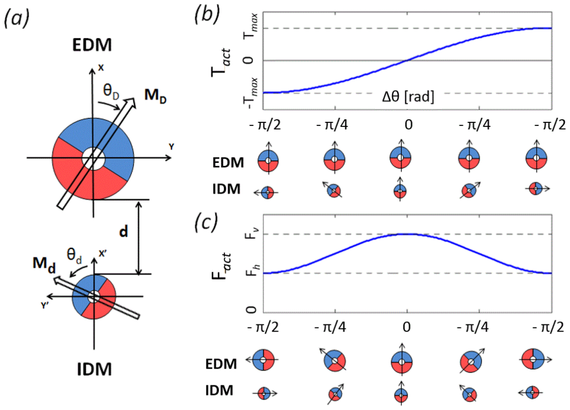

Figure G.4: (a) Schematic cross-section of the EDM and IDM composing the actuation unit. (b) Torque transferred from the EDM to the IDM as a function of the angular displacement between EDM and IDM. The cross-section view of the actuation unit is reported below the plot. (c) Vertical attraction force generated by the actuation unit as the magnets rotate. This plot assumes $\Delta\theta = 0$. The cross section view of the actuation unit is reported below the plot.

The selected IDM was 9.52mm in outside diameter (OD), 2.38 mm in internal diameter (ID), and 9.52 mm in length (L). It was made out of NdFeB, with a relative magnetic permeability of 1.05, and a magnetization grade of N42 (1.32 T magnetic remanence). The EDM was 25.4 mm in OD, 6.32 mm in ID, 25.4 mm in L, and presented the same magnetic features as the IDM.

Given the two selected magnets, we ran a set of FEA simulations to predict T_{max}, F_v, and F_h as functions of d. In estimating F_v and F_h, we assumed $\Delta\theta = 0$. The impact of this assumption is discussed in section G.5.3.2. In the FEA simulations, we used a mesh with more than 3,500,000 elements and we varied d from 2 cm to 6 cm in 0.2 cm increments. Simulation results and exponential regressions fitting the data are reported in Fig. G.5.a for T_{max} and in Fig. G.5.b for F_v and F_h.

From Fig. G.5.a, it is interesting to observe that if compared to EM motors having a volume similar to the IDM [125, 126], the torque available for driving a mechanism is larger as long as d remains below 5 cm.

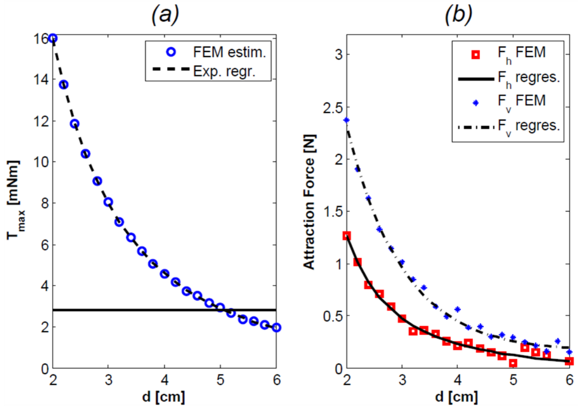

Figure G.5: (a)T_{max} and its exponential regression at different separation distances, the solid horizontal line represents the average nominal torque for commercially available EM motors that would fit a volume similar to the IDM [26-28]. (b)$F_v and F_h$ and their exponential regressions at different separation distances, assuming $\Delta\theta = 0$.

Considering that the speed ratio from the EDM to the IDM is 1:1, the overall mechanical power that can be provided to a mechanism inside the abdominal cavity mainly depends on the speed of the external motor spinning the EDM. As the size is not a primary constraint in selecting the external actuator, a fast motor that is powerful enough to spin the EDM can easily overcome the mechanical power that can be delivered by an embedded EM motor, constrained in size to fit a 12-mm surgical port.

G.5.2 Mechanical train design

G.5.2.1 Planetary Gearhead

The first module of the mechanical train consists of a PG with three stages having a 1:64 gear ratio (GR$_{pg}$). The annular ring (A in Fig. G.6.a) and the entire PG is 11 mm in outer diameter and 17 mm in length. For each stage, the load is transferred from the sun to the annular ring via the planets. The more the planets, the lower is the local stress at the interface between each planet and the annular ring. Therefore, to optimize the loadability of the system, we maximized the number of planets by using four of them for each stage. Suns (S in Fig. G.6.a) and planets (P in Fig. G.6.a) were designed with 10 involute profile teeth, 0.32 module, 22.5 pressure angle, 3.2 mm pitch diameter, and 3.125 mm thickness. The parts were fabricated in Aluminum 6061-T6 (tensile strength - yield 276 MPa; tensile strength - ultimate 310MPa; relative magnetic permeability 1.004) by spark erosion.

Stainless steel pins with a diameter of 0.8 mm were used to mate the suns and the carriers (C in Fig. G.6.a), while 2 mm diameter pins were adopted to assemble the planets. The single components of the three-stage PG are presented in Fig. G.6.a, while a single stage after assembly is shown in Fig. G.6.a.

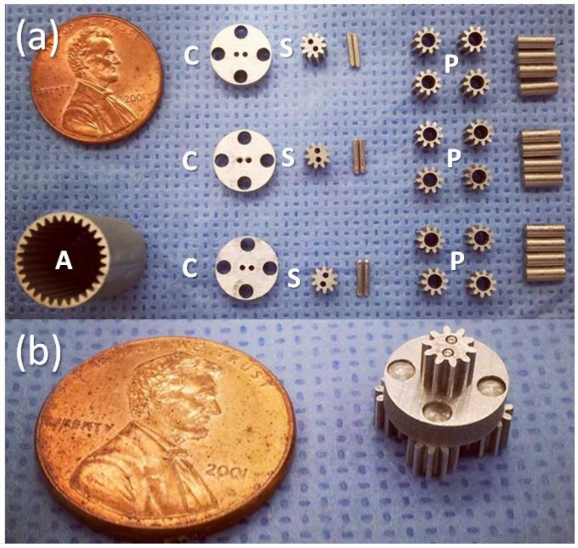

Figure G.6: (a) Three-stage PG components fabricated by spark erosion. (b) One of the three stages assembled.

The PG efficiency was characterized via a custom-made bench test presented in Fig. G.7. A laser-cut structure was fabricated to hold an EM motor (2342S-024CR, Faulhaber, Germany) connected to the PG input sun. A two-channel optical encoder (HEDS 5500, Avago Technologies, USA) with 96 counts per revolution was connected to the EM motor to measure the input angular velocity, ω_{in}. The PG output carrier was connected to a hysteresis brake (H3, Placid Industries, USA). The brake was controlled in current by a PC-based workstation to increase the output torque, τ_{out}, during the trial.

The torque applied by the EM motor to the PG input – referred to as τ_{in} – was measured by monitoring the current drained by the EM motor. Similarly, τ_{out} was derived by monitoring the current drained by the hysteresis brake. The output velocity, ω_{out}, was measured by connecting a diametrically magnetized permanent magnet to the output shaft and measuring the rotation of the magnetic field via a stationary Hall effect sensor (CY-P15A, ChenYang Technologies, Germany).

The PG efficiency, defined as

$$\eta_{pg} = \frac{\tau_{out}\omega_{out}}{\tau_{in}\omega_{in}} \cdot 100\% \tag{G.3}$$

was derived from the experiments by using a constant ω_{in} at 1700 RPM, while τ_{out} was increased from 0 mNm to 80 mNm within a time period of 15 s. This trial was repeated three times and the average efficiency resulted in 61.25±3.16%.

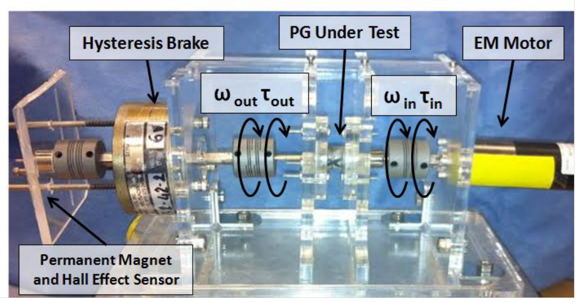

Figure G.7: Experimental setup used to test the efficiency of the PG

Concerning loadability, the PG working range was estimated from the safe tooth load via the Lewis' equation as

$$W = \frac{S \cdot F \cdot Y}{D_p} \tag{G.4}$$

where W [N] is the safe tooth load, S is the maximum bending stress of the material, F is the face width of the gear, D$_p$ is the diametric pitch, and Y is the Lewis' form factor. Considering a pitch radius of 1.6 mm and a four-planet arrangement, a PG safe output torque (T$_{safe}$) of 134.96 mNm was estimated.

G.5.2.2 Power Screw

A PS with a single thread was designed to mate with a 7 mm squared nut. The PS has a pitch diameter d$_m$ of 4.8 mm, a length of 25 mm, a pitch P of 0.2725 mm/rad, a thread angle ϑ of 30, and a lead angle α of 18.3. The nut has a thickness of 6 mm and its motion is used to actuate the OCM. Connection between the PS and the OCM was achieved via 2 mm pins placed in the nut sides.

The PS parts were fabricated in brass (tensile strength - yield 310 MPa; tensile strength - ultimate 476 MPa; magnetic permeability 1.05).

The torque τ_r that must be applied to the PS for achieving a force F$_{nut}$ can be estimated via the following equation

$$\tau_r = \frac{d_m \cdot F_{nut}}{2}[\frac{\mu_s + \cos\theta \tan\alpha}{\cos\theta - \mu_s \tan\alpha}] + \frac{d_{mc}\mu_c W}{2} = \frac{W}{\beta_{ps}} \tag{G.5}$$

where d_{mc} represents the mean collar diameter, μ_s the static friction coefficient between screw and nut, μ_c the static friction coefficient at the collar surface, and β_{ps} is the PS transfer function between the input torque and the output force. The collar friction was assumed negligible since we used low friction Delrin bearings. With the designed geometrical parameters and the static friction coefficient of dry brass to brass (i.e., $\mu_s = 0.1$ [246]), β_{ps} resulted in 0.9117 N/mNm.

The PS efficiency η_{ps} was assessed with a weight lifting test. The EM motor used in the previous experiment was rigidly connected to the PS. A weight ranging from 0.4535 kg to 4.5349 kg in 0.4535 kg increments was applied to the nut, and the torque τ_{mot} required by the EM motor to lift the weight was measured by monitoring the supply current.

For each weight, three trials were performed and the average efficiency η_{ps} was calculated assuming no loss in the nut velocity (i.e., the nut velocity V_{nut} was estimated from the motor speed ω_{mot} via the pitch P of the PS) by using the following equation:

$$\eta_{ps} = \frac{F_{nut}V_{nut}}{\tau_{mot}\omega_{mot}} \cdot 100\% = \frac{F_{nut}P}{\tau_{mot}} \cdot 100\% \tag{G.6}$$

The efficiency η_{ps} resulted in 69.85 ± 5.44 %.

G.5.2.3 Offset Crank Mechanism

The final component of the mechanical train was the OCM operating the retracting lever. The OCM link dimensions, the initial configuration, and the required motion range were identified to achieve a total angular displacement of $\pi/2$ at the crank angle γ. The retracting lever integrated in the OCM can thus generate a total vertical displacement of the retracted tissue equal to its own length. Via quasi-static analysis, assuming a slow motion of the nut and negligible inertia of the links, we defined the OCM mechanical pseudo-advantage Γ – unit of mNm/N – as the ratio between the crank mechanism output torque, τ_{cran} in Fig. G.8, and the related input force acting on the slider, F_{nut}. Considering the schematic diagram in Fig. G.8, we can express Γ as a function of γ as follows:

$$\Gamma(\gamma) = \frac{\tau_{cran}}{F_{nut}} = \overline{AO}\sin(\gamma) + \overline{AO}\cos(\gamma)tg(\delta) \tag{G.7}$$

Where the angle γ is defined zero for the initial configuration – retracting lever closed – and $\pi/2$ when the retracting lever is fully open. Considering that $\overline{OC}$ - the nut horizontal displacement - is the input parameter of the 1-DOF OCM system, the angle δ can be expressed as a function of γ by solving the following system of equations in $\overline{OC}$:

$$\gamma = \frac{2\tan^{-1}(-2\overline{ABBC} - \sqrt{(-2\overline{OCAB})^2 + (2\overline{ABBC})^2 - (\overline{OC}^2 + \overline{BC}^2 + \overline{AB}^2 - \overline{AO}^2)^2})}{-2\overline{OCBA} - \overline{OC}^2 - \overline{BC}^2 - \overline{BA}^2 + \overline{AO}^2} \tag{G.8}$$

$$\delta = \frac{2\tan^{-1}(-2\overline{AOBC} - \sqrt{(-2\overline{OCAO})^2 + (2\overline{AOBC})^2 - (\overline{OC}^2 + \overline{BC}^2 + \overline{AO}^2 - \overline{BA}^2)^2})}{-2\overline{OCAO} - \overline{OC}^2 - \overline{BC}^2 - \overline{AO}^2 + \overline{BA}^2} \tag{G.9}$$

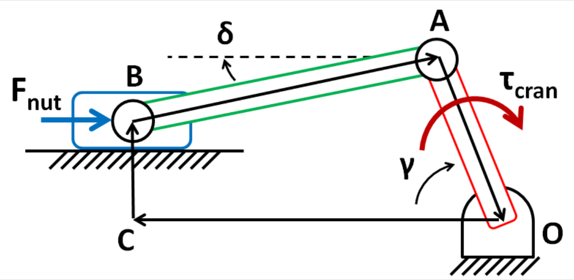

Figure G.8: Schematic representation of the OCM. The slider is placed with an offset ($\overline{BC}$) with respect to the hinge point of the crank (O). Thanks to the connecting rod ($\overline{AB}$), the nut linear motion is converted in a crank angular displacement γ.

The length of the two links (i.e., $\overline{AB} = 25mm$, $\overline{AO}$=9.43 mm) and the offset of the slider with respect to the hinge point (i.e., $\overline{BC}$ =4 mm) provide a $\pi/2$ angular displacement in γ for a 12.7 mm motion of the slider. The mechanical pseudo-advantage Γ as the lever angle γ varies – obtained via iterative computation by assuming negligible inertia and a quasi-static regime – is presented in Fig. G.9, together with its 3^{rd} order polynomial regression (R^2 =0.990).

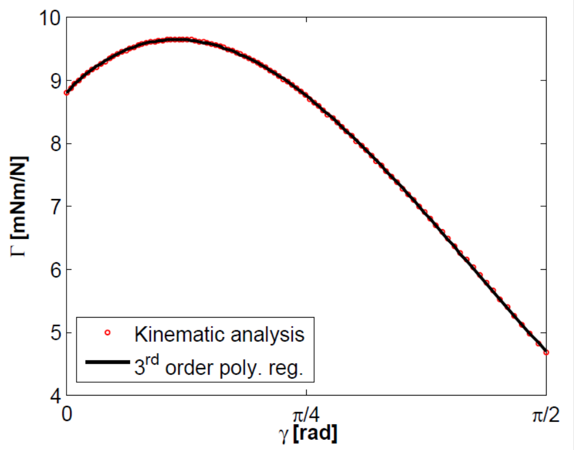

Figure G.9: Mechanical pseudo-advantage Γ [mNm/N] of the OCM and its polynomial regression as a function of the lever angle γ [rad]. A maximum value of 9.63 mNm/N is obtained for $\gamma = 2\pi/17$, while a 4.67 mNm/N minimum occurs for the fully-open configuration (i.e., $\gamma = \pi/2$).

The OCM parts were fabricated in aluminum 6061-T1 (tensile strength - yield 55 MPa;

tensile strength - ultimate 120 MPa; magnetic permeability 1.004) via traditional machining. Stainless steel pins of 1 mm and 1.5 mm diameter were used for mating the parts.

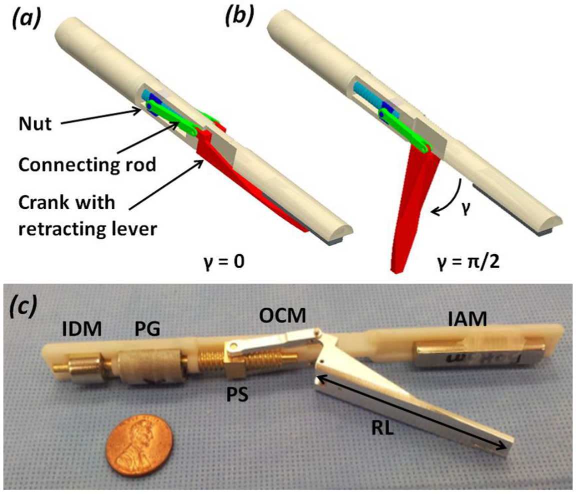

Figure G.10: Perspective rendering of the assembled LapR-LMA in the closed (γ=0) configuration (a) and in the open ($\gamma = \pi/2$) configuration (b). (c) The LapR-LMA prototype, where part of the outer shell was removed to shows the internal components.

G.5.2.4 Additional components and system integration

The LapR-LMA body, designed to embed the described components, was fabricated by rapid prototyping (Objet 30 pro, Stratasys, Israel) in Vero White+ plastic. The outer diameter was set to 12.5 mm to prevent mechanical failure. The device body was fabricated in two halves to facilitate the assembly of the internal components. The mechanical train alignment was guaranteed by DelrinR planar bearings (6 mm OD, 3 mm ID, 3 mm L) that offer low friction and high wear resistance. Two connecting rods were used to couple the OCM with the PS, thus balancing the nut motion and splitting the transmitted force to lower the internal stresses among mating components. The retracting lever, designed to mate with the two connecting rods, rotates about a hinge point in the device body. The retracting lever length, denoted as RL, is 58.5 mm and enables a total vertical tissue displacement of about 6 cm for the full span of γ. Buttresses in the lever design prevent it from bending. In the current version of the LapR-LMA, the OCM and the PS are exposed to verify their motion during the trials. In the future, they can be encapsulated within the outer shell of the device.

As presented in Fig. G.10, the mechanical train components are arranged around a thick extrusion in the core of the device. This feature guarantees structural resistance for the LapR-LMA.

The fabricated prototype, presented in Fig. G.10.c, is 154 mm long, 12.5 mm in diameter, and weights 39.16 g.

G.5.3 LapR-LMA modeling

Once the main components of the LapR-LMA were designed, two simple models were developed to predict the overall performance.

A first mathematical model aimed at providing an estimation of the tissue lifting performance of the device from the torque that can be transmitted over the magnetic coupling and the efficiencies of the single sub-modules. This model can also be used to predict the angular displacement $\Delta\theta$ corresponding to the weight at the gripper.

The second model we developed was a free body diagram of the LapR-LMA. This can be used to predict how much weight can be statically supported by the magnetic attraction force provided by both the anchoring unit and the actuation unit.

G.5.3.1 Tissue lifting model

Assuming no power losses due to internal friction, the weight W$_L$ [g] that can be lifted up as the rotation of the EDM is activated can be predicted as follows:

$$W_L < \begin{cases} \dfrac{10^3}{9.8}\dfrac{(T_{act}GR_{pg}\eta_{pg}\beta_{ps}\eta_{ps})}{RL}\Gamma(\gamma), if T_{act} < \dfrac{T_{safe}}{GR_{pg}\eta_{pg}} \\ \dfrac{10^3}{9.8}\dfrac{(T_{safe}\beta_{ps}\eta_{ps})}{RL}\Gamma(\gamma), if T_{act} > \dfrac{T_{safe}}{GR_{pg}\eta_{pg}} \end{cases} \tag{G.10}$$

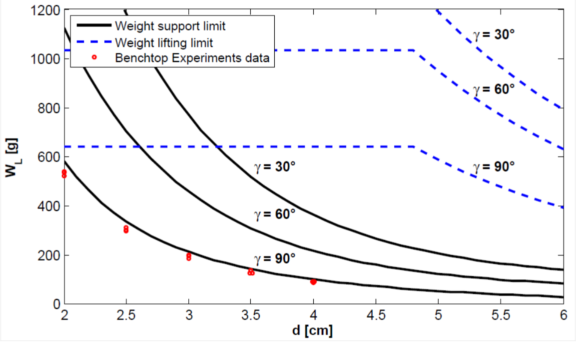

Figure G.11: Maximum weight that can be lifted by operating the LapR-LMA (dashed line), and maximum weight that can be statically supported by the LapR-LMA (solid line). Both weight limitations are plotted as functions of the intermagnetic distance and the opening angle of the retracting lever. The measurements obtained during benchtop experiments are presented as single data points.

As represented by dashed blue lines in Fig. G.11, W$_L$ is constant with d, as long as T$_{act}$ exceeds the safe tooth-loading regime of the PG (Eq. G.4). In this working regime – which covers the entire range of d from 2 cm to 4 cm specified in section G.3 – the overall efficiency of the mechanical train is 42.78%. In most of this region, the angular displacement $\Delta\theta$ stays below $\pi/18$ (i.e., 10), therefore we can assume $\Delta\theta^{max} = \pi/18$. It is also worth mentioning that W_L and the mechanical train efficiency increase as θ goes from $\pi/2$ to zero thanks to the OCM contribution presented in Fig. G.9. This is an advantage in doing controlled retraction, as the portion the tissue (and its weight) increases as this is being lifted.

G.5.3.2 Tissue supporting model

To predict the weight that can be statically supported by the LapR-LMA at different d and γ, we studied the free-body diagram of the device that is presented in Fig. G.12. The model considers F_{anc} as described in section G.5.1.1, the weight force acting on the LapR-LMA, denoted with F_{lap}, and the force F_W required to lift the weight W_L at the gripper. The model also considers F_{act} as described in section G.5.1.2, but scaled for $\Delta\theta^{max} = \pi/18$. In case of $|\Delta\theta| < \pi/18$, we estimated via FEA simulation a variation of F_h and F_v below 2.7% of the values reported in Fig. G.5.b. In our structural model, the device body was assumed as a beam in which the magnetic forces, acting on the IAM and the IDM, are responsible for anchoring the LapR-LMA against the abdominal wall (here assumed as a rigid constraint). The force F_w was assumed to act downward on a point whose position depends on the angular coordinate of the lever γ. As presented in Fig. G.12.a, the LapR-LMA is designed so that F_w is always applied to a position in between the points of application of F_{anc} and F_{act} (B and D in Fig. G.12.b), thus improving the stability during controlled retraction.

Since F_{anc} is larger than F_{act} for any d – as presented in Fig. G.3 and Fig. G.5.b – anchoring failure would most likely occur with the LapR-LMA pivoting about the edge next to the IAM (i.e., point A in Fig. G.12.b). In particular, the worst-case scenario occurs for $\gamma=\pi/2$, as F_w is applied at the lever hinge point (i.e., C in Fig. G.12.b) and its moment arm around A is maximized. The condition for a stable anchoring can then be expressed by considering the rotational equilibrium in A, as

$$F_W < \frac{F_{Anc} \cdot AB + F_{act} \cdot AD - F_{lap} \cdot AX}{AC} \tag{G.11}$$

where F_{lap} is the force required to lift the LapR-LMA and X is the position of the LapR-LMA center of mass. This stability condition is plotted with solid black lines in Fig. G.11, showing the maximum weight W_L that can be statically supported by the LapR-LMA as a function of d and γ. Also in this case, the performance improves as γ goes from $\pi/2$ to 0, since the point of application of F_W moves closer to the pivoting point (i.e., A in Fig. G.12.b). By plotting together the tissue lifting and the tissue support models, as in Fig. G.11, we can derive the operative range for the LapR-LMA as the area below the

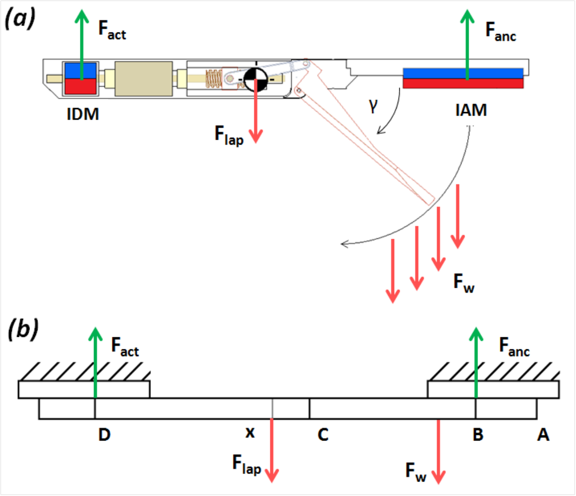

Figure G.12: Structural model used to predict the weight that the LapR-LMA can statically support. (a) Cross-section of the LapR-LMA with the points of application of the different forces. (b) Free body diagram of the LapR-LMA. A is the extremity of the device at the side of the IAM, B is the point of application of F $_{anc}$, C is the point where the hinge of the lever is located, D is the point of application of F$_{act}$, X is the LapR-LMA center of mass.

minimum value of W$_L$ that can be supported and lifted at the same time. Considering the geometrical features of the LapR-LMA and the values of the anchoring forces within the operative range, the pressure exerted by the device on the abdominal wall always stays below 30.7 kPa, thus satisfying the condition on safety specified in section G.3.

G.5.4 External Controller

The external controller was designed to host the EDM, the EAM and the EM motor (2342S-024CR, Faulhaber, Germany) in a plastic handle. A shape with five cavities – where the operator can insert his/her own fingers – was obtained by laser-cutting and assembling Plexiglas sheets. As presented in Fig. G.13, the EDM was rigidly connected to the EM motor via a shaft coupler. Bearings were used to support the shaft. Spacing between the EDM and the EAM mirrored the positioning of the IDM and the IAM inside the LapR-LMA. A two-state switch was connected to the motor controller to change the direction of rotation for the EDM. This enabled switching between lifting up and lowering down the tissue connected to the grasper. An adjustable clutch arm – not presented in Fig. G.13 – can be connected to the controller to hold it in place during the surgical procedure.

G.6 Experimental Assessment

A three-tier validation approach was adopted to assess the LapR-LMA performance. First, a benchtop experiment was performed to verify the weight that the device can controllably lift and hold at different intermagnetic separation distances. Then, an *ex vivo*

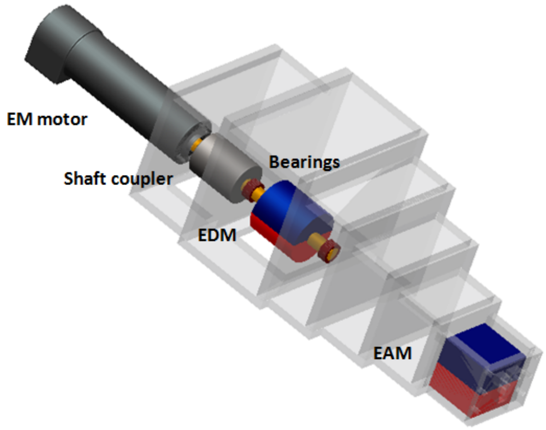

Figure G.13: Perspective rendering of the external controller.

experiment, using freshly excised porcine tissues, was performed to investigate the feasibility of using the LapR-LMA for liver retraction. Finally, the same procedure was performed laparoscopically in a porcine model to assess the usability and the safety of the device.

G.6.1 Benchtop Experiments

The main goal of this experiment was to confirm the operative range of the LapR-LMA as estimated in section G.6.1. As presented in Fig. G.14, the external controller was affixed to a vertical adjustable slider and coupled with the LapR-LMA through a rigid plastic surface. The weight was connected to the lever - starting at $\gamma = \pi/2$ – via an inextensible wire. Then, the external EM motor was activated with a step command at a speed of 1,700 rpm. The direction of rotation was reversed when γ reached zero, and the lever was moved back to its starting position. The maximum value of weight that was successfully lifted up and lowered down was recorded for each trial. This test was performed three times for each intermagnetic distance ranging from 2 cm to 4 cm, with 0.5 cm increments, and the results are presented in Fig. G.11.

The trial performed at d=2cm lifting a weight of 500 g is presented in Fig. G.15. The overall result of this experiment showed that the model in Fig. G.11 always overestimated W_L with an error of 9.06 ± 0.52%. This may be due to the cross-talking effect between the anchoring module and the actuation module, which was neglected while modeling the LapR-LMA.

During the experiments, failure always occurred for $\gamma = \pi/2$, with the device losing the magnetic coupling with the external controller (i.e., failure in anchoring). The actuation module always performed correctly, never entering the pole-slipping regime. This confirmed the assumption of a small $\Delta\theta^{max}$. The average time to conclude a single trial was 41.65

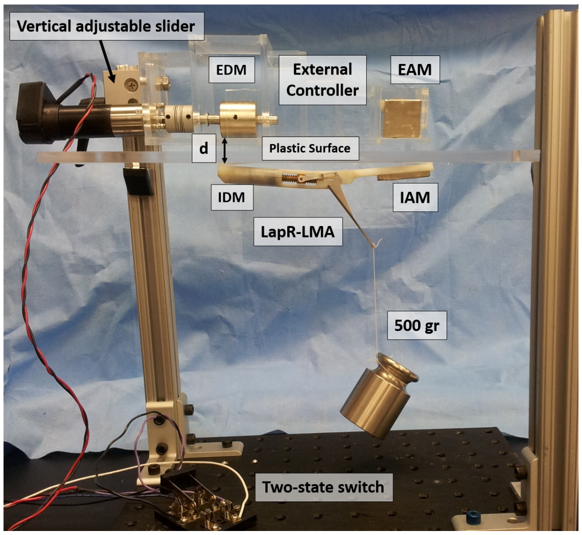

Figure G.14: Experimental setup during the benchtop experiments.

± 2.11 s. Finally, the benchtop experiment confirmed that the designed mechanism is not backdrivable, as the lever was able to maintain its position for γ=0.

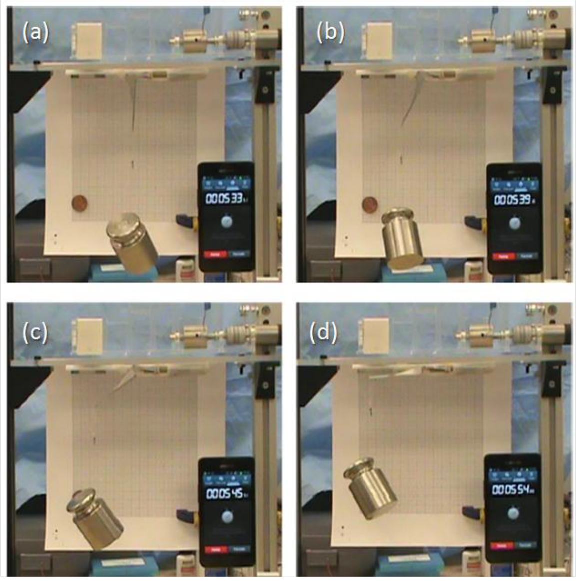

Figure G.15: Sequence showing a single trial with a weight of 500g at d=2 cm. Lifting up the weight required 21 s, as indicated by the stopwatch in the lower right corner.

G.6.2 Ex vivo trials

A typical task for a surgical retractor is to lift up the liver and hold it in position. The gallbladder and the stomach lie underneath it. To expose them and to achieve an adequate visibility of the surgical workspace, the surgeon usually has to lift the right lobe of the liver. This procedure was simulated with the same setup described in section G.6.1, using a freshly excised porcine liver (672 g) instead of the weight. The liver was placed 15 cm away from the plastic surface. A crocodile grasper – connected to the LapR-LMA lever via an inextensible wire – was secured to a lobe of the liver. Retraction was performed starting from $\gamma=\pi/2$ for d=2cm (Fig. G.16.a) and d=4cm (Fig. G.16.b). The EM motor was driven at 1,700 rpm. Three trials were performed for each distance and the liver was always lifted up and lowered down successfully. From the frames in Fig. G.16, it is possible to appreciate how the portion of suspended tissue increases during retraction. As previously discussed, this is compensated by the increase in lifting and supporting capacity for the LapR-LMA as γ decreases from $\pi/2$ to zero.

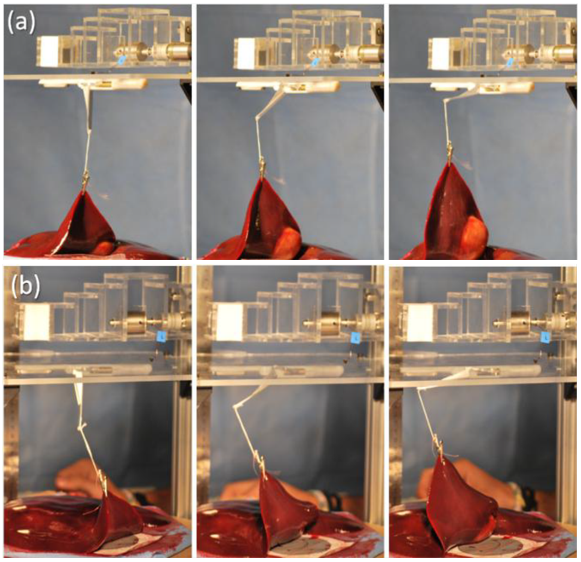

Figure G.16: Ex vivo liver retraction using the LapR-LMA. In the sequence presented in (a), the intermagnetic distance is 2 cm, while in the sequence in (b) is 4 cm.

G.6.3 In vivo trials

The primary goal of the *in vivo* trials was to qualitatively assess the functionality, the usability, and the safety of the LapR-LMA on an anesthetized porcine model. In particular, having a compliant tissue in between the external controller and the LapR-LMA allows the retractor to vibrate in the vertical direction under the effect of the varying F_{act}. This vertical wobbling may affect the lifting and the anchoring capacity, whereas the magnetic pinching may pose a safety risk to the tissue in between the external controller and the LapR-LMA.

The surgical procedure was performed at Vanderbilt University, with the assistance and collaboration of a specially trained medical team (IACUC Approval number M/14/163), in accordance with all ethical considerations and the regulations related to animal experiments. A 55-kg female Yorkshire swine was used for this study. After intravenous sedation, minimally invasive access was gained by one 5-mm trocar (5 Versaport Plus, Covidien, Norwalk, CT, USA) and one 12-mm trocars (5-12Versaport Plus, Covidien, Norwalk, CT,USA). The LapR-LMA was introduced in the abdominal cavity and coupled with the external controller. An abdominal thickness of 2 cm was measured by the surgeon at the insertion point, before the placement of the port. Then, a pneumoperitoneum was achieved with carbon dioxide gas.

Under endoscopic vision, the external controller was manually operated to drag the LapR-LMA next to the liver. The surgeon used a standard laparoscopic grasper to attach the crocodile jaws to one lobe of the liver. Retraction was then activated by rotating the driving magnet until the tissues below the liver were exposed, as shown in Fig. G.17. This procedure was repeated five times, always changing the position of the LapR-LMA and the point at which the liver was grasped. The animal was sacrificed at the end of the procedure. The region of abdominal tissue at which the LapR-LMA was anchored during retraction was then explanted and examined by an expert pathologist, reporting no sign of tissue damage due to magnetic pinching.

While the retraction was always successful and the LapR-LMA never lost the magnetic coupling with the external controller, the length of the device sometimes hampered the mobility inside the abdominal cavity. This limited the positioning of the LapR-LMA by only a few degrees off the sagittal plane of the animal. Placing the LapR-LMA along the transverse direction was not possible. This limited the reachable workspace and the possible approaching angles to the tissue to be retracted.

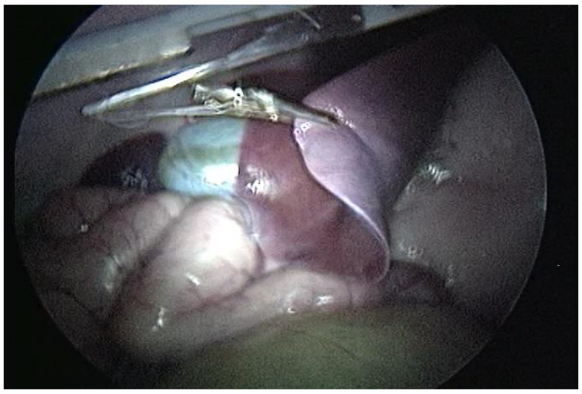

Figure G.17: LapR-LMA performing liver retraction during the *in vivo* trials.

G.7 Conclusions and Future Developments

Magnetic fields can be harnessed to transfer controllable mechanical power from outside the patient's body to a laparoscopic instrument within the body. Combining magnetic units with different functions, i.e. anchoring or actuation, it is possible to design surgical robots that do not require motors on board, nor take up port space during the procedure.

Given the constraints in diameter and volume of a MIS instrument, the proposed approach enables the transfer of a larger amount of mechanical power than what is possible to achieve by embedding typical electromechanical actuators on board. At the same time, due to magnetic coupling, triangulation is enhanced and invasiveness is reduced.

In this study, we demonstrated the feasibility of using the LMA approach to design a tetherless laparoscopic tissue retractor. The same design steps (i.e., medical consideration and technical requirements related to magnetic coupling, magnetic modeling, selection of the magnets, interfacing between the IDM and the mechanical train, and modeling of the overall device performance) can be adopted to implement LMA-based surgical robots performing different and more complex tasks.

The LapR-LMA is 12.5 mm in diameter and can be introduced laparoscopically. If the abdominal wall thickness is about 2 cm, the LapR-LMA is able to retract more than ten times its own weight. Bench trials demonstrated that the designed mechanism is not backdrivable and guarantees accurate and controllable motion of the retraction lever in both directions. The mechanism is able to cover the full range of motion in about 20 s. While the motion is slower if compared with manual operation of a laparoscopic retractor, the surgeon has the ability to adjust precisely the degree of retraction achieved by the LapR-LMA. Should a shorter time be required, the motor in the external controller can be replaced with a faster one.

In situations of overload, failure occurs in anchoring rather than actuation. If the anchoring failure occurs, the LapR-LMA needs to be recoupled with the external controller by the surgeon during the procedure. However, no failure was observed during the liver retraction experiment that was performed on a porcine model presenting an abdominal tissue thickness of 2 cm. The same experiment showed no abdominal wall tissue damage due to magnetic pinching.

While this study showed promising results, a number of challenges remain for future research.

Regarding LapR-LMA modeling, the maximum weight that can be lifted was overestimated by about 9%. This was mainly due to the assumption of no cross-coupling between the anchoring and the actuation units. Therefore, a more comprehensive model, capturing the interactions among all the magnets in the device, must be developed. The closer the anchoring and the actuation units, the stronger the cross-coupling between them, thus, a better model will be crucial for designing a shorter version of the LapR-LMA. Reducing the length of the device would improve maneuverability and provide better access to the surgical target, as observed during the *in vivo* trials.

As the main goal of this study was to assess the mechanical power transfer that can be achieved via the LMA approach, we did not focus extensively on the part of the device interacting with the tissue to be retracted. In particular, liver retraction was performed with traumatic graspers because of their availability. This is not applicable to a clinical case, where suction cups [151] or a fan-shaped end effector [115] must be used instead to prevent damaging the hepatic tissue. The current version of the LapR-LMA can be used whenever the retracted tissue must be removed at the end of the surgical procedure (e.g., cholecystectomy). While the current device is wireless, a thin tethered connection can be introduced to facilitate retrieval at the end of the procedure. Future studies involving surgeons will be devoted to assess and to improve, if needed, the usability and the ergonomics of the device.

The permanent magnets that were embedded in the LapR-LMA maintain their magnetic properties up to 80^oC. If autoclave sterilization is needed, they must be replaced with more expensive magnets - still available from the same supplier - that can withstand a temperature up to 150^oC. An alternative is to conceive the LapR-LMA as a single-use disposable device. If the mechanical parts are mass fabricated, the overall cost of the device may fall to a few dollars.

Concerning the fabrication material, the LapR-LMA body was obtained by rapid prototyping using Vero White+ plastic. Moving forward to clinical trials, a biocompatible material must be used. Either computer numerical control machining or injection molding can be adopted to fabricate the body as part of a reusable or disposable instrument, respectively.

Stronger retraction forces at larger distances can be obtained by using external permanent magnets with higher magnetization grades or larger volumes. The proposed modeling methods can be used to select the appropriate magnets to fit specific requirements, possibly extending the reach of this approach to obese patients.

Finally, an intriguing direction of future research is to design an LMA-based surgical robot with multiple DOFs. Such a device would be able to achieve complex surgical tasks, such as surface scanning with an optical probe or even suturing. Combining a number of actuation units and one or more anchoring units in a device that can fit a laparoscopic access requires advanced modeling and, most likely, the use of shielding material [152] between units.

Appendix H

SURGICAL ROBOTIC MANIPULATOR BASED ON LOCAL MAGNETIC ACTUATION

Christian Di Natali, Alireza Mohammadi, Denny Oetomo, Pietro Valdastri

From: Design of Medical Devices (DMD) Conference,
Status: Submitted

H.1 Background

Magnetic coupling is a strategy to transmit actuation forces across a physical barrier. This approach can be applied to remotely control and manipulate robotic instruments in Minimally Invasive Surgery (MIS) [40]. Interrupting the mechanical continuity of such system by having surgical instruments and laparoscopic camera magnetically coupled across the abdominal wall greatly enhances both the workspace of operation and triangulation without the need for multiple abdominal incisions [247]. On the other hand, continuum robots are able to provide a large amount of mechanical power to accomplish surgical tasks [85]. Focusing on the typical surgical task of suturing a tissue, 1 N of force in any direction and 180^o per second rotational speed must be achieved throughout a 50X50X50mm^3 workspace [85].

In [121], the authors introduced the concept of Local Magnetic Actuation (LMA), where mechanical power is transmitted across the patient abdomen by specific magnetic couplings to drive the Degrees of Freedom (DoF) of the robotic surgical instrument. This approach removes the need for electromagnetic motors on board and wired connections.

The LMA-based surgical retractor presented in [143] combines two pairs of magnets, one providing anchoring and the other transferring motion to the internal mechanism actuating a single DoF. This study shows the feasibility for the LMA approach to transfer a relevant amount of mechanical power to produce forces of up to 5 N.

Previous papers, such as [248], have proposed the use of cable-driven mechanism in surgical applications. Major advantages of cable-actuation are the light weight, small size, transmission of force to hard-to-reach location and high bending radii.

The design presented in this paper aims to develop a surgical manipulator for MIS able to perform surgical tasks combining mechanical power transmission based on LMA and cable-driven actuation of a novel design of spherical parallel wrist.

H.2 Methods

This robotic manipulator features an LMA-actuated 4 DoF cable-driven spherical wrist, which is schematically represented in Fig.H.1.A and referred to as MultiDOF-LMA. The MultiDOF-LMA design has three Actuation Units (AcU) and an Anchoring Unit (AnU). Each AcU provides the mechanical power to actuate one DoF of the wrist through a pair of antagonistic cable drive. The anchoring unit provides for the gross positioning, support, and through its ability to translate, also provides the actuation of the tilt angle (θ_1) DoF of the MultiDOF-LMA.

The AcU consists in a couple of diametrically magnetized magnets – the External Driving Magnet (EDM) and the Internal Driven Magnet (IDM) – designed to transmit mechanical power from the external motor to the mechanism embedded inside each of the Transmission Modules (TM)1-3. The gear transmission inside the TM amplifies the torque delivered by the IDM to the antagonistic-cables attachment. Each TM is equipped with a planetary gear train (1:16 gear ratio), a set of spur gears (1:14 gear ratio) and a cable reel (2.5 mm radius). The two antagonistic-cables lines are connected with the reel and rolled-up by lengths S_1, S_2 and S_3, respectively, for each actuated DoF of the spherical wrist. Each TM is connected to the link 1 of the manipulator through flexible pipes hosting each pair of antagonistic cables.

The AnU consists of a pair of axial magnetized permanent magnets. The External Anchoring Magnets (EAMs) are connected to each other by motorized linear slide. The EAMs are magnetically coupled with the Internal Anchoring Magnets (IAMs) generating the forces to support the MultiDOF-LMA during operation by offering two points of contact with the abdominal wall. For a typical abdominal surgery procedure, we considered a cubic workspace of 50X50X50mm^3 side located 10 to 15 cm below the insufflated abdominal wall. The AnU also provides the actuation of joint 1 (J_1) to orient the manipulator tip along the direction of interest.

The MultiDOF-LMA design has a novel configuration for a 3 DoF cable-driven parallel wrist with no kinematic singularity in the joint limited workspace and decoupled cables actuation. The spherical wrist, showed in Fig. H.1.B, features a simple design with a parallel configuration. It is composed by a U-joint followed by a helical actuated serial joint [144]. The U-joint provides the parallel actuation of the tip along the axes $\mathbf{x}_0$ and $\mathbf{y}_0$ in a range of $\pm 60^o$ with respect to the wrist frame coordinate system. The ends of the two pairs of antagonistic cables are connected to the U-joint output link (UOL) and spaced by 90^o to each other. The helical actuated joint is composed by two cylindrical links, H_1 and H_2, one on top of the other, where H_1 can freely rotate relative to H_2. The helically

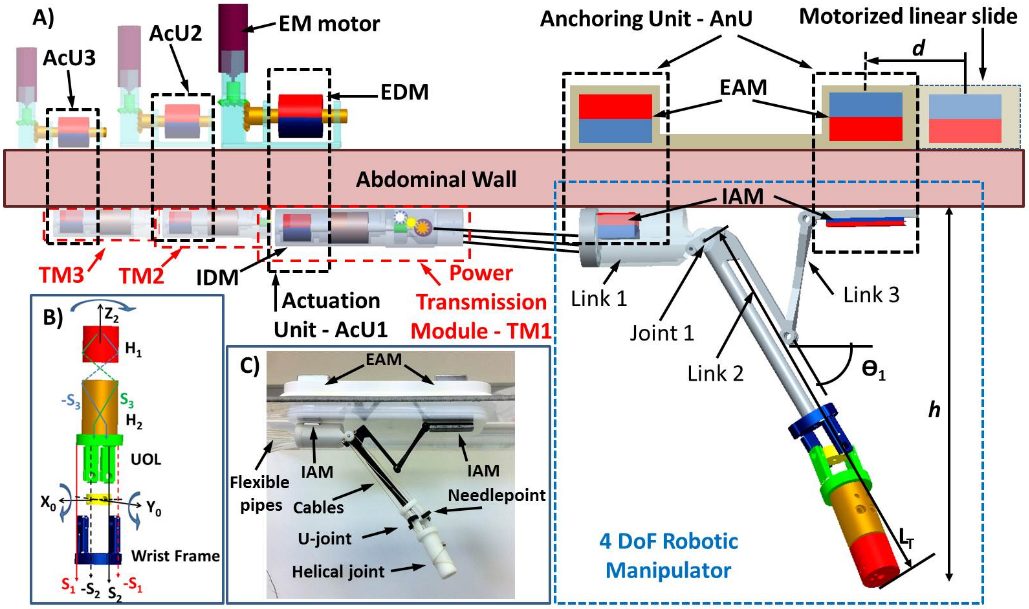

Figure H.1: Schematic view of the MultiDOF-LMA design (A), the spherical wrist schematic design (B) and the prototype implementation picture (C).

actuated joint is mounted on top of the UOL and provides the tip rotation about $\mathbf{z}_2$ of the UOL coordinate system. The antagonistic cables are connected on the outer side of H_1 and helically rolled around H_1 and H_2, one clockwise and the other counterclockwise. This cable arrangement allows for a rotation of $\pm 180^o$ around $\mathbf{z}_2$ in either direction, depending on the cable that is remotely pulled.

On the tip of the manipulator, a cable-driven endoscopy flexible grasper could be attached to achieve the desired surgical tasks. The flexible grasper is inserted through the single abdominal access; it enters from the posterior of the MultiDOF-LMA and exits from the tip of the manipulator. The flexible grasper could be externally actuated to generate up to 40 N grasping forces [85].

H.3 Results

A prototype implementing the design described above has been fabricated and tested confirming the functionality of the novel cable-driven spherical wrist (Fig. H.1.C).The permanent magnets implementing both AcUs and AnUs have been tested and reported in [143]. Typical attraction forces are within the range of 1 N to 5 N, and actuating torque within 2 mNm to 8 mNm, considering a distance between the external and internal magnets below 6 cm.

The tilt angle θ_1 about J_1 achieved by the relative motion d between the EAMs is defined as following: $\theta_1 = cos^{-1}[(L-d)/(2l)]$, where L is the initial distance between the EAMs, and l is the length of both links 2 and 3. L_T is the whole length of the MultiDOF-LMA from J_1 to the tip. If the EAM is moved by d, the robotic tip reaches the distance h from the abdominal wall, such as: $h = L_T sin\{cos^{-1}[(L-d)/(2l)]\}$.

The two pairs of antagonistic cables connected at the U-joint actuate the angles θ_2 and θ_3, as shown in Fig. H.1.B. Each cable goes down along the U-joint structure passing through a needlepoint at the Cross Link Junction (CLJ). This cable constraint provides an even cable length variation during the U-joint actuation, thus decoupling the cables. The kinematic equation relating the antagonist cable displacements S_1, S_2 and the angles θ_2 and θ_3 is ΔS_1, $l_2 = l_u - (l_u^2 + r_u^2)^{1/2} cos(tan^{-1}(r_u/l_u) + \theta_{2,3})$, where l_u is the UOL length and r_u is the UOL radius.

The antagonistic cables actuating the helical joint are connected on the outer side of H_1, controlling the rotational angle θ_4. The cables follow a helical path along the outer cylindrical surface of radius r and pitch $2\pi l_h$, where r is the helical joint radius and l_h is the length of both H_1 and H_2. The following parametric function describes the cable trajectory helically rolled along H_1 and $H_2 : t \rightarrow [rcos(t), rsin(t), l_h t/(2\pi)]$, where $t \in [0, 2\pi]$. In order to achieve $\theta_4 = \pm 180^o$, the cable displacement S_3 is actuated as follows: $\Delta S_3 = l_h/(\pi\theta_4)$. The cable decoupling is achieved by pushing the cable pair through the CLJ center hole. The estimated transmitted force at the tool tip, considering 2 mNm available torque at each AcU and a 50% of efficiency, is about 16 N for each direction of motion. The maximum estimated speed at the tool tip, considering the IDM rotating at 10000 rpm, is $58^o/s$, thus it covers the entire workspace for the U-joint in two seconds.

H.4 Interpretation

Thanks to the LMA actuation strategy and to the presented cable-driven mechanism, battery and motors are located externally, resulting in a manipulator with significant torque/speed performance. The final prototype has a diameter less than 15 mm allowing it to enter from a standard 15-mm trocar for MIS. The novel spherical wrist design is antagonistically cable-driven, has no kinematic singularity and presents cable decoupling. The proposed design paves the way for disposable low-cost implementation of robotic laparoscopic surgery.

Bibliography

[1] A. C. Lehman, J. Dumpert, N. A. Wood, L. Redden, A. Q. Visty, S. Farritor, B. Varnell, and D. Oleynikov, “Natural orifice cholecystectomy using a miniature robot,” *Surgical endoscopy*, vol. 23, no. 2, pp. 260–266, 2009.

[2] J. F. Rey, H. Ogata, N. Hosoe, K. Ohtsuka, N. Ogata, K. Ikeda, H. Aihara, I. Pangtay, T. Hibi, S. Kudo, and H. Tajiri, “Feasibility of stomach exploration with a guided capsule endoscope,” *Endoscopy*, vol. 42, no. 7, pp. 541–545, Jul 2010.

[3] S. Best and J. Cadeddu, “Development of magnetic anchoring and guidance systems for minimally invasive surgery,” *Indian Journal of Urology*, vol. 26, no. 3, p. 418, 2010.

[4] J. Cadeddu, R. Fernandez, M. Desai, R. Bergs, C. Tracy, S.-J. Tang, P. Rao, M. Desai, and D. Scott, “Novel magnetically guided intra-abdominal camera to facilitate laparoendoscopic single-site surgery: initial human experience,” *Surgical endoscopy*, vol. 23, no. 8, pp. 1894–1899, 2009.

[5] A. Arezzo, A. Menciassi, P. Valdastri, G. Ciuti, G. Lucarini, M. Salerno, C. Di Natali, M. Verra, P. Dario, and M. Morino, “Experimental assessment of a novel robotically-driven endoscopic capsule compared to traditional colonoscopy,” *Digestive and Liver Disease*, vol. 45, no. 8, pp. 657–662, 2013.

[6] M. Simi, P. Valdastri, C. Quaglia, A. Menciassi, and P. Dario, “Design, fabrication, and testing of a capsule with hybrid locomotion for gastrointestinal tract exploration,” *Mechatronics, IEEE/ASME Transactions on*, vol. 15, no. 2, pp. 170–180, 2010.

[7] C. Hu, M. Li, S. Song, R. Zhang, M.-H. Meng *et al.*, “A cubic 3-axis magnetic sensor array for wirelessly tracking magnet position and orientation,” *Sensors Journal, IEEE*, vol. 10, no. 5, pp. 903–913, 2010.

[8] S. Hashi, S. Yabukami, H. Kanetaka, K. Ishiyama, and K. Arai, “Wireless magnetic position-sensing system using optimized pickup coils for higher accuracy,” *Magnetics, IEEE Transactions on*, vol. 47, no. 10, pp. 3542–3545, 2011.

[9] F. Carpi, N. Kastelein, M. Talcott, and C. Pappone, “Magnetically controllable gastrointestinal steering of video capsules,” *Biomedical Engineering, IEEE Transactions on*, vol. 58, no. 2, pp. 231–234, 2011.

[10] The End for Mechanical Gearboxes?: http://www.mywindpowersystem.com/2014/06/21/the-end-for-mechanical-gearboxes .

[11] S. Mezani, K. Atallah, and D. Howe, “A high-performance axial-field magnetic gear,” *Journal of applied physics*, vol. 99, no. 8, p. 08R303, 2006.

[12] C. Liu and K. Chau, “Electromagnetic design of a new electrically controlled magnetic variable-speed gearing machine,” *Energies*, vol. 7, no. 3, pp. 1539–1554, 2014.

[13] P. VaLdastri, "Mesoscale mobile robots for gastrointestinal minimally invasive surgery (mis)," 2012.

[14] O. Ergeneman, G. Dogangil, M. P. Kummer, J. J. Abbott, M. K. Nazeeruddin, and B. J. Nelson, "A magnetically controlled wireless optical oxygen sensor for intraocular measurements," *Sensors Journal, IEEE*, vol. 8, no. 1, pp. 29–37, 2008.

[15] S. Martel, O. Felfoul, J.-B. Mathieu, A. Chanu, S. Tamaz, M. Mohammadi, M. Mankiewicz, and N. Tabatabaei, "Mri-based medical nanorobotic platform for the control of magnetic nanoparticles and flagellated bacteria for target interventions in human capillaries," *The International journal of robotics research*, vol. 28, no. 9, pp. 1169–1182, 2009.

[16] N. A. Patronik, T. Ota, M. A. Zenati, and C. N. Riviere, "A miniature mobile robot for navigation and positioning on the beating heart," *Robotics, IEEE Transactions on*, vol. 25, no. 5, pp. 1109–1124, 2009.

[17] S. R. Platt, J. A. Hawks, and M. E. Rentschler, "Vision and task assistance using modular wireless in vivo surgical robots," *Biomedical Engineering, IEEE Transactions on*, vol. 56, no. 6, pp. 1700–1710, 2009.

[18] M. E. Rentschler, J. Dumpert, S. R. Platt, K. Lagnernma, D. Oleynikov, and S. M. Farritor, "Modeling, analysis, and experimental study of in vivo wheeled robotic mobility," *Robotics, IEEE Transactions on*, vol. 22, no. 2, pp. 308–321, 2006.

[19] T. Hu, P. K. Allen, N. J. Hogle, and D. L. Fowler, "Insertable surgical imaging device with pan, tilt, zoom, and lighting," *The International Journal of Robotics Research*, 2009.

[20] F. Carpi and C. Pappone, "Stereotaxis niobe® magnetic navigation system for endocardial catheter ablation and gastrointestinal capsule endoscopy," *Expert review of medical devices*, vol. 6, no. 5, pp. 487–498, 2009.

[21] P. Swain, A. Toor, F. Volke, J. Keller, J. Gerber, E. Rabinovitz, and R. I. Rothstein, "Remote magnetic manipulation of a wireless capsule endoscope in the esophagus and stomach of humans (with)," *Gastrointestinal endoscopy*, vol. 71, no. 7, pp. 1290–1293, 2010.

[22] G. Ciuti, P. Valdastri, A. Menciassi, and P. Dario, "Robotic magnetic steering and locomotion of capsule endoscope for diagnostic and surgical endoluminal procedures," *Robotica*, vol. 28, no. 02, pp. 199–207, 2010.

[23] P. Valdastri, R. J. Webster, C. Quaglia, M. Quirini, A. Menciassi, and P. Dario, "A new mechanism for mesoscale legged locomotion in compliant tubular environments," *Robotics, IEEE Transactions on*, vol. 25, no. 5, pp. 1047–1057, 2009.

[24] J. Keller, C. Fibbe, F. Volke, J. Gerber, A. C. Mosse, M. Reimann-Zawadzki, E. Rabinovitz, P. Layer, D. Schmitt, V. Andresen *et al.*, "Inspection of the human stomach

using remote-controlled capsule endoscopy: a feasibility study in healthy volunteers (with videos)," *Gastrointestinal endoscopy*, vol. 73, no. 1, pp. 22–28, 2011.

[25] J.-F. Rey, H. Ogata, N. Hosoe, K. Ohtsuka, N. Ogata, K. Ikeda, H. Aihara, I. Pangtay, T. Hibi, S.-E. Kudo *et al.*, "Blinded nonrandomized comparative study of gastric examination with a magnetically guided capsule endoscope and standard videoendoscope," *Gastrointestinal endoscopy*, vol. 75, no. 2, pp. 373–381, 2012.

[26] A. W. Mahoney and J. J. Abbott, "Generating rotating magnetic fields with a single permanent magnet for propulsion of untethered magnetic devices in a lumen," *IEEE Transactions on Robotics*, 2014. In press, available on-line.

[27] S. Yim and M. Sitti, "Design and rolling locomotion of a magnetically actuated soft capsule endoscope," *IEEE Trans. Robot.*, vol. 28, no. 1, pp. 183–194, 2012.

[28] G. Ciuti, P. Valdastri, A. Menciassi, and P. Dario, "Robotic magnetic steering and locomotion of capsule endoscope for diagnostic and surgical endoluminal procedures," *Robotica*, vol. 28, no. 2, pp. 199–207, 2009.

[29] J. Keller, C. Fibbe, C. Volke, J. Gerber, A. C. Mosse, M. Reimann-Zawadzki, E. Rabinovitz, P. Layer, D. Schmitt, V. Andresen, U. Rosien, and P. Swain, "Inspection of the human stomach using remote-controlled capsule endoscopy: a feasibility study in healthy volunteers (with videos)," *Gastrointestinal Endoscopy*, vol. 73, no. 1, pp. 22–28, 2011.

[30] J.-F. Rey, H. Ogata, N. Hosoe, K. Ohtsuka, N. Ogata, K. Ikeda, H. Aihara, I. Pangtay, T. Hibi, S.-e. Kudo, and H. Tajiri, "Blinded nonrandomized comparative study of gastric examination with a magnetically guided capsule endoscope and standard videoendoscope." *Gastrointestinal Endoscopy*, vol. 75, no. 2, pp. 373–381, 2012.

[31] ASGE Technology Committee, "Magnets in the GI tract," *Gastrointestinal Endoscopy*, vol. 78, no. 4, pp. 561–567, 2013.

[32] C. Di Natali, M. Beccani, K. Obstein, and P. Valdastri, "A wireless platform for in vivo measurement of resistance properties of the gastrointestinal tract," *Physiological measurement*, vol. 35, no. 7, p. 1197, 2014.

[33] A. Mahoney and A. Jake, "5-dof manipulation of an untethered magnetic device in fluid using a single permanent magnet," in *Proceedings of Robotics: Science and Systems*, Berkeley, USA, July 2014.

[34] G.-P. Haber, M. A. White, R. Autorino, P. F. Escobar, M. D. Kroh, S. Chalikonda, R. Khanna, S. Forest, B. Yang, F. Altunrende *et al.*, "Novel robotic da vinci instruments for laparoendoscopic single-site surgery," *Urology*, vol. 76, no. 6, pp. 1279–1282, 2010.

[35] J. Ding, R. E. Goldman, K. Xu, P. K. Allen, D. L. Fowler, and N. Simaan, "Design and coordination kinematics of an insertable robotic effectors platform for single-port

access surgery," *IEEE/ASME Trans. Mechatronics*, vol. 18, no. 5, pp. 1612–1624, 2013.

[36] A. Lehman, N. Wood, S. Farritor, M. Goede, and D. Oleynikov, "Dexterous miniature robot for advanced minimally invasive surgery," *Surgical Endoscopy*, vol. 25, pp. 119–123, 2010.

[37] J. Shang, C. J. Payne, J. Clark, D. P. Noonan, K.-W. Kwok, A. Darzi, and G.-Z. Yang, "Design of a multitasking robotic platform with flexible arms and articulated head for minimally invasive surgery," in *Proc. IEEE/RSJ Int. Conf. Intell. Robots Syst.*, 2012, pp. 1988–1993.

[38] G. Tortora, P. Dario, and A. Menciassi, "Array of robots augmenting the kinematics of endocavitary surgery," *IEEE/ASME Transactions on Mechatronics*, 2014, in press, available on-line.

[39] M. Piccigallo, U. Scarfogliero, C. Quaglia, G. Petroni, P. Valdastri, A. Menciassi, and P. Dario, "Design of a novel bimanual robotic system for single-port laparoscopy," *Mechatronics, IEEE/ASME Transactions on*, vol. 15, no. 6, pp. 871–878, 2010.

[40] I. S. Zeltser, R. Bergs, R. Fernandez, L. Baker, R. Eberhart, and J. A. Cadeddu, "Single trocar laparoscopic nephrectomy using magnetic anchoring and guidance system in the porcine model," *The Journal of urology*, vol. 178, no. 1, pp. 288–291, 2007.

[41] M. Simi, R. Pickens, A. Menciassi, S. D. Herrell, and P. Valdastri, "Fine tilt tuning of a laparoscopic camera by local magnetic actuation two-port nephrectomy experience on human cadavers," *Surgical innovation*, vol. 20, no. 4, pp. 385–394, 2013.

[42] P. Vartholomeos, C. Bergeles, L. Qin, and P. E. Dupont, "An MRI-powered and controlled actuator technology for tetherless robotic interventions," *The International Journal of Robotics Research*, vol. 32, no. 13, pp. 1536–1552, 2013.

[43] "Globocan," 2008, uRL http://globocan.iarc.fr/.

[44] "Centers for Disease Control and Prevention," 2013, uRL http://www.cdc.gov.

[45] C. Pox, W. Schmiegel, and M. Classen, "Current status of screening colonoscopy in Europe and in the United States," *Endoscopy*, vol. 39, no. 02, pp. 168–173, 2007.

[46] J. L. Toennies, G. Tortora, M. Simi, P. Valdastri, and R. J. Webster III, "Swallowable medical devices for diagnosis and surgery: the state of the art," *Proceedings of the Institution of Mechanical Engineers, Part C: Journal of Mechanical Engineering Science*, vol. 224, no. 7, pp. 1397–1414, 2010.

[47] R. Eliakim, K. Yassin, Y. Niv, Y. Metzger, J. Lachter, E. Gal, B. Sapoznikov, F. Konikoff, G. Leichtmann, Z. Fireman *et al.*, "Prospective multicenter performance evaluation of the second-generation colon capsule compared with colonoscopy," *Endoscopy*, vol. 41, no. 12, pp. 1026–1031, 2009.

[48] C. Spada, F. De Vincentis, P. Cesaro, C. Hassan, M. E. Riccioni, L. M. Grazioli, S. Bolivar, A. Zurita, and G. Costamagna, "Accuracy and safety of second-generation PillCam COLON capsule for colorectal polyp detection," *Therapeutic Advances in Gastroenterology*, vol. 5, no. 3, pp. 173–178, 2012.

[49] P. Valdastri, M. Simi, and R. J. Webster III, "Advanced Technologies for Gastrointestinal Endoscopy." *Annual Review of Biomedical Engineering*, vol. 14, pp. 397–429, 2012.

[50] P. Valdastri, R. J. Webster, C. Quaglia, M. Quirini, A. Menciassi, and P. Dario, "A new mechanism for mesoscale legged locomotion in compliant tubular environments," *Robotics, IEEE Transactions on*, vol. 25, no. 5, pp. 1047–1057, 2009.

[51] L. J. Sliker, M. D. Kern, J. A. Schoen, and M. E. Rentschler, "Surgical evaluation of a novel tethered robotic capsule endoscope using micro-patterned treads," *Surgical Endoscopy*, vol. 26, no. 10, pp. 2862–2869, 2012.

[52] M. P. Kummer, J. J. Abbott, B. E. Kratochvil, R. Borer, A. Sengul, and B. J. Nelson, "Octomag: An electromagnetic system for 5-dof wireless micromanipulation," *Robotics, IEEE Transactions on*, vol. 26, no. 6, pp. 1006–1017, 2010.

[53] J. J. Abbott, O. Ergeneman, M. P. Kummer, A. M. Hirt, and B. J. Nelson, "Modeling magnetic torque and force for controlled manipulation of soft-magnetic bodies," *Robotics, IEEE Transactions on*, vol. 23, no. 6, pp. 1247–1252, 2007.

[54] A. G. Ciutia, P. Valdastria, and P. Darioa, "Robotic magnetic steering and locomotion of microsystems for diagnostic and surgical endoluminal procedures," *Robotica*, 2009.

[55] T. D. Than, G. Alici, H. Zhou, and W. Li, "A review of localization systems for robotic endoscopic capsules," *Biomedical Engineering, IEEE Transactions on*, vol. 59, no. 9, pp. 2387–2399, 2012.

[56] X. Wang, M.-H. Meng, and C. Hu, "A localization method using 3-axis magnetoresistive sensors for tracking of capsule endoscope," in *Engineering in Medicine and Biology Society, 2006. EMBS'06. 28th Annual International Conference of the IEEE.* IEEE, 2006, pp. 2522–2525.

[57] M. Hocke, U. Schöne, H. Richert, P. Görnert, J. Keller, P. Layer, and A. Stallmach, "Every slow-wave impulse is associated with motor activity of the human stomach," *American Journal of Physiology-Gastrointestinal and Liver Physiology*, vol. 296, no. 4, pp. G709–G716, 2009.

[58] B. Laulicht, N. J. Gidmark, A. Tripathi, and E. Mathiowitz, "Localization of magnetic pills," *Proceedings of the National Academy of Sciences*, vol. 108, no. 6, pp. 2252–2257, 2011.

[59] I. Wilding, P. Hirst, and A. Connor, "Development of a new engineering-based capsule for human drug absorption studies," *Pharmaceutical science & technology today*, vol. 3, no. 11, pp. 385–392, 2000.

[60] I. Aoki, A. Uchiyama, K. Arai, K. Ishiyama, and S. Yabukami, "Detecting system of position and posture of capsule medical device," Jul. 6 2010, uS Patent 7,751,866.

[61] K. M. Miller, A. W. Mahoney, T. Schmid, and J. J. Abbott, "Proprioceptive magnetic-field sensing for closed-loop control of magnetic capsule endoscopes," in *Intelligent Robots and Systems (IROS), 2012 IEEE/RSJ International Conference on.* IEEE, 2012, pp. 1994–1999.

[62] H. Li, G. Yan, and G. Ma, "An active endoscopic robot based on wireless power transmission and electromagnetic localization," *The International Journal of Medical Robotics and Computer Assisted Surgery*, vol. 4, no. 4, pp. 355–367, 2008.

[63] M.-G. Kim, Y.-S. Hong, and E.-J. Lim, "Position and Orientation Detection of Capsule Endoscopes in Spiral Motion," *International Journal of Precision Engineering and Manufacturing*, vol. 11, no. 1, pp. 31–37, 2010.

[64] A. W. Mahoney and J. J. Abbott, "Control of Untethered Magnetically Actuated Tools with Localization Uncertainty using a Rotating Permanent Magnet," in *IEEE International Conference on Biomedical Robotics and Biomechatronics (BioRob)*, Jun. 2012, pp. 1632–1637.

[65] G. Ciuti, M. Salerno, G. Lucarini, P. Valdastri, A. Arezzo, A. Menciassi, M. Morino, and P. Dario, "A comparative evaluation of control interfaces for a robotic-aided endoscopic capsule platform," *Robotics, IEEE Transactions on*, vol. 28, no. 2, pp. 534–538, 2012.

[66] M. Salerno, G. Ciuti, G. Lucarini, R. Rizzo, P. Valdastri, A. Menciassi, A. Landi, and P. Dario, "A discrete-time localization method for capsule endoscopy based on on-board magnetic sensing," *Measurement Science and Technology*, vol. 23, 2012, 015701 (10 pp).

[67] M. Salerno, F. Mulana, R. Rizzo, A. Landi, and A. Menciassi, "Magnetic and inertial sensor fusion for the localization endoluminal diagnostic devices," in *International Journal of Computer Assisted Radiology and Surgery (CARS)*, vol. 7, no. S1, May 2012, pp. 229–235.

[68] C. Di Natali, M. Beccani, and P. Valdastri, "Real-time pose detection for magnetic medical devices," *IEEE Trans. Magn.*, vol. 49, no. 7, pp. 3524–3527, 2013.

[69] K. Atallah and D. Howe, "A novel high-performance magnetic gear," *Magnetics, IEEE Transactions on*, vol. 37, no. 4, pp. 2844–2846, 2001.

[70] F. T. Jørgensen, T. O. Andersen, and P. O. Rasmussen, "The cycloid permanent magnetic gear," in *Industry Applications Conference, 2006. 41st IAS Annual Meeting. Conference Record of the 2006 IEEE*, vol. 1. IEEE, 2006, pp. 373–378.

[71] S. Kikuchi and K. Tsurumoto, "Design and characteristics of a new magnetic worm gear using permanent magnet," *Magnetics, IEEE Transactions on*, vol. 29, no. 6, pp. 2923–2925, 1993.

[72] C.-C. Huang, M.-C. Tsai, D. G. Dorrell, and B.-J. Lin, “Development of a magnetic planetary gearbox,” *Magnetics, IEEE Transactions on*, vol. 44, no. 3, pp. 403–412, 2008.

[73] R. C. Holehouse, K. Atallah, and J. Wang, “Design and realization of a linear magnetic gear,” *Magnetics, IEEE Transactions on*, vol. 47, no. 10, pp. 4171–4174, 2011.

[74] J. Rens, R. Clark, S. Calverley, K. Atallah, and D. Howe, “Design, analysis and realization of a novel magnetic harmonic gear,” in *Electrical Machines, 2008. ICEM 2008. 18th International Conference on.* IEEE, 2008, pp. 1–4.

[75] X. Li, K.-T. Chau, M. Cheng, and W. Hua, “Comparison of magnetic-geared permanent magnet machines,” *Progress In Electromagnetics Research*, vol. 133, pp. 177–198, 2013.

[76] K. Atallah and D. Howe, “A novel high-performance magnetic gear,” *IEEE Transactions on Magnetics*, vol. 37, no. 4, pp. 2844–2846, 2001.

[77] K. Ikuta, M. Shunichi, and A. Suguro, “Non-contact magnetic gear for micro transmission mechanism,” in *Proc. IEEE Micro Electro Mechanical Syst.*, 1991, pp. 125–130.

[78] R. H. Taylor and D. Stoianovici, “Medical robotics in computer-integrated surgery,” *Robotics and Automation, IEEE Transactions on*, vol. 19, no. 5, pp. 765–781, 2003.

[79] G. Guthart and J. K. Salisbury Jr, “The intuitivetm telesurgery system: Overview and application.” in *ICRA*, 2000, pp. 618–621.

[80] M. Bessler, P. D. Stevens, L. Milone, M. Parikh, and D. Fowler, “Transvaginal laparoscopically assisted endoscopic cholecystectomy: a hybrid approach to natural orifice surgery,” *Gastrointestinal endoscopy*, vol. 66, no. 6, pp. 1243–1245, 2007.

[81] D. J. Abbott, C. Becke, R. Rothstein, W. J. Peine *et al.*, “Design of an endoluminal notes robotic system,” in *Intelligent Robots and Systems, 2007. IROS 2007. IEEE/RSJ International Conference on.* IEEE, 2007, pp. 410–416.

[82] S. Phee, S. Low, Z. Sun, K. Ho, W. Huang, and Z. Thant, “Robotic system for no-scar gastrointestinal surgery,” *The International Journal of Medical Robotics and Computer Assisted Surgery*, vol. 4, no. 1, pp. 15–22, 2008.

[83] M. Kroh, K. El-Hayek, S. Rosenblatt, B. Chand, P. Escobar, J. Kaouk, and S. Chalikonda, “First human surgery with a novel single-port robotic system: cholecystectomy using the da vinci single-site platform,” *Surgical endoscopy*, vol. 25, no. 11, pp. 3566–3573, 2011.

[84] Medgadget.com, New Single-port Minimally Invasive Robotic Systems from Intuitive Surgical (2014): `www.medgadget.com`.

[85] J. Ding, K. Xu, R. Goldman, P. Allen, D. Fowler, and N. Simaan, “Design, simulation and evaluation of kinematic alternatives for insertable robotic effectors platforms in single port access surgery,” in *Robotics and Automation (ICRA), 2010 IEEE International Conference on.* IEEE, 2010, pp. 1053–1058.

[86] K. Harada, E. Susilo, A. Menciassi, and P. Dario, “Wireless reconfigurable modules for robotic endoluminal surgery,” in *Robotics and Automation, 2009. ICRA'09. IEEE International Conference on.* IEEE, 2009, pp. 2699–2704.

[87] A. Dubrowski, R. Sidhu, J. Park, and H. Carnahan, “Quantification of motion characteristics and forces applied to tissues during suturing,” *The American Journal of Surgery*, vol. 190, no. 1, pp. 131–136, 2005.

[88] J. Peirs, J. Clijnen, D. Reynaerts, H. V. Brussel, P. Herijgers, B. Corteville, and S. Boone, “A micro optical force sensor for force feedback during minimally invasive robotic surgery,” *Sensors and Actuators A: Physical*, vol. 115, no. 2, pp. 447–455, 2004.

[89] P. Valdastri, M. Simi, and R. J. Webster III, “Advanced technologies for gastrointestinal endoscopy,” *Annual review of biomedical engineering*, vol. 14, pp. 397–429, 2012.

[90] E. P. Furlani, *Permanent magnet and electromechanical devices: materials, analysis, and applications.* Academic Press, 2001.

[91] E. Furlani and M. Knewtson, “A three-dimensional field solution for permanent-magnet axial-field motors,” *Magnetics, IEEE Transactions on*, vol. 33, no. 3, pp. 2322–2325, 1997.

[92] F. C. A. Devices, “Using an accelerometer for inclination sensing,” *Application note AN-1057*, 2011.

[93] H. J. Luinge, P. H. Veltink, and C. T. Baten, “Estimating orientation with gyroscopes and accelerometers,” *Technology and health care*, vol. 7, no. 6, pp. 455–459, 1999.

[94] M. Ignagni, “Optimal strapdown attitude integration algorithms,” *Journal of Guidance, Control, and Dynamics*, vol. 13, no. 2, pp. 363–369, 1990.

[95] J. Favre, B. Jolles, O. Siegrist, and K. Aminian, “Quaternion-based fusion of gyroscopes and accelerometers to improve 3d angle measurement,” *Electronics Letters*, vol. 42, no. 11, pp. 612–614, 2006.

[96] D. Whitney, “Resolved Motion Rate Control of Manipulators and Human Prostheses,” *IEEE Transactions on Man Machine Systems*, vol. 10, no. 2, pp. 47–53, Jun. 1969.

[97] J. Nocedal and S. J. Wright, *Numerical Optimization*, T. V. Mikosh, S. M. Robinson, and S. Resnick, Eds. Springer, 2006.

[98] E. P. Furlani, *Permanent Magnet and Electromechanical Devices.* Elsevier, 2001, pp. 131–135.

[99] G. S. Chirikjian and J. W. Burdick, "A Modal Approach to Hyper-Redundant Manipulator Kinematics," *IEEE Transactions on Robotics and Automation*, vol. 10, no. 3, pp. 343–354, 1994.

[100] J. Zhang, K. Xu, N. Simaan, and S. Manolidis, "A pilot study of robot-assisted cochlear implant surgery using steerable electrode arrays," in *Medical Image Computing and Computer-Assisted Intervention–MICCAI 2006.* Springer, 2006, pp. 33–40.

[101] J. Zhang, J. T. Roland, S. Manolidis, and N. Simaan, "Optimal path planning for robotic insertion of steerable electrode arrays in cochlear implant surgery," *Journal of medical devices*, vol. 3, no. 1, 2009.

[102] H. F. Davis, *Fourier series and orthogonal functions.* DoverPublications. com, 1963.

[103] N. Csanyi[1] and C. K. Toth, "Some aspects of using fourier analysis to support surface modeling," 2005.

[104] J. Brewer, "Kronecker products and matrix calculus in system theory," *Circuits and Systems, IEEE Transactions on*, vol. 25, no. 9, pp. 772–781, 1978.

[105] P. Lancaster and Miron Tismensky, *The Theory of Matrices*, 2nd ed. Academic Press, 1985.

[106] K. M. Miller, A. W. Mahoney, T. Schmid, and J. J. Abbott, "Proprioceptive magnetic-field sensing for closed-loop control of magnetic capsule endoscopes," in *IEEE/RSJ International Conference on Intelligent Robots and Systems (IROS)*, 2012, pp. 1994–1999.

[107] A. Petruska and J. Abbott, "Optimal permanent-magnet geometries for dipole field approximation," *IEEE Trans. Magn.*, vol. 49, no. 2, pp. 811–819, 2013.

[108] M. Salerno, R. Rizzo, E. Sinibaldi, and A. Menciassi, "Force calculation for localized driven capsule endoscopes," in *IEEE International Conference on Robotics and Automation (ICRA)*, 2013, pp. 5334–5339.

[109] E. P. Furlani, *Permanent Magnet and Electromechanical Devices.* Elsevier, 2001, pp. 131–135.

[110] Takktile by Y. Tenzer, L. Jentoft, I. Daniher, and R. Howe: www.takktile.com .

[111] X. Wang and M. Q. Meng, "An experimental study of resistant properties of the small intestine for an active capsule endoscope," *Proceedings of the Institution of Mechanical Engineers, Part H: Journal of Engineering in Medicine*, vol. 224, no. 1, pp. 107–118, 2010.

[112] C. Zhang, H. Liu, R. Tan, and H. Li, "Modeling of velocity-dependent frictional resistance of a capsule robot inside an intestine," *Tribology Letters*, vol. 47, no. 2, pp. 295–301, 2012.

[113] H. Zhou, G. Alici, T. D. Than, and W. Li, "Modeling and experimental investigation of rotational resistance of a spiral-type robotic capsule inside a real intestine," *IEEE/ASME Trans. Mechatronics*, vol. 18, no. 5, pp. 1555–1562, 2013.

[114] C. Di Natali, T. Ranzani, M. Simi, A. Menciassi, and P. Valdastri, "Trans-abdominal active magnetic linkage for robotic surgery: Concept definition and model assessment," in *Robotics and Automation (ICRA), IEEE International Conference on*, 2012, pp. 695–700.

[115] S. Park, R. A. Bergs, R. Eberhart, L. Baker, R. Fernandez, and J. A. Cadeddu, "Trocar-less instrumentation for laparoscopy: magnetic positioning of intra-abdominal camera and retractor," *Annals of surgery*, vol. 245, no. 3, p. 379, 2007.

[116] N. Simaan, K. Xu, W. Wei, A. Kapoor, P. Kazanzides, R. Taylor, and P. Flint, "Design and integration of a telerobotic system for minimally invasive surgery of the throat," *The International journal of robotics research*, vol. 28, no. 9, pp. 1134–1153, 2009.

[117] S. L. Best, R. Bergs, M. Gedeon, J. Paramo, R. Fernandez, J. A. Cadeddu, and D. J. Scott, "Maximizing coupling strength of magnetically anchored surgical instruments: how thick can we go?" *Surgical endoscopy*, vol. 25, no. 1, pp. 153–159, 2011.

[118] J. A. Liu, M. Etemadi, J. A. Heller, D. Kwiat, R. Fetcher, M. R. Harrison, and S. Roy, "Roboimplant ii: Development of a noninvasive controller/actuator for wireless correction of orthopedic structural deformities," *ASME Journal of Medical Devices*, vol. 6, pp. 031 006–1–5, 2012.

[119] R. Montague, C. Bingham, and K. Atallah, "Servo control of magnetic gears," *IEEE/ASME Trans. Mechatronics*, vol. 17, no. 2, pp. 269–278, 2012.

[120] R. Montague and C. Bingham, "Nonlinear control of magnetically-geared drive-trains," *International Journal of Automation and Computing*, vol. 10, no. 4, pp. 319–326, 2013.

[121] C. Di Natali, T. Ranzani, M. Simi, A. Menciassi, and P. Valdastri, "Trans-abdominal active magnetic linkage for robotic surgery: Concept definition and model assessment," in *Robotics and Automation (ICRA), 2012 IEEE International Conference on*. IEEE, 2012, pp. 695–700.

[122] M. Simi, G. Gerboni, A. Menciassi, and P. Valdastri, "Magnetic torsion spring mechanism for a wireless biopsy capsule," *Journal of Medical Devices*, vol. 7, no. 4, p. 041009, 2013.

[123] M. T. Spring, "Design, development and scaling analysis of a variable stiffness magnetic torsion spring."

[124] R. Montague, C. Bingham, and K. Atallah, "Servo control of magnetic gears," *Mechatronics, IEEE/ASME Transactions on*, vol. 17, no. 2, pp. 269–278, 2012.

[125] Namiki precision jewel CO, 10 mm DC micromotors, http://www.namiki.net/product/dcmotor/coreless.htm .

[126] Faulhaber miniature drive system, 10 mm DC micromotors, http://www.fmcc.faulhaber.com/type/PGR_13813_13801/PGR_13818_13813/en/ .

[127] "Non-ionizing radiation frequencies," 2014. [Online]. Available: http://www.icnirp.org/en/frequencies/index.html

[128] G. Zhang and J. Furusho, "Speed control of two-inertia system by PI/PID control," *IEEE Trans. Ind. Electron.*, vol. 47, no. 3, pp. 603–609, 2000.

[129] E. Furlani, "A two-dimensional analysis for the coupling of magnetic gears," *Magnetics, IEEE Transactions on*, vol. 33, no. 3, pp. 2317–2321, 1997.

[130] R. G. Montague, C. Bingham, and K. Atallah, "Magnetic gear pole-slip prevention using explicit model predictive control," *IEEE/ASME Trans. Mechatronics*, vol. 18, no. 3, pp. 1535–1543, 2013.

[131] G. Zhang, "Speed control of two-inertia system by pi/pid control," *Industrial Electronics, IEEE Transactions on*, vol. 47, no. 3, pp. 603–609, 2000.

[132] N. Garbin, C. Di Natali, J. Buzzi, E. De Momi, and P. Valdastri, "Laparoscopic tissue retractor based on local magnetic actuation," *Journal of Medical Devices*, vol. 9, no. 011005, pp. 1–10, 2015.

[133] SBL04-0829PG0443, Namiki Precision Jewel Co. : `www.namiki.net`.

[134] 1016-012G, Faulhaber Miniature Drive Systems: `www.faulhaber.com`.

[135] 1024-012S, Faulhaber Miniature Drive Systems: `www.faulhaber.com`.

[136] DCX10L, Maxon Motor : `http://www.maxonmotor.com/`.

[137] 1219-012G, Faulhaber Miniature Drive Systems: `www.faulhaber.com`.

[138] 1224-012SR, Faulhaber Miniature Drive Systems: `www.faulhaber.com`.

[139] Nano Core 110-001, Precision Microdrivers: `www.precisionmicrodrives.com`.

[140] Micro Core 112-001, Precision Microdrivers: `www.precisionmicrodrives.com`.

[141] SCL12-3003, Namiki Precision Jewel Co. : `www.namiki.net`.

[142] M. Beccani, E. Susilo, C. Di Natali, and P. Valdastri, "Smac: a modular open source architecture for medical capsule robots," *International Journal of Advanced Robotic Systems, in press*, 2014.

[143] N. Garbin, C. Di Natali, J. Buzzi, E. De Momi, and P. Valdastri, "Laparoscopic tissue retractor based on local magnetic actuation," *Journal of Medical Devices*, vol. 9, no. 1, p. 011005, 2015.

[144] M. C. Lei and D. Oetomo, "Modelling of cable wrapping phenomenon towards improved cable-driven mechanisms," in *Advanced Intelligent Mechatronics (AIM), 2013 IEEE/ASME International Conference on.* IEEE, 2013, pp. 649–655.

[145] A. W. Mahoney and J. J. Abbott, "Managing magnetic force applied to a magnetic device by a rotating dipole field," *Applied Physics Letters*, vol. 99, no. 13, pp. 134 103–134 103, 2011.

[146] G. Ciuti, P. Valdastri, A. Menciassi, and P. Dario, "Robotic magnetic steering and locomotion of capsule endoscope for diagnostic and surgical endoluminal procedures," *Robotica*, vol. 28, no. 2, pp. 199–207, 2010.

[147] P. Valdastri, G. Ciuti, A. Verbeni, A. Menciassi, P. Dario, A. Arezzo, and M. Morino, "Magnetic air capsule robotic system: Proof of concept of a novel approach for painless colonoscopy," *Surgical Endoscopy*, vol. 26, no. 5, pp. 1238–1246, 2012.

[148] M. Beccani, C. Di Natali, M. E. Rentschler, and P. Valdastri, "Wireless tissue palpation: Proof of concept for a single degree of freedom," in *IEEE International Conference on Robotics and Automation (ICRA)*, 2013, pp. 703–709.

[149] S. N. Vukosavic and M. R. Stojic, "Suppression of torsional oscillations in a high-performance speed servo drive," *IEEE Trans. Ind. Electron.*, vol. 45, no. 1, pp. 108–117, 1998.

[150] A. W. Mahoney and J. J. Abbott, "Generating rotating magnetic fields with a single permanent magnet for propulsion of untethered magnetic devices in a lumen," *IEEE Transactions on Robotics*, vol. 30, no. 2, pp. 411–420, 2014.

[151] P. Gan, "A novel liver retractor for reduced or single-port laparoscopic surgery," *Surgical endoscopy*, vol. 28, no. 1, pp. 331–335, 2014.

[152] R. D. Brewer, K. E. Loewke, E. F. Duval, and J. K. Salisbury, "Force control of a permanent magnet for minimally-invasive procedures," in *Biomedical Robotics and Biomechatronics, 2008. BioRob 2008. 2nd IEEE RAS & EMBS International Conference on.* IEEE, 2008, pp. 580–586.

[153] H. Keller, A. Juloski, H. Kawano, M. Bechtold, A. Kimura, H. Takizawa, and R. Kuth, "Method for navigation and control of a magnetically guided capsule endoscope in the human stomach," in *IEEE International Conference on Biomedical Robotics and Biomechatronics (BioRob)*, Jun. 2012, pp. 859–865.

[154] M. Gao, C. Hu, Z. Chen, H. Zhang, and S. Liu, "Design and Fabrication of a Magnetic Propulsion System for Self-propelled Capsule Endoscope." *IEEE Trans. Bio-Med. Eng.*, vol. 57, no. 12, pp. 2891–2902, 2010.

[155] X. Wang, M. Q. H. Meng, and X. Chen, "A Locomotion Mechanism with External Magnetic Guidance for Active Capsule Endoscope." in *Annual International Conference of the IEEE Engineering in Medicine and Biology Society*, Jan. 2010, pp. 4375–4378.

[156] T. D. Than, G. Alici, H. Zhou, and W. Li, "A Review of Localization Systems for Robotic Endoscopic Capsules." *IEEE Trans. Bio-Med. Eng.*, vol. 59, no. 9, pp. 2387–2399, 2012.

[157] "Northern digital inc., www.ndigital.com/medical/aurora.php," 2005.

[158] S. Isao Aoki, Y. Uchiyama, S. Arai, S. Ishiyama, and S. Yabukami, "Detecting system of position and posture of capsule medical devices," 2005, United States Patent US-2005/1216231 A1.

[159] K. M. Miller, A. W. Mahoney, T. Schmid, and J. J. Abbott, "Proprioceptive Magnetic-Field Sensing for Closed-loop Control of Magnetic Capsule Endoscopes," in *(IEEE) Int. Conf. Intelligent Robots and Systems (IROS), in press*, Oct. 2012.

[160] E. Durand, *Electrostatique.* Masson Editeur, 1964, vol. 1, pp. 248–251.

[161] R. Ravaud, G. Lemarquand, V. Lemarquand, and C. Depollier, "Analytical Calculation of the Magnetic Field Created by Permanent-Magnet Rings," *IEEE Transactions on Magnetics*, vol. 44, no. 8, pp. 1982–1989, 2008.

[162] M. Beccani, C. Di Natali, M. E. Rentschler, and P. Valdastri, "Wireless Tissue Palpation : Proof of Concept for a Single Degree of Freedom," in *Robotics and Automation (ICRA), IEEE International Conference on*, May 2013, in press.

[163] J. Fuller, W. Scott, B. Ashar, and J. Corrado, "Laparoscopic trocar injuries: A report from a U.S. Food and Drug Administration (FDA) Center for Devices and Radiological Health (CDRH) Systematic Technology Assessment of Medical Products (STAMP) committee," 2003, www.fda.gov/medicaldevices/safety/alertsandnotices/ucm197339.htm.

[164] P. Puangmali, H. Liu, L. Seneviratne, P. Dasgupta, and K. Althoefer, "Miniature 3-axis distal force sensor for minimally invasive surgical palpation," *Mechatronics, Transaction on IEEE*, vol. 17, no. 4, pp. 646–656, 2012.

[165] Intuitive Surgical website, http://www.intuitivesurgical.com. .

[166] H. Liu, J. Li, X. Song, L. Seneviratne, and K. Althoefer, "Rolling indentation probe for tissue abnormality identification during minimally invasive surgery," *Robotics, IEEE Transactions on*, vol. 27, no. 3, pp. 450–460, 2011.

[167] B. F. Kaczmarek, S. Sukumar, F. Petros, Q. D. Trinh, N. Mander, R. Che, M. Menon, and C. Rogers, "Robotic ultrasound probe for tumor identification in robotic partial nephrectomy: Initial series and outcomes," *Int J Urol*, vol. 20, no. 2, pp. 172–176, 2013.

[168] C. M. Schneider, P. D. Peng, R. H. Taylor, G. W. Dachs, C. J. Hasser, S. P. DiMaio, and M. A. Choti, "Robot-assisted laparoscopic ultrasonography for hepatic surgery," *Surgery*, vol. 151, no. 5, pp. 756–762, 2012.

[169] S. D. Herrell, R. L. Galloway, and L. M. Su, "Image-guided robotic surgery: update on research and potential applications in urologic surgery." *Current Opinion in Urology*, vol. 22, no. 1, pp. 47–54, 2012.

[170] G. McCreery, A. Trejos, M. Naish, R. Patel, and R. Malthaner, "Feasibility of locating tumours in lung via kinaesthetic feedback." *The International Journal of Medical Robotics and Computer Assisted Surgery*, vol. 4, no. 1, pp. 58–68, 2008.

[171] E. C. Lai, C. N. Tang, J. P. Ha, D. K. Tsui, and M. K. Li, "The evolving influence of laparoscopy and laparoscopic ultrasonography on patients with hepatocellular carcinoma," *Am J Surg*, vol. 196, no. 5, pp. 736–740, 2008.

[172] R. Yakoubi, R. Autorino, H. Laydner, J. Guillotreau, M. A. White, S. Hillyer, G. Spana, R. Khanna, W. Isaac, G. P. Haber, R. J. Stein, and J. H. Kaouk, "Initial laboratory experience with a novel ultrasound probe for standard and single-port robotic kidney surgery: increasing console surgeon autonomy and minimizing instrument clashing," *Int J Med Robot*, vol. 8, no. 2, pp. 201–205, 2012.

[173] L. Fratt, "Ultrasound opens new doors in robotic surgery," *Health Imaging*, vol. 10, no. 5, pp. 12–17, May/June 2012.

[174] P. Dario and M. Bergamasco, "An advanced robot system for automated diagnostic tasks through palpation," *Biomedical Engineering, IEEE Transactions on*, vol. 35, no. 2, pp. 118–126, 1988.

[175] R. Howe, W. Peine, D. Kantarinis, and J. Son, "Remote palpation technology," *IEEE Engineering in Medicine and Biology*, vol. 14, no. 3, pp. 318–323, 1995.

[176] T. Ohtsuka, A. Furuse, T. Kohno, J. Nakajima, K. Yagyu, and S. Omata, "Application of a new tactile sensor to thoracoscopic surgery: Experimental and clinical study," *The Annals of Thoracic Surgery*, vol. 60, no. 3, pp. 610–614, 1995.

[177] M. Ottensmeyer and J. Salisbury, "In vivo data acquisition instrument for solid organ mechanical property measurement," in *Medical Image Computing and Computer-Assisted Intervention – MICCAI 2001*. Springer, 2001, pp. 975–982.

[178] E. Samur, M. Sedef, C. Basdogan, L. Avtan, and O. Duzgun, "A robotic indenter for minimally invasive measurement and characterization of soft tissue response," *Medical Image Analysis*, vol. 11, no. 4, pp. 361–373, 2007.

[179] J. Rosen, J. Brown, S. De, M. Sinanan, and B. Hannaford, "Biomechanical properties of abdominal organs in vivo and postmortem under compression loads," *Journal of Biomechanical Engineering*, vol. 130, no. 021020, pp. 1–17, 2008.

[180] K. Lister, Z. Gao, and J. Desai, "Development of in vivo constitutive models for liver: Application to surgical simulation," *Annals of Biomedical Engineering*, vol. 39, pp. 1060–1073, 2011.

[181] O. Van der Meijden and M. Schijven, "The value of haptic feedback in conventional and robot-assisted minimal invasive surgery and virtual reality training: a current review," *Surgical Endoscopy*, vol. 23, pp. 1180–1190, 2009.

[182] G. Tholey and J. P. Desai, "A compact and modular laparoscopic grasper with tri-directional force measurement capability," *ASME Journal of Medical Devices*, vol. 2, no. 3, pp. 031 001–9, 2008.

[183] B. Kübler, U. Seibold, and G. Hirzinger, "Development of actuated and sensor integrated forceps for minimally invasive robotic surgery," *The International Journal of Medical Robotics and Computer Assisted Surgery*, vol. 1, no. 3, pp. 96–107, 2005.

[184] M. Stark, T. Benhidjeb, S. Gidaro, and E. Morales, "The future of telesurgery: a universal system with haptic sensation," *Journal of the Turkish-German Gynecological Association*, vol. 13, no. 1, pp. 74–76, 2012.

[185] J. Gwilliam, Z. Pezzementi, E. Jantho, A. Okamura, and S. Hsiao, "Human vs. robotic tactile sensing: Detecting lumps in soft tissue," in *IEEE Haptics Symposium*, 2010, pp. 21–28.

[186] R. E. Goldman, A. Bajo, and N. Simaan, "Algorithms for autonomous exploration and estimation in compliant environments," *Robotica*, vol. 31, no. 1, pp. 71–87, 2013.

[187] A. Talasaz and R. V. Patel, "Integration of force reflection with tactile sensing for minimally invasive robotics-assisted tumor localization," *IEEE Trans. Haptics*, 2013, in press, available on-line.

[188] M. T. Perri, A. L. Trejos, M. D. Naish, R. V. Patel, and R. A. Malthaner, "Initial evaluation of a tactile/kinesthetic force feedback system for minimally invasive tumor localization," *Mechatronics, IEEE Transactions on*, vol. 15, no. 6, pp. 925–931, 2010.

[189] ——, "New tactile sensing system for minimally invasive surgical tumour localization," *The International Journal of Medical Robotics and Computer Assisted Surgery*, vol. 6, no. 2, pp. 211–220, 2010.

[190] X. Wang, J. A. Schoen, and M. E. Rentschler, "Quantitative comparison of soft tissue compressive viscoelastic model accuracy," *Journal of Mechanical Behavior of Biomedical Materials*, vol. 20, pp. 126–136, 2013.

[191] P. Valdastri, K. Harada, A. Menciassi, L. Beccai, C. Stefanini, M. Fujie, and P. Dario, "Integration of a miniaturised triaxial force sensor in a minimally invasive surgical tool," *Biomedical Engineering, IEEE Transaction on*, vol. 53, no. 11, pp. 2397–2400, 2006.

[192] Y. Hu, R. Katragadda, H. Tu, Q. Zheng, Y. Li, and Y. Xu, "Bioinspired 3-D tactile sensor for minimally invasive surgery," *Journal of Microelectromechanical Systems*, vol. 19, no. 6, pp. 1400–1408, 2010.

[193] P. Baki, G. Székely, and G. Kósa, "Design and characterization of a novel, robust, tri-axial force sensor," *Sensors and Actuators A: Physical*, vol. 192, no. 1, pp. 101–110, 2012.

[194] S. Song, B. Li, W. Qiao, C. Hu, H. Ren, H. Yu, Q. Zhang, M. Q.-H. Meng, and G. Xu, "6-d magnetic localization and orientation method for an annular magnet based on a closed-form analytical model," *Magnetics, IEEE Transactions on*, vol. 50, no. 9, pp. 1–11, 2014.

[195] D. M. Pham and S. M. Aziz, "A real-time localization system for an endoscopic capsule," in *Intelligent Sensors, Sensor Networks and Information Processing (ISSNIP), 2014 IEEE Ninth International Conference on.* IEEE, 2014, pp. 1–6.

[196] K. M. Popek, A. W. Mahoney, and J. J. Abbott, "Localization method for a magnetic capsule endoscope propelled by a rotating magnetic dipole field," in *Robotics and Automation (ICRA), 2013 IEEE International Conference on.* IEEE, 2013, pp. 5348–5353.

[197] S. Yim and M. Sitti, "3-d localization method for a magnetically actuated soft capsule endoscope and its applications," *Robotics, IEEE Transactions on*, vol. 29, no. 5, pp. 1139–1151, 2013.

[198] M. Salerno, R. Rizzo, E. Sinibaldi, and A. Menciassi, "Force calculation for localized magnetic driven capsule endoscopes," in *Robotics and Automation (ICRA), 2013 IEEE International Conference on*, 2013, pp. 5354–5359.

[199] Y. Nakamura, *Advanced Robotics: Redundancy and Optimization*, 1st ed. Boston, MA, USA: Addison-Wesley Longman Publishing Co., Inc., 1990.

[200] M. S. Grewal, L. R. Weill, and A. P. Andrews, *Global positioning systems, inertial navigation, and integration.* John Wiley & Sons, 2007.

[201] B. Barshan and H. F. Durrant-Whyte, "Inertial navigation systems for mobile robots," *Robotics and Automation, IEEE Transactions on*, vol. 11, no. 3, pp. 328–342, 1995.

[202] M. Kaess, H. Johannsson, R. Roberts, V. Ila, J. J. Leonard, and F. Dellaert, "isam2: Incremental smoothing and mapping using the bayes tree," *The International Journal of Robotics Research*, p. 0278364911430419, 2011.

[203] M. Kaess, A. Ranganathan, and F. Dellaert, "isam: Incremental smoothing and mapping," *Robotics, IEEE Transactions on*, vol. 24, no. 6, pp. 1365–1378, 2008.

[204] V. Indelman, S. Williams, M. Kaess, and F. Dellaert, "Factor graph based incremental smoothing in inertial navigation systems," in *Information Fusion (FUSION), 2012 15th International Conference on.* IEEE, 2012, pp. 2154–2161.

[205] L. Carlone, R. Aragues, J. A. Castellanos, and B. Bona, "A fast and accurate approximation for planar pose graph optimization," *The International Journal of Robotics Research*, p. 0278364914523689, 2014.

[206] L. Carlone and A. Censi, "From angular manifolds to the integer lattice: Guaranteed orientation estimation with application to pose graph optimization," *arXiv preprint arXiv:1211.3063*, 2012.

[207] M. Simi, P. Valdastri, C. Quaglia, A. Menciassi, and P. Dario, "Design, fabrication, and testing of a capsule with hybrid locomotion for gastrointestinal tract exploration," *IEEE/ASME Trans. Mechatronics*, vol. 15, no. 2, pp. 170–180, 2010.

[208] B. S. Terry, A. C. Passernig, M. L. Hill, J. A. Schoen, and M. E. Rentschler, "Small intestine mucosal adhesivity to *in vivo* capsule robot materials," *Journal of the Mechanical Behavior of Biomedical Materials*, vol. 15, pp. 24–32, 2012.

[209] J.-S. Kim, I.-H. Sung, Y.-T. Kim, E.-Y. Kwon, D.-E. Kim, and Y. Jang, "Experimental investigation of frictional and viscoelastic properties of intestine for microendoscope application," *Tribology Letters*, vol. 22, no. 2, pp. 143–149, 2006.

[210] A. B. Lyle, J. T. Luftig, and M. E. Rentschler, "A tribological investigation of the small bowel lumen surface," *Tribology International*, vol. 62, pp. 171–176, 2013.

[211] M. Samsom, A. Smout, G. Hebbard, R. Fraser, T. Omari, M. Horowitz, and J. Dent, "A novel portable perfused manometric system for recording of small intestinal motility," *Neurogastroenterology and Motility*, vol. 10, no. 2, pp. 139–148, 1998.

[212] J. Kim, I. Sung, Y. Kim, D. Kim, and Y. Jang, "Analytical model development for the prediction of the frictional resistance of a capsule endoscope inside an intestine," *Proceedings of the Institution of Mechanical Engineers, Part H: Journal of Engineering in Medicine*, vol. 221, no. 8, pp. 837–845, 2007.

[213] C. Bellini, P. Glass, M. Sitti, and E. S. Di Martino, "Biaxial mechanical modeling of the small intestine," *Journal of the Mechanical Behavior of Biomedical Materials*, vol. 4, no. 8, pp. 1727–1740, 2011.

[214] G. Hounnou, C. Destrieux, J. Desme, P. Bertrand, and S. Velut, "Anatomical study of the length of the human intestine," *Surgical and Radiologic Anatomy*, vol. 24, no. 5, pp. 290–294, 2002.

[215] E. Miller and D. Ullrey, "The pig as a model for human nutrition," *Annual review of nutrition*, vol. 7, no. 1, pp. 361–382, 1987.

[216] M. Beccani, C. Di Natali, L. Sliker, J. Schoen, M. E. Rentschler, and P. Valdastri, "Wireless tissue palpation for intraoperative detection of lumps in soft tissue," *IEEE Trans. Biomed. Eng*, 2013, in press, available on-line.

[217] G. Ciuti, M. Salerno, G. Lucarini, P. Valdastri, A. Arezzo, A. Menciassi, M. Morino, and P. Dario, "A comparative evaluation of control interfaces for a robotic-aided endoscopic capsule platform," *IEEE Trans. Robot.*, vol. 28, no. 2, pp. 534–538, 2012.

[218] S. J. Kline and F. A. McClintock, "Describing uncertainties in single-sample experiments," *Mechanical Engineering*, vol. 75, no. 1, pp. 3–8, 1953.

[219] K. D. Wang and G. Z. Yan, “Research on measurement and modeling of the gastro intestine’s frictional characteristics,” *Measurement Science and Technology*, vol. 20, no. 1, p. 015803, 2009.

[220] A. Irimia and L. A. Bradshaw, “Theoretical ellipsoidal model of gastric electrical control activity propagation,” *Physical Review E*, vol. 68, no. 5, p. 051905, 2003.

[221] ——, “Theoretical and computational methods for the noninvasive detection of gastric electrical source coupling,” *Physical Review E*, vol. 69, no. 5, p. 051920, 2004.

[222] ——, “Ellipsoidal electrogastrographic forward modelling,” *Physics in medicine and biology*, vol. 50, no. 18, p. 4429, 2005.

[223] J. L. Gorlewicz, S. Battaglia, B. F. Smith, G. Ciuti, J. Gerding, A. Menciassi, K. L. Obstein, P. Valdastri, and R. J. Webster III, “Wireless insufflation of the gastrointestinal tract,” *IEEE Transactions on Biomedical Engineering*, vol. 60, no. 5, pp. 1225–1233, 2013.

[224] A. C. Lehman, N. A. Wood, S. Farritor, M. R. Goede, and D. Oleynikov, “Dexterous miniature robot for advanced minimally invasive surgery,” *Surgical endoscopy*, vol. 25, no. 1, pp. 119–123, 2011.

[225] R. A. Joseph, N. A. Salas, M. A. Donovan, P. R. Reardon, B. L. Bass, and B. J. Dunkin, “Single-site laparoscopic (ssl) cholecystectomy in human cadavers using a novel percutaneous instrument platform and a magnetic anchoring and guidance system (mags): reestablishing the critical view,” *Surgical endoscopy*, vol. 26, no. 1, pp. 149–153, 2012.

[226] M. Simi, N. Tolou, P. Valdastri, J. Herder, A. Menciassi, and P. Dario, “Modeling of a compliant joint in a magnetic levitation system for an endoscopic camera,” *Mechanical Sciences*, vol. 3, no. 1, pp. 5–14, 2012.

[227] C. Richards, J. Rosen, B. Hannaford, C. Pellegrini, and M. Sinanan, “Skills evaluation in minimally invasive surgery using force/torque signatures,” *Surgical Endoscopy*, vol. 14, no. 9, pp. 791–798, 2000.

[228] S. L. Best, W. Kabbani, D. J. Scott, R. Bergs, H. Beardsley, R. Fernandez, L. B. Mashaud, and J. A. Cadeddu, “Magnetic anchoring and guidance system instrumentation for laparo-endoscopic single-site surgery/natural orifice transluminal endoscopic surgery: lack of histologic damage after prolonged magnetic coupling across the abdominal wall,” *Urology*, vol. 77, no. 1, pp. 243–247, 2011.

[229] C. Di Natali and P. Valdastri, “Remote active magnetic actuation for a single-access surgical robotic manipulator,” *International Journal of Computer Assisted Radiology and Surgery*, vol. 7, pp. S169–S171, 2012.

[230] S. Maeso, M. Reza, J. Mayol, J. Blasco, M. Guerra, E. Andradas, and M. Plana, “Efficacy of the Da Vinci surgical system in abdominal surgery compared with that

of laparoscopy: a systematic review and meta-analysis," *Annals of Surgery*, vol. 252, no. 2, p. 254, 2010.

[231] M. Simi, R. Pickens, A. Menciassi, S. D. Herrell, and P. Valdastri, "Fine tilt tuning of a laparoscopic camera by local magnetic actuation: Two-port nephrectomy experience on human cadavers," *Surgical Innovation*, vol. 20, no. 4, pp. 385–394, 2013.

[232] A. Lehman, J. Dumpert, N. Wood, L. Redden, A. Visty, S. Farritor, B. Varnell, and D. Oleynikov, "Natural orifice cholecystectomy using a miniature robot," *Surgical Endoscopy*, vol. 23, pp. 260–266, 2009.

[233] S. Yim and M. Sitti, "Design and rolling locomotion of a magnetically actuated soft capsule endoscope," *Robotics, IEEE Transactions on*, vol. 28, no. 1, pp. 183–194, 2012.

[234] C. Di Natali, M. Beccani, K. L. Obstein, and P. Valdastri, "A wireless platform for in vivo measurement of resistant properties of the gastrointestinal tract," *Physiological Measurements*, 2014, in press, available on-line.

[235] B. E. Padilla, G. Dominguez, C. Millan, and M. Martinez-Ferro, "The use of magnets with single-site umbilical laparoscopic surgery," in *Seminars in pediatric surgery*, vol. 20, no. 4. Elsevier, 2011, pp. 224–231.

[236] G. Tortora, P. Dario, and A. Menciassi, "Array of robots augmenting the kinematics of endocavitary surgery," 2014.

[237] M. Simi, M. Silvestri, C. Cavallotti, M. Vatteroni, P. Valdastri, A. Menciassi, and P. Dario, "Magnetically activated stereoscopic vision system for laparoendoscopic single-site surgery," *Mechatronics, IEEE/ASME Transactions on*, vol. 18, no. 3, pp. 1140–1151, 2013.

[238] P. Vartholomeos, C. Bergeles, L. Qin, and P. E. Dupont, "An mri-powered and controlled actuator technology for tetherless robotic interventions," *The International Journal of Robotics Research*, vol. 32, no. 13, pp. 1536–1552, 2013.

[239] J. A. Liu, M. Etemadi, J. A. Heller, D. Kwiat, R. Fechter, M. R. Harrison, and S. Roy, "Roboimplant ii: Development of a noninvasive controller/actuator for wireless correction of orthopedic structural deformities," *Journal of Medical Devices*, vol. 6, no. 3, p. 031006, 2012.

[240] C. Di Natali and P. Valdastri, "Surgical robotics and instrumentation," *Surgery*, vol. 245, no. 3, pp. 379–384, 2012.

[241] P. Berkelman and J. Ma, "A compact, modular, teleoperated robotic minimally invasive surgery system," in *Biomedical Robotics and Biomechatronics, 2006. BioRob 2006. The First IEEE/RAS-EMBS International Conference on.* IEEE, 2006, pp. 702–707.

[242] N. A. Wood, "Design and analysis of dexterous in vivo robots for notes," Ph.D. dissertation, University of Nebraska–Lincoln, 2008.

[243] D. Canes, A. C. Lehman, S. M. Farritor, D. Oleynikov, and M. M. Desai, "The future of notes instrumentation: flexible robotics and in vivo minirobots," *Journal of endourology*, vol. 23, no. 5, pp. 787–792, 2009.

[244] J. S. Agashe and D. P. Arnold, "A study of scaling and geometry effects on the forces between cuboidal and cylindrical magnets using analytical force solutions," *Journal of Physics D: Applied Physics*, vol. 41, no. 10, p. 105001, 2008.

[245] K. Ikuta, S. Makita, and S. Arimoto, "Non-contact magnetic gear for micro transmission mechanism," in *Micro Electro Mechanical Systems, 1991, MEMS'91, Proceedings. An Investigation of Micro Structures, Sensors, Actuators, Machines and Robots. IEEE.* IEEE, 1991, pp. 125–130.

[246] A. M. Chowdhury, D. Nuruzzaman, A. Mia, and M. Rahaman, "Friction coefficient of different material pairs under different normal loads and sliding velocities," *Tribology in Industry*, vol. 34, no. 1, pp. 18–23, 2012.

[247] S. L. Best and J. A. Cadeddu, "Development of magnetic anchoring and guidance systems for minimally invasive surgery," *Indian journal of urology: IJU: journal of the Urological Society of India*, vol. 26, no. 3, p. 418, 2010.

[248] S. A. Hamid and N. Simaan, "Design and synthesis of wire-actuated universal-joint wrists for surgical applications," in *Robotics and Automation, 2009. ICRA'09. IEEE International Conference on.* IEEE, 2009, pp. 1807–1813.